Supramolecular Architectures for Neural Prostheses

by

Luke Satish Kumar Theogarajan

Submitted to the Department of Electrical Engineering and Computer Science
in partial fulfillment of the requirements for the degree of

Doctor of Philosophy

at the

MASSACHUSETTS INSTITUTE OF TECHNOLOGY

June 2007

Author .....
Department of Electrical Engineering and Computer Science
May 18, 2007

Certified by .....
Marc A. Baldo
Associate Professor
Thesis Supervisor

Accepted by .....
Arthur C. Smith
Chairman, Department Committee on Graduate Students

Supramolecular Architectures for Neural Prostheses

by

Luke Satish Kumar Theogarajan

Submitted to the Department of Electrical Engineering and Computer Science
on May 18, 2007, in partial fulfillment of the
requirements for the degree of
Doctor of Philosophy

Abstract

Neural prosthetic devices offer a means of restoring function that have been lost due to neural damage. The first part of this thesis investigates the design of a 15-channel, low-power, fully implantable stimulator chip. The chip is powered wirelessly and receives wireless commands. The chip features a CMOS only ASK detector, a single-differential converter based on a novel feedback loop, a low-power adaptive bandwidth DLL and 15 programmable current sources that can be controlled via four commands. Though it is feasible to build an implantable stimulator chip, the amount of power required to stimulate more than 16 channels is prohibitively large.

Clearly, there is a need for a fundamentally different approach. The ultimate challenge is to design a self-sufficient neural interface. The ideal device will lend itself to seamless integration with the existing neural architecture. This necessitates that communication with the neural tissue should be performed via chemical rather than electrical messages. However, catastrophic destruction of neural tissue due to the release of large quantities of a neuroactive species, like neurotransmitters, precludes the storage of quantities large enough to suffice for the lifetime of the device. The ideal device then should actively sequester the chemical species from the body and release it upon receiving appropriate triggers in a power efficient manner.

This thesis proposes the use of ionic gradients, specifically K^+ ions as an alternative chemical stimulation method. The required ions can readily be sequestered from the background extracellular fluid. The parameters of using such a stimulation technique are first established by performing in-vitro experiments on rabbit retinas. The results show that modest increases ($\approx$10mM) of K^+ ions are sufficient to elicit a neural response.

The first building block of making such a stimulation technique possible is the development of a potassium selective membrane. To achieve low-power the membranes must be ultrathin to allow for efficient operation in the diffusive transport limited regime. One method of achieving this is to use lyotropic self-assembly; unfortunately, conventional lipid bilayers cannot be used since they are not robust enough. Furthermore, the membrane cannot be made potassium selective by simply incorporating ion carriers since they would eventually leach away from the membrane.

A single solution that solves all the above issues was then investigated in this thesis. A novel facile synthesis of self-assembling receptor functionalized polymers was achieved. By combining the properties of hydrophobic and hydrophilic interactions of two polymers a triblock co-polymer was synthesized. The middle hydrophobic block was composed of biocompatible polysiloxanes and further derivatized to posses ion recognition capabilities via pendant crown ether chains. The hydrophilic blocks were composed of biocompatible polyoxazolines. The self-assembling properties of the membrane were then studied by electroforming them into vesicular structures. The ion responsive properties of these polymers were then examined. These polymers show emergent behavior such as, spontaneous fusion and shape transformation to ionic stimuli due to the synergy between form and function.

The results from the thesis show that it is feasible to build a renewable chemically based neural prosthesis based on supramolecular architectures. However, there remains a lot of fundamental work that needs to be pursued in the future to bring the idea to complete fruition.

Thesis Committee:
Prof. Marc A. Baldo, EECS, MIT
Prof. Carmen Scholz, Department of Chemistry, U. Alabama, Huntsville
Prof. Jing Kong, EECS, MIT

Thesis Supervisor: Marc A. Baldo
Title: Associate Professor

Acknowledgments

It has been a very long an arduous journey and I would not have made it through the past 6 years here at MIT if not for the kindness and generosity of the people I have met along the way. My advisor Prof. Marc Baldo who was kind enough to provide an environment where I could do my work and supported my work even though it was not his main area of interest. Prof. Carmen Scholz who took me under her wing even though she realized that I did not know much chemistry she never made me feel like I could not do it. Her classical statement to me was " It will take you 10 years and 25 chemists to do what you want". I think her current estimate is revised to probably 3 Chemists(with me being one of them) and 3 years. Nevertheless, she has always entertained all my goofy ideas. Prof. Jing Kong who was kind enough to agree to serve on my thesis committee and was very patient with me regarding the final written document.

Though I did not agree with my previous advisor Prof. John L. Wyatt on certain issues, I appreciate all that he has done for me. He gave me the freedom to explore my interests and also encouraged me along the way in his own way. Dr. Joseph Rizzo, at MEEI, has always been someone I could turn to when I had difficulty finding resources or support for my ideas.

I cannot say enough about Dr. Ralph Jensen and the help he has provided me. He is not just a great mentor but has become a very good friend from whom I have learned a lot. He taught me what it was to be a great experimentalist and also patiently taught me the different aspects of retinal neurophysiology. What he has imparted also goes beyond the lab, his even keel attitude to life and general modesty is something I very much admire in him.

My namesake and one of my best friends Luke Firmansjah, a much more competent chemist than me, had an uncanny ability to make me feel like I was his equal. He always answered the most mundane questions I had about chemistry and was always willing to discuss the various aspects of the syntheses with me. Salil Desai, who I met when he was an undergrad at Carnegie Mellon and later met up with here at MIT

(much to his dismay as he constantly mentions!) has been tremendously helpful in figuring out the electroformation of vesicles. Mariana Markova, who thinks of herself as my first student and is one of my best friends, has always been a staunch supporter of my ideas and someone I could always turn to in times of need. She also designed the initial version of the power and data transmitter that I used. Kaveh Milaninia who helped me setup the chemistry lab and also helped me in any way he could along the way which made my life easier. Milan Raj who was instrumental in developing a test bench for the chips that I have designed. Greg Swider who patiently took much of the chip data, Bill Drohan who did a superb job in architecting the final version of the test bench and Shawn Kelly who helped with the power and data transmitters.

All the members of the Boston retinal implant project who have been helpful along the way, especially Lotfi Merabet who has been a very good friend and has gotten me through some tough times. The members of the soft-semiconductor group, Mihail Bora, Jon Mapel, Michael Segal, Michael Currie, Priya Jadhav, Tim Heidel, Kemal Celebi, Benjie Limetkai, Carlijn Mulder and Jiye Lee who have accepted me as one of their own. Prof. Scholz's students Jeff Sparks and especially Joy Bowman who has done quite a bit for me in a lot of ways. Prof. Scholz's post-doc Dr. Willy Vayaboury who taught me how to distill oxazoline and also on how to conduct polymerization on a Schlenk line. The members of the MIT DCIF Bob Kennedy, Jeff Simpson and Li Li who have been tremendously helpful on various aspects of spectroscopy. All my friends at MIT on the 8th floor of building 36, Jung Hoon Lee, Jay Bardhan, David Willis, Annie Vithayathil, Xin Hu, Thomas Klemas and Dimitry Vasilyev. The members of the AVNSL group for various discussions on analog VLSI and prostheses in general. Omar Roushdy who spent some long nights in the lab with me and Diana Young who has been a good friend.The Catalyst Foundation, especially Ken Suyama, and the Boston, VA for funding much of this work. MOSIS, especially Caesar Pina and Wes Hansford, who generously fabricated the chips at no cost. My friends Ron Varghese, Yatin Rao, Anjali Rao, Badari Kommandur, Leena Kamath and Dan Hartman who have gotten me through some very rough times.

Mary Rowe without whose encouragement and support I would not have made it

this far. David Feinstein, Audrey Ja-Jin Lee, John Rockway, Prof. Tom Knight and Prof. Jacob White who provided strong words of encouragement and support when I needed it the most. Prof. David Perreault, Prof. Mike Perrott and Prof. Rahul Sarpeshkar have had numerous discussions with me helping me understand various concepts along the way. Prof. Barabara Imperiali and her students for helping me get started on the synthesis. All the baristas at Starbucks on main street, especially Matt, Tamir, Laney, Amanda and Charlotte who I have now come to think of as friends provided an escape from the everyday drudgery of lab work.

On the personal side I would like to thank Mary O'Malley who has been a integral part of my life. My parents and my sister who have given me the strength of their unwavering support that has been instrumental in my success. If not for all the people that I have listed above and some that I might have inadvertently forgotten (for which I apologize), I would not have come this far. This thesis is dedicated to all of these people who have helped me get here, THANK YOU!

Contents

List of Figures

List of Tables

Chapter 1

Introduction

1.1 Motivation

Vision is arguably the most important sense that we posses and diseases that cause an impairment of this sense results in a debilitating condition. Additionally age related causes of blindness, such as age-related macular degeneration(AMD), are exacerbated by the increase in average lifespan especially in developed countries. It is imperative then, that a means of restoring a useful level of vision to these patients who have become blind be pursued.

Three main questions naturally arise and must be addressed at the outset 1) What are the diseases that will be amenable to restoration by an engineering approach 2) Where is the ideal placement of this device? 3) What are the strategies that one could use to restore vision?

The retina is often referred to as an approachable part of the brain [33] and is composed of exquisite neural circuitry that performs an amazing level of processing. Hence, the greatest chance of building a successful retinal prosthesis is to start with diseases that leave much of the retinal architecture intact. There are two such diseases that affect only the sensory transduction layer, the photoreceptor layer, of the retina. The first is AMD and the second is retinitis pigmentosa (RP), both these diseases result in a lost of photoreceptors, see figure 1-1.

The answer to the second question needs careful consideration of the pros and cons

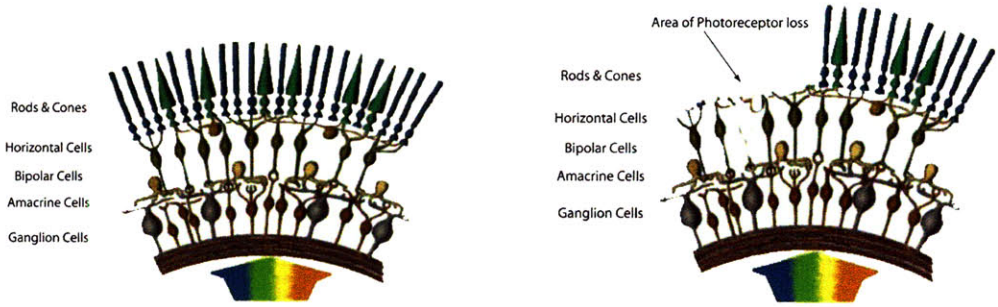

(a) Normal Retina (b) Degenerated Retina

Figure 1-1: Schematic of retinal degeneration

of placing the device in a specific location. There are three logical placements of the device 1) The retina, which can be further be divided into epi-retinal and sub-retinal. The epi-retinal referring to the side that faces the vitreous and the sub-retinal to the side that is adjacent to the choroid. 2) The visual cortex and 3) the optic nerve.

If the device were placed in the retina, and if we are able to harness much of the processing capability of the remaining intact neural tissue, it offers the most seamless and natural method. This is mainly due to the fact that it does not bypass the natural flow of information. However, it also places the most stringent demands on the prosthesis. The retina is an extremely delicate tissue with the consistency of wet tissue paper, placing a device here is a daunting surgical challenge. As to epi-retinal versus sub-retinal, the epi-retinal approach is easier form a surgical point of view but the mechanical anchoring of the implant to the epi-retinal surface is difficult [112]. A schematic of the epi-retinal approach is shown in figure 1-2. This can be alleviated by placing the device subretinally [153] see figure 1-3, though the surgery becomes more difficult.

Cortical implants offer another means of restoring visual function by placing a device that interfaces directly with the brain. This is advantageous since it does not require an intact optic nerve and hence has a wider range of diseases that can be treated. However, the columnar organization of the visual cortex [61] and the fact that much of the preprocessing that occurs in the retina and the lateral geniculate nucleus is bypassed, makes the conversion of the visual image into a meaningful

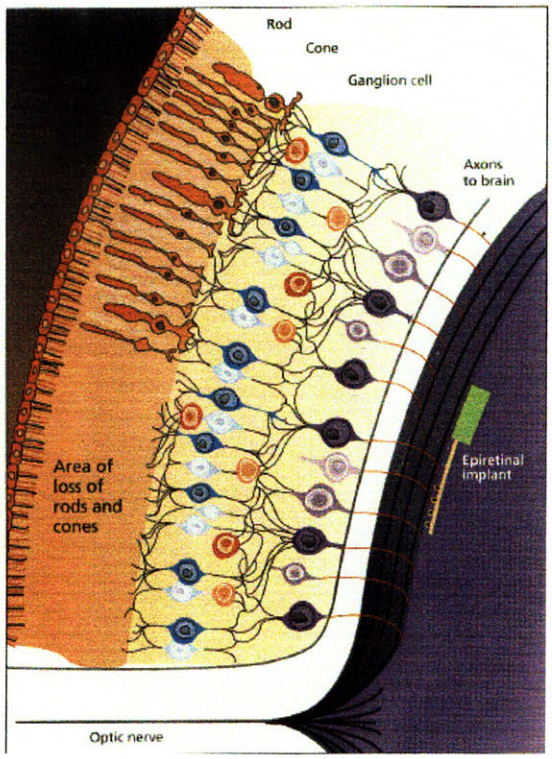

Figure 1-2: Epi-retinal placement of a retinal prosthesis. Taken from reference [112]

cortical stimulus rather difficult.

The optic nerve [138] is another possible location, this has the advantage of easy surgical access but the bundle organization makes the spatiotemporal mapping onto the optic nerve rather challenging. Though it is partially this author's bias, the placement of the prosthesis in the retina seems to be the best choice. Furthermore, since the mechanical anchoring seems to be the more difficult than the surgical task, subretinal implantation is preferred to epi-retinal implantation.

1.2 Basic neural physiology

It has been a tacit assumption until this point that there is an established method of communicating with neural tissue and that once the first two questions are answered the third question should be fairly trivial. Since the discovery of electrically excitable cells by Galvani [141], the primary method of communicating with neural tissue is

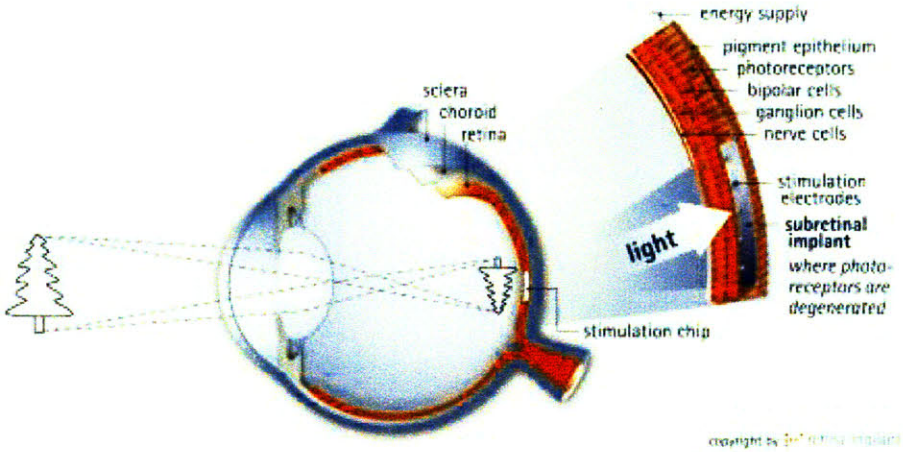

Figure 1-3: Subretinal approach for a retinal prosthesis. (source: www.eye-chip.com)

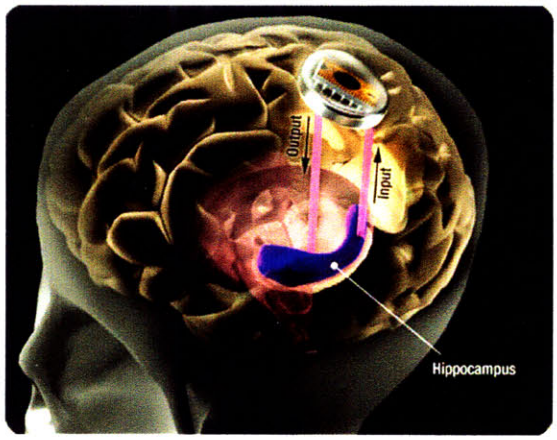

Figure 1-4: Schematic of a Cortical prosthesis.(source: http://met.usc.edu/research-/projects/bioimplantation/cortical.jpg)

by electrical stimulation. Before understanding the exact mechanism underlying the electrical excitability of cells the general characteristics of a neuron needs to be understood. A typical neuron is shown if figure 1-5, it consists of a cell body an axon and dendrites. The axon maybe myelinated depending on the type of neuron. Myelin serves as an insulating membrane since the natural neural membrane is leaky to ions, gaps in the myelination are referred to as nodes of ranvier. The reason for myelination and the gaps in them can be understood once the basic mechanism of cell firing is understood. A schematic of the neural membrane is shown in figure 1-6. The membrane is composed of a lipid bilayer and contains various ion channels and pumps. The ion channels can be voltage gated or ligand gated. Voltage gated channels are present predominantly at the axons and axonal terminals while ligand gated channels are primarily found in synaptic terminals at the dendrites. Voltage gated channels either open (normally closed) in response to a depolarizing (increasing) membrane potential or close (normally open) due to a depolarizing membrane potential. A neuron at rest maintains specific ionic gradients across its membranes and the resting values are shown in figure 1-7, also shown is the change in intracellular concentration when the cell is depolarized. The ion gradient is maintained by active pumps usually powered by ATP, the most notable is the Na^+/K^+ pump which pumps $3K^+$ into the cell and pumps out $2Na^+$ for every ATP molecule consumed. Since an active ion gradient is maintained and the membrane contains ion channels there is also a finite leakage current present which is compensated for by the active pump. The ionic gradients in-turn give rise to the resting membrane potential, V_m^0, and can be calculated by using the Goldmann equation [140] and is given in equation 1.1.

$$V_m^0 = \frac{RT}{F} \ln \left(\frac{\sum_{z_n=+1} P_n c_n^o + \sum_{z_n=-1} P_n c_n^o}{\sum_{z_n=+1} P_n c_n^i + \sum_{z_n=-1} P_n c_n^i} \right) \tag{1.1}$$

Where z_n is the valence of the n^{th} ion, P_n is the permeability of n^{th} ion, c_n^i and c_n^o are the concentrations of the n^{th} ion on the intracellular and extracellular sides respectively. The permeability is related to the partition coefficient k_n by the relationship $k_n = \frac{D_n}{d}$, where D_n is the diffusion coefficient of the n^{th} ion and d is the

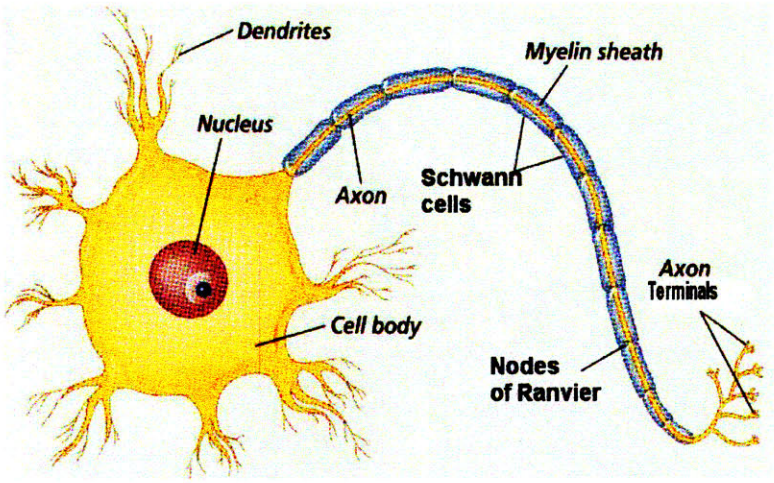

Figure 1-5: Schematic of a typical neuron. (source: www.sirinet.net/ jgjohnso/neuronproject.html)

thickness of the membrane.

The Goldmann equation can be further simplified by noting that only K^+, Na^+ and Cl^- are responsible for the generating the resting membrane potential. If all the quantities are normalized by the permeability of potassium, P_{K+}, it yields the Goldmann-Hodgkin-Katz equation given in equation 1.2.

$$V_m^0 = \frac{RT}{F} \ln \left(\frac{[K^+]^o + \frac{P_{Na+}}{P_{K+}}[Na^+]^o + \frac{P_{Cl-}}{P_{K+}}[Cl^-]^o}{[K^+]^i + \frac{P_{Na+}}{P_{K+}}[Na^+]^i + \frac{P_{Cl-}}{P_{K+}}[Cl^-]^i} \right) \tag{1.2}$$

The normalization is done to aid in understanding the magnitude of the resting membrane potential. At rest the cell is more permeable to K^+ than the other ions. Hence in the limit,$P_{K+} \gg P_{Na^+}$, the resting membrane potential should closely approximate the Nernstian potential due to the potassium ionic gradient, which can be calculated to be -86mV with respect to the extracellular potential.

Neurons communicate via chemical messengers called neurotransmitters that are released at the presynaptic terminal of the neuron and received by a nearby neuron on the post-synaptic terminal. Neurotransmitters come in two major forms the fast acting non-peptide neurotransmitters and the slow acting peptide neurotransmitters. The most common of the non-peptide neurotransmitters are acetylcholine, noradrenaline, dopamine, GABA (gamma-aminobutyric acid) and glycine. Addition-

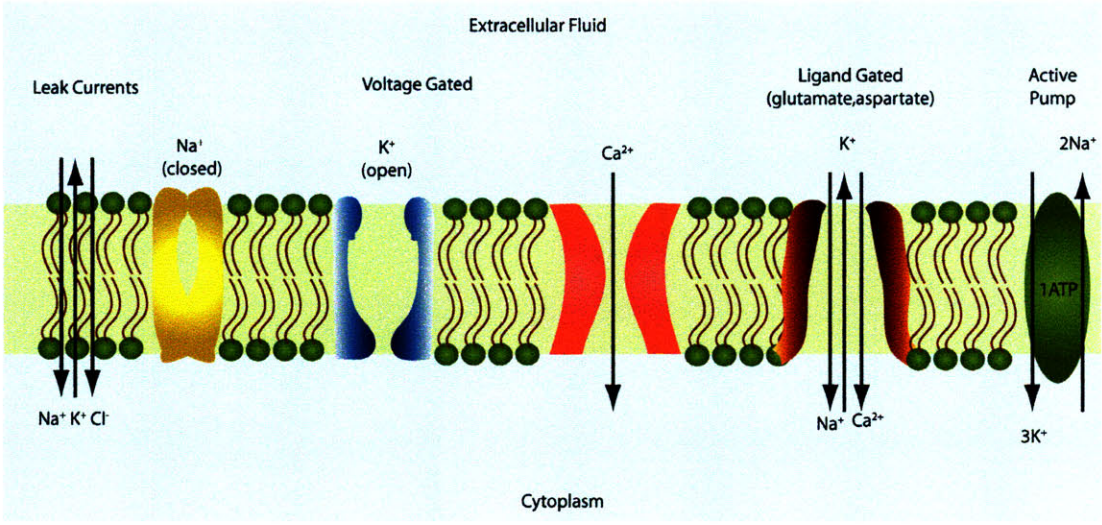

Figure 1-6: Schematic of a patch of neural membrane showing the various channels and their gating variables

ally, dopamine, noradrenaline and adrenaline, collectively called catecholamines since they are derivates of catechol are both active in both the central nervous system (CNS) and the symphathetic nervous system. When one of these neurotransmitters is bound to the appropriate receptor they produce a conformational change that changes that makes the membrane more permeable to sodium ions. To understand how this change in membrane potential initiates the action potential one must turn to the Hodgkin-Huxley model.

1.3 The Hodgkin-Huxley Model

The most quantitative and insightful model of the neuron was derived by Hodgkin and Huxley in their seminal investigation of the giant squid axon [56, 57, 58, 59]. The first step is to model the membrane in terms of electrical components. The model is shown in figure 1-8, the conductance represents the conductance of the membrane to the particular ion, the battery represents the Nernst potential due to that ion (see figure 1-7. By modeling the neuron as a cable with the intracellular fluid as the inner conductor and the extracellular fluid as the second conductor the cable model for the neuron can be developed [141]. This can the predict how the membrane potential

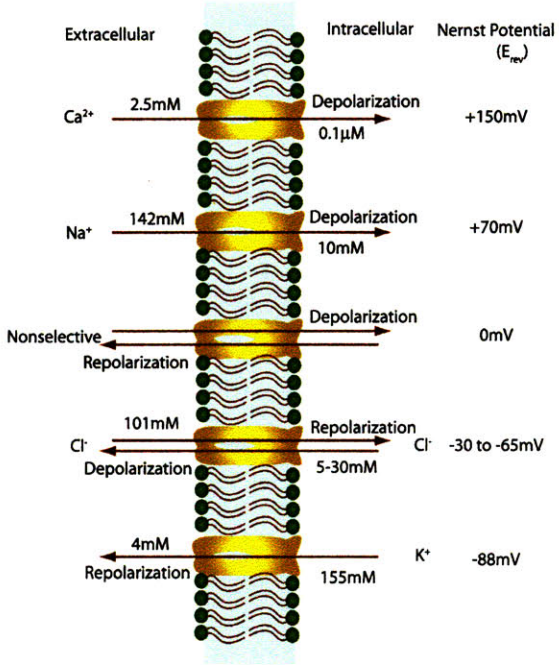

Figure 1-7: Normal Ionic concentration found in a neuron at rest. The arrows indicate the flow of ions during the generation of the action potential.

propagates.

The most important result of Hodgkin and Huxley was their explanation of the ionic basis for the neural action potential. In the model shown in figure 1-8 the ionic conductances are voltage dependent, through some very clever experimental techniques and insights they measured the voltage dependencies of these conductances. After some fitting they arrived at the following relationships for the sodium conductance, G_{Na}, and potassium conductance,G_K.

$G_K = n^4\overline{G_K}$

$G_{Na} = m^3h\overline{G_{Na}}$

$\overline{G_{Na}}, \overline{G_K}$ represents the average conductance of the channel. The parameters m,h and n follow kinetics of a first order reversible reaction [141]. The rate and time constants of these reactions are themselves dependent on the membrane potential, see figure 1-9. The nature of the constants are termed either activating or inactivating. Both m and n is an activating parameter meaning that higher values increase channel conductance and h is inactivating in nature. Hodgkin and Huxley did physical mea-

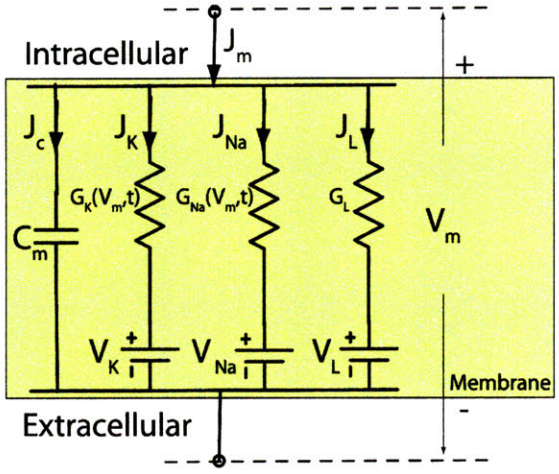

Figure 1-8: Electrical model of a patch of neural membrane. The values of the voltages are equal to the resting Nernst potential for that ion.

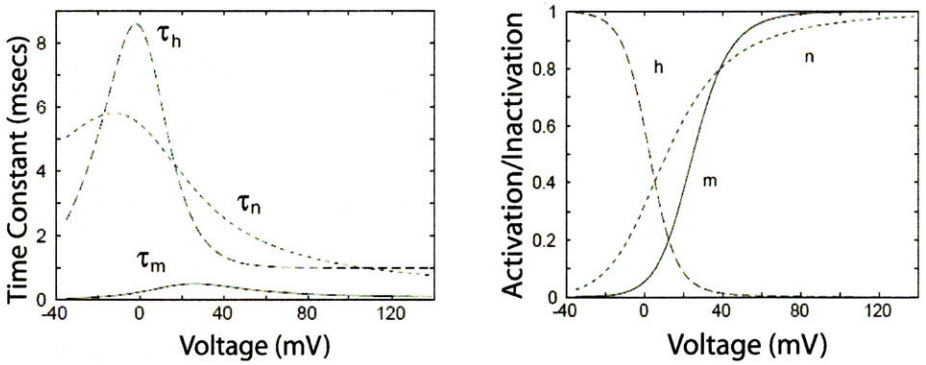

Figure 1-9: Voltage dependency of the activation and inactivation parameter of the Hodgkin-Huxley model

surements and predicted the voltage dependency using physical arguments and the exact form of their equations can be found in Weiss [141]. Instead of going over their arguments the benefit of hindsight will be used here to arrive at the same equations via the molecular basis of ion gating.

Instead of abstractly considering the parameter m,h and n, they can be thought of as the voltage dependent probability of the channel opening and closing. This directly leads to the answer for the next question of the origin of the exponent. If the potassium channel can be considered to be gated by 4 independent channels then this would mean that the probabilities would multiply, yielding the fourth power depen-

dence. Similarly a model can be derived for the sodium channel with 3 independent channels whose probabilities of being *open* increases as the voltage increases and 1 channel whose probability of being *closed* increases as the membrane potential increases. A schematic version of this model is shown in figure 1-10. To develop of quantitative model for the different gating parameters, one can model the open and closing of a channel as a reversible chemical reaction [141], similar to the one put forth by Hodgkin and Huxley.

$C \overset{\alpha,\beta}{\longleftrightarrow} O$

If $\eta(t)$ is the total number of channels/unit area that are open at any given time, t and if N is the total number of channels/unit area. Then one can write the rate of opening of channels as the difference between the number of channels going from closed to open state and the number of open channels going to closed state

$\frac{d\eta(t)}{dt} = \alpha(N - \eta(t)) - \beta\eta(t)$

Dividing the above equation by N and defining $\chi(t)$ as the probability that the channel is open yields

$\frac{d\chi(t)}{dt} = \alpha(1 - \chi(t)) - \beta\chi(t)$

or $\frac{d\chi(t)}{dt} + (\alpha + \beta)\,\chi(t) = \alpha$

This is a first order differential equation, the solution to which can be found by summing the responses of the natural or the zero-input response and the steady state response. The zero-input response can be obtained by setting the differential equation to zero i.e.

$\frac{d\chi(t)}{dt} + (\alpha + \beta)\,\chi(t) = 0$, separating the variables and integrating yields

$\int \frac{d\chi(t)}{\chi(t)} = -\int \frac{1}{(\alpha+\beta)} dt$

$\ln \chi(t) = -\frac{1}{(\alpha+\beta)} t + C$

$\chi(t) = Ae^{\frac{-t}{\tau}}$ where $\tau = \frac{1}{(\alpha+\beta)}$. Both A and C are constants that can be determined from the boundary conditions. The particular solution is the steady state response when $t = \infty$ and $\frac{d\chi(t)}{dt} = 0$, therefore $\chi(\infty) = \frac{\alpha}{(\alpha+\beta)}$, so the entire solution is the sum $\chi(t) = Ae^{\frac{-t}{\tau}} + \chi(\infty)$. At time t=0, we have $\chi(0) = A + \chi(\infty)$ and therefore we have $A = \chi(0) - \chi(\infty)$ or $\chi(t) = (\chi(0) - \chi(\infty))\, e^{-\frac{t}{\tau}} + \chi(\infty)$. The proper definition of $\chi(t)$ is state occupation probability. Now an expression for the rate constants α, β can be

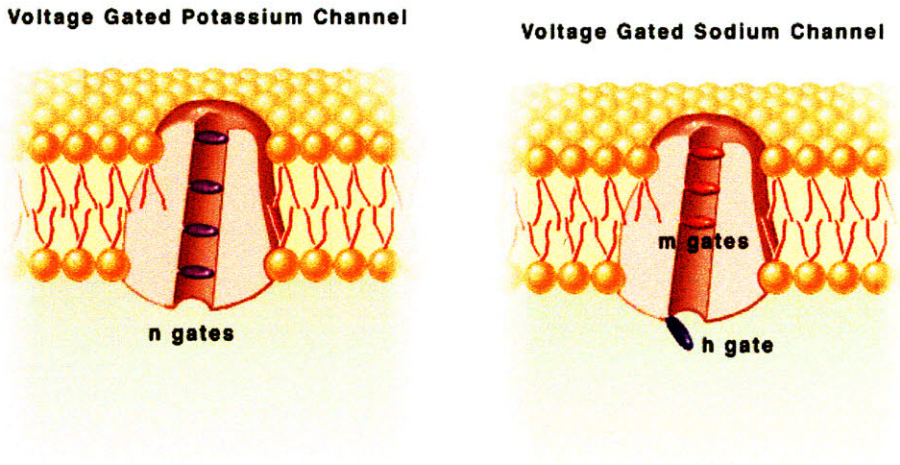

(a) (b)

Figure 1-10: A schematic model of the molecular basis of the activation and inactivation parameters of the Hodgkin-Huxley model. Source http://www.lib.mcg.edu/edu/eshuphysio/program/section1/1ch4/s1ch4_11.htm

found. Since the opening and closing was modeled as a reversible chemical reaction, the transition state theory (TST) can be used to get an expression for α and β. The forward and reverse rates will then be given by $\alpha = Ae^{\frac{E_B - E_C}{kT}}$ and $\beta = Ae^{\frac{E_O - E_B}{kT}}$, where E_B represents the energy of the transition state in the reaction co-ordinate, E_C the energy of the channel in the closed configuration and E_O is the energy of the channel in its open configuration, see figure 1-11a.

The steady value $\chi(\infty)$ can then be expressed as

$$\chi(\infty) = \frac{1}{1 + e^{\frac{E_O - E_C}{kT}}} \tag{1.3}$$

Equation 1.3 shows that the steady state probability of a channel going from the closed to open only depends on the difference in energy between the open and closed states. The voltage dependency of the rate constant can be modeled by a simple intuitive model by reflecting the change in membrane potential as a change in the energy of the open state of the channel [141], see figure 1-11b. An explanation as to why only the energy of the closed state of the channel gets affected by the membrane potential can be explained by figure 1-12. Here, the gating action is modeled as the change in

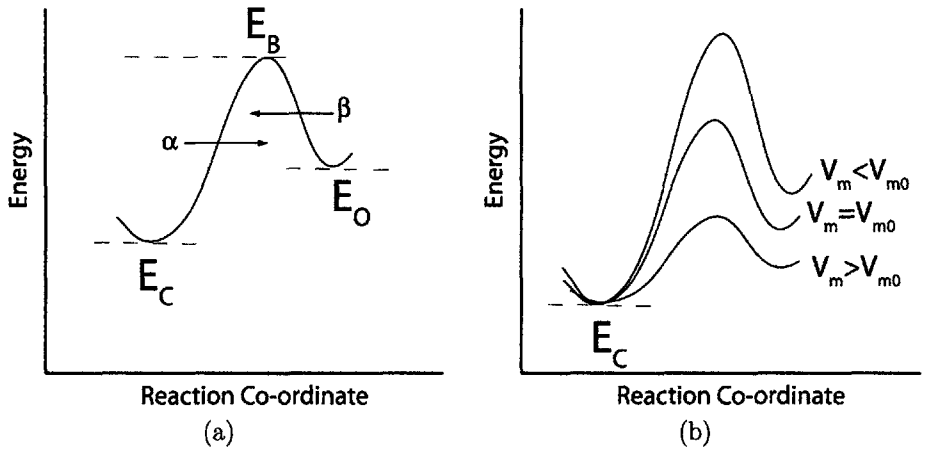

Figure 1-11: Modeling of the channel as a first order reaction a) Reaction modeled with no voltage dependence b) Reaction modeled with the energy of the closed state depending on the membrane potential. Adapted from [141]

position of an electric dipole of length l. The energy of the closed state is independent of the gating electric dipole since it is perpendicular to the electric field setup by the membrane potential. However in its open state, the energy is given by the product of the field V_m/d and the dipole moment Ql of the electric dipole i.e. the energy in the open state is $QV_m\frac{l}{d}$. Though this gives an intuitive picture of how the parameters can be derived from a molecular basis it does not fit all the observed phenomena. A more advanced model can be constructed by using a multistate channel rather than just the two states assumed here, see Weiss [141] for a detailed explanation.

After having developed an intuitive picture of the molecular basis for all the parameters, we can now develop a full model for the generation of an action potential. From the electrical model, the total membrane current J_m is given by

$$J_m = J_C + J_{Na} + J_K + J_L$$

$$J_m = C\frac{dV_m(t)}{dt} + G_{Na}(V_m - V_{Na}) + G_K(V_m - V_K) + G_L(V_m - V_L)$$

$$J_m = C\frac{dV_m(t)}{dt} + m^3h\overline{G_{Na}}(V_m - V_{Na}) + n^4\overline{G_K}(V_m - V_K) + G_L(V_m - V_L)$$

In steady state with no external currents $J_m = 0$, however, if there is some brief current injected into the interior of the cell $J_m = J_{inj}(t)$ then the membrane potential

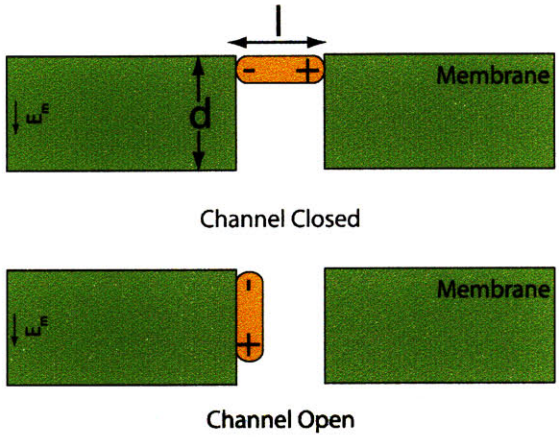

Figure 1-12: Modelling of the channel open and closing as a movement of an electric dipole. The membrane potential affects only the dipole moment only when the channel is open since the field is perpendicular to the dipole when the gate is closed. Adapted from [141]

will adjust to account for the change. The changing membrane potential, however, changes the conductances of sodium and potassium channels, since as noted earlier it changes the probability of a channel opening and closing. The actual shape of the Hodgkin-Huxley parameters plays a crucial role. Figure 1-9a reveals that the time constants of the all the HH parameters are not the same. The shapes of m and n are similar with m having a steeper slope, in electrical parlance the small signal gain $\frac{dm}{dV_m}$ is higher than that for n. The shape of h is a reflection of m about the y-axis, indicating that it is inactivating (gain is inverting). The more important differences that play a significant role in the generation of the action potential is the time constants τ_m, τ_h and τ_n. The time constant for the activating parameter for the sodium channel τ_m is much smaller than both the inactivating parameter h and the potassium channel activating parameter n. This indicates that the activation of the sodium channel is much faster than its inactivation. The potassium channel is slow to begin with but speeds up as the membrane potential increases. How do these differences reflect in the generation of the action potential? At rest the membrane potential will closely resemble the potassium Nernst potential which is negative for normal ionic gradients. As soon as the membrane potential increases the sodium channel conductance increases faster than the potassium channel conductance. This allows for an inward

rush of sodium which increases the membrane potential toward the sodium Nernst potential which is positive for normal ionic gradients. As the membrane potential increases both the inactivating parameter h and the potassium channel parameter n eventually start competing with the activating sodium channel parameter. The inactivating gate reduces the effect of sodium i.e. closes the channel while simultaneously the potassium channel increases the potassium channel conductance. Since the membrane potential is a weighted average it will be biased more toward the potassium Nernst potential and the membrane potential will start decreasing. The overall effect being a rise in the membrane potential after the stimulus and then a decrease after sometime giving the characteristic shape of the action potential. This is illustrated in figure 1-13 obtained by simulating the Hodgkin-Huxley model using a simulator [133]. It can be seen in the conductance graphs shown in figure 1-13 that the sodium conductance rises much faster than the potassium conductance. The potassium conductance, however, has a much higher resting value than the sodium conductance. Also shown are the activation and inactivation parameters to illustrate how they influence the action potential. Another way to look at the generation of the action potential is to think of two independent feedback loops that are working concurrently. One, the activating parameter of the sodium channel, is a positive feedback loop since increases in membrane potential increase the conductance which further increases the membrane potential. The second is an inactivating negative feedback loop that decreases the membrane potential as that particular parameter increases, one by reducing the positive feedback and two via the increase in potassium channel conductance that increases the negative feedback. In the beginning the positive feedback loop is dominant and later the negative feedback takes over restoring the system back to its resting condition. This delicate interplay depends on the actual channel parameters, in fact it is possible to get oscillatory behavior by adjusting the value of the negative and positive feedback loops. Though the entire argument has been made by injecting a small current intracellularly so as to make the positive feedback loop active, the same effect can be achieved by changing the membrane potential via ligand gated channels as it happens in the natural system. Propagation can be under-

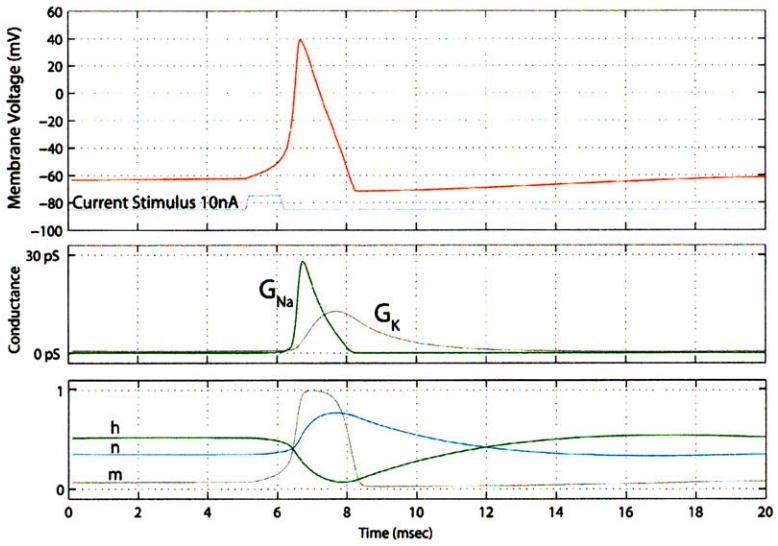

Figure 1-13: Simulation of the Hodgkin-Huxley model using the HHsim program. The action potential is shown in the top trace, the sodium and potassium conductances are shown in the middle trace and the time course of the Hodgkin-Huxley parameters are shown in the bottom trace. The resting value of the potassium conductance is 0.25mS/cm^2 while the resting value of the sodium conductance is $0.3\times10^{-3}\text{mS/cm}^2$

stood by coupling the Hodgkin-Huxley model to the cable model, see Weiss [141] for an excellent explanation. The voltage gated channels along the membrane regenerate the action potential as it propagates along the axon. However, this mechanism is slow and ineffective for very long signalling distances. In these cases the neuron has voltage gated channels only at certain repeat points and it is a passive cable between these points. To enhance the speed of conduction along the passive cable the neuron is myelinated so as to minimize the leakage currents from the membrane. This myelination is broken at points where the voltage gated channels are present, the nodes of ranvier as shown in figure 1-5, serve to regenerate the action potential much like a repeater station in conventional communication channels.

1.4 Electrical Excitation of Neurons

The key to action potential generation is the control of the membrane potential. A very simple and intuitive model can be developed [84] and more sophisticated models are available, see the following references [36, 117, 108, 107]. Ideally a voltage would

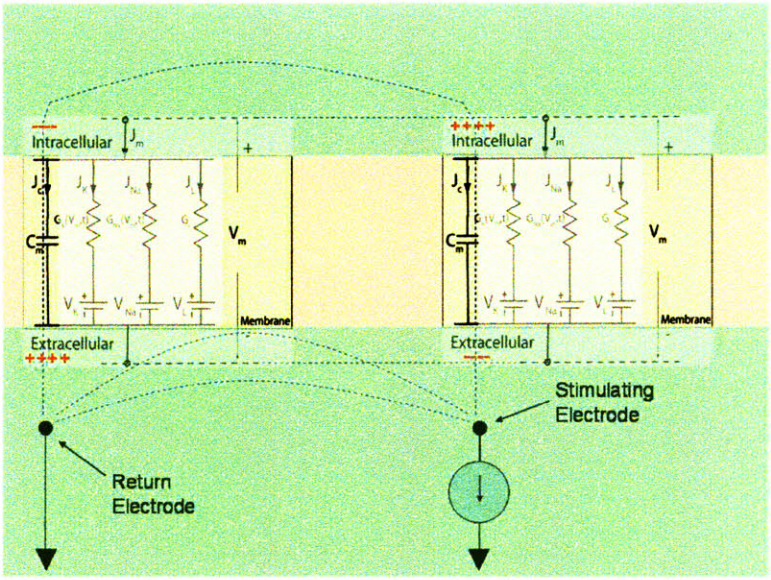

Figure 1-14: Electrical Stimulation of neurons by injecting an current in the vicinity of the neuron. A fraction of the current will flow through the membrane capacitance charging the membrane, see text for details.

be placed across the membrane, unfortunately one cannot do this without causing damage to the cell. Hence a non-invasive method needs to be adopted. Considering the electrical model of the membrane patch in figure 1-8, it would be natural to think that applying an extracellular potential would couple it intracellularly via the resistances in the membrane. However, these resistances are ion specific and are not electrically accessible since the rearrangment of ions due to an applied potential is not ion specific. Furthermore, these ion will predominantly be composed of sodium and chlorine ions since the are the dominant species extracellularly and the channels at rest are highly impermeable to these ions. So from an electrical perspective the ion channels can be neglected and the access is primarily via the membrane capacitance. This rules out the direct modulation of the intracellular potential via an extracellular applied voltage.

An alternative is to inject current in the vicinity of the neural membrane, as shown in figure 1-14. Some of this current will charge the membrane, with current flowing out of the membrane depolarizing the membrane and current flowing into the membrane hyperpolarizing it. Hence for a patch that depolarizes there will be another patch

nearby that will hyperpolarize due to the change in the current direction [106]. For electrical stimulation to be highly effective the electrode must be fairly close to the neuron. The other problem is that the low resistivity of the surrounding electrolyte compared to the neural membrane will also shunt much of the current away from the nerve if the electrode is not very close.

1.5 Alternatives to Electrical Stimulation

The exponential growth in microelectronics and microfabrication makes it possible to fabricate fairly sophisticated devices in an extremely small area. Naturally one would assume that this enables the goal of making the retinal prosthesis a reality. Unfortunately, electrical stimulation typically suffers from the following challenges 1) High current densities that are neurotoxic 2) Need for an external high power supply 3) The diverging nature of the field that leads to non-focal stimulation and 4) The need to protect the electrical components from the biological environment.

The other way of communicating with neural tissue is to mimic biology, i.e. stimulate tissue using neurotransmitters. This is obviously the preferred approach but it suffers from the issue of renewability. Unlike the ubiquitous electron, neurotransmitters need to be replenished by either synthesizing them *in-situ* or by storing a large enough quantity to last the lifetime of the device. The first solution is too complex to be implemented with current technology and the latter poses a serious risk should there be a leak from the storage system, since large quantities of neurotransmitter are highly toxic.

Clearly there is a need for a fundamentally different approach. The ultimate challenge is to design a self-sufficient neural interface. The ideal device will lend itself to seamless integration with the existing neural architecture. Communication with the neural tissue should then be performed via chemical rather than electrical messages. Since storage of the chemical species is not viable, the ideal device then should actively sequester the chemical species from the body and release it upon receiving appropriate triggers in a power efficient manner. One such approach that

will be pursued in this thesis is the communication with the interior of the neuron via the ion channels using the specific ions, namely K^+ ions.

1.6 Organization of this thesis

This thesis is divided into two main parts. In the first part a conventional electrical approach is discussed, the major contribution of this work being the development of a wirelessly powered implantable stimulator chip capable of receiving and responding to external commands. In the second part of this thesis the idea of building a renewable chemical prosthesis is developed. The fundamental building block for such a prosthesis is a self-assembling selective membrane and the synthesis and characterization of such a membrane will form the second part of this thesis. Chapter 2 is basically part I and elucidates the design and implementation of the stimulator chip. Chapter 3 discusses the overall idea of how a supramolecular prosthesis can be designed. Chapter 4, presents the data from the *in-vitro* neural recordings from rabbit retinal ganglion cells that support the hypothesis of using ionic stimulation. Chapter 5 gives experimental details on the various synthetic chemical aspects of the membrane. Chapter 6 discusses the self-assembling characteristics of these membranes. Chapter 7 concludes and touches upon future work.

Chapter 2

Low Power Implantable Stimulator Chip

As explained in chapter 1 the goal of an artificial retinal prosthesis is to stimulate the remaining healthy layers of retinal neurons using brief biphasic pulses of current. These current pulses produce a sensation of vision in the brain which is termed a phosphene. We hope that over time that the patient will be able to integrate these phosphenes into useful vision. A key step toward this goal is the development of a chronic implant. Our design philosophy is based on the following requirements: 1) the implant must be powered via an external source (i.e. no batteries). 2) Ability to communicate wirelessly with the implant via external commands. 3) Allow for parameter tuning i.e. current amplitude, duration and interpulse timing. The first and second constraints were met by using an inductively coupled power and data link. The third was enabled by implementing a flexible stimulator chip architecture as discussed in section 2.1.1.

Our physical implant design is based on a minimally invasive ab-externo approach, which is schematically shown in figure 2-1. In this approach only the electrode array is placed in the sub-retinal space (underneath the retina), while the secondary coils and stimulator chip are placed outside on the eyeball.This technique minimizes the number of components that are placed in these retinal space which provides the following key advantages: 1) Minimizes the risk of infection due to the implant 2)

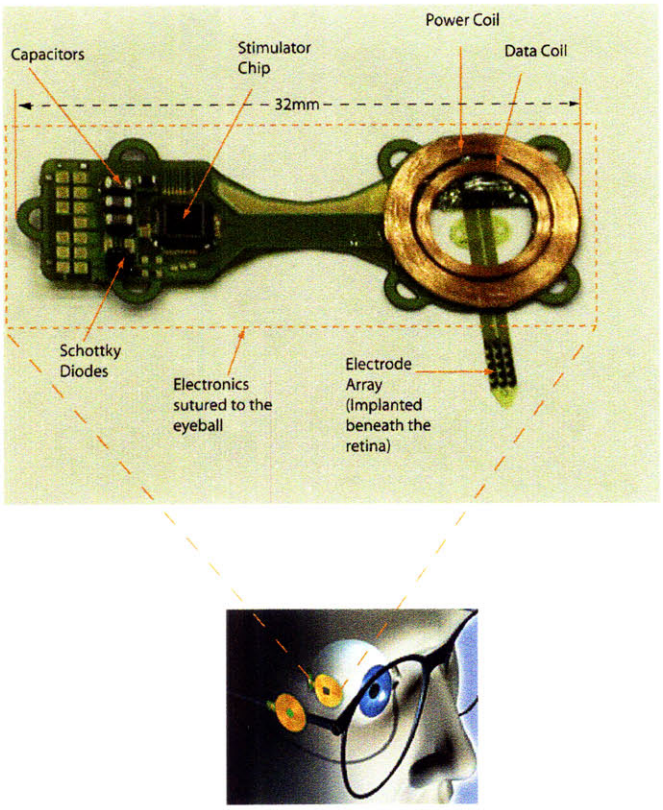

Figure 2-1: Schematic representation of the minimally invasive ab-externo approach. The transmitter coils are placed outside on a pair of eyeglasses and the receiver coils and the stimulator chip are placed on the eyeball. The electrode array is placed in the subretinal space through a scleral flap.

Increases the amount of power that can be safely transmitted to the secondary 3) Larger physical space in which the implant resides which allows for larger secondary coils.

2.1 Stimulator Chip

2.1.1 Architectural Overview

The basic architecture of the stimulator chip is shown in figure 2-2. The chip is powered via an inductive link; the power signal is rectified and filtered using off-chip diodes and capacitors with the nominal supply voltage being $\pm$ 2.5V. The data is received through a separate coil placed concentric to the power coil. The digital

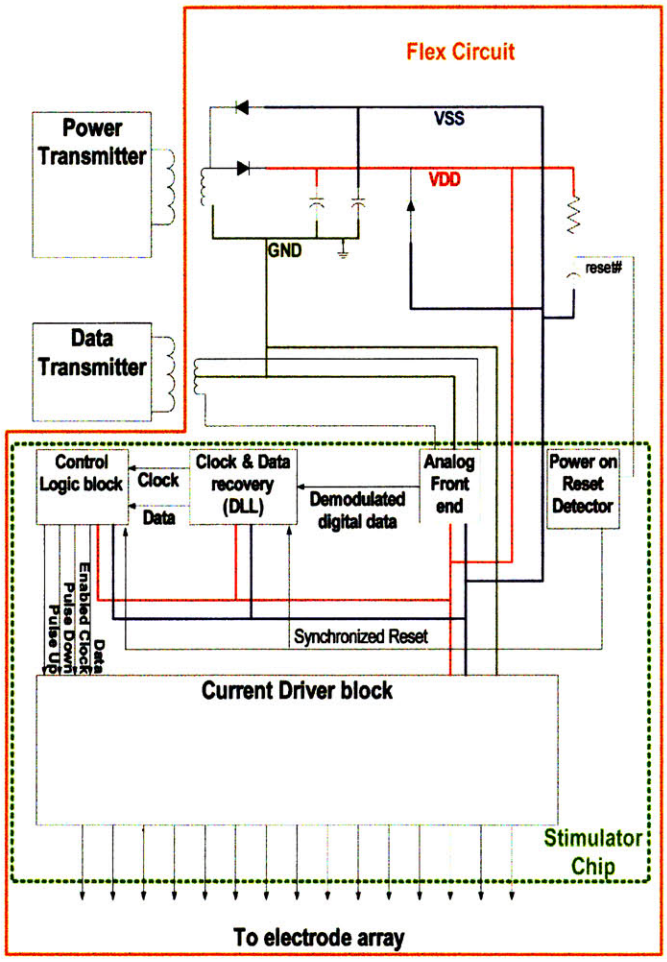

Figure 2-2: Architectural overview of the current retinal implant. The blocks that correspond to the stimulator chip are outlined in green. The chip receives data and power through two separate inductive links, demodulates the signal, recovers the data and the clock and outputs biphasic current pulses upon receiving the appropriate commands.

data is transmitted using as an amplitude shift keyed (ASK) waveform. The carrier frequencies of the power and data are 125 KHz and 13.56 MHz respectively. The front-end decouples the power and data signals, demodulates and restores the data signal to digital levels. The symbol is encoded as a pulse width modulated signal, a 50-50% duty cycle encodes a 0 and 30-70% duty cycle encodes a 1. The data and clock are recovered by the delay locked loop and fed to a control logic block. The signals from the control block control the current driver array which outputs biphasic current pulses to the electrode array.

2.1.2 Analog Front-End

Due to the nature of transmission the power signal is a very strong noise source on the data coil and needs to be filtered. Though active filtering was originally pursued the linearity requirement increased the power dissipation and hence was abandoned. A passive three stage RC high-pass filter was chosen instead due to its inherent linearity and gives sufficient attenuation of the power signal due to the large separation between the power and data frequencies.

A transistor only current biasing network was designed to bias all the circuits in the analog front end and is shown in figure 2-3. A transistor only implementation was chosen for the low area and portability to other processes. The circuit is based on the classical constant gm current reference [66], the resistor here being implemented by a transistor in the linear regime. Transistors M1-M8 and Mr from the core of the bias network. Transistor Mr is forced into the linear regime due to the feedback present in the loop. The feedback forces the drain of the transistor Mr to be V_{eff} (i.e. $V_{gs1} - V_t$), If the ratio of M1 to M3 is chosen to be 4, while its gate is at $4V_{eff} + 2V_t$ as demanded by the feedback network, since $V_{ds} < V_{gs} - V_t$ the device will be in the linear regime. Ignoring the body effect, the current I_b through the bias network can be determined as shown in equation 2.1. Since transistor Mr is the linear regime,
$I_b = K_r((4V_{eff} + 2V_t - V_t)V_{eff} - \frac{V_{eff}^2}{2})$ where $V_{eff} = V_{gs1} - V_t = \sqrt{\frac{2I_b}{K_1}}$
$I_b = K_r((4\sqrt{\frac{2I_b}{K_1}} + V_t)\sqrt{\frac{2I_b}{K_1}} - \frac{I_b}{K_1})$
$I_b(1 + 8K_r\frac{1}{K_1} + \frac{1}{K_1}) - K_rV_t\sqrt{\frac{2I_b}{K_1}} = 0$
Solving the quadratic in $\sqrt{I_b}$ and squaring gives

$$I_b \cong 8K\mu_nC_{ox}\frac{W_r}{L_r}V_t^2, K = \frac{1}{\frac{W_1L_r}{W_rL_1} + 49\frac{W_rL_1}{W_1L_r} - 14} \tag{2.1}$$

A novel envelope detector was designed to demodulate the data and is shown in figure 2-4a. The circuit basically works like a diode; however it decouples the input and the output. The basic principle that the circuit works is that source coupling of NMOS transistors leads to the source following the greater of the input signals [17, 101]. This property when combined with negative feedback forces the circuit

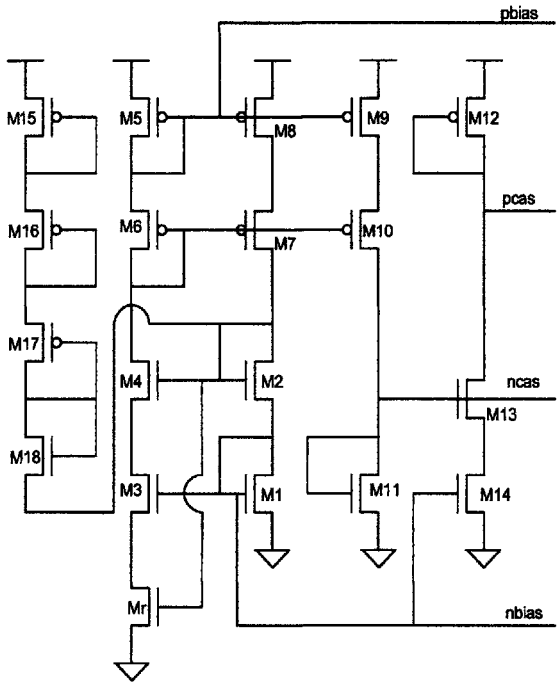

Figure 2-3: Transistor only bias network that is used to bias the analog front end blocks. The circuit is a modification of the classical constant gm current source with transistor Mr playing the role of the resistor.

to follow the greater of the two signals much like a diode, however here the turn-on voltage can be completely controlled. The other transistors in the circuit form a folded cascode load which yields higher open loop gains.

For demodulation purposes the inputs to the circuit are the differential ASK waveform from the passive filter. The circuit will then effectively full wave rectify the signal and by placing a moderate capacitive load at the output only the slower data signal will be followed. The cascode load also helps in lowering the load capacitance that needs to be used. The circuit uses total current of 7.2μA (36μW of power with a 5V supply) and can demodulate data signals till 1.356 MHz. The advantage of the above circuit over the conventionally used peak detector demodulators is that it does not need any tunable leak currents that control the release characteristics. This is crucial in the current implementation since the falling edges encode the symbol and any distortion of the pulse width in the demodulation process will lead to spurious data recovery. The only disadvantage of not using a peak detector like characteristic

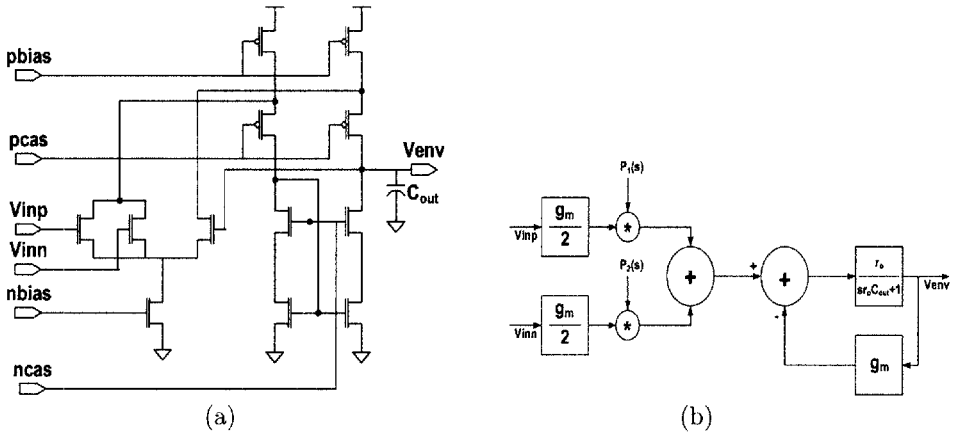

Figure 2-4: a): The ASK demodulator based on the source coupling property of nmos transistors. b) The canonical model for the demodulator, where P1(s) and P2(s) are the laplace transform of the signals p1(t) and p2(t) as described in the text and $\circledast$ represent a convolution.

is that the entire half lobe of the sine wave is integrated so there is an attenuation factor. A canonical model, shown in figure 2-4b, can be developed if we model the rectification action as a multiplication of the input signal by a square wave.

The positive input gated by a square wave $p_1(t)$ which has the rising edge located at $t = 0^+$ and the falling edge at $t = \frac{T}{2}$. The negative input is gated by $p_2(t)$ which has the falling edge at $t = \frac{T}{2}$ and the falling edge at t=T. The transfer function can then be derived as shown in equation 2.3.

$V_{env} = \frac{g_m}{2}(V'_{inp}(s) + V'_{inn}(s))\frac{r_o}{g_m r_o + 1 + sCr_o}$

where $V'_{inp}(s) = P_1(s) \circledast V_{inp}(s), V'_{inn}(s) = P_2(s) \circledast V_{inn}(s)$

$V_{env} = \frac{1}{2}(V'_{inp}(s) + V'_{inn}(s))\frac{1}{1+\frac{1+sCr_o}{g_m r_o}}$

since $\frac{1}{g_m r_o} << 1, V_{env} \cong \frac{1}{2}(V'_{inp}(s) + V'_{inn}(s))\frac{1}{1+\frac{sCr_o}{g_m r_o}}$

if $\frac{sC}{g_m} >> 1$, then $V_{env} \cong \frac{1}{2}(V'_{inp}(s) + V'_{inn}(s))\frac{g_m}{sC}$

Defining

$$p_1(t) = \begin{cases} 1, 0 \le t \le \frac{T}{2} \\ 0, \frac{T}{2} \le t \le T \end{cases}$$

$$p_2(t) = \begin{cases} 0, 0 \le t \le \frac{T}{2} \\ 1, \frac{T}{2} \le t \le T \end{cases}$$

By converting the equation into the time domain and since $T = \frac{2\pi}{\omega_c}$,

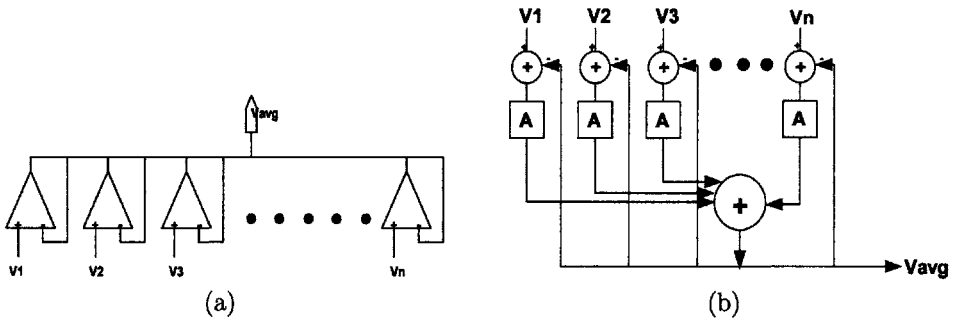

Figure 2-5: Principle of the averaging amplifier a) schematic form b) canonical form

$$v_{env}(t) = \frac{g_m}{2C}\left(\int_{nT}^{nT+\frac{T}{2}} v_{inp}(t)dt + \int_{nT+\frac{T}{2}}^{(n+1)T} v_{inn}(t)dt\right) \tag{2.2}$$

If we assume that the carrier amplitude is assumed to be constant through the peroid of the carrier cycle and also the carrier to be sinusoidal. Then the amplitude of the inputs can be rewritten as

$v_{inp}(t) = \sum_{n=0}^{\infty} V_p(n)Sin(\omega_c t)$ and $v_{inn}(t) = \sum_{n=0}^{\infty} V_n(n)Sin(\omega_c t + \pi)$, inserting this into equation 2.2 and integrating gives

$$v_{env}(t) = \frac{\omega_o}{\omega_c}\sum_{n=0}^{\infty}(V_p(n) + V_n(n)) \tag{2.3}$$

The result in equation 2.3 makes intuitive sense since the detector has a low pass characteristic and the carrier is attenuated by the ratio of the cut-off frequency to the carrier frequency. Due to this inherent attenuation of the demodulator and the additional attenuation introduced by the passive filter some amplification is required to enable the detector to detect low signal levels. So an amplification stage with a gain of 2 was placed after the demodulator. This gain stage was implemented without using any resistors and was done using the principle of averaging amplifiers, which for two stages degenerates to a differential difference amplifier (DDA) [116]. A simple average (weighted if the current sources are scaled differently) can be performed by coupling n followers [85] as shown in figure 2-5. The output will follow the average between the n signals as shown in equation 2.4.

$V_{out} = A\left(\sum_{i=1}^{n}(V_i - V_{out})\right) = A\sum_{i=1}^{n} V_i - nAV_{out}$

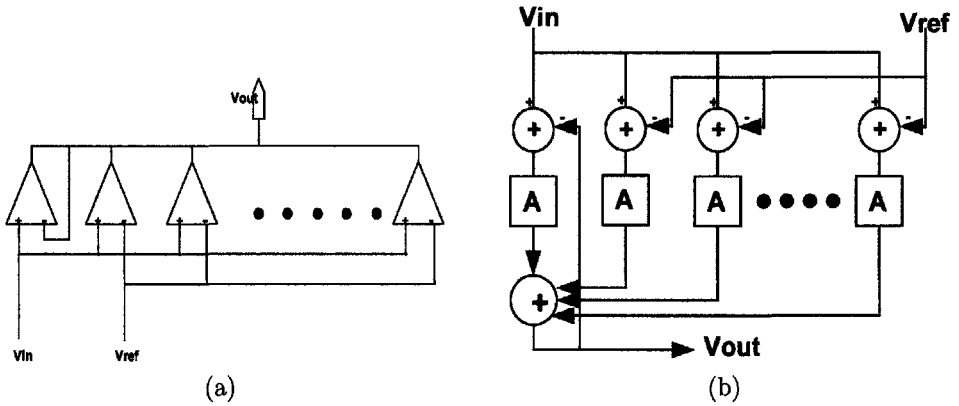

Figure 2-6: Principle of precise amplification without using resistors. a) schematic representation b) canonical forms

$$V_{out} = \frac{A}{nA+1}\sum_{i=1}^{n} V_i \cong \frac{1}{n}\sum_{i=1}^{n} V_i \tag{2.4}$$

However, if the output is not fed back to all the n amplifiers and the input to all the amplifiers are the same, as shown in figure 2-6a then amplification by a factor of n will occur as is shown using the feedback block diagram in figure 2-6b. Of course the n-1 amplifiers can also be replaced by a single one with a current source which is scaled by a factor of n-1, as derived in equation 2.5. A gain of 2 was chosen for this implementation to save area, power and ensure reasonable bandwidth.

$$V_{out} = A(V_{in} - V_{out}) + A(n-1)(V_{in} - V_{ref}) = nA(V_{in} - V_{ref}) + AV_{ref} - AV_{out}$$

$$V_{out} \cong nA(V_{in} - V_{ref}) + V_{ref} \tag{2.5}$$

The negative envelope can be recovered if a P-input demodulator was used instead of the N-input version shown here since the P-source coupled pair will follow the minimum of the input signals.

2.1.3 Peak Locked Loop

The small signal output from the demodulation stage needs to be restored to digital levels. A simple implementation would be to employ a comparator with a signal

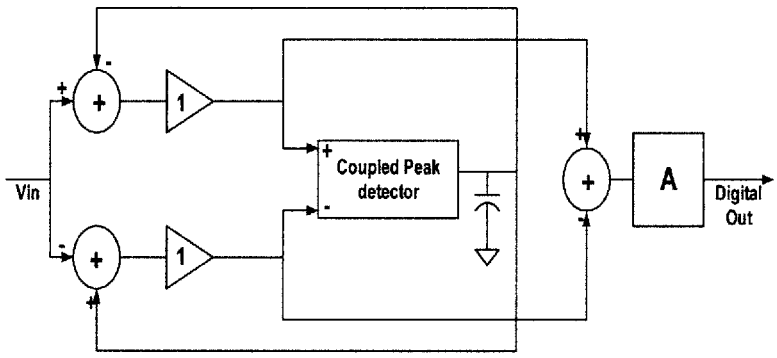

Figure 2-7: Block diagram of the Peak locked loop.

derived reference level. However, the value of this reference level is crucial since its value can change the pulse width of the signal. Since the symbol is encoded in the pulse width, maintaining pulse width integrity is crucial. A simple averaging cannot be used due to the varying duty cycle, another solution is to use an alternate mark encoding [81]. This however compromises the noise margin between the one and the zero and precludes the possibility of transmitting more than a single bit per cycle in future implementations.

To solve this problem a single-differential converter using a novel feedback loop was invented and termed the peak locked loop (PeaLL). The PeaLL is shown in canonical form in figure 2-7. The peak locked loop intuitively works as follows: the incoming signal is inverted with a gain of one using an arbitrary reference level, the peak of this waveform is compared with the a buffered version (for matching purposes) of the incoming signal and the difference drives a charge pump which moves the reference level, this locks the two signal and creates a truly differential signal which can be fed to a comparator. In actual implementation both the positive and negative waveforms are moved towards each other.

The entire PeaLL circuit is shown in schematic form in figure 2-9. The heart of the PeaLL is based on the DDA [116] shown in figure 2-8a. The circuit is very well described by its inventors and basically uses current subtraction to implement an instrumentation amplifier. The DDA can be configured as a inverting amplifier [116] and is used for inverting (and buffering) the incoming signal in this implementation.

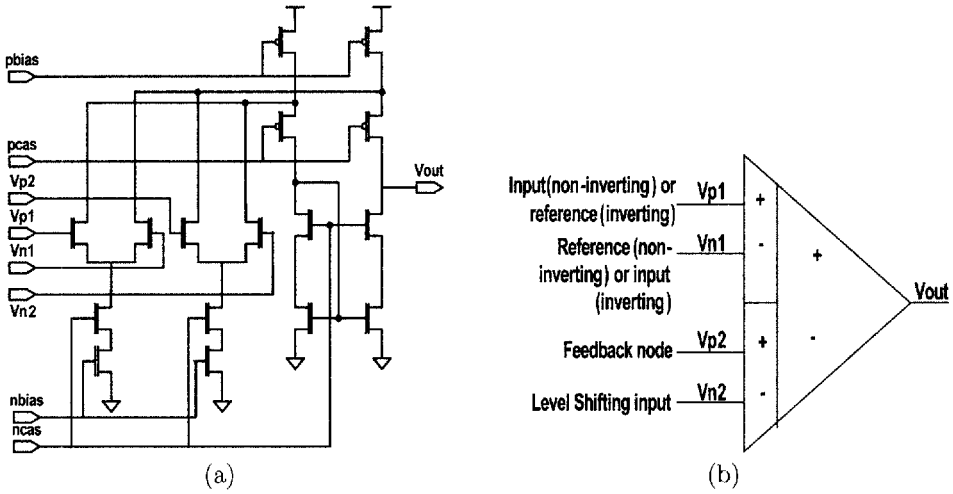

Figure 2-8: The differential difference amplifier a) circuit b) symbol.

Alternatively, a P-input demodulator can be used to give the negative envelope, however this was not used for two reasons one to prevent any mismatches and the other is power. The DDA inputs can be classified into the input or reference, the feedback node and the level shifting input as shown in figure 2-8b. For the inverting configuration used here the reference and the level shifting node are tied to the control voltage. For the buffer amplifier which was also implemented using the DDA the reference was tied to the control voltage and the level shifting input was tied to mid-rail, to ensure negative feedback.

The PeaLL employs a coupled peak detector [17] and is shown in figure 2-9. The coupled peak detector forces the source coupled node to follow the higher of the two input signals. The discharge current is biased (node nblo in figure 2-9) in the subthreshold regime and is derived from a diffusive bias network [30] shown in figure 2-23. The current from the coupled peak detector can then be used to drive a simple current based charge pump as shown. The positive input will drive the current into the capacitor and the inverted input will pump current out of the capacitor. The directions are chosen to ensure negative feedback in the path. Since the peak is a duty cycle invariant parameter the loop is also duty cycle invariant. When the positive input is greater than the negative input the pump will move the voltage on the capacitor up this will move the non-inverted signal lower while shifting the

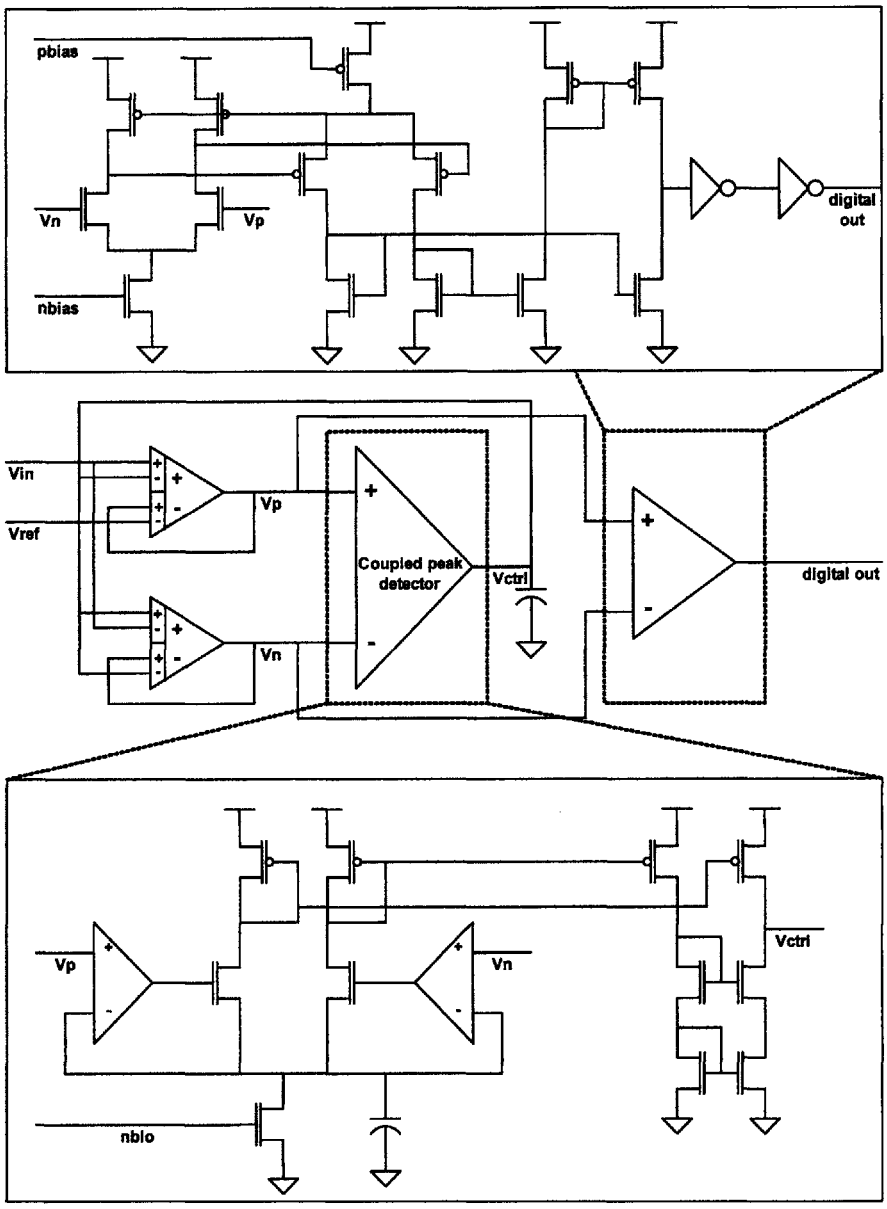

Figure 2-9: The circuit diagram of the peak locked loop.

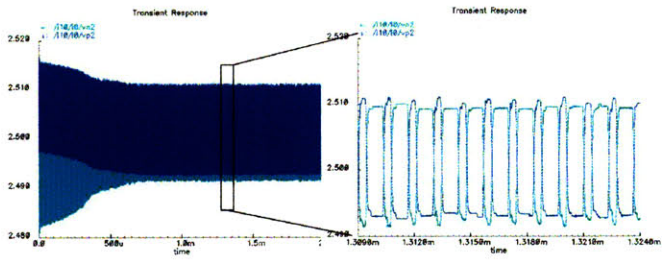

Figure 2-10: Simulation results of the PeaLL for a 750KHz signal with an amplitude of 20mV. Locking behavior of the differential output signals and zoomed version of the locked signals showing the accuracy of the lock

inverted waveform higher until lock is achieved, the situation is reversed when the loop starts in the opposite configuration. Typical locking behavior is shown for a 750 kHz waveform with a 20mV signal in figure 2-10. The differential signal is then fed to a two stage comparator shown in figure 2-9. The comparator was implemented in two stages to reduce the miller effect that will distort the input edges. The comparator uses a feedback coupling between the first two stages to ensure the correct common mode operation and a full swing output stage which performs a differential-single ended conversion.

2.1.4 Clock and Data Recovery

Self-Biased DLL

In order to simplify the clock and data recovery a pulse width modulation scheme that was used by Wentai Liu *et. al.* [81] was chosen to transmit the symbol, with some important differences. Since the power and the data are on separate frequencies we can independently optimize the symbol pulse width and modulation index yielding better noise margin. In this implementation a zero is a 50% duty cycle waveform and the one is a 30-70% duty cycle waveform. The pulse width is modulated by moving the falling edge in time. This scheme greatly simplifies the clock recovery since there is one edge that is always fixed in time. The data is recovered in a similar fashion as described in reference [81]. Briefly, the incoming data is fed into a delay line that is tuned to be equal to exactly one period of the clock. The delay line taps are all

registered using the incoming clock. This effectively does a time to space conversion. By observing the different outputs the location of an edge can be determined and hence the symbols can be recovered.

The delay line was designed using a low power and low area technique [79] shown in figure 2-11. The delay element that was used was a simple CMOS inverter pair shown in figure 2-11. By controlling the power supply voltage to the inverter the delay of the line can be controlled. The inverter delay line has the following advantages, the gain of the delay line is low and this translates to low jitter.

While the implant power supply is unregulated and can cause undesirable power supply induced jitter, in this implementation the control voltage is regulated as shown in figure 2-11 and hence the inverter's power supply is regulated. The inverter is also not as sensitive to mismatches, uses few devices and has less routing than other commonly used delay elements such as differential elements and current starved inverters. This makes the CMOS inverter based delay line very attractive for a low area implementation. It should be noted that for the current retinal implant the data rates are quite low (100-750kbits/s) so the inverter delays had to be made quite long and 32 delay elements were used to implement the delay line. The larger number of taps is not a disadvantage since it gives better edge localization. As explained in [79] the power of this delay line is low even when the number of delay elements increases since the inverters do not consume static power.

The entire DLL is self biased, i.e., it has no external biasing circuits that set constant bias currents. This makes the design implementable in digital processes. Furthermore, it dynamically biases the circuit so that it is at its optimal operating point in terms of loop bandwidth by adjusting the charge pump current with the control voltage [79, 83].

Two new techniques were used to better the implementation the delay line. The first of these was the phase detector (PD), the most commonly used phase/frequency detector (PFD) is shown in figure 2-12a. This phase detector has a capture range of $\pm 2\pi$, it also produces brief and equal up/down pulses at lock preventing the static phase offset during lock. Though, this PFD has been used by many designers

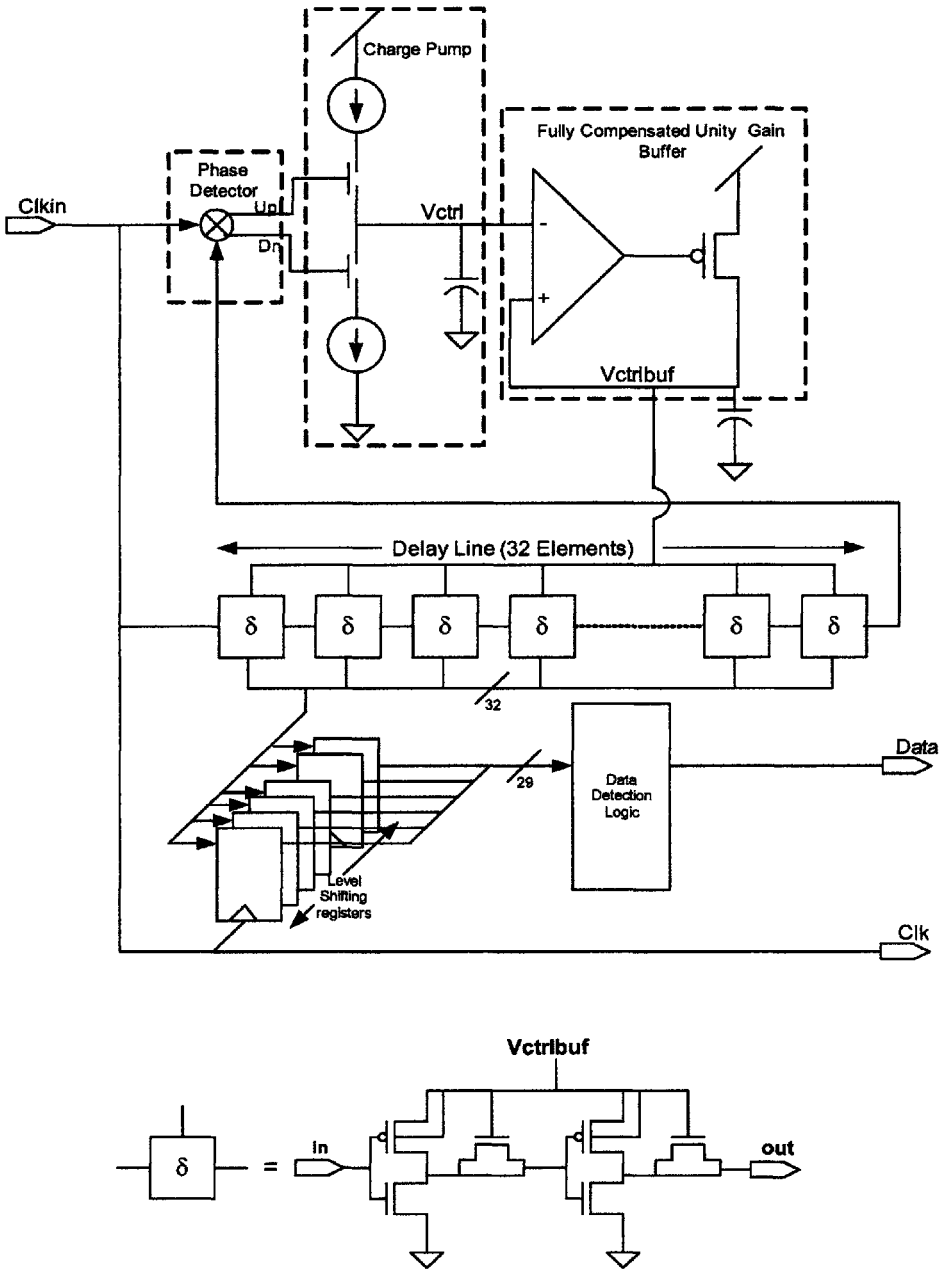

Figure 2-11: Schematic of the low power, low area delay locked loop (DLL). For clarity the level shifters for the reference and the feedback clock are omitted. Additionally the input clock feed into a few delay elements to ensure that the matching between the first element of the delay line and subsequent elements. The CMOS inverter based delay element that was used is shown at the bottom of the figure.

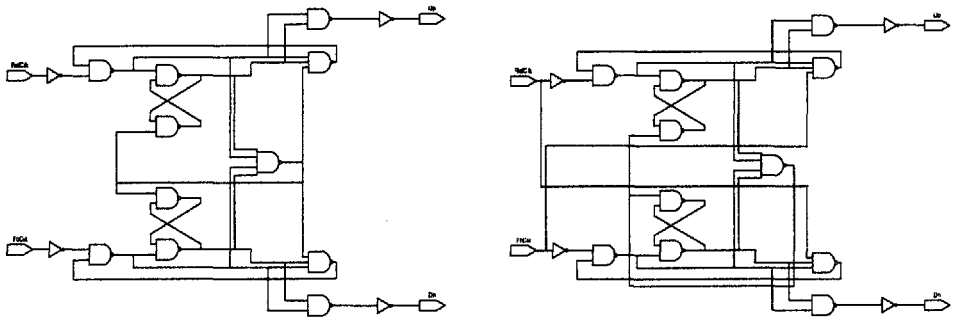

(a) Phase Frequency Detector (b) Phase Only Detector

Figure 2-12: a) Commonly used Phase/Frequency detector(PFD) b) Phase only detector used in this design for robustness as mentioned in the text

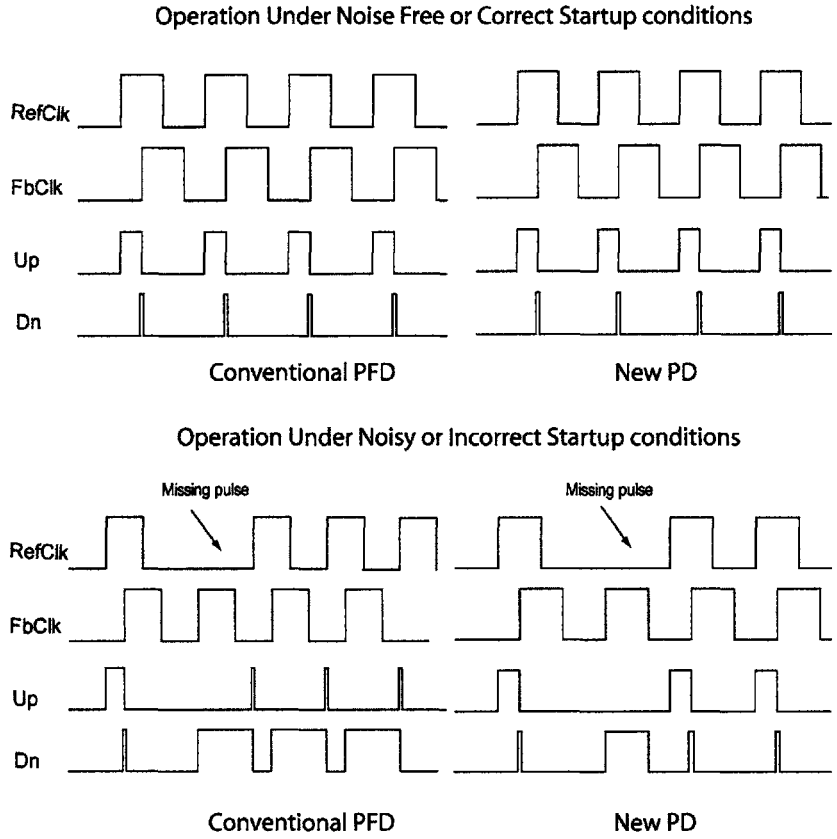

Figure 2-13: Schematic that elucidates the operation of the new phase detector that is robust to missing pulses or incorrect startup conditions. Under normal conditions the PD and the PFD operate identically,. However, when there is a missing pulse the PFD pegs the DLL on one end of its operating range, while the newly designed PD recovers on the next cycle.

in DLL's, it should not be used since it has an extra state in its state transition diagram which makes it also function as a frequency detector. This, though desirable in PLL's, is undesirable in DLL's since the DLL has no way of wrapping the phase (no frequency control) which can lead the DLL to get pegged in one end of its tuning range[10]. One way that is usually used to solve this problem is to ensure that the DLL starts in the right state. This method is however not robust since noise on the line can cause the DLL to get into an undesirable state. The other way is to use a phase only detector shown in [8], however this detector does not produce equal up and down pulses and the reset structure is not symmetric. The commonly used PFD [83], shown in figure 2-12a, was converted into a PD, shown in figure 2-12b, by adding a reset path directly from the input. The operation of the new PD is compared to the conventional PFD is shown schematically in figure 2-13. Under normal operation since there is overlap between the two inputs the operation of the controlled flip-flop in the new PD always acts as a flip-flop and hence is identical in operation to the conventional PD. However, when there is no overlap in the inputs, due to noise or incorrect star-up conditions, the PFD gets into a wrong state but the PD returns back to correct operation after a single cycle.

This retains the advantages of the PFD i.e. it produces equal up and down pulses at lock. However, by virtue of being a phase detector the capture range is reduced to $\pm\pi$. Additionally at lock the input and output clocks are in 180° out of phase, to get the system to lock in phase the feedback clock needs to be delayed by 180°. This delay can be easily achieved by inverting the feedback clock; however this technique is only valid when the clock has a 50% duty cycle. The incoming clocks are however are not always 50% duty cycle. Analog duty cycle correctors consume too much power, so a single bit digital divider was used to ensure 50% duty cycle. Though lower in power adding the digital divider reduces the noise rejection bandwidth of the system by 2. This is not a severe constraint in the DLL since it does not integrate phase noise like a PLL.

Though self biasing yields an optimal operating point it also changes the bias current of the regulating amplifier and hence its gain. Additionally the load to the

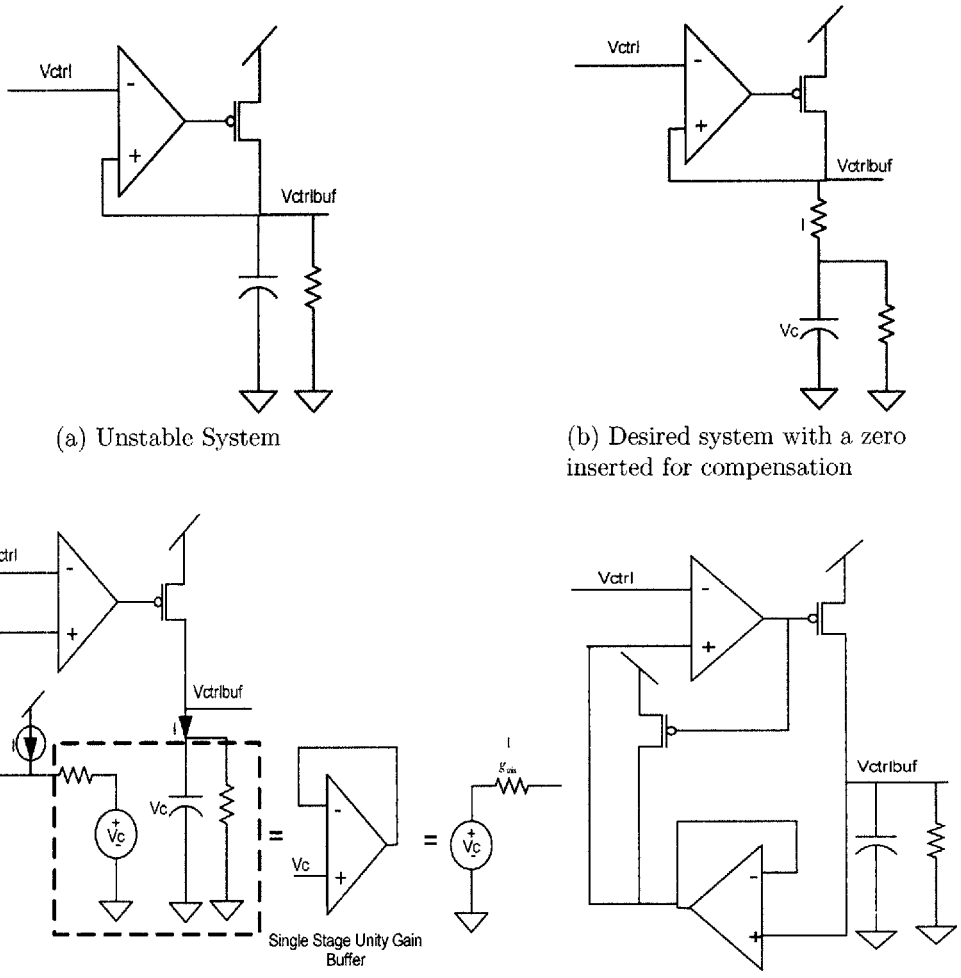

(a) Unstable System

(b) Desired system with a zero inserted for compensation

(c) Electrically equivalent system to one in (b)

(d) Actively compensated system

Figure 2-14: Active compensation for the unity gain buffer used. a) The system before compensation b) desired compensation strategy c) Conversion of passive strategy in (b) to an active strategy d) Fully compensated system.

amplifier changes before lock since the delay line stops drawing current when the edge has finished traversing the line. For these reasons conventional lead-lag compensation becomes hard to implement and it also needs extra passive elements which increases the area. In order to solve this problem a variation of the idea presented in [83, 88] was used. Ideally the system should look like the one shown in figure 2-14a. The figure 2-14 show how to convert the system shown in figure 2-14a to the system in figure 2-14b. This entails the use of an additional follower and a fraction of the output current. The second unity gain follower is also biased by the same dynamic bias, derived from the control voltage, as the first stage differential pair. In a unity gain follower configuration the output resistance of the amplifier is determined by the g_m of the input differential pair transistor and since the g_m scales with the bias current, this circuit adapts the zero as the bias points change so that system remains fully compensated. Furthermore there is an additional diode connected device on the internal load of the differential amplifier to prevent an asymmetry in the differential circuit which would lead to offsets. The complete circuit schematic is shown in figure 2-15.Transistors Mn1-4 and Mp1-4 implement the adaptive bias network that outputs a current that is proportional to $(V_{ctrl} - V_t)^2$. It is modification of the classical V_t reference bias generator [48], with the transitor Mn1 replacing the resistor. This modification forces the drain of Mn1 to also be V_{ctrl} ensuring a square law operation and maintains the required relationships to ensure constant damping as derived in equation 2.11. Transistors Mn11-12 provide a static bias when the level of V_{ctrl} falls below V_t. Transistor Mn5-7 and Mp5-6 implement the first stage amplifier, Transistors Mn-8-10 and Mp7-8 implement the follower buffer which along with transistors Mp10 and Mp9 implement the adaptive zero compensation. Transistor Mp11 is the output device and is scaled with respect to Mp10. Mp12 and Mn4 implement the reset initialization where the output is pulled up to Vdd.

The starting point for a formal derivation is the canonical feedback block diagram shown in figure 2-16a.

$$V_{fb} = \left(V_x g_{mMp10} + V_{ctrlbuf} \frac{g_{mMn9}}{1+k_1} - V_{fb} g_{mMn10} \right) r_o$$

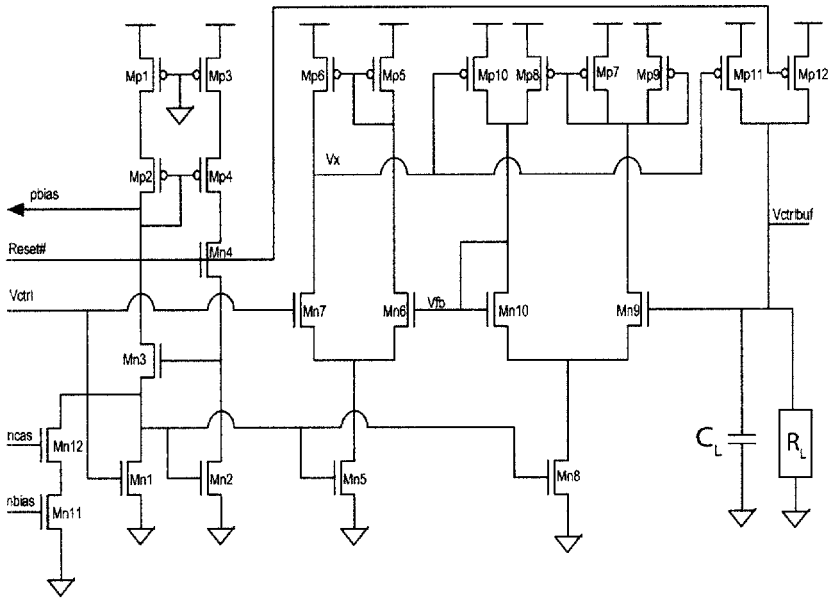

Figure 2-15: Transistor level schematic of the fully compensated feedforward buffer amplifier

where $\frac{g_{mMp7}}{g_{mMp8}} = 1$ and $\frac{g_{mMp9}}{g_{mMp8}} = k_1$

Since $g_{mMn10} r_o >> 1$

$$V_{fb} \cong \left(V_x \frac{g_{mMp10}}{g_{Mn10}} + V_{ctrlbuf} \frac{1}{1+k_1} \right) \tag{2.6}$$

From the canonical block diagram shown in figure 2-16a $V_{ctrlbuf} = V_x \frac{g_{mMp11} R_L}{1+sC_L R_L}$

$$V_x = V_{ctrlbuf} \frac{1+sC_L R_L}{g_{mMp11} R_L} \tag{2.7}$$

Substituting equation 2.7 in equation 2.6, yields

$V_{fb} \cong V_{ctrlbuf} \left(\frac{k_2(1+sR_L CL)}{g_{mMn10} R_L} + \frac{1}{1+k_1} \right)$, where $k_2 = \frac{g_{mMp10}}{g_{mMp11}}$ and $k_3 = 1 + k_1$

$$V_{fb} \cong V_{ctrlbuf} \frac{k_4}{k_3} \left(1 + \frac{2C_L k_2 k_3}{k_4 g_{mMn10}} \right), k_4 = 1 + \frac{k_2 k_3}{g_{mMn10} R_L} \tag{2.8}$$

Using the results of equation 2.8 the feedback block diagram can be simplified to the one shown in figure 2-16b, which clearly shows that the feedback transfer function has a zero in the feedback path.

$$\frac{V_{fb}(s)}{V_{ctrl}(s)} = \frac{\frac{k_4}{k_3}(1+s\tau_z)}{\frac{\tau_1\tau_2 s^2}{A_1A_2} + \left(\frac{\tau_1+\tau_2}{A_1A_2} + \tau_3\right)s + \left(\frac{1}{A_1A_2} + \frac{k_4}{k_3}\right)} \tag{2.9}$$

where $\tau_1 = (r_{oMn7} \parallel r_{oMp6})\, C_x, \tau_2 = R_L C_L, \tau_3 = \frac{C_L k_2}{g_{mMn10}}, \tau_z = \frac{C_L k_2 k_3}{k_4 g_{mMn10}}$,
$A_1 = g_{mMn7}\,(r_{oMn7} \parallel r_{oMp6}), A_2 = g_{mMp11} R_L$
Since $A_1A_2 \gg 1$,

$$\frac{V_{fb}(s)}{V_{ctrl}(s)} \cong \frac{\frac{A_1A_2k_4}{\tau_1\tau_2k_3}(1+s\tau_z)}{s^2 + \frac{A_1A_2k_4\tau_z}{\tau_1\tau_2k_3}s + \frac{A_1A_2k_4}{\tau_1\tau_2k_3}} \tag{2.10}$$

This is in the conventional form of a second order system in series with a system that contains only a single zero and no poles. From the above equation the unity gain bandwidth,ω_o and damping factor ζ of the system can be calculated.

$$\omega_o = \sqrt{\frac{A_1A_2k_4}{\tau_1\tau_2k_3}} = \sqrt{\frac{k_4 g_{mMn6} g_{mMp11}}{k_3 C_L C_x}}$$

$$\zeta = \frac{\tau_z}{\omega_o} = \frac{1}{2}\sqrt{\frac{C_L k_2 k_3 g_{mMn6} g_{mMp11}}{C_x k_4 g_{mMn10}^2}}$$

The current in transistor Mp11 is equal to the current drawn by the delay line and is proportional to $(V_{ctrlbuf} - V_t)^2$. The bias current Ibias that flows in the bias network is proportional to $(V_{ctrl} - V_t)^2$. Using this property we can show that the damping is independent of the unity gain bandwidth and only depends on geometrical ratios as shown in equation 2.11.

$g_{mMn6} \propto \sqrt{I_{bias}} = k_5(V_{ctrl} - Vtn)$, $g_{mMp11} \propto \sqrt{I_{Delayline}} = k_6(V_{ctrlbuf} - Vtn)$, $g_{mMn10} \propto \sqrt{I_{bias}} = k_7(V_{ctrl} - Vtn)$
where $k_5 = \mu_n C_o x \frac{W_{Mn6}}{L_{Mn6}}$, $k_6 = \mu_n C_o x \frac{W_{Mninv}}{L_{Mninv}}$, $k_7 = \mu_n C_o x \frac{W_{Mn10}}{L_{Mn10}}$
Additionally, we can make the following simplifications
$\frac{k_3}{k_4} = \frac{k_3}{1+\frac{k_2k_3}{g_{mMn10}R_L}} \cong k_3$, $\frac{k_2k_3}{g_{mMn10}R_L} << 1$ and $V_{ctrlbuf} \cong V_{ctrl}$, using these relationships yields

$$\zeta \cong \frac{1}{2}\sqrt{\frac{k_2k_3k_5k_6C_L}{k_7C_x}} \tag{2.11}$$

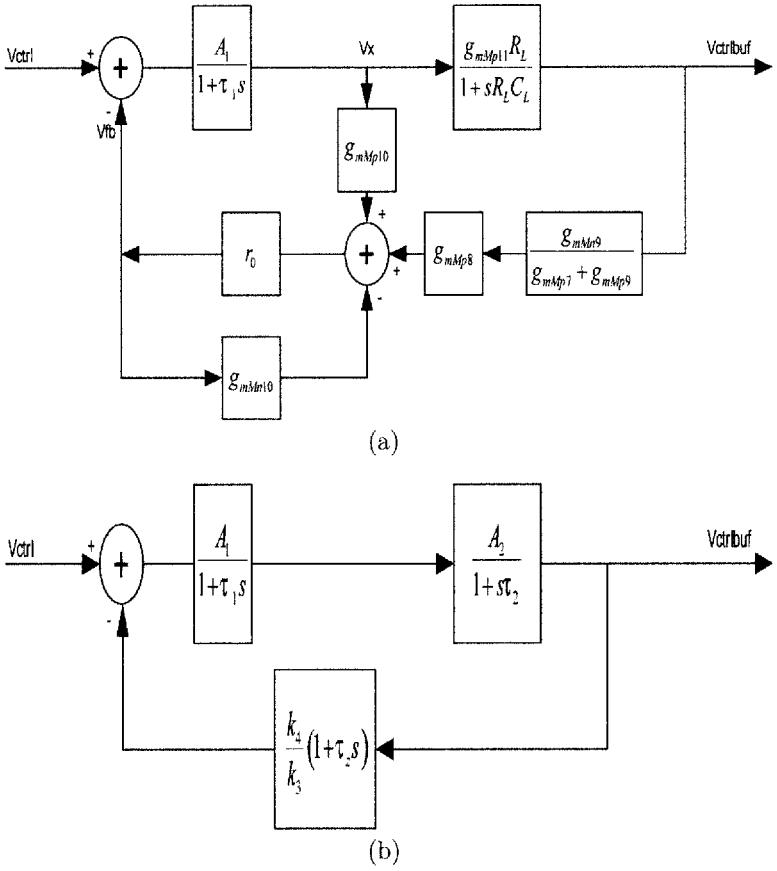

Figure 2-16: Feedback block diagram representation of the control voltage buffer

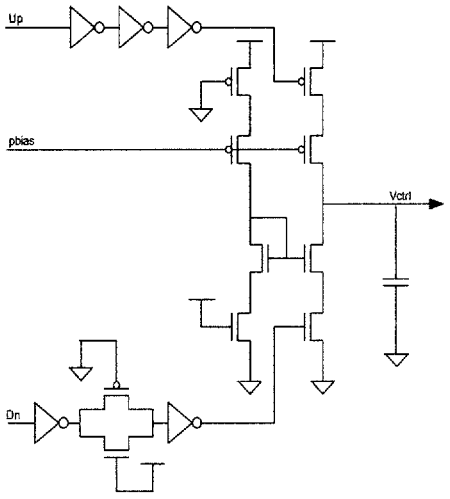

Figure 2-17: Simple current mirror based charge pump, pbias is derived from the control voltage therby enabling an adaptive bandwidth implementation.

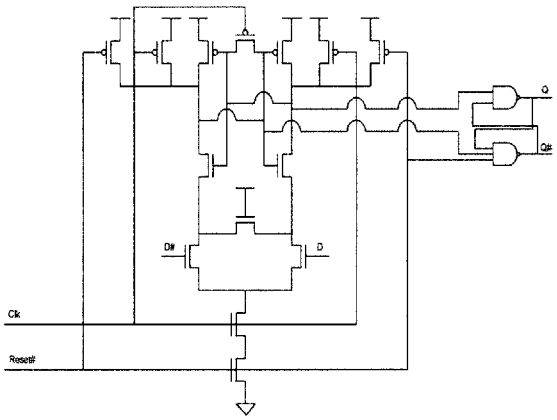

Figure 2-18: The differential edge triggered flip-flop that was also used as a level shifter in the clock and data recovery unit.

A simple current mirror based charge pump was used and is shown in figure 2-17. Since the bias voltage, pbias, is proportional to the control voltage the circuit dynamically adjusts the loop bandwidth with the operating delay. Pass gates that are always are on are used to match the delay of the up and down signals.

The final point worth mentioning is that the output of the delay line taps need to be restored to full rail. Though this can be done with level shifting amplifiers they consume static power. In order to lower the power the register and the level shifting function were combined by using a differentially pre-charged register [27] and is shown in figure 2-18.

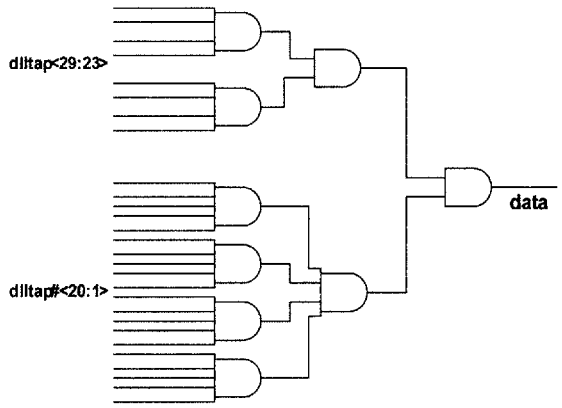

Figure 2-19: Data detection logic block, the taps on either side on the edge have been ignored to increase the jitter tolerance of the circuit.

Data detection logic

To ensure robust data recovery most of the DLL taps were used and the logic is shown in figure 2-19. The advantage of using this over an edge detector is that false symbol recovery is avoided. A single tap delay on either sides of the edge was omitted to ensure that symbol recovery was accurate even if the input data jittered. It should be noted that there is possibility of subharmonic false symbol recovery. Since the DLL always starts from the lowest delay setting this problem can be avoided.

2.1.5 Control Block

The chip can receive four 16-bit commands , configure(3928'h), pulse-up(8F8C'h), pulse-down(1CA7'h) and stop(4871'h). Each command is decoded by a state machine which examines the incoming data stream. The state machine design was done using the CAD program SIS which is available from UC, Berkeley [118]. The configure command tells the chip that the next 170 bits are part of the data sequence. The format of the data sequence is shown in figure 2-21. The pulse up command asserts the rising edge of the pulse up signal that enables the positive current output. The pulse down command is similar to the pulse up command the difference being that it asserts the pulse down signal. The stop command de-asserts both pulse up and down signals. Thus the duration of the pulse up and pulse down commands is the

difference between the arrival times of the pulse up or down commands and the stop command. The duration between the previous stop command and the next pulse command determines the inter-pulse interval. If a pulse up (down) is followed by a pulse down (up) then the system assumes that no inter-pulse interval was needed. The next smallest inter-pulse interval that is allowed is 16 clock cycles. This method of externally controlling the pulse width was chosen over using internal clock dividers so that the system is independent of the chosen clock frequency and also leads to lower area. By allowing the system to be clock frequency independent power saving features such as clock throttling can be investigated. A timing diagram of the instruction sequence is shown in figure 2-20.

2.1.6 Current Driver Block

The chip consists of 16 programmable current sources capable of sourcing a maximum of 775μA each. The current source has a range of 0-775μA in steps of 25μA(5bit control). The current source is capable of driving biphasic pulses, either cathodic first or anodic first depending on which command is received first pulse up or pulse down. All bias voltages for the current driver block are derived using a supply insensitive Vt referenced bias network [48] shown in figure 2-22. The reference resistor was implemented using high resistance (1036$\Omega/\square$) poly2 layer available in this process. To account for reference resistor value variation due to process, all on chip reference resistors are programmable (3 bits). The subthreshold biases were derived from the main biasing network using a diffusive bias network [30] shown in figure 2-23. The advantage of the diffusive bias network is that yields multiple bias voltages, by using an interpolating amplifier shown in figure 2-24, the voltages can be effectively multiplexed. Unlike simple one hot multiplexing the interpolating amp allows the bias voltages to be a linear weighted combination of the input voltages.

The voltage value of the electrode bias was set by controlling the power supply of the subthreshold current pull-up. The electrode bias supply voltage was derived employing the same trick of using an interpolating amplifier and is shown in figure 2-25. By using just four voltage levels and a four input interpolating amplifier, sixteen

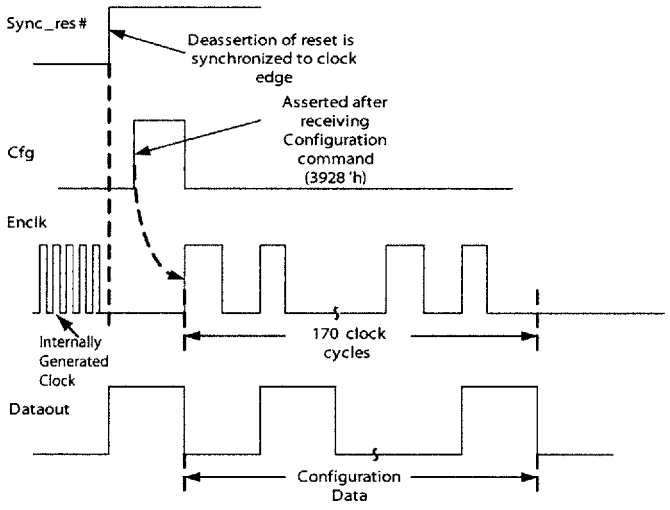

(a)

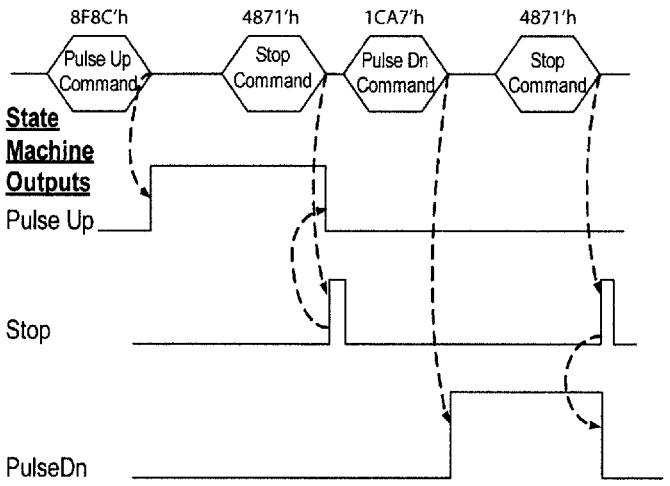

(b)

Figure 2-20: Timing diagram for the control logic block. a) Configuration data setup b) Pulse Up and Pulse Down generation using the predefined commands.

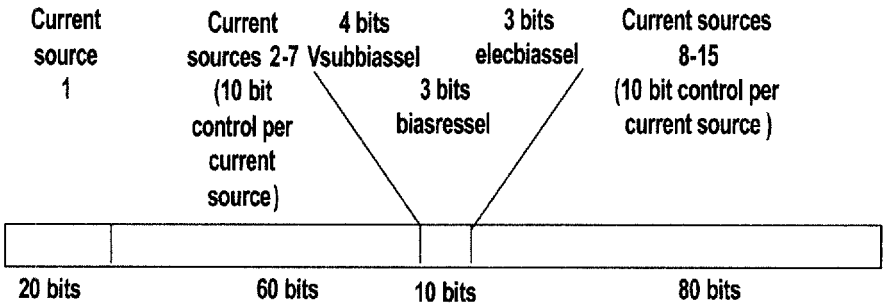

Figure 2-21: Configuration data format, Vsubbias controls the electrode bias value, biasressel controls the resistor used to determine the bias current and elecbiassel controls the current through the electrode bias pull up.

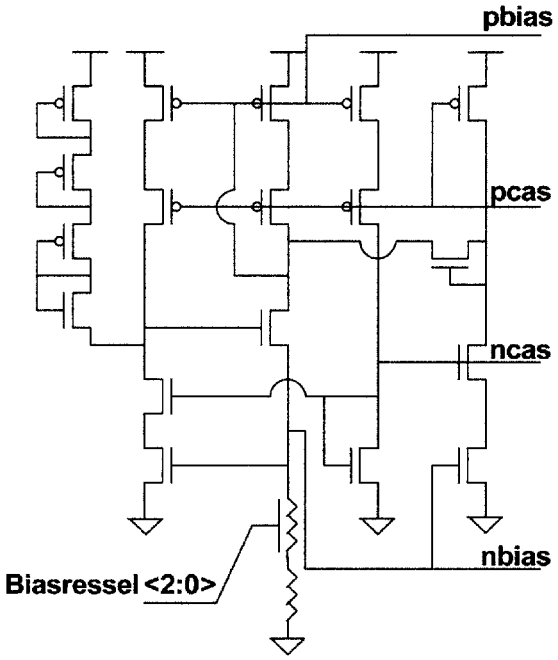

Figure 2-22: Vt dependent constant current reference with analog startup and programmable resistors for process variation compensation.

levels can be selected. The select has no decoder in the path which saves area. A table showing the input digital values and the output analog values is also shown in figure 2-25.

The schematic of the biphasic current driver is shown in figure 2-26. It basically implements a current weighted DAC and is similar to the one implemented by DeMarco *et al.* [31]. However, in this implementation the cascode device is used as the switch. The currents are turned on and off by switching the input of the cascode transistor between the appropriate bias and the appropriate supply rails respectively. The switch is designed so that there is no contention between the cascode bias node and either the pull up or pull down transistor during switching. In order to prevent undesirable interaction between the switching nodes and the bias network the cascode bias nodes were isolated using a follower, which was a high gain folded cascode amplifier in unity gain configuration.

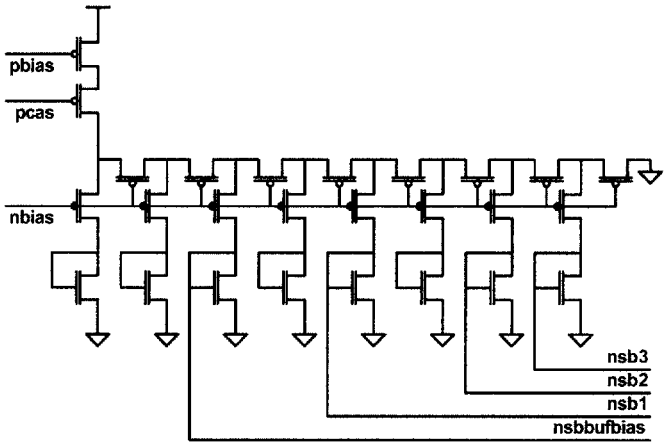

Figure 2-23: Diffusive network bias generator for generating the subthreshold biases for the electrode bias buffer amplifier and the subthreshold bias interpolator. The p-tranistors connected to nbias act like resistors and form a 1-D resistive grid which forces weighted currents through each branch.

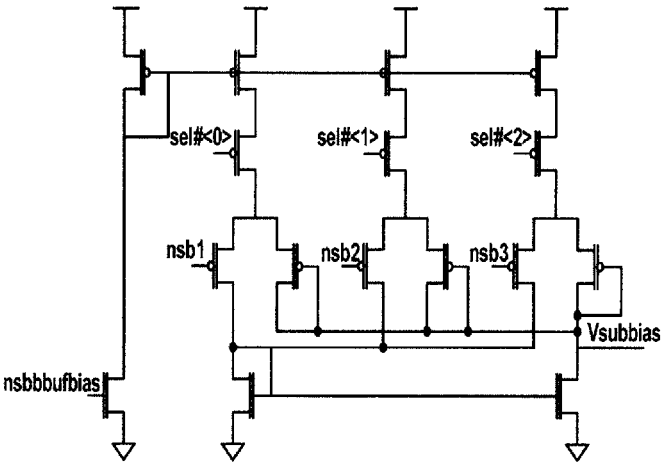

Figure 2-24: Subthreshold bias interpolator based on the averaging amplifier used to derive the subthreshold bias voltage for the electrode bias. The value of the bias network is either one of the values of the diffusive bias network or a weighted combination of them.

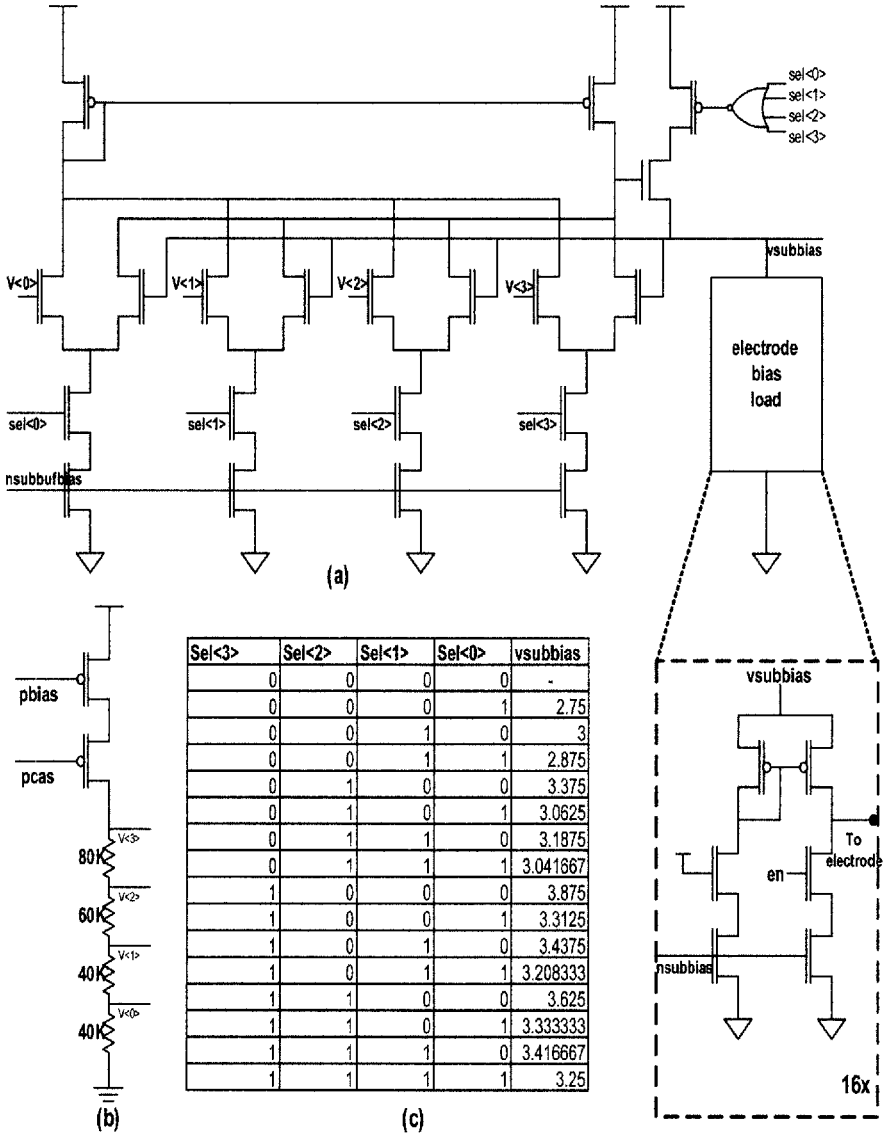

Sel<3>	Sel<2>	Sel<1>	Sel<0>	vsubbias
0	0	0	0	-
0	0	0	1	2.75
0	0	1	0	3
0	0	1	1	2.875
0	1	0	0	3.375
0	1	0	1	3.0625
0	1	1	0	3.1875
0	1	1	1	3.041667
1	0	0	0	3.875
1	0	0	1	3.3125
1	0	1	0	3.4375
1	0	1	1	3.208333
1	1	0	0	3.625
1	1	0	1	3.333333
1	1	1	0	3.416667
1	1	1	1	3.25

(c)

Figure 2-25: Electrode bias value buffer amplifier. This scheme allows for fine interpolation between the four reference values which saves area and power. The bias voltage is either one of the 4 voltages shown or a weighted combination of them. b) The network used to derive the reference voltages c) Table showing the various possible voltage outputs and the digital select values needed.

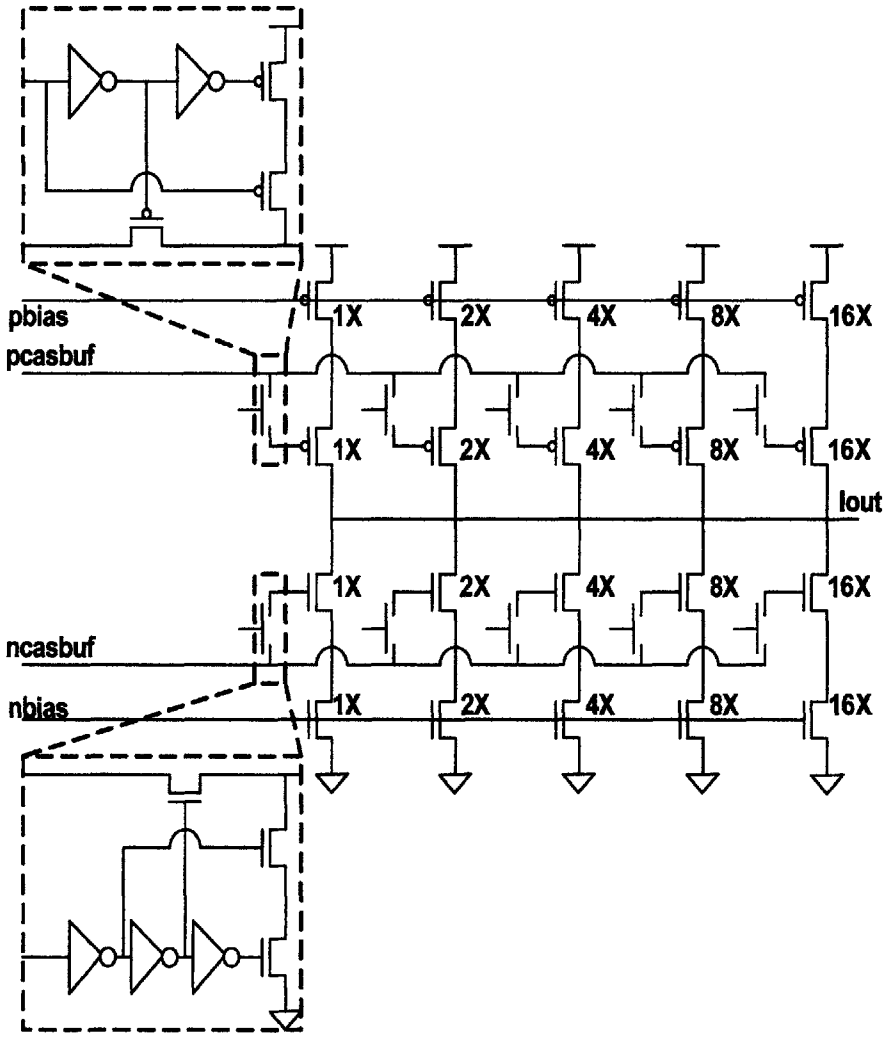

Figure 2-26: Current driver with binary weighting which allows for 5-bit control of the current amplitude for both anodic and cathodic current pulses. The switches shown in the inset perform break before make function which minimizes the contention current during switching

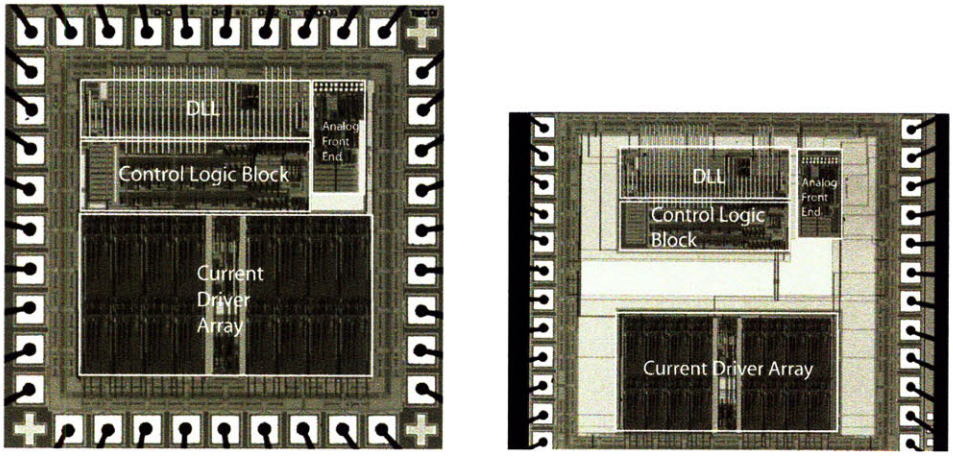

(a) Stimulator Chip (b) Test Chip

Figure 2-27: a)Microphotograph of the complete stimulator chip, the chip has a total area of $5.612mm^2$ and contains approximately 30,000 transistors. b) microphotograph of the test chip with the various blocks decoupled from each other so that they can be tested individually. The chip also allows for the blocks to be connected to each other externally to verify complete functionality. The chip has 52 pads with an area of $9.187mm^2$ and contains approximately 30,000 transistors.

2.2 Experimental Results

Two versions of the chip were fabricated and the microphotographs of the die are shown in figure 2-27. One was a final version that would be incorporated in the implant and the second version was configured to allow for complete observability and controllability. This test-chip is configured so that each block can be tested in isolation or can receive inputs from the previous sections of the chip. This involved the modification of the pads to achieve the necessary drive strength. Sensitive analog signals were buffered in the pad. The chip was tested using a custom software platform designed using the LabView PXI platform [34] and were inductively coupled into the test board to simulate implant conditions. All individual block data discussed below was obtained from the test chip platform. Wireless testing of the chip was done by using a custom power and data transmitter [72]. All experimental results were done by Greg Swider under my guidance [126].

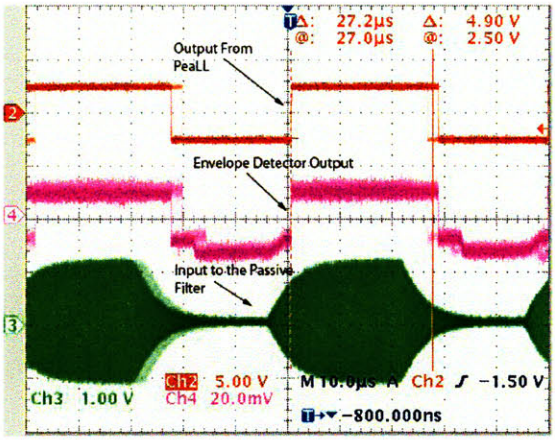

Figure 2-28: Envelope detector output

2.2.1 Analog Front-End

The envelope detector was tested first and the resulting waveform is shown figure 2-28. A 20KHz data signal on a 13.56 MHz carrier was inductively coupled via a transformer into the test chip. It can be seen that the envelope detector reliably recovers the data, however, there is a tremendous attenuation due to the passive filter and the ratio of carrier frequency to the signal frequency as discussed earlier. The output of the PeaLL is shown in figure 2-29, the figure clearly shows that the integrity of the pulse width is maintained for the two cases. Additionally, the jitter of the falling edge is also shown and is below a single tap delay, except in the 30-70% duty cycle case for the high frequency where it is slightly above a single DLL tap delay of 43nS.

2.2.2 DLL

The output clock and the input clock for two input frequencies are shown in figure 2-30. To clearly illustrate that the delay of the DLL at lock is exactly one period, an alternating duty cycle varying waveform was used as the input. Also the data recovered by the data detection unit is shows that the recovered data was interpreted as a string of alternating 0's and 1's. The control voltages were buffered out using self biased unity gain amplifiers [18]. The voltages on the charge pump capacitor

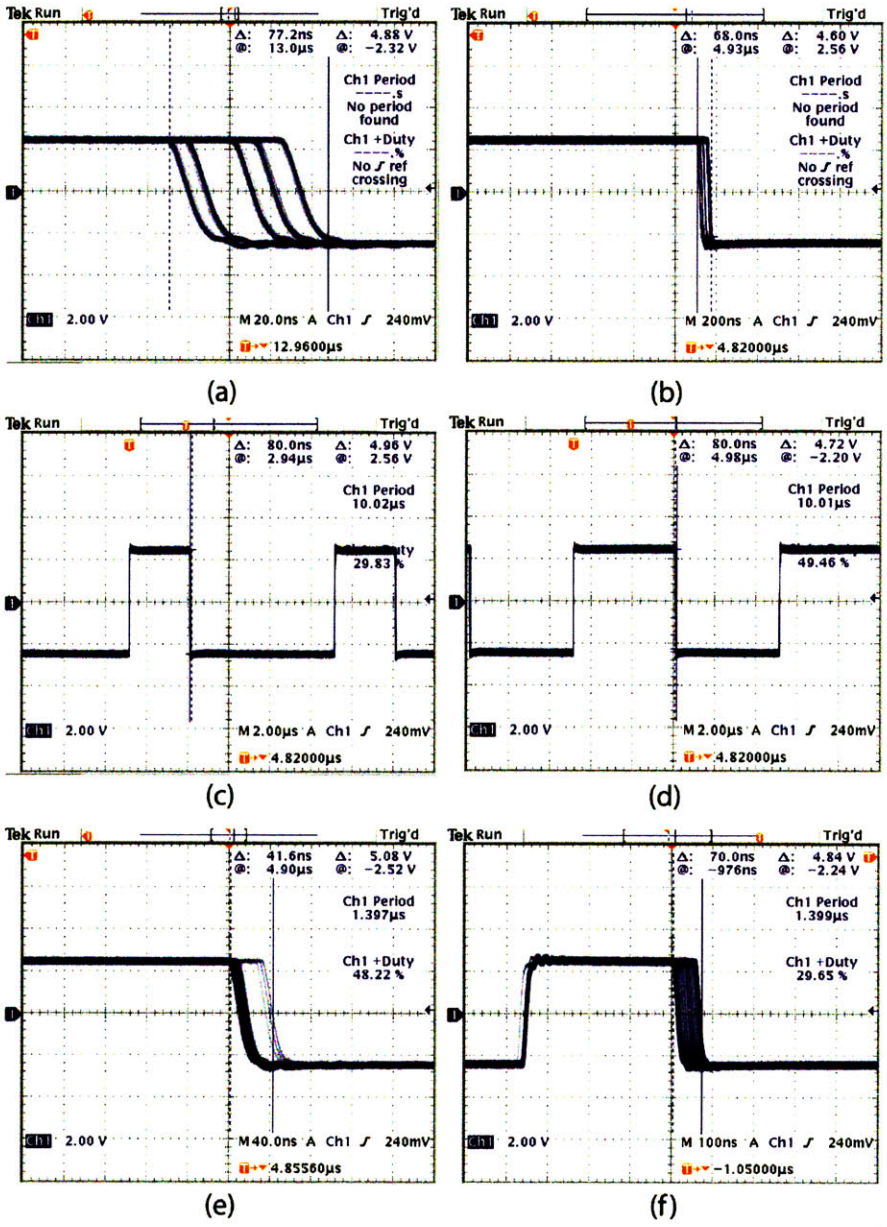

Figure 2-29: Recovered pulse width modulated outputs of the peak locked loop at a data rate of 100kb/s and 714kb/s driven by an ASK modulated waveform through an inductive link. e) Duty cycle recovered when the incoming signal is a 50-50 duty cycle waveform. The jitter incurred is 41.6ns. f) Duty cycle recovered when the incoming signal is a 30-70 duty cycle waveform. The jitter incurred is 70ns.

(Vctrl) and the buffered control voltage (Vctrlbuf), the supply of the inverters, are shown in figure 2-31. It can be seen that the gain of the CMOS inverter based delay line is quite low as expected. Furthermore, the low gain translates to low jitter, in the current design the clock would move by 230Hz for a change of 1mV at lock. At 100kHz(worst case) the clock would change by 0.23% for a 1mV change in the control voltage. It can also be seen the gain of the delay line is linear. Though made of non-linear elements the gain of the delay line is linear due to the inverse scaling of current (square law) and the swing (linear). As the frequency increases the current goes as the square but the swing also increases, the effects of this on delay are inverse to each other resulting in a single order dependence on control voltage, there also exist differential delay elements with such characteristics [83]. If the control voltage drops to a level where the CMOS inverter starts operating in the sub-threshold region this relationship will not hold and gain will scale non-linearly, the jitter would also be high in this region due the high gain of the delay line. For these reasons the operation in this region must be avoided.

2.2.3 Control logic Block

The control sequence crucially controls the entire working of the chip and the experimental results from this block are shown in figure 2-32. The first was to test the reliably serial data transfer following the reception of the command word. The chip was configured so that the input data stream could be read out from the registers on the following configure command cycle, using this procedure the data integrity was tested. The 170 clock cycle burst that clocks the data registers in shown in figure 2-32. The Pulse-Down command, followed by a stop (which controls the pulse width of the current pulse) was transmitted and then the transmit sequence was repeated for the Pulse-Up command. The command sequence, the assertion and deassertion of this experiment can be clearly seen in figure 2-32. The pulse width commanded and obtained were within the accuracy of experimental error as shown in figure 2-32.

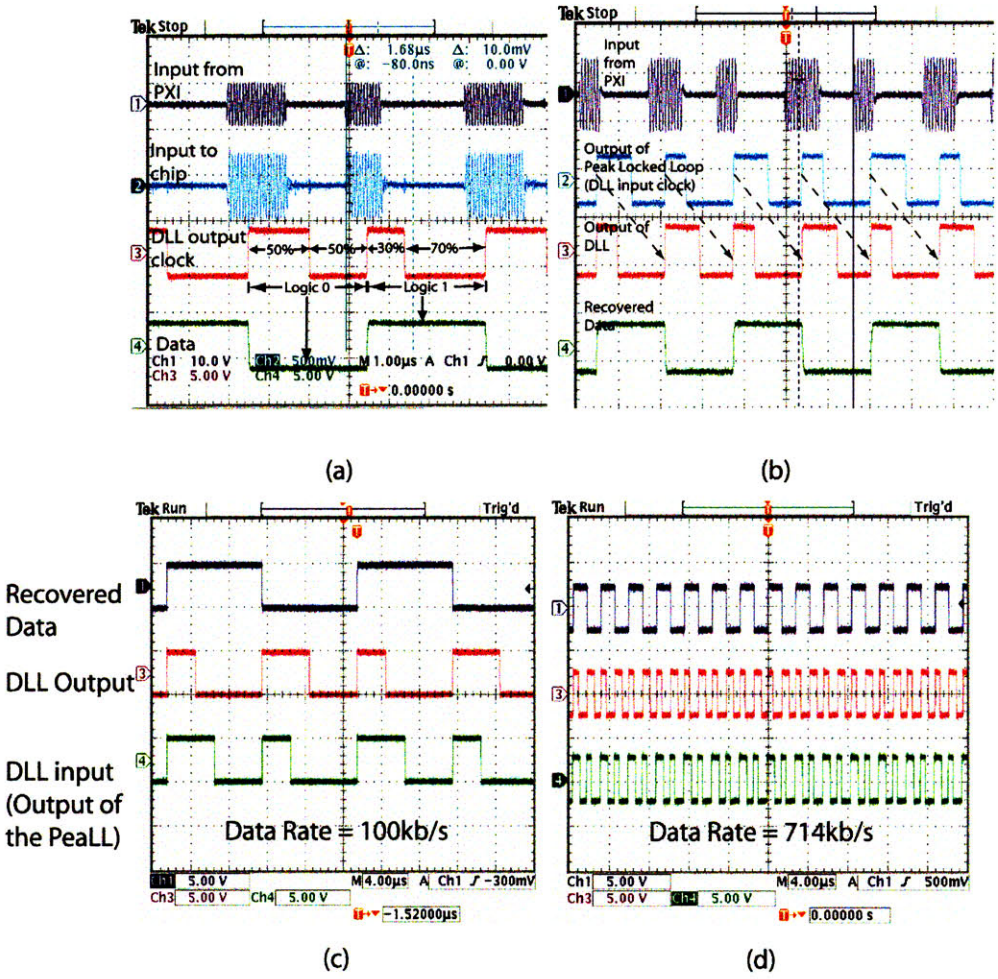

Figure 2-30: Experimental results from the DLL a) Chip successfully receives a string of alternating ones and zeroes. b) Input and output clocks of the DLL are locked exactly one period apart. Output of the clock and data recovery block at two different data rates b) 100 kb/s b) 714 kb/s. The input stream is a string of alternating ones and zeroes, or in PWM parlance a 30-70 duty cycle waveform followed by a 50-50 duty cycle waveform. The input and output of the DLL are locked exactly one period out of phase. The integrity of the recovered data is also shown.

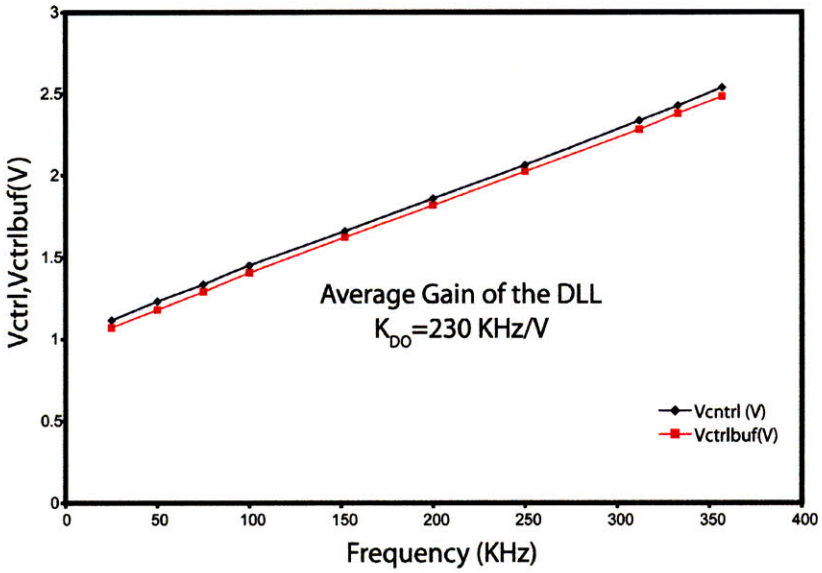

Figure 2-31: Experimental results showing the linear relationship between the clock frequency and the control voltage. The control voltage of the delay line before and after the unity gain buffer. The gain of the delay line at lock is 230kHz/V as indicated on the graph

2.2.4 Current Driver

The current DAC was tested by using a representative current source out of the 15 available and recording the current values for each DAC setting. The results of this measurement are shown in figure 2-33. It can be seen that the current DAC is pretty linear and the mismatch between the pull-up and pull-down current sources is fairly small. Though the chip was initially designed to supply 775μA in step of 25μA, the variation due to fabrication in the value of the poly resistor, even with the smallest digital setting, allowed a minimum current of 30μA, so instead the current output was from 0-960μA in steps of 30μA. Addtionally as shown in figure 2-34, the pulse width of the Pulse-Up and Pulse-Down signals is the width of the current pulses that are output.

2.2.5 Full Chip

All the above tests were performed on the test-chip to ensure that each block was functioning as designed. The next step was to see if the implantable retinal stimula-

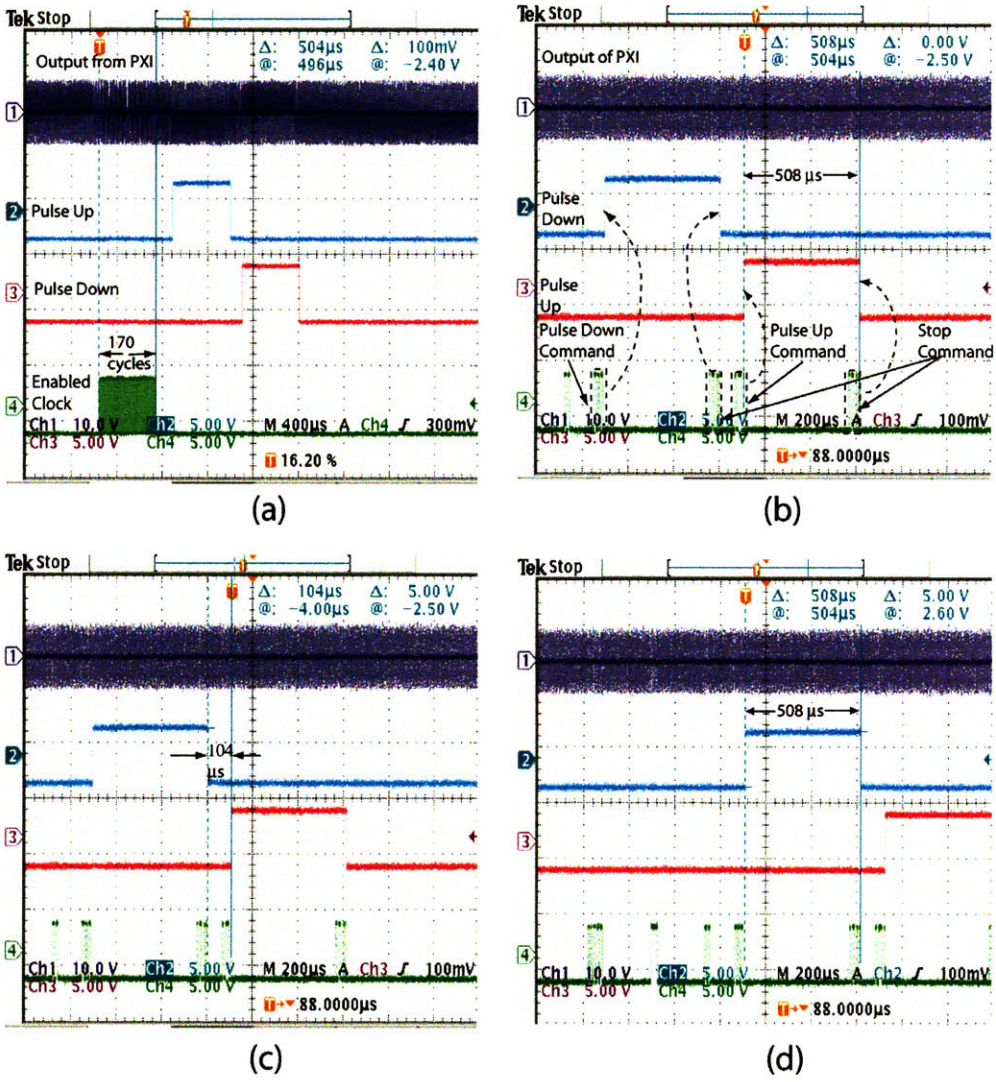

Figure 2-32: For these tests the LabView PXI system output was fed into a transformer and the secondary connected to the input of the chip. a) Successful decoding of Pulse Up, Pulse Down and Stop commands is evidenced by the Pulse Up and Pulse Down signals. The 170 clock cycle burst shows that the Configure command has been decoded successfully. b) Pulse Up and Pulse Down durations are generated by the arrival of the Pulse Up, Pulse Down and Stop commands. The width of the Pulse Down signal was 508μs (pulse width commanded by the software was 506μs). c) Measurement of the interpulse interval (commanded=105μs, measured=104μs). d) Measurement of the Pulse Up signal duration (commanded = 506μS, measured = 506μS). Minor discrepancies in the numbers arise from measurement errors rather than functional errors

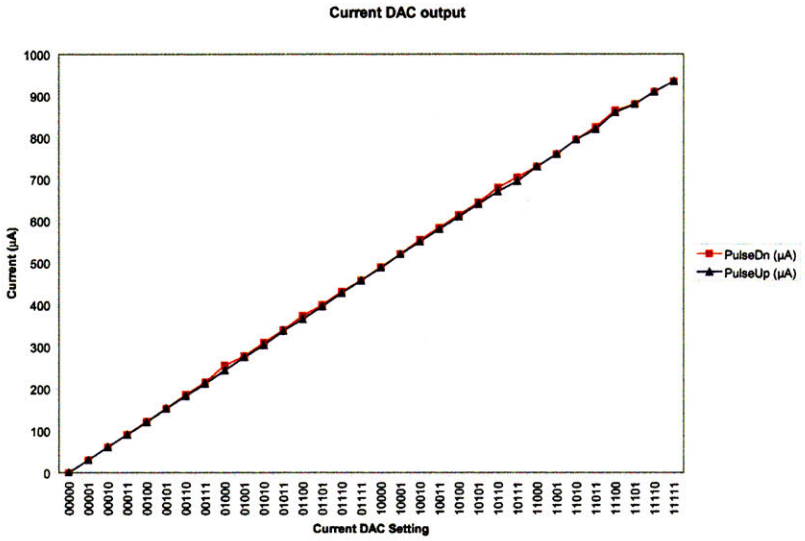

Figure 2-33: Results from current driver DAC. The current between the Up and Down pulses are well matched

tor chip would function as designed when powered wirelessly while driving a 400um diameter iridium oxide electrode immersed in saline. The results of this experiment are shown in figure 2-35, the separation between the primary and secondary coils are 15mm. The data from the register was additionally recorded to ensure data integrity. The full metrics of the chip are listed in Table 2.1. Another metric of interest is the power consumption as a function of data frequency and the experimental results are shown in figure 2-36. It can be seen that the increase power is an order of magnitude smaller than the increase in the data rate demonstrating the scalabilty of this architecture.

2.3 Conclusions

A fully implantable 15 channel low power retinal stimulator chip was designed and tested. The chip works according to the design specifications. This chip is currently being tested in-vitro in animals. It can be seen that even with a modest number of electrodes due to the high current requirements the power needed for an electrical prosthesis will be very high. In the next chapter some possible alternatives to electrical

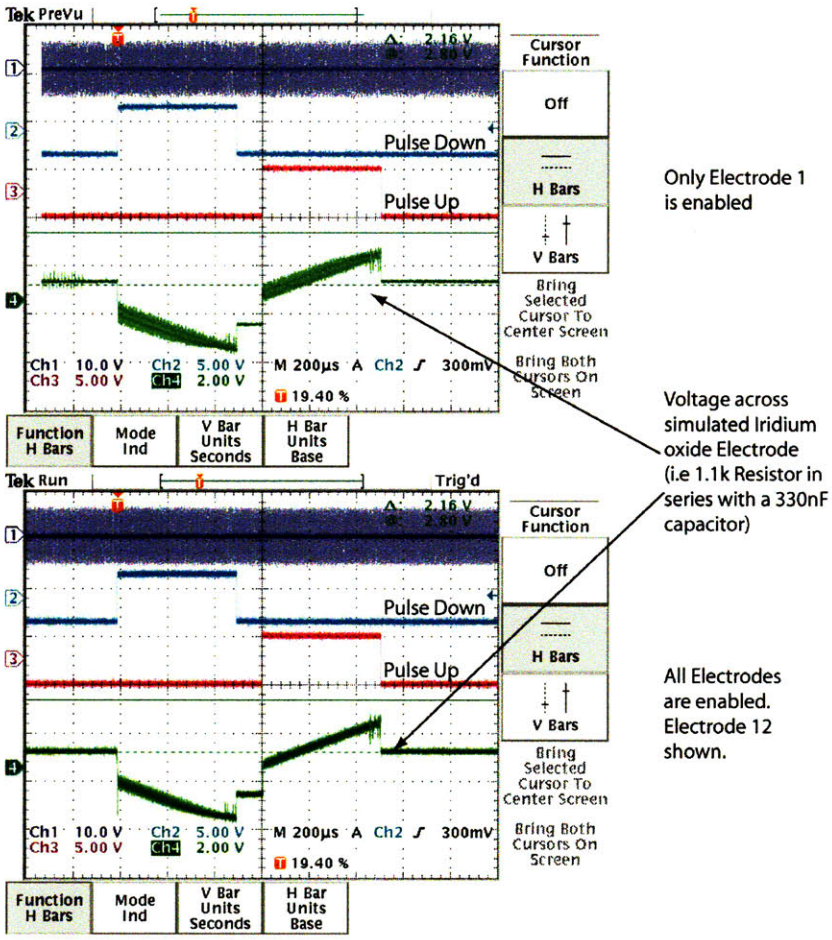

Figure 2-34: Results showing that the pulse width commanded is the pulse width of the current waveform. The output drives a series RC which simulates the impedance presented by the iridium oxide electrode.

Chip Metrics	
Technology	AMI 0.5μm
Die Size	2.3mm x 2.3mm
Carrier Frequency[1]	5-9Mhz
Number of Current generators[2]	15
Number of electrodes	15
Data Rate	25kb/s-714 kb/s
Current amplitude resolution	5 bits
Timing Resolution	1.4μs-4μs (data rate dependent)
Power consumption	Min.−1.2mW@25kb/s Max. - 3.2mW@714Kb/s
Maximum frame rate with 1ms up and down pulses	440 frames/sec

Table 2.1: Full Chip Metrics

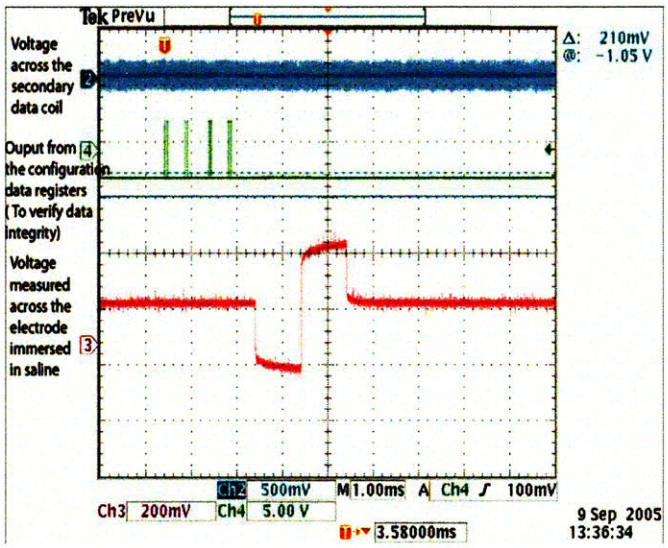

Figure 2-35: Output of the wirelessly driven and powered stimulator chip driving an electrode immersed in saline . The separation between the primary and secondary coils are 15mm.

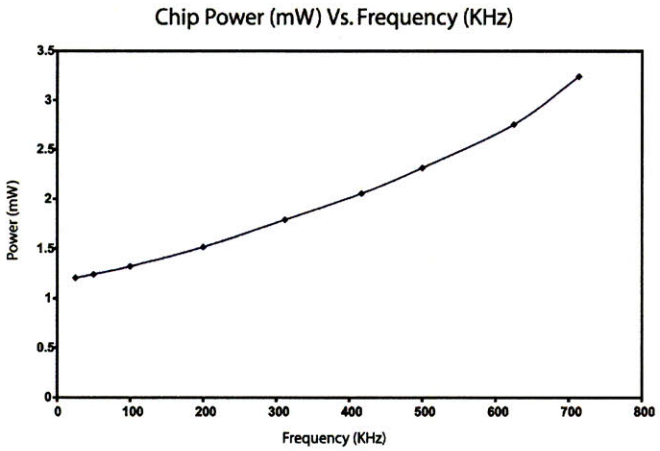

Figure 2-36: Power consumed by the chip (excluding the current sources) at different data rates. As the data rate increases by a factor of 28, chip power increases by a factor of 2.7.

stimulation will be explored, namely a supramolecular neural prosthesis.

Chapter 3

Supramolecular Retinal Prosthesis

3.1 Motivation

Current neural prosthetic devices use electrical stimulation to excite the neural tissue of interest. Electrical stimulation, though relatively easy to implement is not the most effective method of neural stimulation. Common issues with electrical stimulation method are lack of focal stimulation, bio-toxicity and high power requirements.

The most natural method to elicit neuronal response is to use chemicals, mainly neurotransmitters. A neuron generates an action potential, except those that exhibit graded potentials, when the membrane potential rises above a certain value called the threshold value. In normal operation this is effected by the binding of the appropriate neurotransmitters at the post-synaptic junction of a target neuron (see chapter 1). Though appealing in many ways the use of neurotransmitters for stimulating neural tissue in neural prosthetic devices poses the following problem. The prosthetic device must have an internal mechanism that can generate the neurotransmitter of interest or it must have an internal reserve that will last for the lifetime of the device. Currently many researchers around the world are pursuing the use of neurotransmitter based devices with the idea of using an internal reserve [62, 40]. This poses a major risk since excess neurotransmitter is highly neurotoxic which may make this method infeasible in practice.

Neurotransmitters, though the most natural method, is not the only way to elicit

a chemically mediated neuronal response. A neuronal response can also be evoked by changing the membrane potential by modulating the ionic gradients. The membrane potential at rest is determined primarily by the concentration difference of potassium (K^+) ions, sodium (Na^+) ions, and chloride (Cl^-) ions between the intracellular and extra-cellular fluids. The membrane potential can be calculated using the Goldmann-Hodgkin-Katz equation (see chapter 1 equation 1.2) and the effective conductance for each ion. At rest, the cell is more permeable (higher conductance) to K^+ than it is to Na^+. By raising the potassium concentration locally around a cell it is possible to depolarize a cell. This is a well known method and has been used in various neurophysiological studies of isolated cells [10, 137]. Jensen has previously shown [65] that rabbit retinal tissue can be excited by focal application of potassium (100mM). We have also recently performed experiments to determine the concentration of potassium that would be needed to excite the rabbit retina. These experiments show that a very modest increase in background concentration ($\approx$10mM) is sufficient to excite the retina, see chapter 4.

Any chemical stimulation method be it neurotransmitter or ionic (in this case potassium) would require the replacement of the lost chemical species. In general this requires the sequestering of the necessary chemical into the device from the background solution that contains a low concentration of the chemical. This requires that the transport be uphill which makes it thermodynamically unfavorable. Furthermore, the transport needs to be selective. Selective transport can be achieved by using specific carriers which forms a complex with the neurotransmitter or ion of interest and translocates it into the device. The transport can be made thermodynamically feasible by supplying energy to the system.

The simplest chemical to replace would be potassium ions since the homeostasis of the body maintains the concentration of potassium in the extracellular fluid. However, it is also possible to sequester neurotransmitters since neurons release neurotransmitter upon depolarization and also certain chemical pumps in glial cells [127, 4] can be made to operate in reverse which release neurotransmitter into the extracellular space. Potassium ions may be taken as a representative chemical for elucidating the

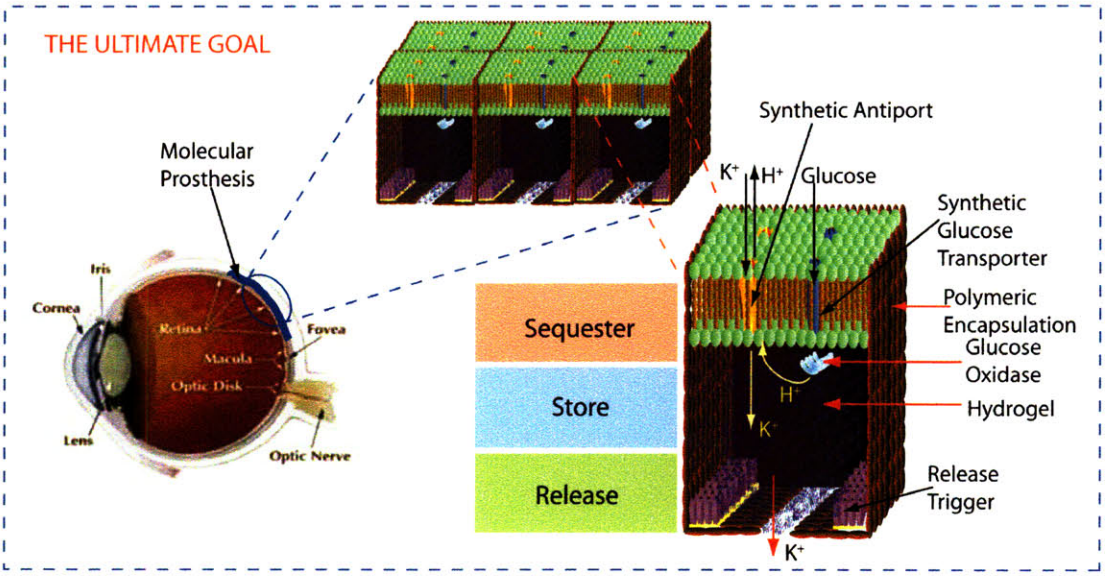

Figure 3-1: Schematic of the envisioned molecular neural prosthesis. The active nano-structure consists of a synthetic amphiphilic copolymeric membrane that serves to compartmentalize the nanobiodevice. Synthetic antiports pump either ions or catecholamines against a concentration gradient by expending a proton motive force (PMF). The PMF is derived by enzymatic oxidation of glucose by glucose oxidase. The membrane contains synthetic glucose transporters that enable the glucose form the surrounding solution to be transported into the device. The neuroactive species that has been sequestered and transported is stored in a hydrogel. In the currently envisioned architecture the release of the stored species is effected by the change in pH by a light driven proton pump. One could also envision the use of electric field or other suitable physiochemical variables to effect a similar change.

concept of renewable chemical neural stimulation.

The idealized version of the final envisioned device is shown in 3-1. The device consists of a synthetic bilayer membrane into which is incorporated a potassium/hydrogen pump, a proton pump to supply energy to drive the potassium/hydrogen pump, a storage/release layer for the potassium ions and a trigger mechanism which releases the potassium.

The device will function as follows: Using either light or chemical energy a proton gradient will be created by the uptake pump and this in turn will drive the incorporation of potassium into the device against its concentration gradient. Both these pumps will be supported in a synthetic bilayer membrane that acts as the semi-permeable membrane. The potassium ions incorporated into the device will be stored

in a pH sensitive hydrogel layer. This ions stored in this layer will then be released by using voltaged gated nanopores microfabricated in silicon. The local increase of potassium concentration elicits the desired neuronal response. The next few sections will explore the components needed to build a supramolecular neural prosthesis.

3.2 Possible approaches

3.2.1 Synthetic Bilayer Membrane

The synthetic bilayer serves as both a chemical barrier and a mechanical support for the various components that are incorporated in. The bilayer needs to posses the following key features:

1. Mechanical Stability
2. Allow for easy fabrication of ultrathin ($\approx$10nm) membranes
3. Allow for the incorporation or covalent attachment of various molecules

In natural membranes the extremely thin dimensions are achieved by using a process of self-assembly. However, these membranes are extremely unstable outside the aqueous environment. Cross-linked polymer membranes can be made mechanically robust but the process of making ultrathin membranes is extremely difficult. As discussed in chapter 5 the approach that can be employed is to synthesize a synthetic ABA triblock amphiphilic copolymer with a polyoxazoline hydrophillic A-block and a polysiloxane hydrophobic B-block.

The middle hydrophobic B-block consists of a copolymer structure that allows for the covalent attachment of the antiport pump as discussed in the next section. Most carrier molecule containing membranes require the use of a plasticizer, which serves as the membrane solvent. However, these molecules usually leach out of the membrane over time. The use of flexible material with a low glass transition temperature like siloxane circumvents this problem since it does not require the use of plasticizers [76]. By using this polymer and conventional bilayer forming techniques and post

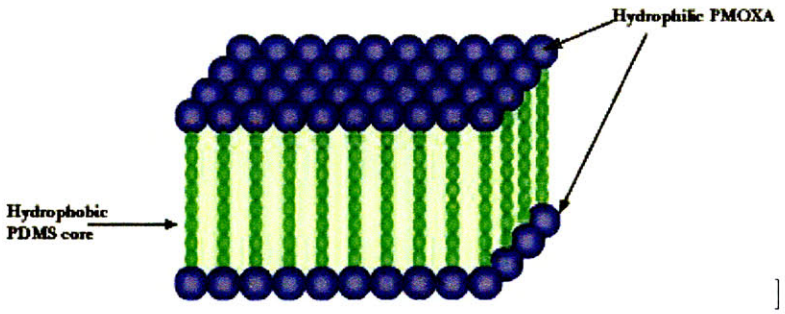

Figure 3-2: A schematic representation of the amphiphilic copolymer that can be used to implement the semipermeable membrane

polymerization of the methacrylate end groups the required characteristics that were outlined in the beginning of the section can be realized.

3.2.2 K^+/H^+ Antiport pump

The key feature of the proposed device is the ability to replenish the lost species by sequestering it from the background solution. In order to perform this task, the device has to selectively recognize (complex) with the intended molecule or ion and translocate it into the device against an uphill concentration gradient. As mentioned earlier potassium will be taken as the representative chemical for the purposes of this implementation.

There exists two carrier mechanisms that translocate potassium the non-electrogenic simple, symmetric carrier which include the naturally occurring macrocyclic carrier valinomycin and the synthetic carriers based on crown ethers or calix[n]arenes, and the electrogenic antiport carriers, which include the naturally occurring acyclic carrier nigericin, synthetic acyclic polyethers and the macrocyclic lariat crown ethers. As discussed below the antiport mechanism is the one that is best suited for the development of the chemical retinal prosthesis.

The most extensively studied carrier that translocates potassium is valinomycin [38] which is a naturally occurring antibiotic macrocycle. There also exist various synthetic analogues based on bis-crown ethers that selectively transport potassium ions. All these carriers are neutral carriers and they become ionized when a complex

is formed with the potassium ion. The translocation can be described by a simple symmetric four state carrier model [140]. The kinetics of the translocation are described by the dissociation or binding constant and the transport rate constant. Since the complex is ionized application of a voltage will increase the transport rate of the molecule in the favored direction(toward the negative potential) and can be used to move the ion up a concentration gradient. This, however, poses two problems: As the ion is translocated it opposes the applied voltage and decreases the energy available for further transport, the efficiency of utilization of the applied voltage is only 44%[148]. Though, applied voltage increases the transport rate in one direction over the other, it does not change the binding and unbinding constant of the complex which makes this type of carrier very inefficient for uphill transport. Ideally the right mechanism would change the binding and unbinding constant of the carrier, which makes uphill transport more efficient.

A general principle is presented here that involves the replacement of the lost chemical species by using chemiosmotic pumping. Chemiosmotic pumping [89] is a mechanism by which a proton gradient (pH gradient) is used to convert a process that is thermodynamically unfavorable to one that is favorable. This is a ubiquitous mechanism present in many biological systems, for example in mitochondria. This can further be extended to include any form of transport that uses an exchange mechanism (antiporters)[26] where the molecule of interest is exchanged for one that is not needed. Recently, the use of pH gradients to uptake drugs into liposmes has been proposed [39] and others have proposed mechanisms which would make uphill transport thermodynamically feasible [125, 134]. Though relevant these mechanism cannot be used in vivo since they rely on esoteric chemical reactions. So using a pH gradient as the driving force for the antiport pump will be the preffered method.

Nigericin is a naturally occurring antiobiotic carrier[109, 110, 105] that exchanges K^+ for H^+. However, like all natural carrier molecules it suffers from low lipophilicity and hence can leach out of the membrane over time. So it is imperative that the carrier be covalently bound to the membrane. Nigericin, however, cannot be easily covalently attached unless the molecular structure is altered by some form of genetic

modification. Alternatively, there exist a class of synthetic molecules called carboxylic crown ethers [63, 51, 123] that perform the same function as nigericin.

Carboxylic crown ethers can be used to pump alkali metal ions against their concentration gradients [43, 45, 44]. The mechanism of ion pumping by carboxylic crown ethers is illustrated in figure 3-3. When a proton gradient is present the carboxylic crown ether will de-protonate at high pH (low $[H^+]$) and will become negatively charged. The crown ether has the right cavity size (in this specific case, it is a 18-crown-6-ether) for complexing a potassium ion, since there is a counterion on the carrier it will make it favorable to form a complex with the positively charged cation. Having formed a complex it will diffuse down its $[H^+]$ gradient where it will re-protonate, this makes the potassium-crown ether complex unstable and hence will dissociate giving up the cation to the low pH (high $[H^+]$) side, the cycle then repeats until the concentration gradients of $[H^+]$ and $[K^+]$ are equal. The R-moiety is usually a long alkyl chain used to increase the lipophilicity of the crown ether carboxylic acid. This enhances the partitioning of the carrier into the membrane phase.In order to further increase the stability of the carrier in the membrane phase we have chosen to attach the carrier[76] to the polymer backbone via the long pendant alkyl chain. Since the carrier is attached this may decrease its mobility and to alleviate this the carrier concentration will be increased to promote a ion hopping [76, 25] mechanism rather than simple carrier diffusion, see figure 3-4.

By using simple four state carrier model [140] with minor modification one can develop a model for the flux though a membrane due to a carboxylic acid crown ether that will aid in the final design. The following chemical reaction takes place in the membrane

$A^-K^+ + H^+ \overset{\alpha,\beta}{\longleftrightarrow} A^-H^+ + K^+$

α= forward rate constant,β = reverse rate constant

The equilibrium constant is then given by, $K_D = \frac{[A^-H^+][K^+]}{[A^-K^+][H^+]}$

The flux of protons ϕ_H and the flux of potassium ions, ϕ_K is given by

$$\phi_K = \alpha\eta_K^i - \beta\eta_K^o \tag{3.1}$$

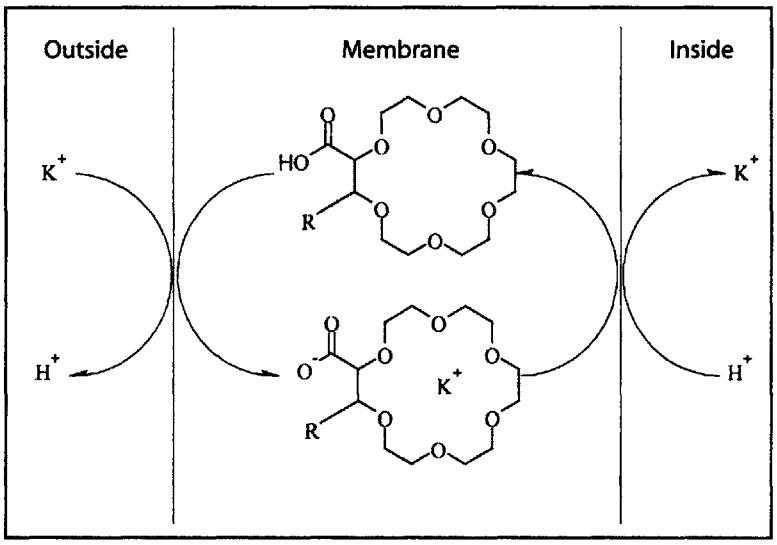

Figure 3-3: Principle of pumping potassium against a concentration gradient.

$$\phi_H = \alpha\eta_H^i - \beta\eta_H^o \tag{3.2}$$

Where $\eta_{K,H}^i$ is the density of carriers complexed to either to potassium or protons and facing the inside of the membrane, $\eta_{K,H}^o$ is the density of complexed carriers facing the outside. Since the carriers cannot leave the membrane face, there is a consevation law that we can impose namely

$\eta_{Tot} = \eta_K^i + \eta_K^o + \eta_H^i + \eta_H^o$

In thermal equilbrium the net flux must be zero i.e. $\phi_H + \phi_K = 0$. Thus

$\alpha\eta_K^i - \beta\eta_K^o + \alpha\eta_H^i - \beta\eta_H^o = 0$

Which can be rearranged and rewritten as

$\frac{\alpha}{\beta}(\eta_K^i + \eta_H^i) = (\eta_K^o + \eta_H^o)$

From the conservation equations we also have $\eta_K^o + \eta_H^o = \eta_{Tot} - (\eta_K^i + \eta_K^i)$

Thus,

$$\left(\frac{\alpha}{\beta} + 1\right)(\eta_K^i + \eta_H^i) = \eta_{Tot} \tag{3.3}$$

The concentration of the chemical species from the chemical reaction in the membrane can also be equated to the density of the carriers. Since the reaction is assumed to happen at the interface between the membrane and extra or intracellular fluid, in the inner face of the membrane $[A^-K^+] = \eta_K^i, [K^+] = C_K^i, [A^-H^+] = \eta_H^i, [H^+] = C_H^i$

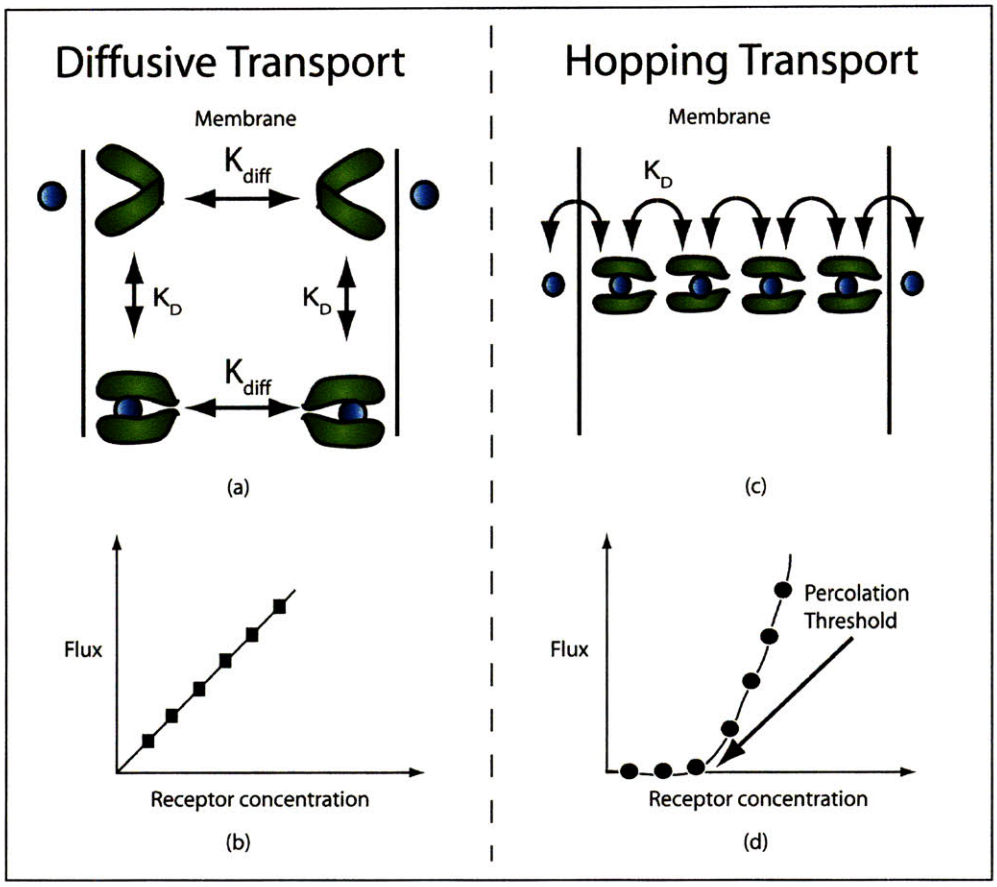

Figure 3-4: Schematic illustrating the difference between diffusive and hopping transport. a) A four state-carrier model of facilitated diffusion b) Graph showing the linear relationship between flux and the amount of receptor present in the membrane.c) Schematic of hopping transport, where the solute hops from carrier to carrier d) Graph showing the presence of a percolation threshold in hopping transport indicating that there needs to be minimum receptor concentration before any appreciable flux is observed.

a similar equation can be written for the outside face of the membrane. Thus the equilibrium constant can be rewritten as

$K_D = \frac{\eta_H^i C_K^i}{\eta_K^i C_H^i} = \frac{\eta_H^o C_K^o}{\eta_K^o C_H^o}$

Substituting this relationship in equation 3.3 and simplfying yields

$\eta_K^i = \frac{\eta_{Tot}}{\left(\frac{\alpha}{\beta}+1\right)\left(1+K_D\frac{C_H^i}{C_K^i}\right)}$

A similar equation can be written for the density of carriers on the outside

$\eta_K^o = \frac{\eta_{Tot}}{\left(\frac{\alpha}{\beta}+1\right)\left(1+K_D\frac{C_H^o}{C_K^o}\right)}$

By substituting these equations of the density of carriers complexed to the inside and outside into the potassium flux equation 3.1, the flux of potassium ions , ϕ_K can be written as

$\phi_K = \phi_{max}\left(\frac{C_K^i}{C_K^i+K_D C_H^i} - \frac{C_K^o}{C_K^o+K_D C_H^o}\right)$, where $\phi_{max} = \eta_{Tot}\frac{\alpha\beta}{\alpha+\beta}$

Similarly, $\phi_H = \phi_{max}\left(\frac{K_D C_H^i}{C_K^i+K_D C_H^i} - \frac{K_D C_H^o}{C_K^o+K_D C_H^o}\right)$

From the conservation law we have $\phi_K = -\phi_H$ using this relationship and after some algebraic manipulation the following equation is obtained

$$\boxed{\phi_K = \phi_{max}\frac{C_H^o}{\left(C_K^i+K_D C_H^i\right)+\left(C_K^o+C_H^o\right)}\left(\frac{C_K^i}{C_K^o} - \frac{C_H^i}{C_H^o}\right)}$$

In thermal equilbrium the flux $\phi_K = 0$ and we get $\boxed{\frac{C_K^i}{C_K^o} = \frac{C_H^i}{C_H^o}}$, this indicates that only the ratio of concentration that need to be equal. So a change of 1 pH unit will give us a 10 fold concetration of K^+. However, the rate at which the concentration will reach this equilibrium value depends on the exact values.

3.2.3 pH gradient generation

In order to operate the antiport pump a pH gradient needs to be established this may be accomplished in one of two ways: light energy can be converted to a proton gradient or chemical energy can be converted to a proton gradient. Conversion of light into proton gradients is a widespread mechanism found in many photosynthetic bacteria, the most popular being bacteriorhodopsin [122]. However, for the case of the retinal prosthesis this pump would serve as the ideal triggering mechanism for the release of potassium. Furthermore, the absorption spectrum of bacteriorhodopsin lies in the visible range which means a background light intensity needs to be present

and this may interfere with the normal operation of the device. Alternatively one could envisage the use of the photosynthetic reaction center of *Rhodopseudomonas viridis* from the purple bacteria which also acts as a light driven proton pump [28]. The absorption spectrum for this protein is in the near infrared and hence could be used.

However, the simplest method of achieving vectorial proton transport is to produce hydrogen inside the device and thereby create a proton gradient. One method to achieve this is to oxidize glucose into gluconic acid using glucose oxidase[11], a naturally occurring enzyme that is used in many amperometric in vivo glucose sensors. Gluconic acid freely dissociates (pKa$\approx$3.6)into gluconate [49, 16] giving up a H^+. Additionally another enzyme catalase maybe used to decompose hydrogen peroxide into water to protect glucose oxidase from peroxide induced degradation[67]. The overall reaction maybe then given by

$$\text{Glucose} + O_2 \overset{Gox,Catalase}{\longrightarrow} \text{gluconate} + H^+ + \tfrac{1}{2}O_2 + H_2O$$

Hence it is necessary to transport glucose into the device i.e. it needs to be permeable to glucose. This maybe achieved by using synthetic glucose carriers based on boronic acids [99]. The mechanism of glucose transport[142] is shown in figure 3-5. The sugar is complexed by the boronic acid moiety and passively transported from one side into the other. Since there is an active consumption of glucose there will be a steady flux of glucose into the cell due to the finite concentration difference between the inside and outside of the device. The glucose carriers can be covalently attached to the siloxane layer of the lipid like membrane to prevent leaching of the carrier. The glucose oxidase can be immobilized in the p(Hema) storage layer using established techniques [104, 12].

3.2.4 Storage and Release Layer

An essential component of any chemically mediated neural prosthesis is the ability to efficiently store the sequestered species and release it in a controlled manner. Some

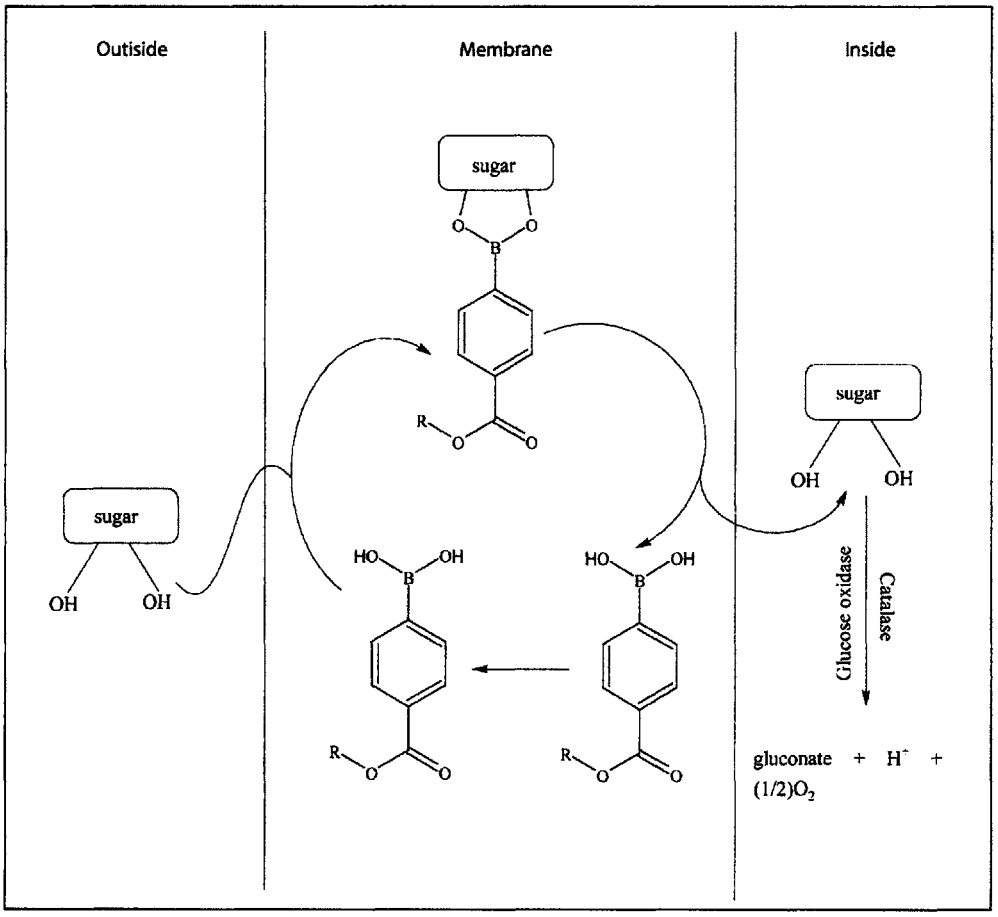

Figure 3-5: Schematic of coupled sugar transport using a boronic acid carrier.

cues from natural systems but in order to maintain manufacturability synthetic techniques may also need to be applied.

The storage needs to provide a liquid-like structure that also provides structural stability for the rest of the device. Hydrogels are three dimensional crosslinked networks of hydrophilic macromolecules surrounded by an aqueous phase. Hydrogels are governed by the polymer-polymer affinity, and by elastic and osmotic forces. The dominant force determines the equilibrium volume attained by the network. Ionic hydrogels contain also ionizable groups along the polymeric chain. At a certain pH the ionizable groups (acidic or basic) place a fixed charge in the hydrogel network. To compensate for the fixed charge mobile ions enter into the hydrogel, which increases the osmotic pressure and causes the hydrogel to swell until elastic forces impose a restoring force. By changing the chemical composition of the polymers the hydrogel can be made sensitive to other physiochemical variables like temperature [1] and electric field [129, 73]. The volume transitions in such hydrogel networks can be rather large ($\gg 2X$), see figure 3-6a.

The hydrogels suitable for this application should undergo volume transitions when the pH in the hydrogel is changed. The hydrogel backbone is comprised of a hydrophilic poly (hydroxyethyl methacrylate-co-acrylic acid) copolymer and the network is crosslinked by tetraethylene glycol diacrylate. To enable microfabrication compatibility the hydrogels are synthesized via UV induced radical polymerization using a photosensitizer (Irgacure) [124, 135]. A simple UV curable gel was synthesized and the patterned using a transparency mask and is shown in figure 3-6b Though one could envision the volume transitions as a mechanism for releasing the neuroactive species stored in the hydrogel, the mechanism is mediated by diffusion and hence takes extended periods of time to swell and deswell. However, by shrinking the macroscale gels to the micrometer scale the timeframe can be greatly reduced. The kinetics can also be modified by introducing grafted chains in the gel layer or by using surfactants, which form water channels allowing for faster incorporation or release of water into and from the gel [152, 68]. Even with these modifications it may not be feasible to rely only on this mechanism for release. To aid this process an additional method for

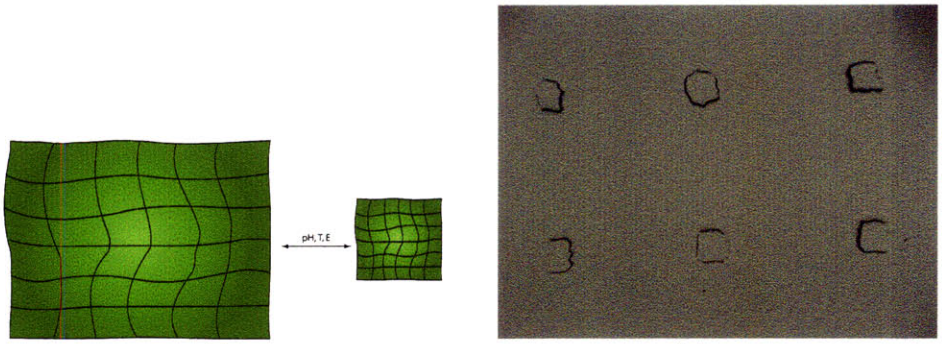

(a) (b)

Figure 3-6: a)Schematic of gel transition under appropriate physiochemical variables like electric field, temperature and pH.b) A photcurable microgel patterned using a transparency mask.

release as discussed below, should be considered.

Nanopore based Voltage gated ion channel

In natural neural systems directional ion transport often occurs via voltage gated ion channels. The channels are sophisticated structures that shield the charge of the ion from the hydrophobic core to enable selective ion transport. The channels also change conformation in response to an applied voltage that allows for unidirectional transport. The incorporation of all these properties is a formidable task for a synthetic system. However, by removing some of these constraints it may be possible to develop a robust synthetic analog. In the proposed system ion selectively is not a requirement since the polymeric self-assembling membrane described earlier already confers this property. The only property that the synthetic ion channel needs to provide is voltage gated transport of the stored ions. The voltages required need to be within the scope of several 100mV's to ensure compatibility with the neural architecture. The currents used will be in the order of a few nA as dictated by the required ion concentration that need to be delivered in a fixed interval of time. Inherently, the power of this system is very low (hundred's of pW).

The nanoscale phenomenon exhibited by nanopores has gained a lot of attention in the recent past [19, 120]. In this system the length scale of the pore is on the order

of certain physical phenomena. When a charged surface is exposed to an electrolyte, charge neutrality, diffusion and the mobile nature of the ion require an exponentially decaying charge density of opposite polarity in the solution. The length scale is called the Debye length and is encountered in many other physical processes as well. For physiologically relevant concentration the Debye length is on the order of a few nanometers. If two charged surfaces are in close proximity as in a nanopore, the Debye layers are able to overlap [120]. Depending on the surface charge the overlapping Debye layer can be either positively charged serving as a cationic barrier as shown in figure 3-7a or can be an anionic barrier. Furthermore, additional effects can be obtained by adjusting the geometry of the nanopore itself.

If the nanopore has an asymmetric profile such as the conical profile shown in figure 3-7, the potential profile at the middle of the nanopore exhibits a Brownian ratchet type potential [3], a minima close to the nanopore tip. If a local potential is superimposed on this nanoscale device, see figure 3-7b, the local minima can be either deepened or raised [50]. This asymmetric behavior of the nanopore to externally applied potentials results in rectified ion transport occurring preferentially from the narrow region of the pore to the wide region of the pore, as shown in figure 3-7

3.3 Conclusions

A possible alternative to electrical stimualtion was proposed. Some possible approaches of implementing a supramolecular prosthesis was outlined. In the next chapter the neurophysilogical data supporting the theory of using potassium ions to stimulate neural tissue is presented.

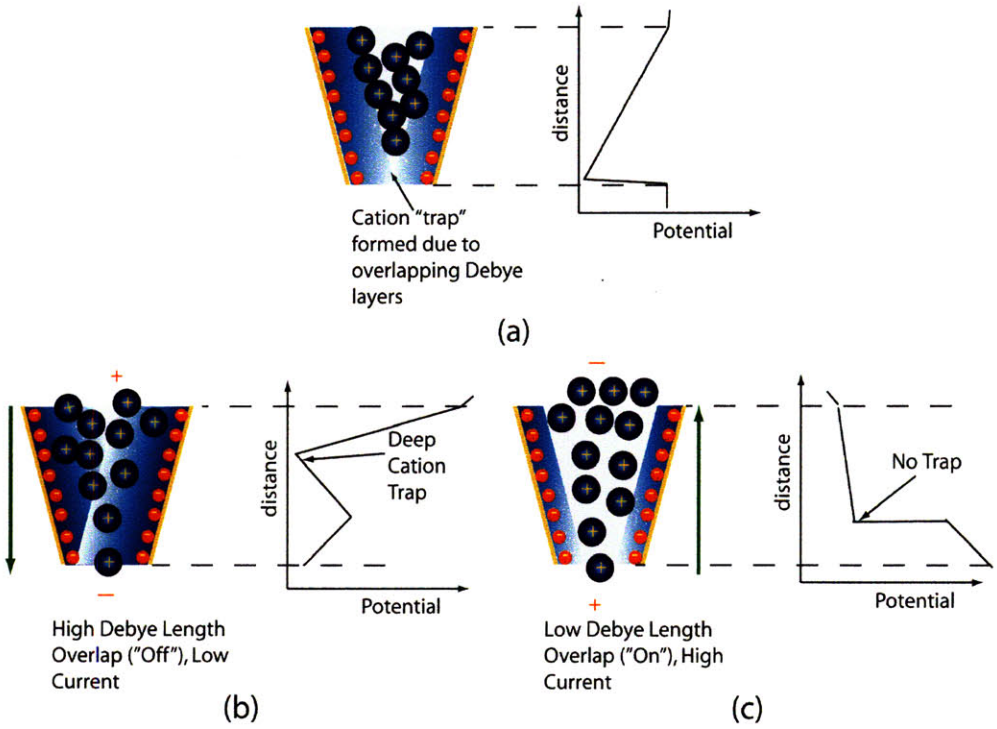

Figure 3-7: Principle of the voltage gated ion channel. a) The nanopore dimensions are on the order of the Debye length of the system and hence they overlap specially near the tip and generate a barrier of cations. Also shown is the potential distribution along the center of the channel. b) Application of a potential in the direction shown causes increase in the overlap causing a deeper trap. The potential profile is a superposition of the potential due to the surface charge and the applied potential and a deep cation trap in the potential can be seen. c) Reversing the potential abolishes the trap and Debye layer overlap is greatly decreased and allows for increased current flow. Adapted from [50]

Chapter 4

Neurophysiology

4.1 Introduction

An immediate aspect of the proposed research that needed to be studied are the neurophysiological parameters. The design parameters as dictated by biology need to be obtained. One pertinent question is what are the neurophysiologically relevant concentrations? To study this and other questions single-cell recordings were made from the axons of ganglion cells with an *in-vitro* rabbit retinal preparation.

4.1.1 Retinal Neurophysiology

Before we delve into the actual experimental result we must become familiar with some basic retinal neurophysiology. Anatomically, the retina is one of the most organized neural architectures and follows a layered architecture. The retina is a thin tissue that lines the back of the eye, see figure 4-1. The blood supply to the mammalian retina mainly comes from the choroid and there is second supply for the inner layer carried by central retinal artery from the optic nerve head. Humans have a region with very high photoreceptor density called the fovea and is the point greatest visual acuity. Around the fovea is a region called the macula, and corresponds to approximately 15° of visual acuity. Degeneration of the photoreceptors around this area that leads to AMD.

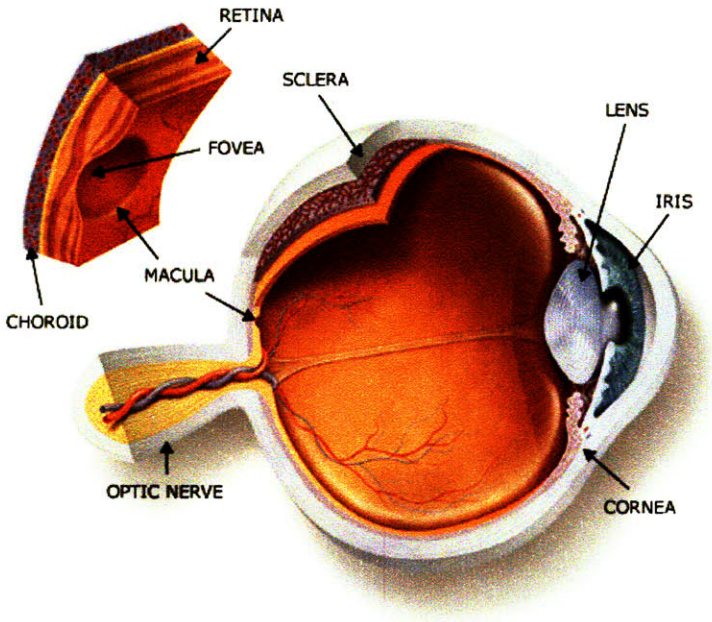

Figure 4-1: Schematic of the eyeball showing details of the human retina. source (www.amdcanada.com)

The detailed structure of the retina with its different layers is shown in figure 4-2. Each layer has very specific function to perform. Most of the discussion that follows is a very condensed version of the excellent book written by Rodieck [113]. Contrary to what would be expected, the photoreceptors are not the first layer that face the incoming light, in fact they are the last layer of the neurosensory retina. One conjecture is that photorecptors have high metabolism and need to have a good source of nutrients and hence need to be close to the choroid. Photoreceptors come in two forms, the rods and cones. Rods are adapted for low light conditions and cones are adapted for bright light conditions. Together the rods and cones span a dynamic range of 10^9 of light intensity!. This amazing dynamic range is due to the adaptation mechanisms, via negative feedback, in the eye where the cells only respond to changes in light intensity and not the absolute light intensity. As an aside this has been mimicked by silicon circuitry to produce similar results [29]. As soon as a photon strikes the photoreceptor the retinal chromophore, retinal, undergoes a cis-trans isomerization that activates a G-channel protein that reduces cyclic guanosine monophosphate (c-GMP) levels that close the sodium channels. This closing of sodium channels hy-

perpolarizes (see chapter 1) the photoreceptor and in turn decreases the amount of glutamate that is released.

There are two cells that receive this input from the photoreceptor, one is the horizontal cell and the other is the bipolar cell. The horizontal cell is sign conserving in its connection from the photoreceptor, i.e the horizontal cell hyperpolarizes if the photoreceptor hyperpolarizes. The horizontal cell has a negative (sign inverting) connection back to the photoreceptor. It is this negative feedback that enables the large adaptation to light levels in the photoreceptor. In addition horizontal cell are coupled to each other (of the same type) via electrical junctions called gap junctions. This electrical coupling gives the retina an interesting spatial image processing capability. The horizontal cells can be thought of as a 2D resistive grid [85], the voltages at each node then should be the solution to the diffusion equation. This is equivalent to a low-pass spatial filter. This extensive lateral coupling also leads to lateral inhibition.

The bipolar cells receive inputs from the photorecptor in either a sign inverting manner via metabotropic receptors or sign conserving via ionotropic receptors. This gives rise to distinct light pathways ON and OFF, the ON referring to pathways that are active when there is an increase in the light level and OFF when light levels decrease. Each pathway makes a distinct connection to a separate layer in the outer synaptic layer. The OFF pathway terminates in the inner part of the inner synaptic layer and the ON pathway to the inner half. Like horizontal cells, bipolar cells are non-spiking in nature, they respond to inputs with graded changes in membrane potential. The bipolar cells also release glutamate as result of the inputs to them. The bipolar outputs are fed as inputs into the ganglion cells which are also separated into ON and OFF pathways. The ganglion cells are spiking in nature and carry their information as quasi-digital information to the brain via their axons that form the optic nerve. The last type of cells are the amacrine cells that provide negative feedback and lateral coupling in the inner synaptic layer. The exact function of the amacrine cells is unknown, though it is believed that they play a role in the center surround response of the ganglion cell layer. Unlike other cell types, the amacrine cells do not use glutamate as their neurotransmitter of choice. Instead many use gamma-

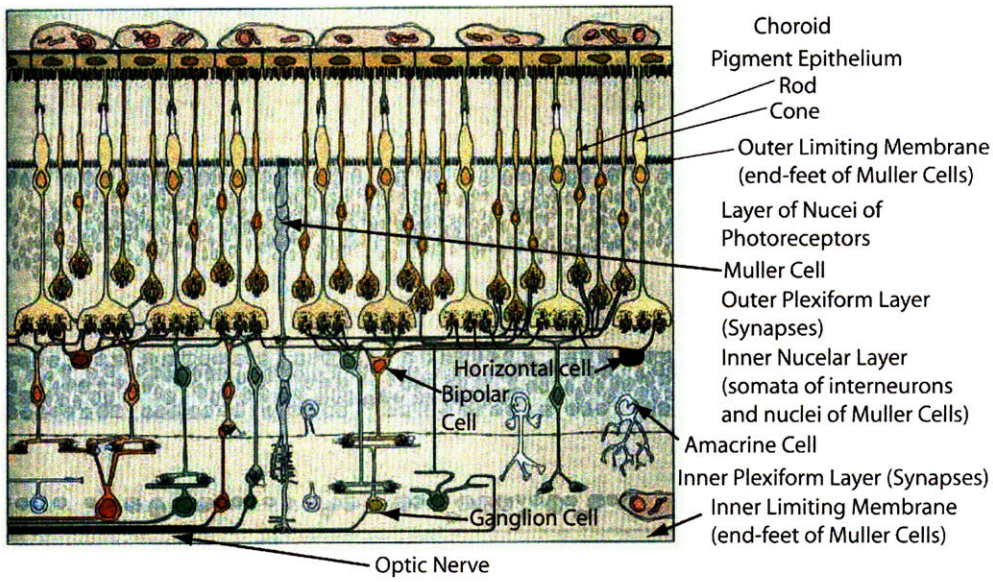

Figure 4-2: The detailed schematic view of the retina is shown. Red cells and pathways are indicate "OFF" and green cells and pathways are "ON".

aminobutyric acid (GABA) or glycine. Acetylcholine, dopamine or neuropeptides may also be used by these cells. Their precise roles in the retina, however, have not been determined.

4.2 Experimental

Rabbit retinal tissue was obtained from freshly excised eyes of New Zealand White rabbits. All surgeries were performed by Dr. Ralph Jensen in accordance with the animal protocol submitted to the committee on animal care at the Veterans Affairs Hospital, Jamaica Plain campus. All *in-vitro* experiments reported here were done under the expert guidance of Dr. Jensen. The excised eye was sliced open and the vitreous was removed by gentle vaccum suctioning. The retinal tissue was then cut into a roughly trapezoidal shape containing the region in the inferior, mid-peripheral retina. The retina was constantly bathed with 95% O_2/5% CO_2 bicarbonate buffered Ames solution to ensure cell viability during the entire procedure. The same procedure was repeated for the second eye and placed in a 95% O_2/5% CO_2 bicarbonate buffered nutritive Ames solution bath for use in a second experiment if necessary. The animal

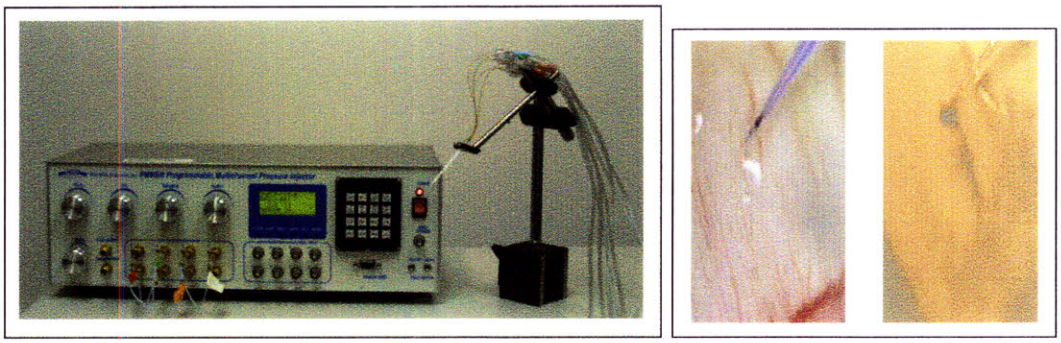

(a) (b)

Figure 4-3: a) Experimental setup used for the K^+ stimulation b) Snapshots of the pipette positioned over the retina, the figure with a red shading is the pipette under red light illumination and shows the KCl solution being ejected with the dark stain caused by the Azure B dye used for visualization. The red light was used to prevent the retina from responding to the ambient light since it is known that these rabbit retinae do not respond to red light.

was euthanized by a injecting a high dose of pentobarbitol immediately after the eyes were excised. The prepared retinal slice was placed on a plastic mount that was perfused continuously with 95% O_2/5% CO_2 bicarbonate buffered Ames solution. The whole preparation was imaged by a CCD camera fitted with a zoom lens and displayed on a monitor to enable visualization of the experiment.

Various concentrations of KCl were prepared (0-30mM) in an osmotically balanced NaCl solution (300 mOsm). All solutions contained approximately 1mg/mL of Azure B to enable visualizations during ejection. The multibarrel pipette was connected either to 28 AWG non-metallic syringe needles (PolyFil, WPI, Sarasota,FL) and then filled with appropriate salt solutions or filled first and then connected to the syringes. The filled multibarrel pipette was color coded and connected to a multichannel pressure ejector (PM8000, MDI Systems). All pressure ejections were effected by controlled pressure pulses of nitrogen delivered to the pipette. The experimental setup is shown in figure 4-3.

An appropriate stimulation spot was determined as follows: After having isolated the spike activity of a retinal ganglion cell (RGC) a small spot of light was moved around to determine the location of the receptive field of the RGC. This was done in two ways first by visually looking at the spike data on the recording system (CED

Retina	Cell	Pressure(psi)	Pulse Width(msecs)
1	1,2,3	40	20
2	1	40.4	100
2	2	50.8	50
3	1,2	20	50

Table 4.1: Pulse widths and pressures used in different experiments

1401, Cambridge Electronic Design,UK) and processed with Spike2. Secondly the recording electrode data was fed to a loud speaker and each spike can be heard as a loud click. In both cases the raw signal from the recording electrode was first fed into a window discriminator (FHC inc., Maine, U.S.A) to ensure noise rejection. The multibarrel pipette was then moved to light spot and the light spot was turned off. All experiments including the light experiments were performed in red light to prevent any background light effects since these rabbit retinae do not respond to red light. Sample pulses of the highest concentration available (30mM KCl) were then ejected with pressures in range of (15-60 p.si) and durations of (10-50msecs) depending on the barrel, see Table 4.1. The satisfactory working of the pipette was evidenced by the release of the salt solutions containing the dye. If there was a satisfactory response then all lights were turned off and the retinal cell was subject to the various concentrations and data was collected. Most experiments were repeated 10 times to ensure repeatability and robustness. The only exceptions to the 10 trial protocol was cell 3 in retina 1 (see figure 4-7a) which had 5 trials, the receptive field and barium response experiments (4 Trials). There was a delay time, usually a few seconds, between repeated trials to ensure that the effects of the earlier pulse had subsided.

To ensure that the pipette volumes were more or less correlated, a pipette calibration was performed on one of the pipettes after the experiment was over(retina #2, in table 4.1. The calibration was done as follows : The pipette tip was placed in dish containing mineral oil and 10 pulses of the dye containing salt solution was ejected. The width of the resulting magnified drop was measured on the monitor using a ruler and this was then repeated for each barrel. The magnification factor was then computed by placing a ruler in the view of the camera and the distance between two

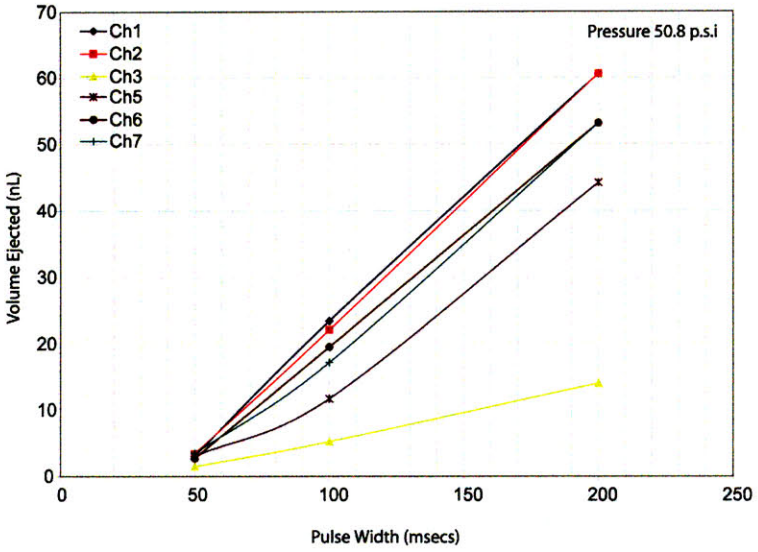

Figure 4-4: Pipette calibration

ruler points was measured and divided by the actual length between the two marks. The results of the pipette calibration are shown in figure 4-4. It can be seen for the low pulse widths that were actually used the pipettes volumes are well correlated, at higher durations some deviations occur. The relationship between volume and pulse duration seems to be linear for the most part. In all other experiments prior and following this calibration the volumes were visually checked for consistency between barrels and the pulse widths were kept between 20 and 50msecs, see Table 4.1.

4.3 Results and Discussion

4.3.1 Dose-Response Curves for K^+ evoked response

The major goal of these experiments was to understand what the neurophysiologically relevant concentrations of K^+ that would evoke a response. The following results were obtained from various cell types of ganglion cells that were located in the inferior, mid-peripheral retina. The control solution which contained 0mM KCl and 150mM NaCl produced no response. Solutions that contained 10-40mM KCl, with appropriately

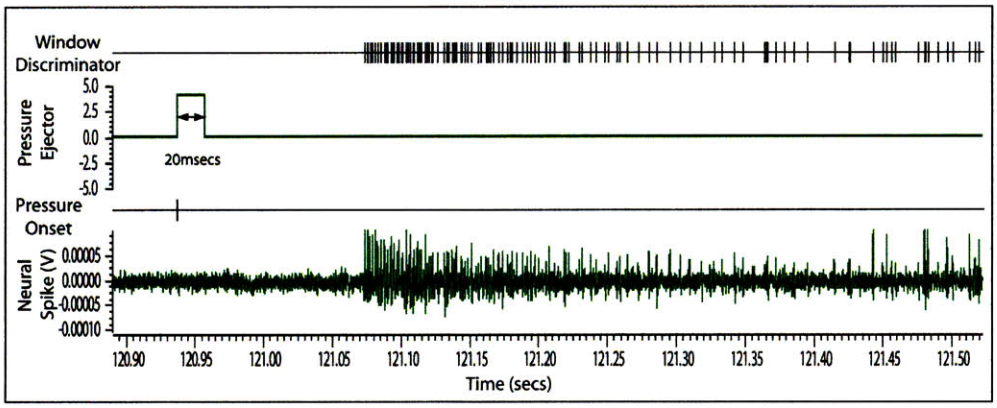

Figure 4-5: Neural spike recording from a rabbit retinal ganglion cell to a potassium stimulus of 30mM of duration 20msecs. This record is the same as the one reported for cell 3 in retina 1 in figure 4-7a

adjusted amounts of NaCl to ensure osmotic balance, produced appreciable responses, with response strength increasing with K^+ concentration. Typical response latencies were 30-120msecs after application of K^+. With a background concentration of about 3mM K^+, it was determined that a minimum concentration of 10mM was needed using a Nernst potential calculation. From the results that were obtained it seems that this is indeed close to the threshold needed for K^+ evoked response. As mentioned earlier all experimental results reported in this section are averages of 10 trials. A typical retinal ganglion cell response to a 20msec pulse of 30mM K^+ is shown in figure 4-5.

A better indicator than the raw spike data is the peristimulus histogram (PSTH) and the corresponding raster plot and is shown in figure 4-6. A PSTH is an analysis done auomatically by the Spike2 software, it plots the number of spikes that occur within a user specified bin. This gives a sense of how strongly correlated the data is from one trial to the other. On top of the PSTH is shown the raster plot which indicates how many trials contributed to that bin. The vertical clustering of the raster plot indicates very high correlation between trials. The PSTH shown in figure 4-6 correspond to cell 2 in figure 4-7b. The PSTH for the control stimulus (150mM NaCl) is shown in figure 4-6a, it can be seen that there are very few spikes that occur in the same bin the 10 trials and that the raster is scattered indicating that this spike pattern is random and is due to the background firing on the retina, the total number

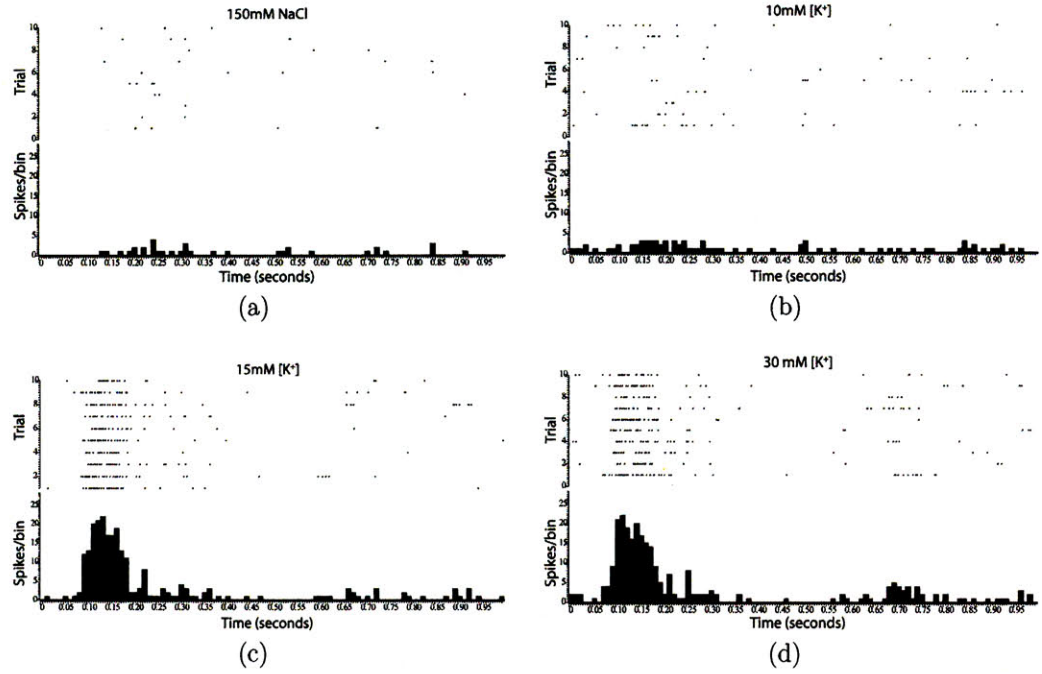

Figure 4-6: Peri-stimulus histograms for a representative cell stimulated by increasing K^+ concentrations. (a) Response to the control solution of 150mM NaCl (b) A modest increase (10mM) in K^+ concentration increases the spike count from the control value of 35 to 80 spikes. Further increases to 15mM(c) and 30 mM(d) increases the spike rate to 240 and 272 spikes, respectively. The response shows the saturating characteristics indicated in the dose-response curve. The histograms are summed responses from 10 trials as indicated by the raster plots and the bin width is 10 msecs

of spikes was 35. In figure 4-6b we see a small clustering of responses when the retina is stimulated with 10mM K^+ and the total number of spikes rose to 80. On a slight increase in K^+ to 15mM there is a tremendous increase in the number of spikes and it can be clearly seen in figure 4-6c that the response was strongly stimulus correlated, the total number of spikes here was 240. Further increases the K^+ to 30mM did not increase the number of spikes by very much though there is a delayed cluster of responses, indicating that there is a saturating behavior.

Dose-Response curves from 3 RGC's in 3 separate experiments are shown in figure 4-7. Curves were then plotted by taking the median rather than the average to prevent outliers from biasing the result. The number of cells contributing to each value is indicated on the caption text accompanying the figure 4-8. The fact that the

shape more or less resembles Cell2 in retina 2 (see figure 4-7b) is a strong indicator that the plot of the median amount of spikes describes a general trend. Since for this cell there is accompanying pipette volume data, see figure 4-4 showing that the volumes ejected at that pressure and duration are approximately equal removing any volume dependent variability which may be present in other data.

4.3.2 Receptive Field

One of the conjectures that was proposed at the outset was that, since the concentration of a bolus of K^+ ions should decrease both spatially and temporally as a Gaussian [140], the receptive field should be narrow. This would be an advantage of ionic stimulation over electrical stimulation. To verify if this was the case, an *in-vitro* retinal preparation was subjected to 30mM concentration pulses via a single 2μm diameter pipette. The higher concentrations were used to get both strong responses and this would also be the largest receptive field one could achieve with ionic stimulation giving an upper limit. The pipette was moved in increments of 50μm using a micromanipulator that had a digital readout of the position. Additionally the same cells' receptive field was also mapped out by using a light spot approximately 100μm in diameter. The trial repetitions for both ionic and light stimulations were 4 as indicated earlier. The results are show in figure 4-9. The potassium evoked receptive field has qualitatively the same features as that of the light stimulation. The widths of both being comparable with potassium having a 400μm overall diameter and light having approximately a 300-400μm diameter receptive field.

4.3.3 Direct Vs Indirect Activation

Until this point it has been implicitly assumed that the K^+ evoked response was due to the direct depolarization of the neuron via increases in the membrane potential. The following experiments were done to provide some insight into the mechanism of activation. This study is a direct extension of the work done earlier by Dr. Jensen [65]. Before addressing these questions some additional background on retinal function is

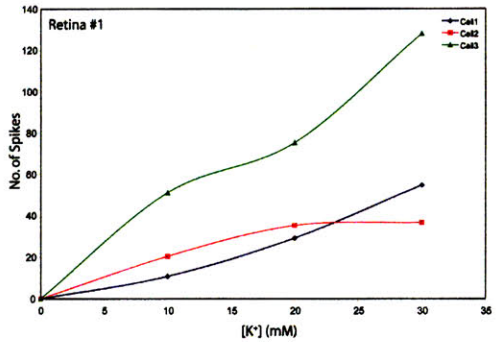

(a)

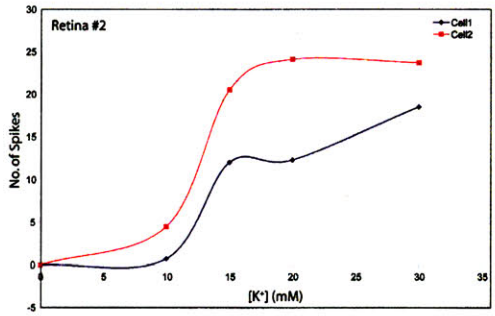

(b)

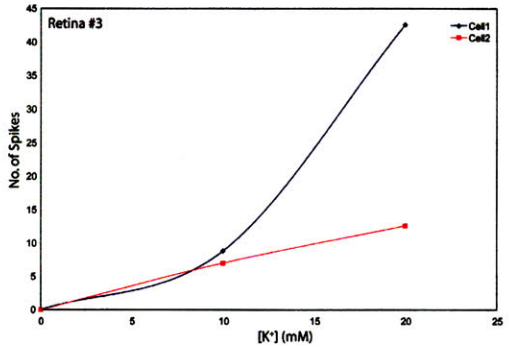

(c)

Figure 4-7: Raw data collected from different cells in retinas from different animals. All data are sums of spikes from the corresponding PSTH and then divided by the number of trials. The background spike count was then subtracted from each concentration.

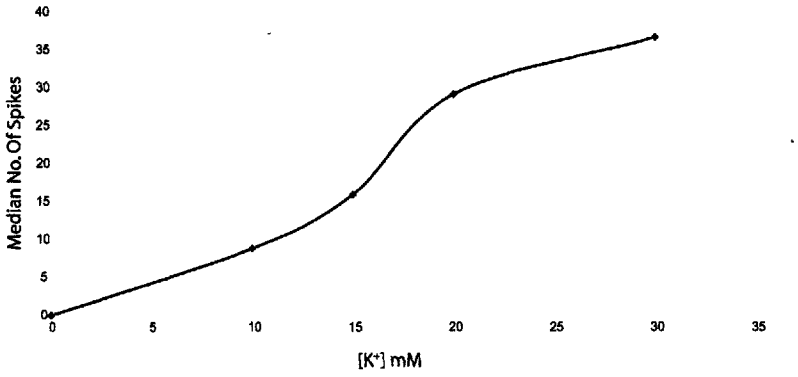

Figure 4-8: Potassium evoked response median data. The number of spikes is the median value of a number of cells 10mM,20mM - 7cells,15mM-2 cells, 30mM-5 cells

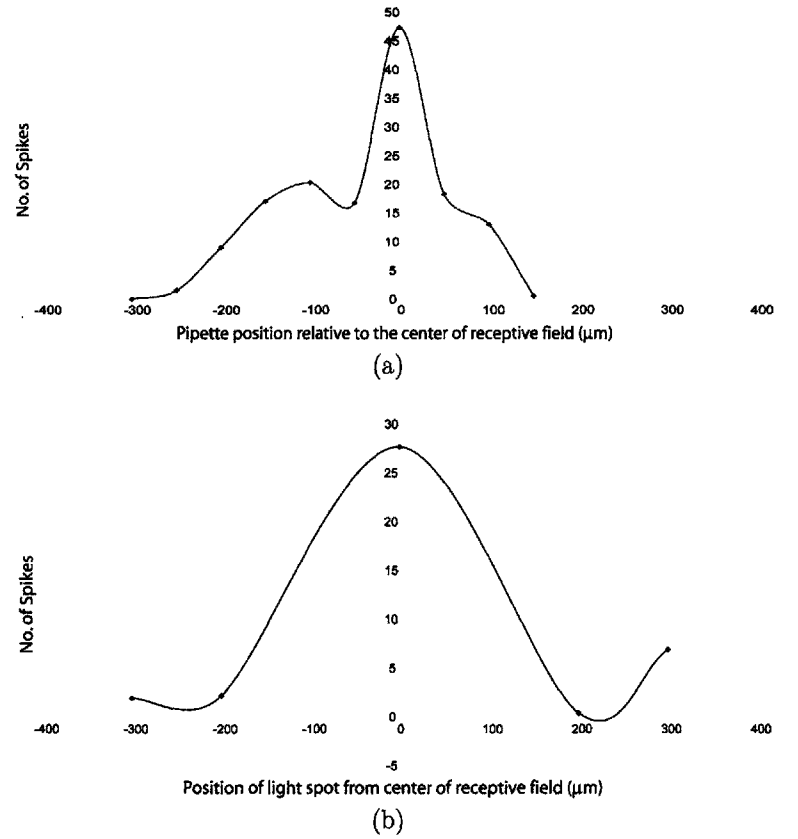

Figure 4-9: (a) Stimulation by 30mM[K^+];(b)Stimulation by a spot of light (100μm diameter). The receptive fields are qualitatively similar in size 300-400μm and shape for both light and potassium evoked responses. The intermediate dip in potassium evoked response maybe due to the fluid flow pattern.

necessary.

One of the cells that has not been explicitly mentioned is the Müller cell which is shown in figure 4-2. This cell belongs to the class of cells called glial cells. For the longest time these cells were relegated to being just passive filler cells that provided only structural support. However, recent investigations have completely changed that picture [70, 95, 13]. The Müller cell traverses the entire retina, it projects microvilli into the subretinal space and projects toward the vitreous body where it expands into the so called end-feet proximal to the basal lamina. The basal lamina and the end-feet together form the inner limiting membrane. The Müller cell has secondary branches from the main trunk that form sheaths with all neuronal cell bodies and dendrites found in both in the inner and outer nuclear layers. It especially forms connections to synapses in both plexiform layers. The Müller cells have been shown to play a key role in the following processes[13]:

- Potassium homestasis
- pH regulation and CO_2 uptake
- Neurotransmitter uptake and recycling
- Photopigment recycling
- Protection against free radicals
- Metabolic support

The processes are summarized in figure 4-10. We will mainly concentrate on the two aspects, potassium homeostasis and the neurotransmitter uptake. The reason for concentrating on K^+ homeostasis is straightforward since it should directly affect the experiments that are under investigations. The reasons for concentrating on neurotransmitter uptake is more subtle but will soon become apparent.

When neurons depolarize to light in the retina there is an increase in the extracellular potassium concentrations and the Müller cells contain a high density of inwardly rectifying potassium channels that immediately provide a low resistance path way for

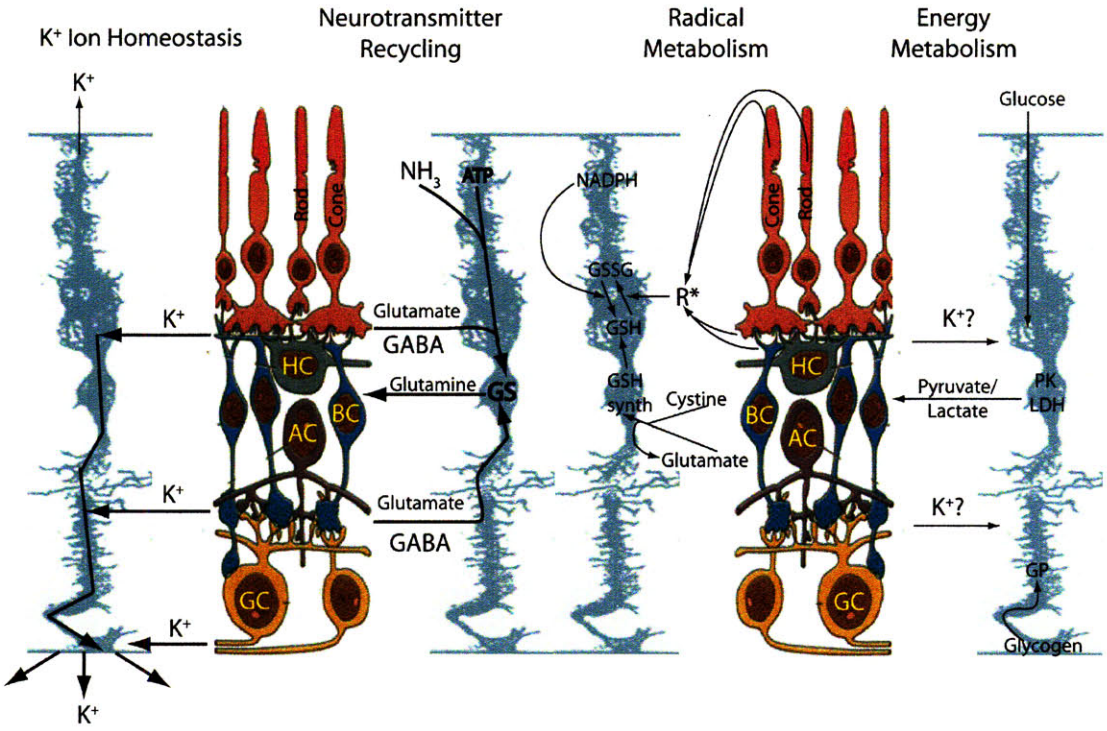

Figure 4-10: Müller cell regulation mechanisms GC:Ganlion cell, AC: Amacrine cell, BC: Bipolar cell, HC: Horizontal cell, GSH: GLutathione, GSSG: Oxidized version of Glutathione, GP: Glycogen phosphorylase, PK: Pyruvate kinase, LDH:Lactose dehydrogenase . Potassium ion homeostasis via siphoning of the potassium via low resistance inward rectifying K-channels. The increase in the extracellular potassium during neuronal depolarization is conducted away by low resistance pathways provided by the Müller cell, toward the vitreal surface. Glutamate and GABA clearance via glutamate uptake pumps that are ion dependent for transport. Radical scavenging via glutathione synthesized by using cystine and glutamate by glutathione synthetase. The oxidized product GSSG is reduced back to GSh by NADPH produced by pentose phosphate pathway in the Müller cell. Glycogenesis and glycolysis is enhanced by increases in extracellular K^+. The PK/LDH enzymes present in the glia release lactate/pyruvate that is used by neurons in their Krebs cycle.Figure adapted and redrawn from [13]

these ions and effectively siphon them from the extracellular space and toward the vitreous driven by potential setup by the ionic gradient[70]. Inward rectifying channels behave opposite to the Hodgkin-Huxley potassium channels described in chapter 1, they show increased potassium conductance to hyperpolarizing conditions rather depolarizing conditions. The siphoning mentioned earlier is the key to maintaining the proper potassium ion concentrations in the retina. Additionally extracellular K^+ decreases near the photoreceptors under illumination so some of the potassium is also siphoned toward the photoreceptors.

In the retina the primary excitatory neurotransmitter that is used is glutamate. Unlike acetylcholine that is used in neuromuscular junctions that is hydrolyzed by acetylchloinesterase there are no such enzymes for glutamate. So in order to terminate synaptic activity the excess glutamate must be removed, since high levels of glutamate is neurotoxic [128]. Here is where Müller cells play a key role, they actively uptake glutmate and break it down to glutamine and release it to the extracellular space where it is taken up by neurons for glutamate synthesis. The glutamate uptake pump is electrogenic and the energy is driven by the transmembrane ionic gradients maintained by the Na^+/K^+ pump. For each cycle of the glutamate uptake pump one glutamate is pumped into the glial cell. Concomitant with transport of one glutamate there is also a transport of $2Na^+$ into the cell [128]. Furthermore, intracellular K^+ must also be transported out of the cell. Recent studies have also shown that there is either a H^+ ion is transported into the cell or a OH^- is transported out of the cell. It is unclear which of these two processes is taking place, the end result however is that it results in the acidification of the interior of the cell [4]. The overall stoichiometry of the pump is shown schematically in figure 4-11.

So how does this shed light on whether K^+ evoked response is direct or indirect? In a seminal investigation by Szatkowski, Barbour and Atwell [127], they showed that this glutamate pump can be made to operate in reverse when the extracellular potassium concentration is raised. So the Müller cells will release neurotransmitter in response to elevated extracellular K^+ and stimulate nearby neurons. In fact it is believed that this is the primary process by which cell death will occur in case of an

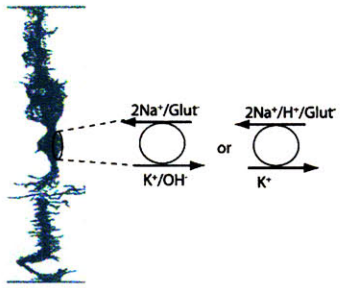

Figure 4-11: Stoichiometry of the Glutamate uptake pump

ischemic event where the extracellular potassium rises to 60mM.

So which one of these effects is actually contributing (if at all) to the K^+ evoked response. One way to investigate whether the processes in the Müller cell plays a role in K^+ evoked response is to block its sensitivity to K^+. This can be effectively done by adding micromolar concentrations of barium to the bathing solution , since barium is known to selectively block the inwardly rectifying K-channel (Kir)[96]. This experiment was performed by applying 200μM Ba^{2+} to the bathing solution and the results are shown in figure 4-12 in form of stimulus histograms. Both light evoked and potassium evoked responses before and after application of barium was recorded. Figure 4-12 shows the time sequence of K^+ evoked responses, it can be seen that after 3mins of application of Ba^{2+} the K^+ evoked responses were completely abolished. However, as seen in figure 4-13 the light evoked response does not seem to be adversely affected. This result is similar to the one obtained by Jensen [65].

Since the K^+ evoked responses are abolished when the Kir channels of the Müller cells are blocked by barium this would suggest that the potassium siphoning by the Müller cells play a central role in K^+ evoked responses. This, however, does not rule out the reversal of the uptake pump since Jensen [65] showed that application of glutamate receptor antagonist 7-nitroquinoxaline-2,3-dione (CNQX) considerably reduced the response to elevated extracellular K^+ but does not completely abolish it. This favor that the responses to K^+ evoked responses are via glutamenergic pathways. Though it is not clear if this via direct depolarization of the presynaptic layers that release of glutamate or if the glutamate release is due to the reversal of the uptake pumps. One intriguing piece of evidence that favors the glutamate release is that glu-

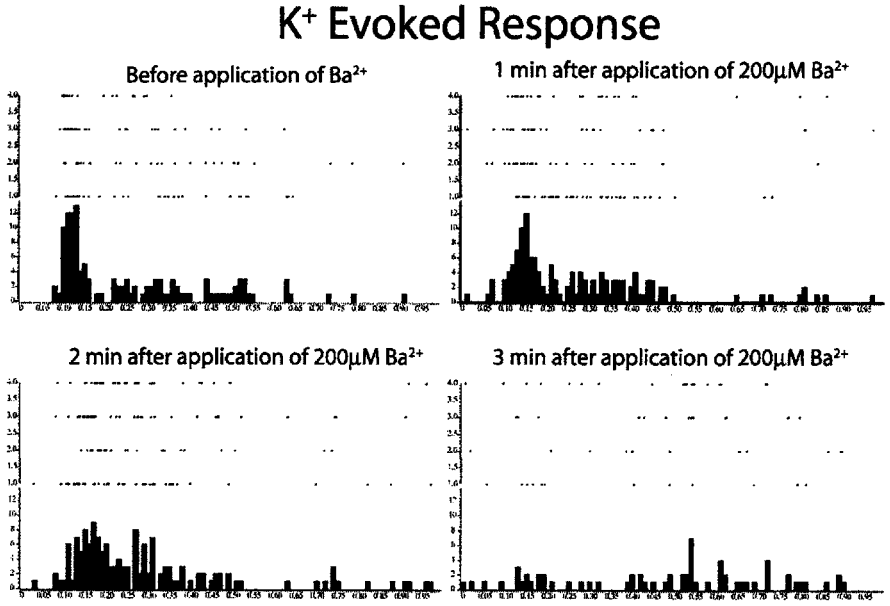

Figure 4-12: Washing the preparation with 200mM barium abolishes the potassium evoked response, but not the light evoked response, see figure 4-13. This result suggests that the potassium evoked response maybe an indirect (i.e. via synaptic pathways) rather than a direct effect. See text for discussion.

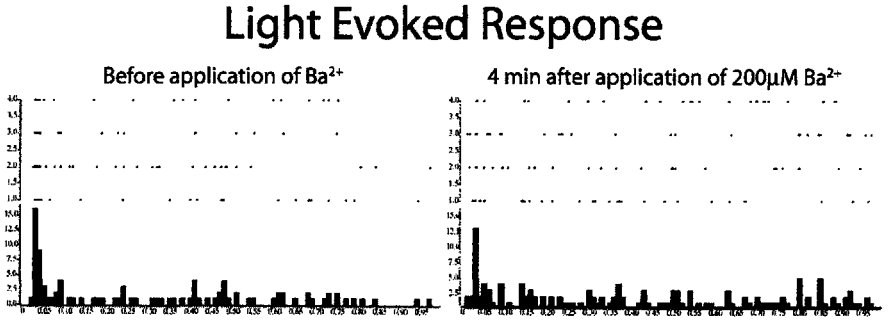

Figure 4-13: Washing the preparation with 200mM barium does not affect the light evoked response. This experiment was performed on the same experimental setup as the one shown in figure 4-12

tamate release due increases in extracellular concentration shows the same saturating behavior for the same concentration levels used in this study[127]. However, one puzzling question is why preventing potassium siphoning abolishes all response, since the direct depolarization of the ganglion cell layer should still be possible. Further pharmacological studies will be necessary to fully resolve these issues. One inevitable conclusion is that direct depolarization of retinal ganglion cell does not seem to be the primary mechanism of K^+ evoked responses. The K^+ evoked response is probably an interplay between the potassium siphoning and glutamate release.

4.4 Conclusion

Potassium evoked response of various cell types in the rabbit retinal ganglion cells were studied *in-vitro*. A dose-response curve was obtained and it shows that only a minimal concentration change over the background concentration is sufficient to elicit a neural response. Furthermore, the dose-response curve exhibits a sigmoidal shape showing a saturating behavior at high concentrations. The receptive fields for both light and K^+ evoked responses are similar, supporting the hypothesis that ionic stimulation is very focal. Initial studies show that the response is most probably through a complex indirect mechanism rather than a direct depolarization of ganglion cells. In the next chapter we will tackle the challenge of synthesizing a self-assembling potassium selective polymer.

Chapter 5

Self-Assembling Receptor Functionalized Membranes

5.1 Introduction

As elucidated in chapter 3, the key to a supramolecular chemical neuronal prosthesis is the development of an self-assembling ion selective membrane. Recently there has been a plethora [75] of polymeric systems that have successfully exploited the self-assembling nature of natural membranes for the purposes of drug delivery, biomedical coatings[103], virus assisted gene delivery [47] and nanoreactors [93]. These are amphiphilic diblock or triblock copolymers, which self-assemble into micelles, worm-like micelles, tubular structures, membranes or vesicles when exposed to a suitable solvent. Additionally, these systems have been functionalized by incorporating biomolecules such as bacteriorhodopsin [55] and porins [86].

The key property of self-assembly is conferred on the membrane by exploiting the hydrophobic and hydrophilic interactions of polymers with the solvent, mainly water. The conventional solution to synthesizing such amphiphilic polymers is via block copolymerization, with the individual blocks being either hydrophobic or hydrophilic. There are, of course, numerous permutations and combinations of polymers that could yield the self-assembling property. However, the requirements for a supramolecular chemical neuronal prosthesis are more stringent. The constraints that must be satis-

fied are

- Bio-compatibility of all the blocks
- Ability to derivatize the hydrophobic block
- Liquid like hydrophobic core
- Facile block attachment

The first requirement is fairly straightforward since the system is meant for a biomedical application. The second constraint is posed by the need to incorporate functionality in the membrane. Some attempts have been made where functionality is conferred to the polymeric membrane by the incorporation of biomolecules such as channel proteins [86]. Unfortunately, the long-term stability of such systems is generally poor. Furthermore, though biomolecules offer exquisite levels of functionality, usually they are not robust to synthetic manipulations and are not simple enough for systematic investigations as part of a macromolecular assembly. Supramolecules are synthetic counterparts to biomolecules and offer similar levels of functionality. They provide a variety of functions from ion channels to enzyme mimics. Molecular recognition can be effected by covalent binding (e.g. glucose binding by phenylboronic acids [100]) or non-covalent complexing, as observed in crown ethers. Though simple physical incorporation of these supramolecules can enable a functional membrane, they do not posses long term stability due to the leaching of the supramolecules from the membrane. In a biological medium the leachate can be toxic, for example, lipophilic crowns have been shown to cause cell death [46]. Long alkyl spacers can be used as a tether to covalently bind such supramolecule to a polymeric backbone and thus achieve improved long-term stability by suppressing the leaching process [76]. The cost for the increase in robustness is the reduction in mobility of the carrier in the membrane phase. However, this can be offset by increasing the carrier concentration along the polymeric backbone. The transport mechanism is now mainly through a hopping mechanism [25] rather than simple diffusion.

The reason for the third constraint follows naturally from the above discussion. Since the carrier is covalently bound to the membrane the diffusional mobility of the carrier in the membrane phase is crucial. Though, it is possible to use rhelogical modifiers such as plasticizers to increase the diffusional mobility this will generally be a less preferred method since plasticizer leaching would pose a problem. In general polymers which have a natural liquid like core will be preferred. There are two main classes of such polymers the self-plasticizing methacrylic copolymers and polysiloxanes. The methacrylic polymers will not be considered because they do not meet the requirement of biocompatilbilty and additionally they also do not lend themselves to facile block attachment.

The last requirement for block attachment needs to be considered carefully. Grafting of the block [5] onto the polysiloxanes is a possibility but usually this is done via hydrosilylation and this will compete with side chain grafting. The better method is to use the polysiloxane as a macrointiator to initiate the polymerization of an appropriate monomer. However, enforcing the biocompatibility andd hydrophilicity requirement severly narrows the choice to 2-oxazolines. Polyoxazolines are both bio and hemocompatible [23]. Furthermore, polymethyloxazoline-polydimethylsiloxane-polymethyloxazoline(PMOXA-PDMS-PMOXA) non-functionalized polymers have been recently synthesized and shown to self assemble into vesicles [92]. A schematic of a structure that incorporates all the ideas discussed is shown in figure 5-1.

The rest of this chapter is organized as follows

1. Polysiloxanes

2. Polyoxazolines

3. Facile and versatile synthesis of triblock co-polymers

5.2 Polysiloxanes: A review

Polysiloxanes are polymers formed by alternating Silicon-oxygen bonds. They are a unique class of "inorganic" polymers [35, 102] with very unique properties. It is the

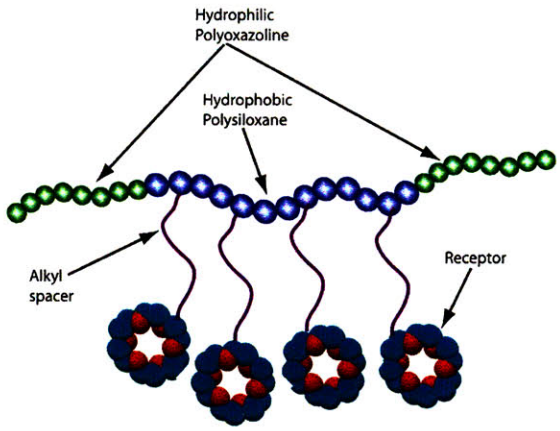

Figure 5-1: Schematic representation of functionalized triblock co-polymers. The amphiphilic co-polymer is composed of hydrophilic polyoxazoline and hydrophobic polysiloxane. The polysiloxane is a copolymer that is derivatized via a hydrosilylation reaction to bind to an active supramolecular moiety. The long alkyl spacer gives the supramolecule translational mobility but prevents it from leaving the membrane phase. To ensure transport the backbone needs to contain a minimum density of carriers enabling a "hopping" mechanism to occur.

unique structure of siloxanes that give rise to these properties. Since the substituents can only appear on the silicon atom and the polymeric structure has alternating oxygens, the substituents are more separated from each relative to polymers with a carbon backbone. This feature allows for very low steric interactions between adjacent substituents. In polydimethylsiloxane(PDMS), the most widely used polysiloxanes, this allows for the methyl groups to be the dominant surface moiety. The combination of the miminal energy configuration by aligning the methyl groups combined with the Langmuir principle gives rise to low surface energy [102]. The most interesting properties of siloxanes, however, arises from the siloxane bond (Si-O).

5.2.1 The Si-O Bond

The bond energies of the various Si-X bonds is given in table 5.1, also shown are carbon bond energies for comparison. The siloxane bond is longer than a C-O bond but shorter than the sum of covalent radii of silicon(1.17Å) and oxygen (0.66Å) [35]. This indicates that this bond is more complex than a simple σ bond that would be assumed on casual inspection. The siloxane bond posses both ionic and double bond

	Bond Energy(kJ/mole)	Bond Length(Å)
Si-O	452-549[1]	1.64
Si-C	318	1.85
Si-H	318	1.48
C-C	346	1.54
C-O	358	1.43
C-H	411	1.09

Table 5.1: The strength of silicon bonds to various substituents are shown. Also shown is the typical bond length. [1] The bond energy varies based on the substituent on the oxygen, the lowest being a methyl substituent and the highest being a silicon substituent. Collected from http://chemviz.ncsa.uiuc.edu/content/doc-resources-bond.html and references [115, 35]

character. The partial ionic character arising from the large difference in Pauling electronegativities (1.9(Si) vs. 3.44(O)). The double bond character is more complex and arises from negative hyperconjugation (also termed the anomeric effect [74]) between the oxygen lone pair and the antibonding ($\sigma*$) Si-X bond, where X is any atom bonded to the silicon under consideration [20],see figure 5-2b. Alternatively, some consider the double bond character [35] to be due to the donation of the oxygen lone pair electron into the vacant low energy 3d-orbitals of silicon forming $p_\pi - d_\pi$ linkage. However, recent theoretical calculations point more to negative hyperconjugation rather than back-donation to be the primary form of stabilization [20]. This extra stabilization of the oxygen lone pair results in the high bond dissociation energy of the Si-O bond and results in high thermal stability of polysiloxanes.

The next feature that has a profound effect on the physical properties of polysiloxanes is their bond angles and low barrier to rotation. The Si-O-Si has a very "soft" bond angle and ranges from 104-180° depending on the nature of the substituents on silicon [35]. For instance in polydimethylsiloxanes the Si-O-Si has a bond angle close to 143°[115], see figure 5-2a. The O-Si-O bond on the other hand is fairly rigid has a bond angle ranging from 102-112° [35] (110° in PDMS, see figure 5-2a. The "softness" of the bond is reflected in the barrier to linearization. The barrier to linearization around the Si-O-Si bond is relatively low (1.3kJ/mol) and around 2.5kJ/mol for the rotation about O-Si-O fragment. The "soft" nature of the bond angle, the relatively

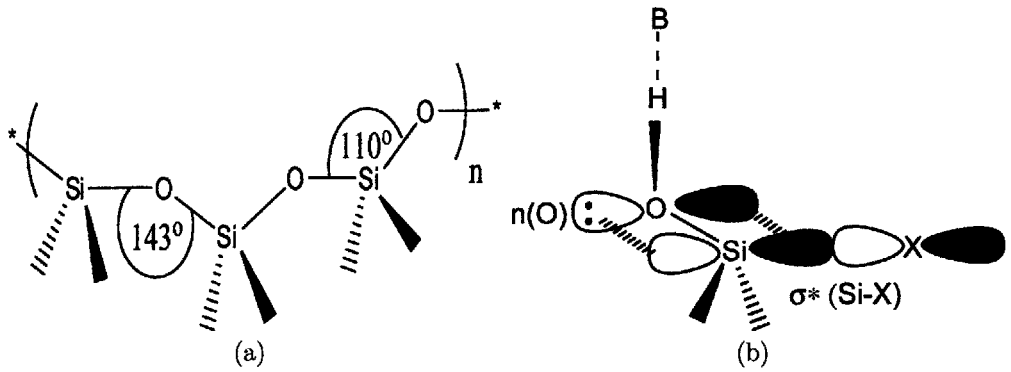

Figure 5-2: (a) Schematic showing the rather large bond angle present in polysiloxanes that gives them the unique physical properties (b) The stabilization of the oxygen lone pair by negative hyperconjugation that gives silanols their high reactivity. B is a generic base

long bond lengths and low steric interaction due to the substituents only appearing on the silicon atom gives polysiloxanes unusual flexibility and allows them to adopt conformations not normally possible. It allows the polysiloxanes to adopt a very open structure making them very susceptible to nucleophilic attack.

5.2.2 Polymerization of siloxanes: mechanistic consideration

The industrial route to siloxanes is based on a two step procedure (see figure 5-3), a disubstituted dimethyl silane, usually a dichlorodimethylsilane, is hydrolytically converted to a silanol oligomer and cyclics and liberates HCl. In the second step the silanol yields a high molecular weight polymer via polycondensation, see figure 5-3. Alternatively, the cyclic products can be converted to high molecular weight linear products via ring-opening polymerization [20]. In a research setting the preferred route is ring-opening polymerization. Before discussing the details of ring opening polymerization siloxane nomenclature needs to be reviewed. Table 5.2 shows the preferred naming conventions used in literature [115]. The R groups in the table usually refer to methyl groups, other groups if present are usually indicated as a superscript or as X if both methyl units are replaced and the number of repeat units appear as a subscript. For example, Tetramethylcyclotetrasiloxane will be denoted

Type	Molecular Formula	Notation
Monofunctional	$R_3(SiO)_{1/2}$	M
Difunctional	$R_2(SiO)_{2/2}$	D
Trifunctional	$R_1(SiO)_{3/2}$	T
Tetrafunctional	$(SiO)_{4/2}$	Q

Table 5.2: Siloxane Nomenclature

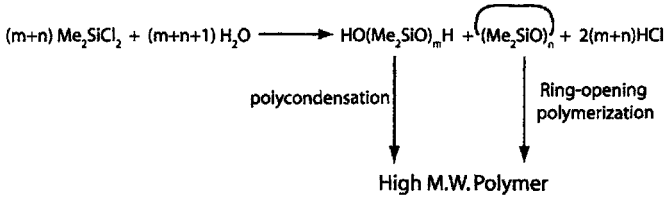

Figure 5-3: Schematic illustrating the industrial route to linear polysiloxanes

as D_4^H, since it is difunctional in each siloxane unit (since it is cyclic), has 4 repeat units and one of the units is a hydrogen.

Equilibration Polymerization

The first step to understanding the anionic or cationic polymerization is to probe into the underlying phenomena that controls the process. The process is under thermodynamic control rather kinetic control, though in early stages of anionic polymerization kinetic control is possible see section 5.2.2. The process can be described as

$D_n + \widehat{D}_x \xleftrightarrow{K_p} D_{x+n}$ where D_n is the linear chain with n-units in the chain present in the polymer mixture $\widehat{D}_x$ is the cyclic species undergoing the ring opening polymerization. It is more convenient to think of the reverse process, since it is the process of intramolecular cyclization and hence it can be described by the Jacobson-Stockmayer theory [64]. This was later modified by the rotational isomeric state model , put forth by Flory and Semlyen [42], that assumes that the skeltal bond can only assume discrete positions. The model by Jacobson and Stockmayer, which forms the basis for a later modification modification by Flory and Semlyen, derives a succinct relationship between the number units in a chain and the probability that it will cyclize and hence the equilibrium constant of the process. For convenience the theory is described in detail and follows the original work fairly closely.

In complete equilibrium between the cylic and the linear species, each species will be in an equilibrium distribution by itself. The fragmenting process in reverse (i.e. the polymerization process), is a polycondesation process and can be described by the theory put forth by Flory. Some notational confusion arises when comparing the original work of Jacobson and Stockmayer [64] and Flory [41]. In his original work Flory denotes the degree of polymerization (or fraction of reacted functional end-groups), p, of the linear species only and no cyclization was considered. In the original work by Jacobson and Stockmayer they develop two notations a notation x for the degree of polymerization for the linear species alone and a notation p for the degree polymerization when referring to the combined process of linears and cyclics. In keeping with the polymer notation, p, will be used here as defined by Flory and will refer to the linear species only. If we consider an n-chain polymer then from mass action considerations one can derive the equilibrium rate constant for the formation of an n-chain polymer as

$$K_p = Ap^n \tag{5.1}$$

where p is the fraction of reacted functional end-groups and A is a normalization constant. Rewriting the equilibrium constant for the reverse process shown earlier yields
$K_{cyc} = \frac{[D_n][\widehat{D_x}]}{[D_{x+n}]}$ using equation 5.1, yields

$$K_{cyc} = \frac{[\widehat{D_x}]}{p^x} \tag{5.2}$$

The problem then becomes one of finding the concentration of cyclics that would be present. One of the key insights of Jacobson and Stockmayer was to break up the process into two steps. Here the linear species first fragments into two linear species and then in a separate step one of the fragments cyclizes. Using the notation earlier, this process would be described by

$$D_{x+n} \overset{K_f}{\longleftrightarrow} D_x + D_n \tag{5.3}$$

$$D_x \overset{K_r}{\longleftrightarrow} \widehat{D}_x \tag{5.4}$$

where K_f and K_r are the forward and reverse equilibrium constants.

It is clear that adding the two processes will give rise to the original process albeit in reverse. The model for the concentration of cyclics can be developed fairly easily by using the idea of a random flight model[32]. One of the key requirements in order for an intramolecular condensation to be possible is that the starting and the ending point of the chain must be within bonding distance (additional requirements such as orbital overlap e.t.c. have been ignored for simplicity). A random flight model is based on the random walk, here the chain either moves forward by one step or one step backward. Since we are concerned with the problem of cyclization during polymer chain growth, the problem can be cast as laying a molecule down one at a time (assuming a single molecule represents one repeat unit, this assumption only changes things by a scale factor) and the chain either moves forward or backward by a single bond length b. Each step is independent of the previous one and the probability that the chain takes m steps in the +ve x direction out of a total number of N steps can be described by a gaussian

$$P(m,N) = Be^{-\frac{2(m-m_o)^2}{N}}$$

where m_o is the most probable no. of steps in the +ve x direction. So the total forward progress,x, is given by forward steps - backward steps, so $x = 2m - N$. The most probable no of steps, m_o in the forward x-direction is N/2 (assuming no bias). So the total distance traveled is = no. of steps * average distance per step. Now the average distance traveled is the average root-mean-square(rms) bond length projection on the x-axis (the normal average would yield zero since there should be as many projection in the -ve direction as there would in the +ve x-direction). The rms bond projection is given by $b/\sqrt{3}$ So we have $x = (2m - N)b/3$, additionally we also know that the most probable number of steps,m_o in the +ve x direction is $N/2$

making these substitutions we get $x = \frac{2b}{\sqrt{3}}(m - m_o)$ or $m - m_o = \frac{\sqrt{3}}{2b}x$

now the probability cab be rewritten as:

$P(x, N) = Be^{-\frac{3x^2}{2Nb^2}}$

The normalization condition can be evaluated from the fact $\int_0^\infty P(x, N) = 1$ this yields

$P(x, N) = \frac{\sqrt{3}}{\sqrt{4\pi Nb^2}}e^{-\frac{3x^2}{2Nb^2}}$

This can be generalized to 3 dimensions to yield $P(r, N) = \left(\frac{3}{2\pi Nb^2}\right)^{3/2} e^{-\frac{3r^2}{2Nb^2}}$

The above calculation for the probability assumes a specific direction, namely the +ve direction of x, and needs to be generalized to any direction since the bonding process is assumed to be isotropic (ignoring orbital overlap constraints). This probability can be calculated by solving the equation

$\int_0^\infty 4\pi r^2 P(r, N)dr = 1$

The probability whether a chain end would be with a bonding distance s, is given by:

$P_{cyc} = \int_0^s 4\pi s^2 P(s, N)dr = \int_0^s 4\pi s^2 P(s, N)dr$

$P_{cyc} = \int_0^s 4\pi r^2 \left(\frac{3}{2\pi Nb^2}\right)^{3/2} e^{-\frac{3s^2}{2Nb^2}} dr$

if $N \gg \frac{3s^2}{2b^2}$ then $e^{-\frac{3s^2}{2Nb^2}} \approx 1$ so the integral reduces to a volume integral which should give the volume in which the bonding process can take place, the value of this integral can be denoted as v_s. Hence

$P_{cyc} = \left(\frac{3}{2\pi Nb^2}\right)^{3/2} v_s$

The equilibrium of cyclics can now be computed using equation 5.4, yielding $K_{cyc} = \frac{[\widehat{D_x}][D_n]}{[D_{x+n}]}$. From fundamental thermodynamics: $[\widehat{D_x}] = \frac{[D_{x+n}]}{[D_n]}e^{\frac{-\Delta G}{kT}}$, therefore

$K_{cyc} = e^{\frac{-\Delta G}{kT}}$, where $\Delta G = \Delta H - T\Delta S$.

Since the number of bonds remains unchanged before and after the reaction, the enthalpy change associated with the reaction $\Delta H = 0$, so now the entropy change associated with the reaction can be calculated. Here is where equations 5.3 and 5.4 are really useful. The change in entropy associated with equation 5.3 can be computed as follows. Before the bond breaks it is confined to the bond volume v_s. After breaking the bonds of that particular molecule can sample the entire reaction volume, V. However, since the break involves two ends there is factor of 2 that needs

to be taken into account. Hence

$\Delta S_{break} = k \ln \frac{V}{2v_s}$

The entropy change due to cyclization is the ratio of finding the end close enough to cyclize to the total number of steps it could have taken which is equal to the chain length. so substituting N=x (to be consistent with equation 5.4) in P_{cyc} yields

$\Delta S_{cyc} = k \ln \frac{\left(\frac{3}{2\pi x b^2}\right)^{3/2} v_s}{x}$

Since $\Delta S = \Delta S_{break} + \Delta S_{cyc}$ substituting and computing the sum yields

$\Delta S = k \ln V \left(\frac{3}{2\pi}\right)^{3/2} \frac{x^{-5/2}}{2b^3}$, which gives the cyclization equilibrium constant

$$K_{cyc} = V \left(\frac{3}{2\pi}\right)^{3/2} \frac{x^{-5/2}}{2b^3} \tag{5.5}$$

By comparing equations 5.2 and 5.5 the concentration of cyclics that will be present in the system is

$$[\widehat{D_x}] = V \left(\frac{3}{2\pi}\right)^{3/2} \frac{x^{-5/2}}{2b^3} p^x \tag{5.6}$$

This is a fundamental relationship for a intramolecular cyclization process, it relates the concentration is related to the chain lengths and decreases as the chains get longer. Additionally, it also relates the concentration of cyclics to the dilution via the reaction volume. Higher dilution increases the probability that a chain will meet itself rather than another molecule which would increase the concentration of cyclics and is consistent with equation 5.6. Equation 5.6 can be simplified further by noting that if the average chain length is long i.e. $\overline{x} \gg 1$, then the degree of polymerization $p = 1 - 1/\overline{x} \approx 1$, yielding:

$$[\widehat{D_x}] = K_{cyc} = V \left(\frac{3}{2\pi}\right)^{3/2} \frac{x^{-5/2}}{2b^3} \tag{5.7}$$

To get a more experimentally relevant measure the concentration of the total number of cyclics of all lengths needs to be determined, this can be obtained directly

from equation 5.7, by computing the expectation i.e.

$$[D_{tot}^{cy}] = K_c = \sum_{x=4}^{\infty} x[\widehat{D_x}] \tag{5.8}$$

The smallest cycle with minimum strain that can be obtained is D_4 and $[\widehat{D_x}]$ can be computed from equation 5.6. This relationship has been experimentally verified for PDMS by van den Hende [136]. Additionally, the relationship to the total cyclization equilibrium constant, K_c is made by using the same condition of long chain lengths. The total concentration of all molecular species is equal to the sum of cyclic and linear species i.e. $[D_{tot}] = [D_{tot}^{lin}] + [D_{tot}^{cyc}]$ where $[D_{tot}^{lin}]$ is the number averaged concentration of linear species. This can be rearranged by dividing by $[D_{tot}]$ and rewritten as the weight average concentration as

$$w_p = 1 - w_c = 1 - \frac{[D_{tot}^{cyc}]}{[D_{tot}]} = 1 - \frac{K_c}{[D_{tot}]} \tag{5.9}$$

This is a fundamental relationship in a equilibrium polymerization. For a linear polymer to exist $\frac{K_c}{[D_{tot}]} \leq 1$ or $[D_{tot}] \geq K_c$ and from the result in equation 5.8 and 5.7 the following equation is obtained

$$[D_{tot}] \geq \sum_{x=4}^{\infty} V \left(\frac{3}{2\pi}\right)^{3/2} \frac{x^{-3/2}}{2b^3} \tag{5.10}$$

The underlying thermodynamics that drives the equilibrium polymerization reaction in siloxanes can also be computed. Rewriting equation 5.9 as $\frac{K_c}{[D_{tot}]} = 1 - w_p$ or $K_c = (1 - w_p)[D_{tot}]$. Using the thermodynamic relationships $\Delta G_c = -RT \ln K_c$ and $\Delta G_c = \Delta H_c - T\Delta S_c$, results in

$\ln(1 - w_p) + \ln[D_{tot}] = -\frac{\Delta H_c}{RT} + \frac{\Delta S_c}{R}$

However, rings higher than size 3 have almost no strain as noted earlier and the number bonds formed and broken in the entire process is zero, we get $\Delta H_c \approx 0$. Using this fact the following is obtained

$$\boxed{\ln(1-w_p)+\ln[D_{tot}]=\frac{\Delta S_c}{R}}$$

This is very important result that clearly shows that the equilibrium polymerization is driven purely by entropy and is independent of temperature (valid for a large range). So if the entropy of cyclization is not negative then polymerization will not proceed. In fact for cyclic siloxanes with either bulky or very polar side groups the polymerization will not proceed. In the next section the actual mechanism of polymerization is described.

Ring Opening Polymerization

Ring opening polymerization of cyclosiloxanes can be performed using two initiation methods. The first is to use an anionic initiator and the second is to use a cationic catalyst. The mechanism of anionic polymerization will be discussed first since it is fairly well understood followed by a discussion of the current state of understanding in cationic polymerization.

Anionic Ring Opening Polymerization

Anionic ring opening polymerization of cyclosiloxanes is generally performed on strained cyclic siloxanes mainly D_3. The reactivity of siloxanes toward bases follows the trend $D_3 \gg D_4 > MD_2M > MDM > MM$[69]. The reactivity scale can be understood by noting the silicon atoms that have more oxygens attached to them are more are more electron deficient and hence more susceptible to nucleophilic attack[20]. The general reactions that take place in a base catalyzed equilibration are [69]

$$B^-Cat^+ + \widehat{D}_n \xrightarrow{k_0} BD_n^-Cat^+$$
$$-D_x- + D_n \xrightarrow{k_1} -D_{x+n}-$$
$$MM + D_x \xrightarrow{k_2} MD_xM$$
$$MD_xM + MM \xrightarrow{k_3} MD_{x-z}M + MD_zM$$
$$MD_xM + MD_yM \xrightarrow{k_4} MD_{x-z}M + MD_{y+z}M$$

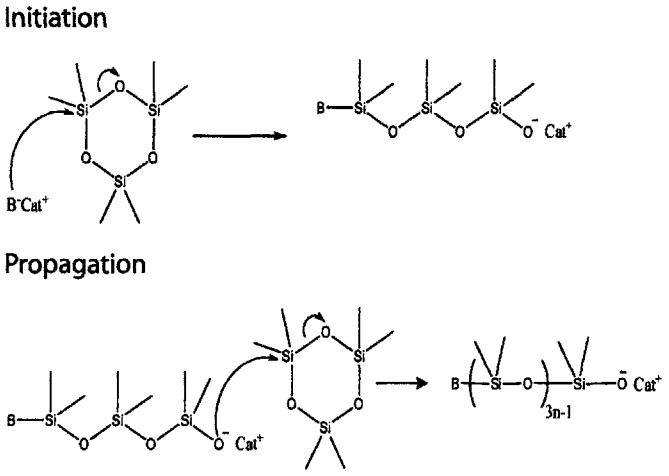

Figure 5-4: Schematic showing the mechanism of anionic ring-opening polymerization. Adapted from [20]

where D_n is either D_3 or D_4. The first reaction is the ring opening polymerization step and is shown schematically in figure 5-4. The second is the chain propagation reaction, the third is the termination. The last two reactions are equilibration reactions due to chain back-biting and produce no change in molecular weight of the mixture they only serve to randomize the chain. In the beginning the first reaction predominates since $k_1 \gg k_2$ until the concentration of D_n in the reaction mixture becomes fairly low then reaction 2 will start to dominate. If the reaction is allowed to proceed further the chains will depolymerize due to chain-biting and the individual chain lengths will be shorter. So the reaction is not entirely under thermodynamic control. In the beginning the reaction is a kinetically controlled process and only in the later stages does the equilibration process take over. To obtain high molecular weights with low polydispersity careful time-controlled quenching of the reaction mixture is necessary. The main advantage of anionic polymerization is that it can be used to polymerize cycles that contain bulky side groups like phenyls that cannot proceed via equilibrium polymerization as noted earlier.

There are some subtle effects that are in play in anionic polymerization. In order for the polymerization to proceed the silanoate anion needs to be sufficiently free of ion pair interaction with the cation. If the ion-ion interaction is too strong it will significantly lower the rate of polymerization. Moreover, ion pair aggregation also

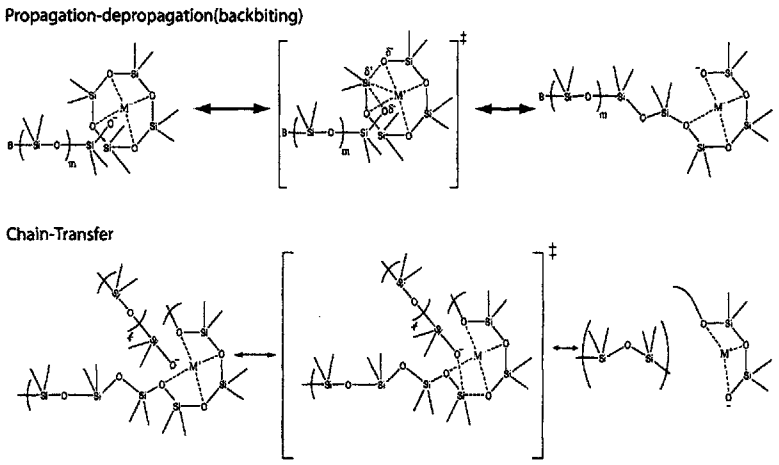

Figure 5-5: Schematic showing the effects of the metal on propagation, back biting and chain transfer. M^+ is the metal cation from the anionic intiator.Adapted from [20]

takes place in solutions that do not allow stabilization of the charge. These effects are pronounced in the kinetic law by exhibiting a fractional order of polymerization in the silanoate [20]. The nature of the cation also plays a role in this process. Cations that are able to stabilize the positive charge allow for a more naked anion and hence increases the rate of polymerization. This is reflected in the reactivity of silanoate complexes $SiO^- \ ^+Li < SiO^- \ ^+Na < SiO^- \ ^+K < SiO^- \ ^+Rb < SiO^- \ ^+Cs \approx SiO^- \ ^+NMe_4 \approx SiO^- \ ^+PBr_3$ in bulk polymerizations. Additionally, solvents that stabilize the cations like THF or polar solvents like DMF and DMSO also promote the polymerization. Supramolecules like cryptands and crowns that chelate cations also lead to enhanced rates of polymerization. Since the initial stages of the reaction are a non-equilibrium process the polymerization can proceed in dilute solutions.

Cations also play a role in both propagation and back-biting. These can be understood by looking carefully at the structure of cyclic siloxanes. They closely resemble metal chelating crown ether and exhibit multidentate interactions with cations see figure 5-5. This also explains the higher reactivity of larger cyclics with the reactivity order $D_4 < D_5 < D_6 < D_7 < D_8$ exhibited in theses systems. However, in the polymerization of D_3 this effect does not increase the rate since the D_3 is very strained and flat so does not exhibit multidentate interactions with cations [20].

Taking all the above into consideration a set of trends can be developed that lead high molecular weight polysiloxanes with low polydispersity. 1) Polymerization in a polar solvent like THF that interacts strongly with the cation, minimizing the multidentate interactions with the cyclic siloxanes and hence lowering back-biting depolymerization reactions that lead to broad polydispersties. 2) Polar additives like DMSO or DMF 3) Very stable cations like NMe_4 or PBR_3 4) Supramolecular chelating agents like crown ethers and cryptands that stabilize the cation. 5) Careful quenching of the system when high monomer conversion is obtained.

Cationic Ring Opening Polymerization (CROP)

Cationic polymerization of cyclic siloxanes is not very well understood since there are multiple processes simultaneously at work. The following account is a concise review of the literature that reflects the current state of understanding. Most of the mechanistic understanding is due to the pioneering work of Chojnowski [21, 145, 146] and Sigwalt [7, 78, 8]. Unlike anionic polymerization the appearance of cyclics is almost immediately and there is no initial peak in the molecular weight [69]. The multiple reactions that take place in cationic polymerization is shown in figure 5-7. Most of the mechanistic studies on CROP have been conducted using D_3 as the monomer except for some by Sigwalt which was performed on D_4. Wilczek *et. al.* performed a detailed study comparing the polymerization of D_4 to D_3. They concluded that both mechanism are similar and attributed the differences to the higher reactivity of the strained D_3 ring and higher basicity [119, 69]. However, in a similar study performed by Sigwalt *et. al.*[97] they pointed out that there are some subtle differences that needed further scrutiny. In their work they came up with a plausible mechanism that was consistent with the experimental data. The main difference between D_3 and D_4 is the formation of cycles, the types of cycles, the point at which they are formed and their differences to intentionally added water as explained later. The main point of contention between the two schools of thought in the general polymerization mechanism are whether the propagation is via a an activated silanol versus an activated ester group. The debate has still not been completely laid to rest and both mecha-

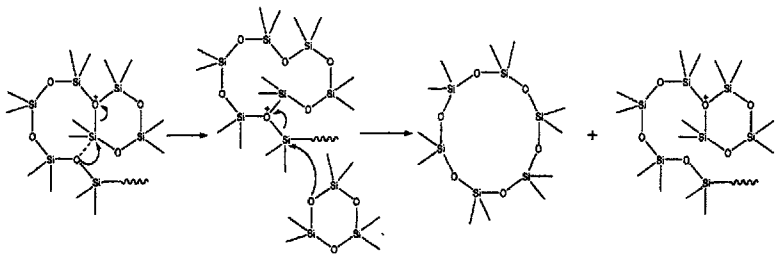

Figure 5-6: The preference in the formation of D_6 in a D_3 acid-catalyzed ring-opening polymerization is reflected in the strainless transition shown. Adapted from [132]

nisms are probably active and depend very highly on the reaction conditions. Though the propagation step is under contention the initiation is universally assumed to proceed by the ring-opening of the cyclic to produce a linear siloxane with one silanol end and one silyl ester end, see figure 5-8. The activated ester mechanisms is shown in figure 5-9 and the silanol activated polymerization is shown in figure 5-10. The debate, however, has brought out some of the peculiarities of cationic ring opening polymerization of cyclic siloxanes. First, the cyclics that are formed in acid catalyzed polymerization of D_3 are mainly in multiples of D_3 i.e. D_{3n} with a high fraction of D_6. A strainless transition state proposed by Sigwalt [132] seems to be the best explanation for this phenomenon, see figure 5-6. Higher cyclics proceed in the D_3 case by a intramolecular condensation between a silanol end group and an activated ester end group. The D_4 polymerization shows no cyclic multiples in D_4 and they are present right from the start of the reaction and this indicates that the formation is mainly due to back biting.

The presence of water affects the polymerization of D_3 profoundly differently from D_4, in the presence of small amounts of water ($\approx$ 10 equivalents with respect to acid) the rate of polymerization of D_3 is accelerated as long as the water is present in-situ. If the acid catalyst is prehydrated before addition then polymerization only progress after an induction period(for small amounts of water. If the acid catalyst is premixed with large amounts of water then reaction does not proceed. The lack of reactivity of D_3 to a hydrated acidic species can be taken as evidence against propagation via an activated silanol group, though the hydrogen in the silanol group is more labile [9] so one cannot rule the possibility of the reaction. Though the reaction in presence

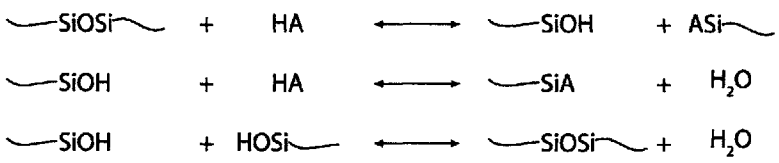

Figure 5-7: Reactions that take place in Cationic ring opening polymerization of cylic siloxanes. A denotes the anion of the acidic catalyst usually a triflate, tosylate or trifluoroacetate

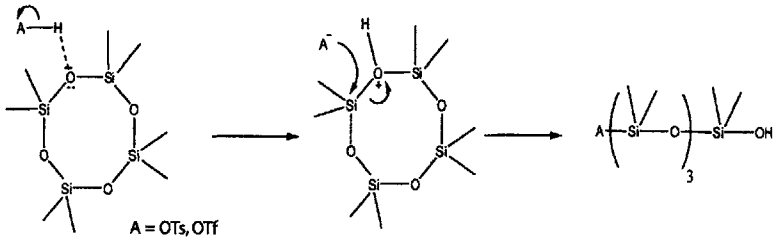

Figure 5-8: Intiation Step in CROP, Adapted from [20]

of water occurs readily for D_3 at 30°, the reaction does not proceed until 80° for D_4. The reason for this probably lies in the fact that strained D_3 is more reactive toward acid catalysis than the almost strain-free D_4. Most of the evidence for propagation seems to point to the conversion of the silanol to an ester which occurs very fast. The polymerization then propagates bidirectionally via an activated ester end group. Other mechanism that may be active to a lesser degree is the heterocondensation of two chains via a silanol end (ester converted to silanol due to presence of water) and a silyl ester liberating the acid or the homocondensation of two silanol ends.

Until this point the polymerization reaction in the presence of an end-blocker has been considered. No studies have been done with disiloxane end-blockers in low concentration, thought there have been multiple studies done with equimolar concentrations of D_3 or D_4 and MM. Here again, D_3 and D_4 can differ since the reactivity to acids to siloxanes proceeds in the order $D_3 > MM > MDM > MD_2M > D_7 > D_6 > D_5 > D_4$. In the studies that were performed using equimolar concentrations of MM and D_3 or D_4, it was found that the cyclic species entered the linear species as a whole unit to give MD_3M or MD_4M sometimes higher species. Other studies [22] with D_3 as the monomer showed that high molecular weight species were formed first and then mono-terminated by the MM unit. This is probably because of the higher

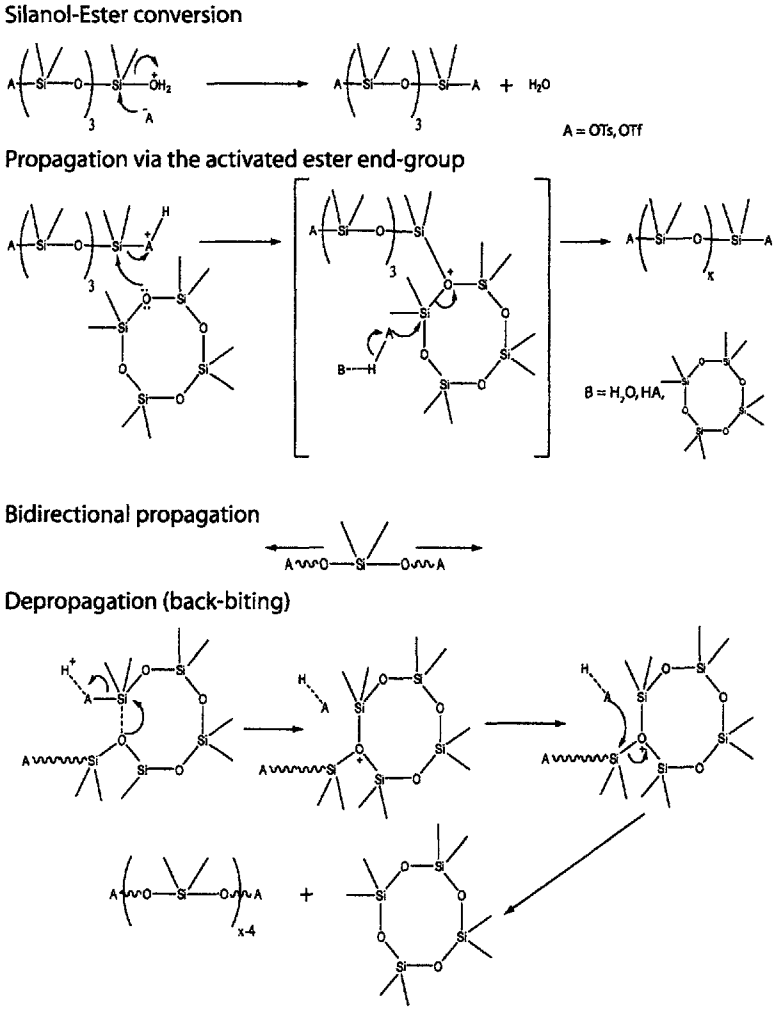

Figure 5-9: Mechanism of CROP via activated ester end group. Adapted from [7, 78, 8]

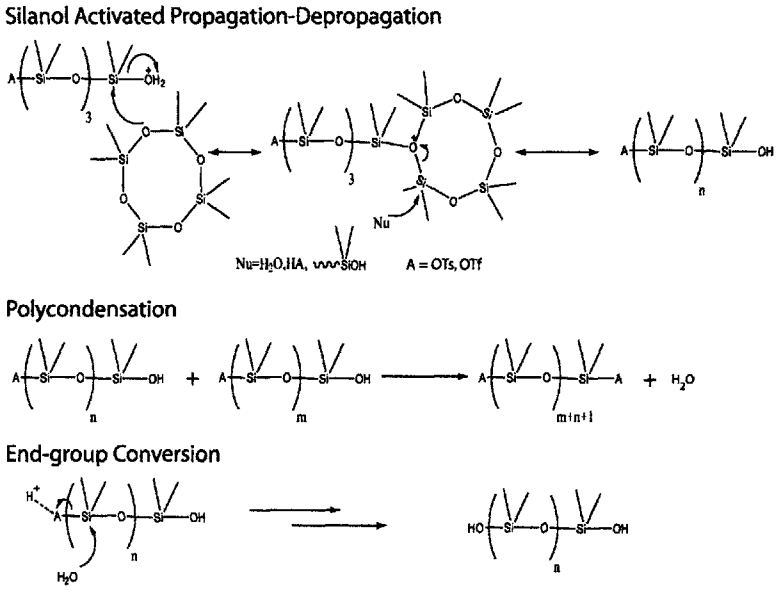

Figure 5-10: CROP via silanol activation. Adapted from [21, 145, 146]

reactivity of D_3 compared to MM. So the chain polymerizes first till the concentration of D_3 decreases and then it termination reaction becomes competitive and terminates the polymerization, a mechanism using this approach is shown in figure 5-11 . This will be more pronounced when the concentration of MM is much smaller than D_3 when it is used as a method to control the molecular weight. If the monomer is D_4 the reaction mechanism is unclear, since the reactivity of $MM \gg D_4$. In fact the reactivity of D_4 toward acid catalysis is comparable to the linear polymer chain [97]. It is plausible that the MM species is not only involved in the termination but also in the initiation reaction (see figure 5-12). Additionally termination may occur via heterocondensation between polymer chains.

The main conclusion from the above discussion is that the cationic equilibrium polymerization of siloxanes seems to only transiently contain a positive charge in the propagation step. This charge is then neutralized by the formation of a silyl ester or silanol. The active propagation center is then reformed again by the activation of the silyl ester or silanol end group. The simple mechanistic picture of an active oxonium site propagating via the ring opening of silyloxonium species by another cycle does not seem to be the dominant mechanism with the conventional catalysts

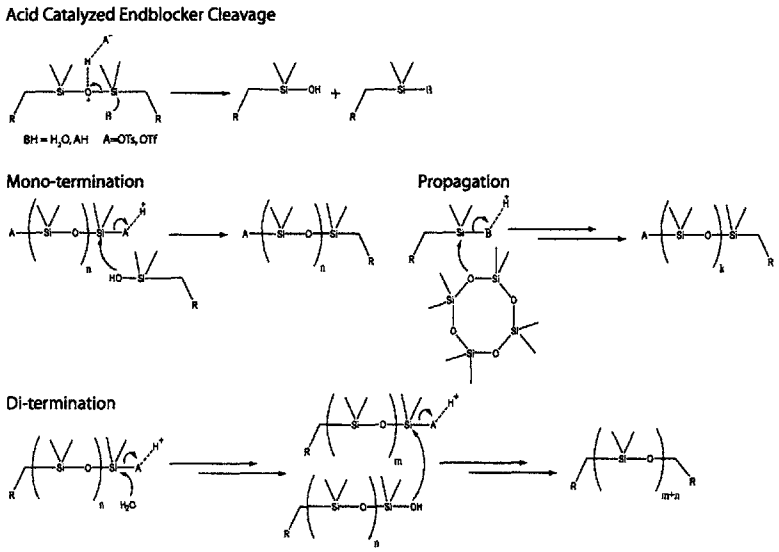

Figure 5-11: CROP polymerization with end-blocker involved only as part of a chain-transfer reaction

used. However, Olah *et al.* [139], showed the presence of a propagating oxonium site when the conjugate base of the active catalyst is incapable of forming a silyl ester. The conjugate base used in their study was a tetrafluorophenylborate.

5.2.3 Hydrosilylation

The next major concept that needs to be reviewed is the grafting of groups onto the polymer backbone via hydrosilylation. Though, different funtional groups can be grafted onto the polymer backbone using different types of organometallic complexes, the most commonly used method is the metal catalyzed cross coupling of terminal olefins to Si-H moities using a Pt(0) complex. The most plausible reaction mechanism was proposed by Chalk and Harrod and is the currently accepted mechanism for Pt(0) catalysed hydrosilylation and more evidence to support the mechanism was recently reported [114]. The first step is the oxidative addition of the silyl hydride into the active metal center(species B in figure 5-13). Then the alkene is co-ordinated onto the metal center (species C in figure 5-13) followed by hydride transfer from the silyl group onto the alkene(species D in figure 5-13). The final silylated species is released in a reductive elimination step to regenerate the active metal center(species A in figure 5-

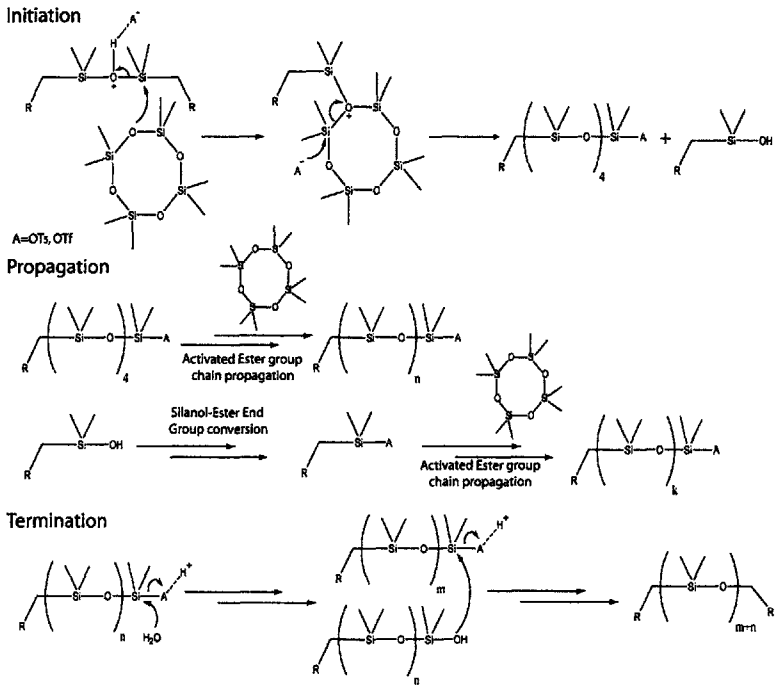

Figure 5-12: Molecular weight controlled polymerization using endblocker: Initiation and termination involvement of end-blocker

13). The most popular platinum catalyst is Karstedt's catalyst (i.e. Platinum (0) co-ordinated to 1,1,3,3,divinyltetramethyldisiloxane), which acts heterogenously and requires an induction period during which the divinyl species is hydrosilylated away. Solvents that stabilize the catalyst prolong the life of the catalyst and hence give improved yield though they lower the reaction rate since they make the Platinum species less reactive by co-ordinating to them. Solvents that are have delocalized electron density like toluene are most commonly used. Additional stabilization can be achieved by using more electron deficient ligands to co-ordinate to the platinum [121].

5.2.4 Ring Opening polymerization of oxazoline

Unlike the cationic ring-opening polymerization of cyclic siloxanes, the ring-opening polymerization of oxazolines is well understood. It is also cationic in nature but does not undergo cyclizations that reduce the molecular weight. Most of the discussion that follows is from an excellent review by Kobayshi and Uyama [77]. Oxazolines

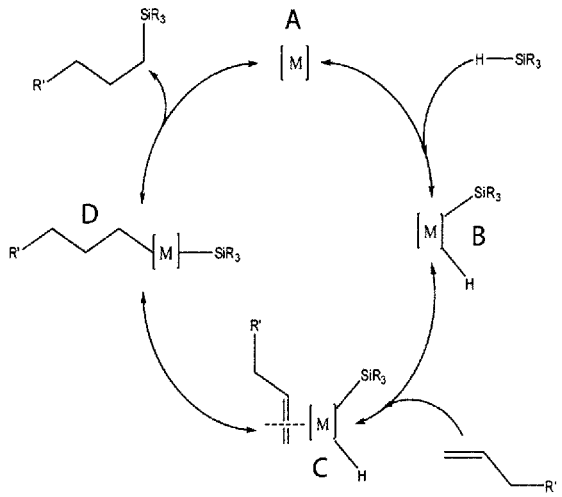

Figure 5-13: The Chalk-Harrod mechanism for Pt(0) catalyzed hydrosilylation. Adapted from [114]

belong to the class of endocyclic imino ethers. The polymerization of oxazolines are initiated by electrophilic species like protic acids, alkyl sulfonates like triflates and tosylates and aklyl halides and hence it is also called electrophilic polymerization. The mechanism of polymerization is shown in figure 5-14. Depending on the nature of the initiator the propagation can proceed through an ionic species or a covalent species or in some cases both. The stability of the propagating species makes the nature of the polymerization living under appropriate conditions, 2-oxazolines can be unsubstituted or substituted and the nature of the substituent determines much of the properties of the polymeric block. If the substituent is methyl or ethyl the block is hydrophillic and bulkier substituents make it hydrophobic. There are some interesting properties of the oxazoline polymerization that can lead to unique polymerization behavior. By varying the nature of the substituent in the 2-position a one pot block copolymerization can be performed. As is illustrated in the case of 2-phenyl and 2-perfluoroethyl 2- oxazolines in figure 5-15 with methyl tosylate. It is important to note that the polymerization of 2-fluoroethyl 2-oxazoline proceeds only after all the 2-phenyl oxazoline has been consumed since it is a weaker nucleophile. Another feature of the polymerization is that the phenyloxazoline propagates via an ionic species but the perfluoro species proceeds via a covalent propagation. This is

probably because of the electron withdrawing nature of the substituent that makes the covalent species more stable than the ionic species. The nature of the initiator is best seen in the example of the double isomerization polymerization that gives two different products depending in the nature of the initiator. Chloride and and bromide initiators give a cyclic urea species in the backbone while initiation with tosylates or triflates yields the normal side chain polyurea. The reason for this initiator dependent product composition is due to the formation of intermediate covalent species in case of halides that leading to the spiro product, see figure 5-16. Another interesting class of polymerization that is not commonly seen is polymerization via a zwitterionic intermediate which proceeds with no catalyst or intiator. Here an oxazoline is the nucleophile and attacks an electophilic monomer producing an intermediate zwitterionic species. Two such zwitterionic molecules now combine to a make a macrozwitterionic species. The macrozwitterion reacts with the multiple zwitterionic intermediates yielding the polymer. This is illustrated for the copolymerization between acrylic acid and oxazoline in figure 5-17. The living nature of the polymerization makes it possible to terminate the polymerization with functional groups yielding macroinitiators and telechelics. One very useful end group is the acrylate group which can be conveniently introduced by terminating the reaction with acrylic acid in an appropriate base like triethylamine or 2,6-lutidine. The carboxylate being nucleophilic enough to terminate the polymerization yielding post polymerizable acrylate end-groups.

5.3 Current Work

As discussed in section 5.1 there has been a renewed interest in self-assembling polymeric membranes due to their potential use in the field of medicine. However, the synthesis and characterization of polymeric membranes that incorporate functionality as an integral part of the membrane has been scarce. The focus of the work presented in this chapter is to develop such a membrane that is a fusion of both form and function. Later in chapter 6, how this union of form and function leads to some very interesting properties. It is the long term goal of the present endeavor to exploit

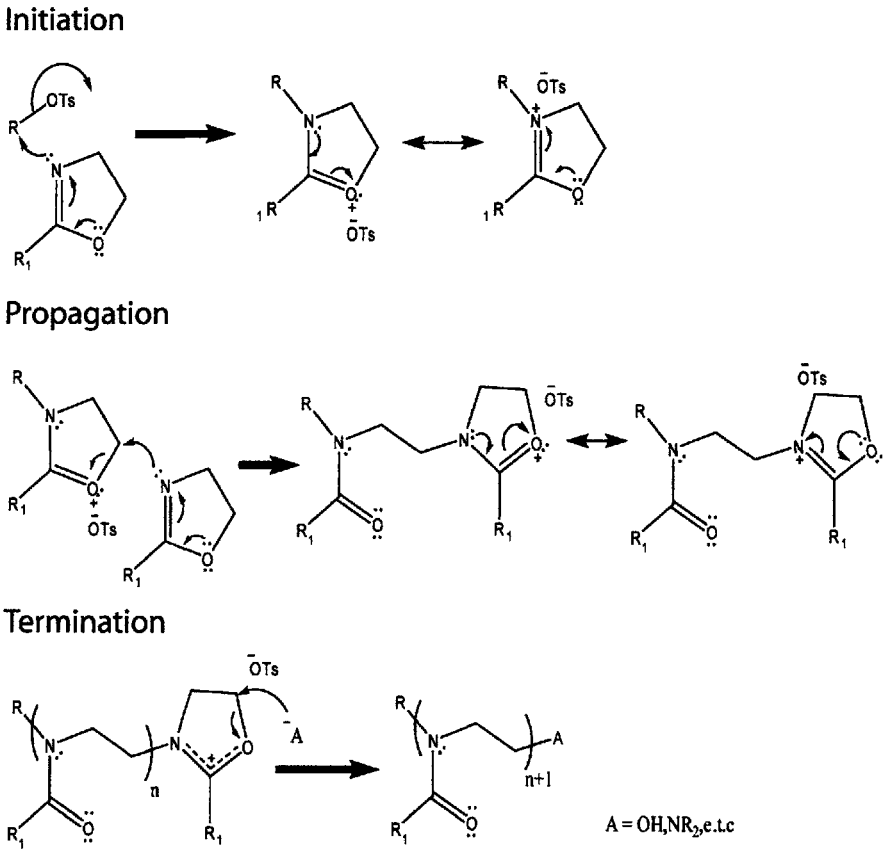

Figure 5-14: Mechanism for the ring-opening polymerization of oxazolines

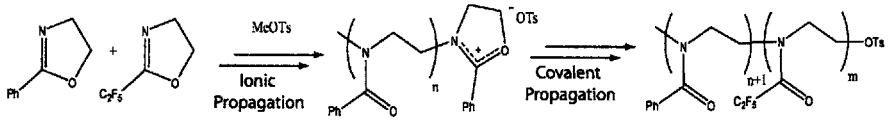

Figure 5-15: One-pot block copolymerization via both ionic and covalent species. Adapted from [77]

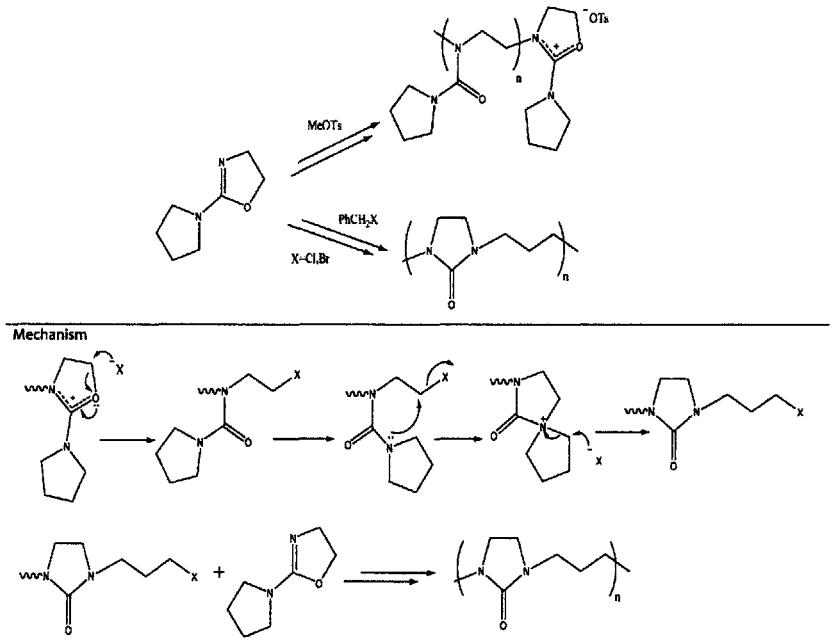

Figure 5-16: Unique polymerization via a spiro intermediate using halide initiators. Using a tosylate, however, goes via the normal route.Adapted from [77]

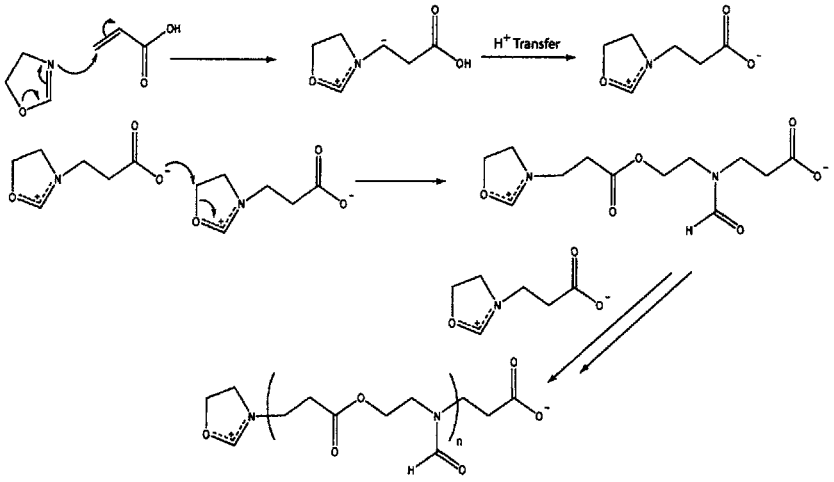

Figure 5-17: Macorzwitterionic polymerization of oxazoline and electrophilic acrylic acid. Adapted from [77]

these structure-function relationships to aid in the development of chemical neural prostheses.

5.3.1 Experimental

Abbreviations

PMOXA: Polymethyloxazoline, PDMS: Polydimethylsiloxane, P(DMS-co-HMS): Poly (dimethylsiloxane-co-hydromethylsiloxane), P(DMS-co-UMBMS): Poly(dimethylsiloxane-co-undecylmethylbenzoatemethylsiloxane), P(DMS-co-UCEMS): Poly(dimethylsiloxane-co-undecylcrownethermethylsiloxane),P(DMS-co-UPBMS): Poly(dimethylsiloxane-co-undecylphenylboronicmethylsiloxane).

Materials

All reagents were used as received without further purification unless otherwise noted. 11-Bromo-1-undecene (97%), Methyl-2,4-dihydroxybenzoate (98%), 10-Undecenoic acid (98%), 2-Methyl-2-oxazoline (98%), p-toluenesulfonic acid monohydrate (TsOH), Lithium iodide and Platinum(0)-1,3-divinyl-1,1,3,3-tetramethyldisiloxane were purchased from Sigma-Aldrich. 2-Hydroxymethyl-18-crown-6 (90%) and 4-Dimethylaminopyridine (DMAP) from Fluka.
Octamethylcyclotetrasiloxane, (D_4), 1,3,5,7- tetramethylcyclotetrasiloxane (D_4^H) and 1,3-Bis(hydroxybutyl)tetramethyldisiloxane were purchased from Gelest, Inc. Potassium carbonate and triethylamine were obtained from Alfa Aesar and synthesis grade Toluene (Drisolv) from EMD Chemicals. Dimethylformamide(DMF), 1,2-Dichloroethane and Dichloromethane(CH_2Cl_2) with low moisture content and stored over molecular sieves were purchased from Sigma-Aldrich.

Instrumentation

^{1}H NMR spectra were recorded on 300MHz and 500MHz Varian spectrometers using 5mm o.d. tubes. Sample concentrations were approximately 10mg/mL in either $CDCl_3$ or CD_3OD. All ^{1}H NMR data can be found in Appendix A.

Purification

Purification of Octamethylcyclotetrasiloxane and Tetramethylcyclotetrasiloxane

To 100mL of appropriate cyclotetrasiloxane an appropriate amout of CaH2 was added and stirred overnight under nitrogen. The flask containing the well stirred solution was then connected to a vigreux column and then connected to a distillation receiver via a condenser. The solution was heated to 40°C and a strong vaccum was applied. The first 15mL of the distillate was collected in the first receiver and discarded. The next 50-60mL was collected in a schlenk flask and purged with nitrogen. This was then transferred to a storage schlenk tube and was kept under argon. The CaH_2 was then carefully neutralized first by placing the vessel in an ice bath and then isopropanol was added dropwise until the vigorous bubbling ceased. The mixture was stirred for an hour and water was then added very slowly in a dropwise manner until the CaH_2 was completely neutralized.

Purification of 2-methyl-2-oxazoline

Approximately 50mL of oxazoline with an appropriate amount of CaH_2 was stirred overnight. The stirred mixture was then connected to a 10cm vigreux column and connected to a distillation receiver with 4 receiving flasks. The mixture was slowly heated from room temp to about 160°C where the distillation of oxazoline begins. The first 5-10mL of the distillate was collected in the first receiver and was not used. The second fraction was collected in a schlenk vessel and appropriate amounts of oxazoline was transferred immediately via syringe into the reaction mixture containing the polysiloxane. The CaH_2 was then neutralized as described earlier.

Synthesis of 1,3-bis(tosyloxybutyl)tetramethyldisiloxane

To a solution of 1,3-Bis(hydroxybutyl)tetramethyldisiloxane (5.6g, 20mmol) cooled to 0°C, p-Toluenesulfonyl chloride (9.5g, 50mmol) and DMAP (0.61g, 5mmol) were added, both dissolved in 200mL of dry CH_2Cl_2. Triethylamine (8.15g, 80mmol) was

added to this solution dropwise over 10 minutes. The mixture was stirred for one hour at 0°C, subsequently the temperature was raised to room temperature and the solution stirred for another 24 h, washed with 1M HCl, saturated $NaHCO_3$ and distilled water. The organic layer was dried over Na_2SO_4, filtered and the solvent was evaporated under reduced pressure. The crude product was purified by column chromatography (Silica gel, 40-63 mesh) using hexanes/ethyl acetate (4:1) to yield 1,3-Bis(tosyloxybutyl)tetramethyldisiloxane (5g, 8.6mmol) as a pale yellow oil, see figure 5-18a.

General procedure for the synthesis of telechelic,α,ω-butyltosyloxy terminated poly(dimethylsiloxane-co-methylhydrosiloxane), P(DMS-co-MHS)

Octamethylcyclotetrasiloxane (D_4) and 1,3,5,7-tetramethylcyclotetrasiloxane (D_4^H) were distilled over CaH_2 under reduced pressure and stored under Argon prior to use. 1,3-bis(tosyloxybutyl)tetramethyldisiloxane was used to control the molecular weight and respective amounts, see Table 5.5, were added to a round bottom schlenk vessel fitted with a reflux condenser and degassed. D_4 and D_4^H were added under a constant nitrogen flow, the amount of D_4^H depended on the desired feeding ratio, see Table 5.5. The mixture was stirred for 1 h at 50°C, then 100μL of TsOH in 1,4-dioxane (125mg/mL) was added. The temperature was raised to 70°C and the mixture was stirred for 48h. Subsequently, the reaction mixture was concentrated in vacuo to remove cyclic side products and the polymer was isolated by precipitating in methanol and extracted with hexanes. The polymer was dried and characterized by ^{1}H NMR, see figure 5-18c

Synthesis of methyl-(2-hydroxy-4-undecenyloxy) benzoate

100mL of dry DMF was added via a syringe to a mixture of Potassium carbonate (5.53g, 30mmol), Lithium iodide (0.8g, 6mmol), 18-crown-6 (1.6g, 6mmol) and Methyl-2,4-dihydroxybenzoate (30mmol, 6.5g (95% pure)), under a constant nitrogen flow. The resulting solution was stirred for 30 minutes. 11-bromoundecene (30mmol, 7g) was added dropwise to this homogenous mixture via an addition funnel. The solution was heated to 85°C and stirred overnight. After cooling to room temperature

the solvent was removed via rotary evaporation. De-ionized water was added, and the mixture was extracted three times with CH_2Cl_2. The organic layer was dried over Na_2SO_4 and the solvent removed via rotary evaporation. The crude product was purified using a short silica gel column with 10:1 hexanes:ethylacetate as the eluent, see figure 5-21, Scheme I. The solvent was evaporated via rotary evaporation to give a clear oil that crystallized upon standing (6.4g, 20mmol) m.p. 39.5-40°C.

Synthesis of (undec-10-enoyloxy)methyl 18-crown-6

The synthesis was adapted from a procedure for the production of a Sodium-chelating 15-crown-5 ether [10]. For the synthesis of the Potassium-chelating crown 18-crown-6 ether 10-Undecenoic acid (10.556g, 57.2mmol), N,N'-Dicyclohexylcarbodiimide, (DCC) (10.98g, 53.2mmol) and DMAP (5.74g, 47mmol) were added to a solution of 2-Hydroxymethyl-18-crown-6 (10.445g, 35.5mmol). 150mL of dry CH_2Cl_2 was added and the solution was stirred for 24h at room temperature. The solution was then filtered to remove the Dicyclohexylurea and the resulting solution was washed thrice with a saturated $NaHCO_3$ solution. The solvent was removed by rotary evaporation and the crude product purified by column chromatography (Silica gel deactivated with 0.4% w/w triethylamine) using hexanes/ethyl acetate (1:1) to yield (undec-10-enoyloxy)methyl 18-crown-6 as a pale yellow oil (9.4g, 20.4mmol) see figure 5-21, Scheme II.

Synthesis of undec-10-enyl 4-(4,4,5,5-tetramethyl-1,3,2-dioxaborolan-2-yl)-benzoate

42.8 mmol (11g) of phenyl boronic acid pinnacol ester, 64.2 mmol (1.5 eq, 13.2g) of DCC was dissolved in 100mL of CH_2Cl_2, 4.3mmol (522mg, 0.1eq) of DMAP and 4.3mmol (567mg, 0.1eq) of hydroxybenzotriazole (HOBt) were stirred for an hour at 0° with a white precipitate forming almost immediately. 62.8 mmol (1.5eq, 10.93g) of undecenyl alcohol was then added dropwise to the stirring mixture and the temperature was slowly allowed to reach room temperature. The mixture was stirred overnight and the dicyclohexylurea was filtered and the filtrate was then concen-

trated via rotary evaporation. The crude mixture was purified using a short silca gel column using a gradient elution of Hexanes:Ethylacetate (10:1 - 1:1) to yield 13.35g of a clear colorless oil, see figure 5-21, Scheme III.

General procedure for polymer analogous hydrosilylation reaction

Hydrosilylation with methyl-((2-hydroxy-4-undecenyloxy) benzoate

To a 1.5g solution of the corresponding telechelic polymer, 2.7g of [(methyl-(2-hydroxy-4-undecenyloxy)-benzoate and 5mL of dry toluene were added. 100μL of a 0.1M platinum-divinyltetrasiloxane complex in xylenes was added to this solution and the resultant mixture was stirred for 24h. The solution turns from a pale yellow to a deep yellow as the reaction proceeds. The solvent was evaporated in vacuo and the resultant solution was washed with distilled water and extracted with diethyl ether. The solvent was evaporated via rotary evaporation to yield a pale yellow oil. This oil was introduced into a silica gel column and eluted first with toluene (to eliminate unreacted benzoate and polymer) and then with diethyl ether to yield a clear colorless oil that was characterized by ^{1}H NMR, see figure 5-23 for the methyl-(2-hydroxy-4-undecenyloxy) benzoate derivative.

Hydrosilylation with (undec-10-enyloxy)methyl 18-crown-6

To a 1.75g solution of the corresponding telechelic polymer a calculated amount of the ω-alkenyl receptor [(undec-10-enyloxy)methyl 18-crown-6)] (1.29g for 8% Si-H content, 2.58g for 16% Si-H content, 5.16g for 32% Si-H content) and 5mL of dry toluene were added. 100μL of a 0.1M platinum-divinyltetrasiloxane complex in xylenes was added to this solution and the resultant mixture was stirred for 24h. The solvent was evaporated in vacuo and the resultant solution was washed with distilled water and extracted with diethyl ether. The solvent was evaporated via rotary evaporation to yield pale yellow (32%,16%) to brown oils (8%). Activated charcoal was added to this mixture and the solution was filtered through Celite to yield either

colorless or yellow oils which were characterized by ^{1}H NMR.

Hydrosilylation with undec-10-enyl 4-(4,4,5,5-tetramethyl-1,3,2-dioxaborolan-2-yl)benzoate

To a 2.2g solution of the corresponding telechelic polymer a calculated amount of the ω-alkenyl receptor [undec-10-enyl 4-(4,4,5,5-tetramethyl-1,3,2-dioxaborolan-2-yl)benzoate] (2.84g for 16% Si-H content, 5.73g for 16% Si-H content, 5.16g for 32% Si-H content) and 5mL of dry toluene were added. 100μL of a 0.1M platinum-divinyltetrasiloxane complex in xylenes was added to this solution and the resultant mixture was stirred for 16h. An addtional 75μL of catalyst was added to the solution and stirred for an additional 16h. The solvent was evaporated in vacuo and the resultant solution was washed with distilled water and extracted with diethyl ether. The solvent was evaporated via rotary evaporation to yield pale yellow oils (3.2g for 16% Si-H, 6.5g for 32% Si-H). Activated charcoal was added to this mixture and the solution was filtered through Celite to yield either colorless or yellow oils which were characterized by ^{1}H NMR.

Synthesis of functionalized amphiphillic triblock copolymers

PMOXA-PDMS-PMOXA Triblock copolymer

1g of Bistosylate terminated polydimethylsiloxane was thoroughly dried by azeotroping with toluene and then drying under high vacuum in a schlenk vessel. The vessel was purged with argon and 1mL of toluene was added to the vessel and stirred while under an argon blanket. 3mL of freshly distilled 2-methyl,2-oxazoline (see section 5.3.1)was added via a syringe. The mixture was allowed to stir for half an hour at room temperature and then heated to 110°C overnight under an argon atmosphere. The resultant pale yellow solid weighing 3.82g was characterized by ^{1}H NMR, see Generation I figure 5-22.

PMOXA-P(DMS-co-HMS)-PMOXA Triblock copolymer

3.25g of bistosylate terminated poly(DMS-co-HMS) was dried extensively and placed under an argon atmosphere in 5mL of toluene under constant stirring in a schlenk flask. 3mL freshly distilled 2-methyl-2-oxazoline was added to this mixture via a syringe. The resultant mixture was stirred for half an hour when the solution viscosity started to increase. The temperature was then raised to 110°C and allowed to stir overight. After cooling to room temperature the solution was the placed in a rotary evaporator and the solvent was removed along with any unreacted oxazoline to yield 4.57g of a white solid that was characterized by ^{1}H NMR, see Generation II figure 5-22.

PMOXA-P(DMS-co-UMBMS)-PMOXA Triblock copolymer

2.5mL of freshly distilled oxazoline was added to a schlenk flask containing 2.85g of thouroughly dried undecenyl benzoate derivatized bistosylate siloxane telechelic and stirred for 1hr at room temperature. The reaction temperature was then raised to 110°C. After about 4 hours a white precipitate started to form. The mixture was allowed to stir overnight to ensure completion. The product was purified by removing any unreacted oxazoline via rotary evaporation to yield 5g of a white solid and was characterized using ^{1}H NMR, see figure 5-23

PMOXA-P(DMS-co-UCEMS)-PMOXA Triblock copolymer

Functionalized telechelic poly(siloxane)s were weighed in (1.65g 8% crown ether content and 3.63g for 32% crown ether content)and 1mL of 2-methyl 2-oxazoline, freshly distilled from CaH_2, was added. One to two mL of dry dichloroethane was added and the resultant solution was stirred at room temperature for 0.5h. The mixture was then heated to 50°C for 15h and to 75°C for an additional 20h when a white precipitate formed. The solution was allowed to cool down to room temperature and 1mL of 0.1M NaOH in MeOH was added and the solution was stirred for an additional hour. The mixture was washed with diethylether/hexane to remove side products and the

solvent was removed by rotary evaporation to yield the functionalized triblock polymers and characterized using ^{1}H NMR, see figure 5-19

PMOXA-P(DMS-co-UPBMS)-PMOXA Triblock copolymer

Boronic acid functionalized polysiloxanes (3.2g for 16% side chain content and 6.5g for 32% Si-H content) that had been previously dried under vaccum were dissolved in 1.5mL of dichloroethane and stirred. Freshly distilled oxazoline (1.4mL for 16% side chain density and 1.8mL for 32% side-chain density) was added to the mixture and stirred at room temperature for 1 hour. The temperature was raised to 60°C for 40hrs and then 80°C untill a white precipitate was observed. The reaction was then quenched by adding 1M NaOH. The polymer yield was low (1g for both mixtures), see section 5.4.2 for a discussion.

5.4 Results and Discussion

Previously reported syntheses of non-functionalized poly(siloxane-b-oxazoline) triblock copolymers relied on one of two major strategies. One approach is to convert a commercially available ,α,ω-bishydroxy-poly(dimethylsiloxane) into a macroinitator by converting the hydroxyl group into a trifluoromethanesulfonic acid ester (triflate) [92], that initiates the ring-opening polymerization of 2-methyl-2-oxazoline. The second approach is to synthesize the polysiloxane with reactive end-groups, namely benzyl chloride, and use this as a macroinitiator for the ring-opening polymerization of 2-ethyl-2-oxazoline with Sodium iodide as catalyst[150]. Another approach to the synthesis of a diblock copolymer that merits attention is based upon the hydrosilylation of a SiH-terminated poly(dimethylsiloxane) with ally alcohol. The hydroxyl end group thus obtained is converted into a tosylate [71] and used as the macroinitiator as in the syntheses described above. The central theme of all the reported syntheses has been to generate a macrointiator capable of initiating the ring-opening polymerization of oxazolines. A wide variety of intiators have been reported of which the triflates are the most effective since they are highly electrophilic [37]. The main

goal is to produce triblock copolymers with the P(DMS-co-HMS)-block (B-block) being available for further derivatization, specifically the attachment of biologically active supramolecules. Hence, the syntheses described in the literature were unsuitable for our purposes since they limit the functional groups that could be attached in polymer analogous reactions to the ones that are stable toward electrophilic attack. Furthermore, triflates are generally less air and moisture stable, requiring very careful handling. The approach of using chlorides was also not very attractive since it needed fairly high temperatures (130°C) and the use of iodide as a catalyst can cause unwanted side reactions in the functional groups. Tosylates offer a good balance between the required leaving group ability, tolerance to other functional groups and stability. Since a copolymer of dimethylsiloxane and methylhydrosiloxane, P(DMS-co-MHS), is required for the intended application reported schemes like the one mentioned earlier [71]cannot be used since it involves a hydrosilylation step. Also, post derivatization of a hydroxyl end-group was not attractive since the termination may neither be quantitative or bi-functional, and may lead to very tedious work-up strategies to isolate the bifunctional tosylates. Additionally, hydroxybutyl and hydroxypropyl terminated polysiloxanes degrade upon heating, through the loss of the end-groups [151]. Recently, we reported [131] a novel and facile route to synthesizing quantitatively terminated bifunctional P(DMS-co-MHS) tosylated telechelics, which is a modification of a reaction reported by Yilgor et al. [149, 150]. This reaction concept was applied throughout this work see figure 5-18b and 5-18c.

Polysiloxanes are generally prepared from cyclic monomers by cationic ring opening polymerization using an acid or base catalyst (see section 5.2). Though the Si-O bond is highly stable under neutral conditions it is readily cleaved in highly acidic or basic conditions. Siloxane bonds are constantly broken and reformed in both the linear and cyclic species, until the reaction reaches a thermodynamic equilibrium. Hence, this polymerization is often termed an equilibration or redistribution polymerization. Unlike the Si-O bond the Si-C bond is stable under these reaction conditions and if molecules containing Si-C bonds are present, they will terminate the growing chain and serve as the end-blocker[149]. The remaining cyclic non-functional side products

can be removed by vacuum distillation or precipitation. If the end-blocker is a siloxane dimer it will yield bifunctional siloxane telechelics and simultaneously provide a method for the control of the molecular weight.

Synthesis of Bistosylate Siloxane Telchelic

A linear siloxane dimer terminated on both ends with tosylate groups was synthesized by converting a commercially available 1,3-bis(hydroxybutyl) tetramethyldisiloxane into the ditosylate. The reaction scheme is shown in figure 5-18a along with the ^{1}H NMR spectrum showing complete conversion of hydroxyl groups into tosylate end groups. Reaction conditions for the tosylation are listed in Table 5.3. DMAP proved to be the most successful tosylation catalyst. Since the siloxane bonds cleave readily under tosylation conditions, 4 equivalent of triethylamine are necessary as proton scavenger thus guaranteeing yields of approximately 40%. Reactions were conducted in methylene chloride for one hour at 0°C followed by 24 hours at room temperature. Using sodium hydroxide with benzyltrimethylammonium chloride as catalyst in a 75:25 THF:H_2O mixture, a procedure that works well for ditosylations of glycols, did not yield tosylated bis(hydroxbutyl)-tetramethyldisiloxane, and reactions with NaOH as base were terminated after 4 hours, since disiloxane bonds were unstable. Substituting potassium carbonate for sodium hydroxide prevents this cleavage but the tosylated product was obtained in very low yields, see Table 5.3.

Synthesis of P(DMS-co-MHS)

Reaction conditions for the copolymer synthesis were established by first investigating the PDMS homopolymer synthesis. Bistosylate disiloxane was used as an end-blocker in the acid (p-TsOH) catalyzed ring-opening polymerization of D4, as shown in figure 5-18b. The associated ^{1}H NMR shown alongside figure 5-18b clearly shows the bifuctional termination of the PDMS homopolymer. Entries 1-3 in Table 5.4 describe reactions in which the monomer concentration was kept constant and end-blocker concentration was varied to control the molecular weight. In those reactions monomer and end-blocker were added to the toluene solution containing the acid catalyst.

Base	Cataylst	Time	Temp.	Yield
Pyridine(4eq)	None	24hrs	20°C	20%
Triethylamine(4eq)	DMAP(0.2eq)	24hrs	20°C	40%
Triethylamine(1eq)	DMAP(0.7eq)	24hrs	20°C	20%
NaOH (9eq)	Benzyl-trimethyl-ammonium Chloride (0.2eq)	4hrs	≤ 5°C	Cleavage Of Disiloxane
K_2CO_3(9eq)	Benzyl-trimethyl-ammonium Chloride (0.2eq) DMAP (0.2eq)	24hrs	20°C	10%

Table 5.3: Reaction conditions for ditosylation of disiloxane endblocker

The obtained polymers show a significant difference between the expected and actual molecular weight. End-blocker and monomer form a suspension rather than a solution in toluene. It was determined that a stable homogeneous monomer - end-blocker suspension must be formed prior to adding the acid catalyst. When the acid catalyst was added to a stable suspension, (entry 4)α,ω-butyltosyloxyl terminated PDMS was obtained with a molecular weight as predetermined by the end-blocker-to-monomer ratio. Since the end-blocker and monomer are initially immiscible, reaction progress can be monitored visually by the change from a heterogeneous suspension to a homogeneous mixture. The yields of the PDMS synthesis are generally low; the molarity of the D4 concentration in toluene affects the ratio of cyclics to linear polymers. As shown in Table 5.4 (entry 1), if the D4 concentration in toluene is 1.58 M, the yield is only 8%, which is in good agreement with work reported by Buese, that states that the polymerization of D4 in concentrations below 2 M yields 80-95% cyclic products [14]. Increasing the concentration to 21M D4 in toluene results in yields of 20 to 30%. The yield can be improved if the product is recovered by solvent extraction rather than precipitation in methanol due to the low molecular weights involved. If extraction in hexanes in used, as for the case of copolymers, see Table 5.5, yields improve to 40 - 75%.

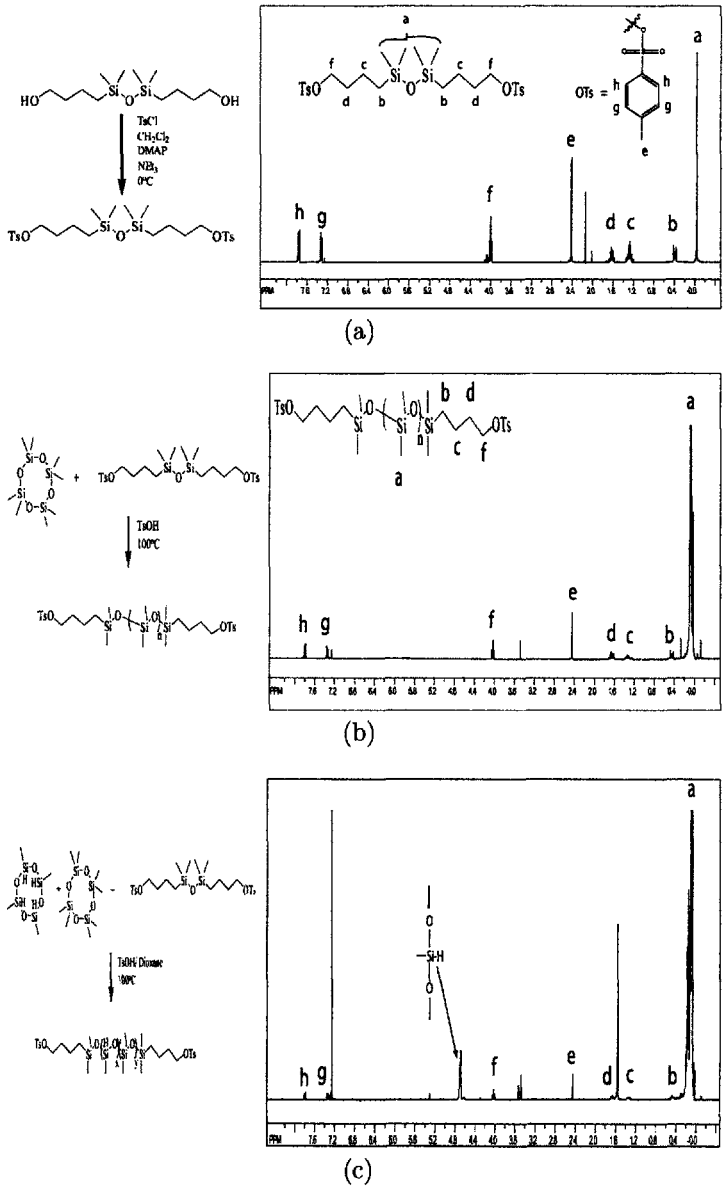

Figure 5-18: (a) Synthesis of the tosylated disiloxane end-blocker and its associated 1HNMR showing successful conversion of the hydroxyl groups into tosylated groups. The peak labeling is indicated on the inset in the figure. (b) Synthesis of a siloxane macroinitiator with reactive tosylate end-groups employing a cationic ring-opening equilibration polymerization. Comparing the ^{1}H NMR of figures a & b easily verifies the presence of the tosylate end-groups. All molecular weights reported were determined using the methyl protons (protons e in figure) of the p-tolunesulfonate moiety as the reference. Peaks not indicated in figure are residual solvent peaks. (c) Synthesis of the siloxane copolymer enabling further functionalization of the siloxane back-bone via the hydrosilylation reaction The Si-H (at 4.7 ppm) group that results from the synthesis can be unambiguously identified in the ^{1}H NMR spectrum. All other peaks are as indicated in b.

A P(DMS-co-MHS) copolymer will constitute the B-block in the final derivatized triblock copolymers, see figure 5-1. These copolymers were synthesized by using the reaction condition that were most suitable for the PDMS homopolymer synthesis, Table 5.4, entry 4. The reaction scheme is shown in figure 5-18c and the corresponding ^{1}H NMR shows the incorporation of methylhydrosiloxane by the appearance of the Si-H protons at 4.7 ppm. To further investigate the versatility of the approach the Si-H was varied content by altering the D4:D4H feed ratio to see if the ratio charged would be the ratio obtained. Again, monomers and the end-blocker were stirred prior to the addition of the acid catalyst thus obtaining a stable suspension. Best results were obtained when the acid catalyst (TsOH) was dissolved in dioxane and added after stirring the suspension for one hour, entries 2-4 in Table 5.5. It was determined that catalytic amounts of TsOH should not exceed 0.001 eq. The methyl protons of the toluenesulfonate moiety (protons e) were used as internal reference during ^{1}H NMR analyses and served as reference for the determination of the Si-H content, and molecular weights, see figure 5-19 . Molecular weights ranged between 4000-5000 Da, as predetermined by the monomer-to-end-blocker ratio, proving that the molecular weight can be controlled by the feed ratio of the end-blocker to the cyclic monomers. The fact that the polymer is a random copolymer with a statistical distribution of Si-H units is reflected in the ^{1}H NMR pattern of Si-H protons [15]. Using the pattern designation found by Cancouet *et al.*[15] the assignment is shown in figure 5-20. Furthermore it can be clearly seen that for higher Si-H content there is more regularity of the Si-H units due to the increased probability that the next segment will also be D^H, while for a low Si-H content (8%), the D^H units are flanked by two D units.

5.4.1 Derivatization of P(DMS-co-HMS) with supramolecules

2-Hydroxy-4-undecenyloxy methyl benzoate was studied as the model receptor and used to establish reaction conditions for hydrosilylation reactions that yield derivatized P(DMS-co-MHS) copolymers. The synthesis scheme for this model receptor is shown in figure 5-21 (Scheme I). Initially, a strong base (sodium hydride) was used,

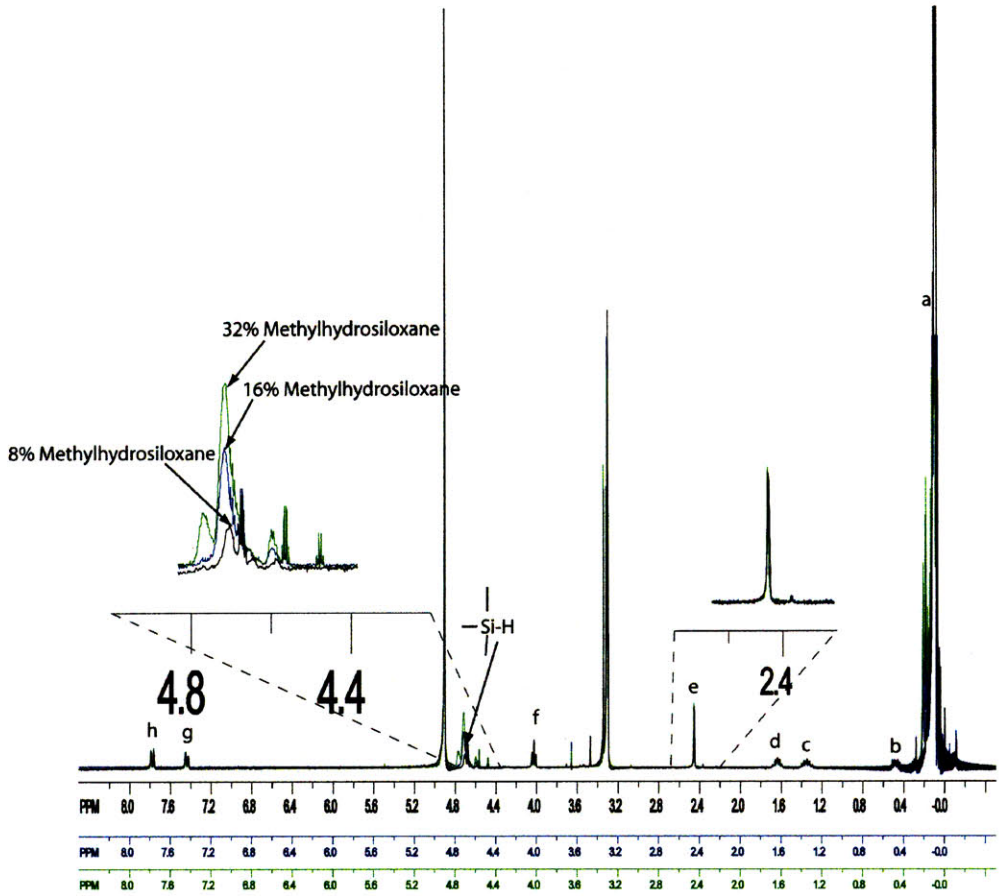

Figure 5-19: ^{1}H NMR results showing the successful modulation of the methylhydrosiloxane content in the co-polymer. The inset in figure shows the relative peak heights of the Si-H goup appearing at 4.7 ppm. Also shown is the expanded region around 2.4 ppm where the methyl group of the p-toluenesulfonate peak appears. It can be clearly seen from the insets that the relative heights of protons e are the same height while the heights of the Si-H protons successively increase corresponding to a larger ratio of methylhydrosiloxane content. The letter assignments are the same as indicated in figure 5-18

D4	Endblocker	Acid Catalyst	Solvent	Expected Mn	Mn(^{1}H NMR)	Yield
31.65mmol	1.67mmol[a]	0.13eq	Toluene (20mL)	5900	22200	8%
32.2mmol	0.85mmol[b]	0.014eq	Toluene (1.5mL)	11400	23100	30%
32.2mmol	1.2mmol[b]	0.008eq	Toluene (1.5mL)	8300	1200	Not Recorded
32.2mmol	1.64mmol[b]	0.012eq	Toluene (1.5mL)	6000	5600	23%

Table 5.4: Reaction conditions for polymerization of Octamethylcyclotetrasiloxane. [a]bishydroxybutyl disiloxane used as the end-blocker. [b]bistosyloxybutyl disiloxane used as the end-blocker.

D_4 (mmol)	D_4^H (mmol)	DSX (mmol)	Acid catalyst	Expected Mn	Mn(^{1}H NMR)	Si-H (Expected)	Si-H (^{1}H NMR)	Yield
50	19.8	3.3	.014eq	6300	10000	32	44	46%
62	6.3	4	.001eq	5000	5500	8	8	37%
55	12.7	4.1	.001eq	4900	6500	16	20	69%
45	25.4	3.9	.001eq	5300	6000	32	40	75%

Table 5.5: Polymerization results for P(DMS-co-HMS) polymerization.

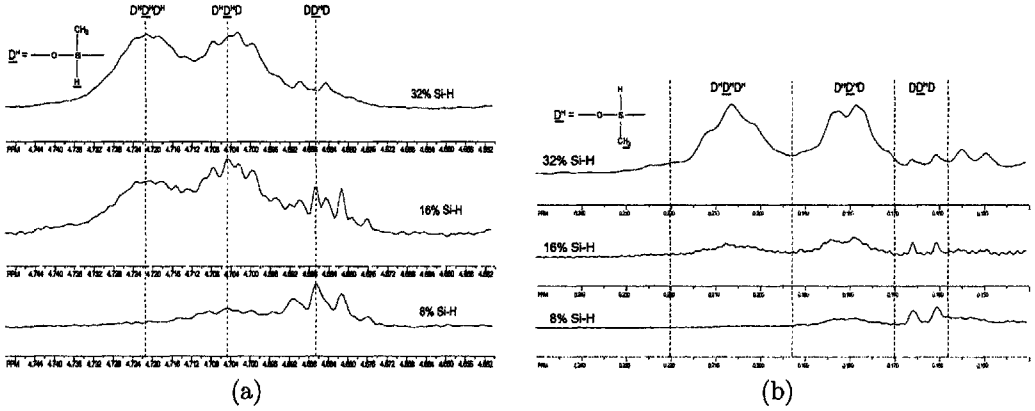

(a) (b)

Figure 5-20: Microstructural composition of the random copolymer determined via ^{1}H NMR. The copolymer with the lower D^H shows more randomization (absence of contiguous D^H units) due to the lower probability in meeting a D^H unit.

however, this approach led to low yields, better results were obtained when K2CO3 activated by catalytic amounts of 18-crown-6 were used along with lithium iodide as a co-catalyst (in-situ Finkelstein reaction). The product was purified by column chromatography, giving a total product yield of 70%. ^{1}H NMR spectroscopy was used to verify the structure.

The receptor of interest, potassium-chelating 18-crown-6-ether, was synthesized by adapting a method by Klok et al. [76] originally developed for the synthesis of sodium-chelating 15-crown-5-ether. An 11-carbon undecenyl spacer was first attached to the hydroxymethyl 18-crown-6-ether via a DCC coupled esterification catalyzed by DMAP, followed by the hydrosilylation reaction. Unlike the hydrophobic benzoate side-chain containing siloxane telechelics, the crown ether containing siloxanes could not be purified using a silica column. In order to make the method more general, a simple procedure for the purification of these copolymers was developed using activated carbon (see Experimental). This method leads to purified telechelics that can be used for the ring-opening polymerization of 2-methyl-2-oxazoline. ^{1}H NMR spectroscopy was used to verify the structure.

A glucose binding receptor was also synthesized. First a lipophilic boronic acid carrier with an ω-alkenyl tail was synthesized. Commercially available carboxyphenylboronic acid pinacol ester was converted into a undecenyl ester. The coupling between undecenyl alcohol and the carboxylic acid effected by the carbodiimide coupling agent (DCC) with added catalysts DMAP and HOBt. This was then attached to the polysiloxane backbone by hydrosilylation in a similar fashion to other receptors.

The receptor (18-crown-6-ether or methyl benzoate) was attached to the P(DMS-co-MHS) backbone using a polymer analogous hydrosilylation reaction. The functionalization was quantitative and can be identified by the disappearance of the vinyl protons (5.9 ppm and 5.4 ppm) and the appearance of the Si-CH_2 peaks at 0.5 ppm, see ^{1}H NMR spectrum in figure 5-23. The presence of the hydroxyl group in the 2-position did not adversely affect the polymerizations and shows the versatility of the synthetic route used. The hydrosilylated siloxane polymer was purified following a literature procedure [54] using a silica column. Briefly, the reaction product

was loaded onto a silica column and unreacted benzoate was eluted with toluene. ^{1}H NMR analysis of the eluate revealed the presence of trace amounts of P(DMS-co-HMS) copolymer. Subsequently, diethylether was used to recover the derivatized copolymer, and the product was obtained by solvent evaporation.

5.4.2 Synthesis of triblock copolymers

Triblock copolymers were synthesized by cationic ring opening polymerization of 2-methyl-2-oxazoline using the bistosylate terminated siloxane telechelics as a macroinitiator. As in the telechelic synthesis, reaction conditions were first determined using the PDMS homopolymer. The reaction scheme (Generation I) is shown in figure 5-22 along with the ^{1}H NMR spectrum of the triblock copolymer. The spectrum exhibits the classical polyoxazoline segment peaks of the side chain methyl protons between 2.0 and 2.3 ppm, and the protons connected to the nitrogen appear at 3.3-3.5 ppm. Similarly, triblock copolymers were formed when P(DMS-co-HMS) was used as macroinitiator, figure 5-22, Generation II. The ^{1}H NMR spectrum verifies the structure of the triblock copolymer, clearly indicating the presence of the poly(oxazoline), Si-CH3, and Si-H moieties. The presence of the fairly reactive Si-H groups does not seem to hinder the block polymerization under the reaction conditions used. The triblock copolymers described above with the methylhydrosiloxane moieties containing B-block were synthesized in an effort to further derivatize the B-block using hydrosilylation reactions. The effect of the reaction order was investigated by either (i) first forming the triblock copolymers followed by the hydrosilylation reaction, and (ii) the hydrosilylation was conducted first, followed by the ring-opening polymerization of 2-methyl-2-oxazoline. One of the most important outcomes of the work presented was the discovery that the hydrosilylation reaction, that is the attachment of the tethered supramolecules to the P(DMS-co-HMS) block needs to be conducted prior to the block copolymer formation with 2-methyl-2-oxazoline, that is option (ii). Reactions in which the triblock copolymer was formed first, option (i), and the supramolecules were tethered later met with failure. This is probably due to the interaction of the platinum metal catalyst with the poly(oxazoline) block. No platinum catalysts other

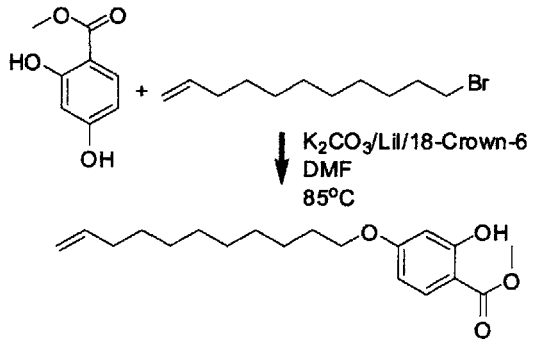

Scheme I

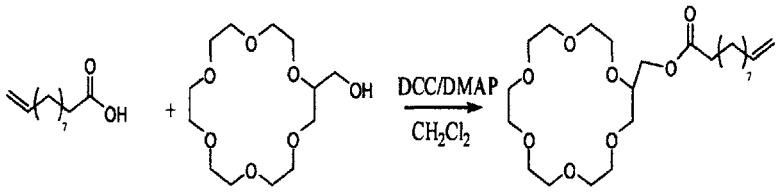

Scheme II

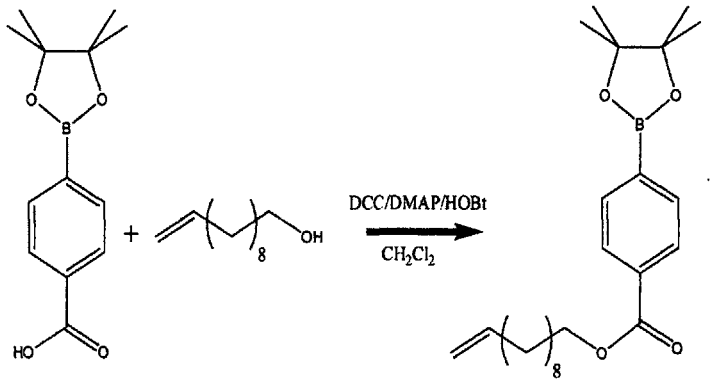

Scheme III

Figure 5-21: Synthesis of the side chain mesogens that were used in this work. Scheme I shows the synthesis of methyl (2-hydroxy,4-undeceneloxy) benzoate by reacting methyl(2,4 dihydroxy) benzoate using potassium carbonate activated with 18-crown-6 and lithium iodide as a co-catalyst. Scheme II shows the synthesis of undecenyl ester of hydroxymethyl 18-crown-6. 10-undecenoic acid was esterified with 18-crown-6 using dicyclohexylcarbodiimde coupled reaction employing DMAP as a catalyst. The boronic deviative was synthesized in a similar manner to the 18-crown-6 receptor i.e. via a DCC coupled esterification. In this reaction both DMAP and HOBt were used as catalysts as shown in Scheme III.

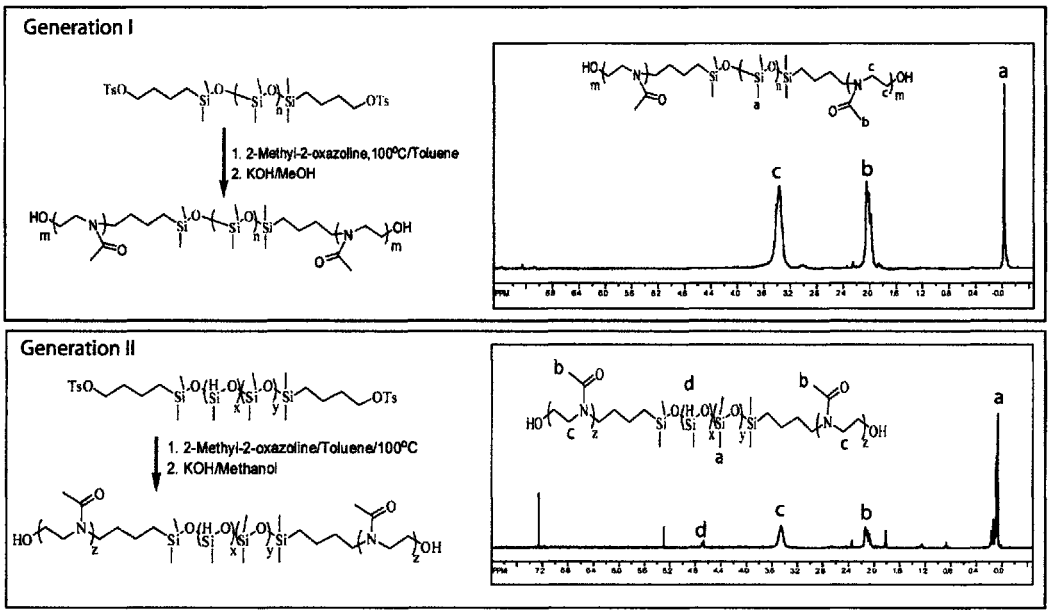

Figure 5-22: Evolutionary synthesis of the active nanostructure. Generation I was used as a proof of concept to verify the synthetic scheme of using a tosylate terminated polysiloxane as a macroinitiator for the ring opening polymerization of 2-methyl-2-oxazoline. The ^{1}H NMR shows the classical polyoxazoline peaks and are indicated as peaks b and c. Generation II was designed so that the polymeric backbone could be derivatized with functional molecules via the hydrosilylation reaction. The Si-H peak d at 4.7 ppm clearly indicate that under the reactions conditions the Si-H protons do no hinder the polymerization. The post derivitization via hydrosilylation employing a platinum catalyst was, however, unsuccessful (see text for details).

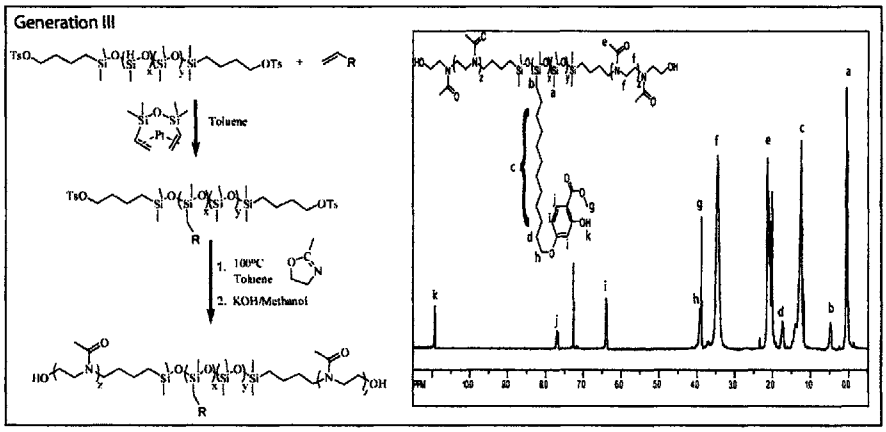

Figure 5-23: Generation III shows a modification to the earlier scheme to yield an active nanostructure. Here the backbone was first derivatized and then used as a macroinitiator for the ring opening polymerization of 2-methyl-2-oxazoline. As evidenced by the ^{1}H NMR this route is successful and is the preferred route for the synthesis of functionalized triblock co-polymers.

than Karstedt's catalyst were investigated since it is the most widely used and gentle method of hydrosilylation. Hence, the reaction scheme was modified so that after the copolymerization of D4 and D4H, a hydrosilylation reaction was performed yielding a P(DMS-co-HMS) copolymer derivatized with an appropriate side-chain, see figure 5-23.

Best results were obtained when PDMS homopolymer was used as macroinitiator without solvent, i.e. the p(oxazoline) A-blocks were obtained in the expected molecular weight, and the overall yield was 94%. Using the PDMS-co-HMS copolymer, or derivatized copolymers respectively, necessitated the use of a solvent. Toluene was used for the copolymer and the benzoate-derivatized copolymers, dichloroethane was used for the crown-ether-derivatized copolymer. Hydrosilylation of the PDMS-co-HMS copolymer derivatized with the 18-crown-6 supramolecule led to a low yield when the side chain density was low, see Table 5.6, 8% MHS. The reason for that is believed to be in the purification steps, future work should focus on optimizing this procedure.

Research focused on 18-crown-6-ether, since this supramolecule is expected to coordinate and potentially translocate potassium ions. Potassium ions are both biologically relevant and play an important role in the maintaining membrane potentials

Triblock	Solvent	Polyoxazoline Block Expected Mn	Polyoxazoline Block Mn (^{1}H NMR)	Yield
PDMS	None	8100	8100	94%
PDMS-co-HMS	Toluene(5mL)	4600	5700	73%
PDMS-co-UBMS	Toluene(2mL)	10500	8100	77%
PDMS-co-UBCE 92:8	Dichloro-ethane(1.5mL)	2300	3100	34%
PDMS-co-UBCE 68:32	Dichloro-ethane(2.5mL)	2500	3100	67%

Table 5.6: Triblock polymerization results

in neural tissue. One of the long-term goals is to modulate the ionic gradient around the neural tissue to elicit a response. The first step toward this goal is to produce a synthetic membrane capable of self-assembling into vesicles and sequestering potassium ions from the extracellular fluid.

Boronic Acid Functionalized Triblock

A glucose sensitive triblock co-polymer synthesis was also attempted. Boronic acids are capable of complexing glucose molecules via the cis-diol moiety and their transport in liposomes has been well studied [143, 144]. There have also been some instances where fixed site lipophlic salts show enchanced flux of glucose through polymeric membranes [111]. The boronic acid functionalized polysiloxane was used as macrointiator for the polymerization of 2-methyl-2-oxazoline. The resulting polymer was obtained in low yield (20%),^{1}H NMR verified the structure. However, these polymers were insoluble in most common organic solvents, except under acidified condition, completely solublility only being obtained in methanol. This is was not the expected behavior since these amphiphilic molecules are expected to solubilize in most organic solvents. Furthermore, deprotection of the pinnacol ester proved difficult.

A clue to the anomalous behavior of these polymers can be found in examining the structure of the boronic acid. Boron is highly electron deficient and usually complexes to electron donating substituents like lone pairs found on oxygen and nitrogen via

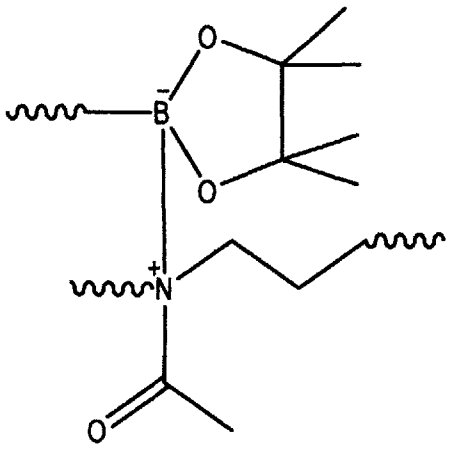

Figure 5-24: Physical cross link due to the donation of the nitrogen lone pair of the oxazoline segment into the empty p-orbital of the boronic acid side chain .

its empty p-orbital. It is presumed that the nitrogen lone pair in the polyoxazoline complexes the boronic acid lone pair. This explains the poor solubility in organic solvents since there are multiple interactions making this a physically cross-linked polymeric structure, see figure 5-24. Addition of acid coordinates the nitrogen lone pair and negates the physical cross linking, rendering the polymeric structure soluble. Deprotection of the pinnacol ester protecting group also proved difficult. Additionally, self assembling studies with this polymer met with failure, probaly becasue of the physical cross linking of the polymer chains. Possible solutions to this problem is the design of boronic acid carriers that contain pendant alkyl amines [98].

5.5 Conclusion

A general facile and versatile synthesis of both non-functionalized and receptor functionalized self-assembling triblock coppolymers was presented. A key to developing a supramolecular neural prosthesis is an ion selective membrane and a crown ether functionalized amphiphilic polymer was synthesized as a first step toward this goal. In the next chapter the unique properties possessed by these membranes will be discussed.

Chapter 6

Ion Responsive Vesicles

6.1 Introduction

In chapter 5 the structural aspects of the self assembling membrane were examined. The functional properties that arise from the structural constraints that have been imposed will now be examined in this chapter. These properties arise namely from the lyotropic (from the latin lyo=solvent and tropic=induced by)behavior of the structure. In a general lyotropic interaction the solvent solubilizes only one part of the structure strongly which leads to phase separations and since the two parts are covalently bonded it leads to separate domains. If water is used as the solvent then these give rise to the familiar hydrophobic and hydrophilic interactions. Though other solvents can exhibit lyotropic behavior we will consider water only since this is the solvent in biological systems. The most striking property of the self-assembling system is one where the collective properties give rise to emergent behavior that is greater than the sum of its parts. This is a ubiquitous principle found in nature and biomembranes are an embodiment of this organizing principle. They are fundamentally important to the functioning of cellular assemblies. They provide a structural framework via a microenvironment and a functional framework by incorporation of channels, receptors, and pumps. Self-assembly is a key property that nature relies on to generate these membranes. By exploiting the hydrophobic-hydrophilic interactions, these membranes assemble into bilayers and other structures.

6.1.1 Physics of Self-Assembly

To appreciate the complex behavior of the interactions between macromolecules and the solvent, the physics of self-assembly needs to be understood. Consider the amphiphilic molecule shown in figure 6-1 where the sphere represents a hydrophilic head group and the tails represent a hydrophobic carbon chain. If these molecules are added into water depending on the concentration of the amphiphile added different behaviors can be observed. . It can be free amphiphilic molecules, a micelle or a vesicle. The free amphiphilic molecules is possible at low concentration since the entropic cost is not too large. At slightly higher concentrations the cost of the loss in entropy will be too great and the enthalpic energy required to aggregate the hydrocarbon chains together so as to exclude water is compensated for the increase in entropy of the water molecules. This configuration is called the micelle. It is possible to develop a simple model that relates the micelle formation to the concentration. Let A_{free} denote a free amphiphilic molecules solution and $A_{micelle}$ the micelles (which are treated as a whole unit). If each micelle contains n amphiphilic molecules the following relationship can be developed:

$nA_{free} \overset{K_{micelle}}{\longleftrightarrow} A_{micelle}$

The equilibrium constant is then given by:

$K_{micelle} = \frac{[A_{micelle}]}{[A_{free}]^n}$

Since a relationship between the number of micellar objects as a function of the concentration of amphiphilic monomers is required, the number of objects needs to be related to the number of amphiphilic monomers. The ratio ν of monomers per object is

$\nu = \frac{[A_{free}]+n[A_{micelle}]}{[A_{free}]+[A_{micelle}]}$ or

$$\nu = \frac{1 + n\frac{[A_{micelle}]}{[A_{free}]}}{1 + \frac{[A_{micelle}]}{[A_{free}]}} \tag{6.1}$$

The equilibrium constant relationship can be rewritten as

$K_{micelle}[A_{free}]^{n-1} = \frac{[A_{micelle}]}{[A_{free}]}$ substituting this in the above and defining $\chi = [A_{free}]$

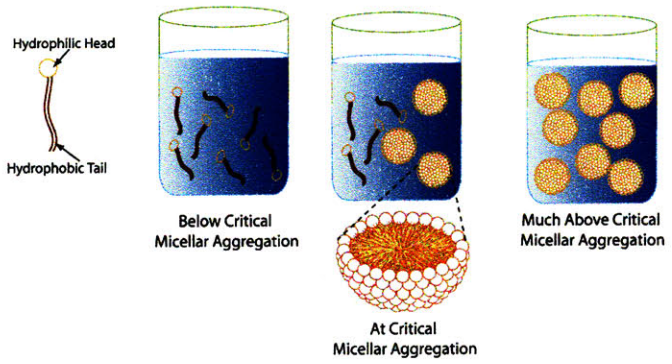

Figure 6-1: Schematic showing the formation of micelles from amphiphiles, see text for details.

for simplicity yields

$$\nu = \frac{1 + nK_{micelle}\chi^{n-1}}{1 + K_{micelle}\chi^{n-1}} \tag{6.2}$$

From equation 6.2 it can be seen that if $K_{micelle}\chi^{n-1} \gg 1$ all the objects are in a micellar configuration and if $K_{micelle}\chi^{n-1} \ll 1$ all the amphiphilic molecules are free. When the concentration is satisfies the relationship $\chi^{n-1} = \frac{1}{K_{micelle}}$ there is a sharp transition from the solutions being mostly in monomeric form to the aggregated micellar form. This is defined as the critical micellar concentration (cmc)[32], see figure 6-1.

To form a vesicle there has to be a transition from the propensity to form monolayers to forming bilayers, this is controlled by what is referred to as the molecular packing parameter [90] given by v_o/al_o. v_o is the molecular volume of the hydrophobic tail, a is the area of the hydrophilic head or more appropriately the surface area occupied by each molecule in the aggregate and l_o is the extended length of hydrophobic tail. From this simple definitions certain predictions about the nature of the aggregate can be readily made. Consider a spherical micelle composed of g molecules with radius R, the volume of the micelle is given by $V = gv_o = (4/3)\pi R^3$, the surface area $A = ga = 4\pi R^2$. From this it can be seen that the radius $R = 3V/A = 3v_o/a$, but if all the volume is occupied by the hydrophobic tails, the maximum value of the radius is $0 < R \leq l_o$ or $0 < v_o/al_o \leq 1/3$. Similarly for a cylindrical micelle $1/3 < v_o/al_o \leq 1/2$. For a bilayer the volume can be modeled as a cuboid with length

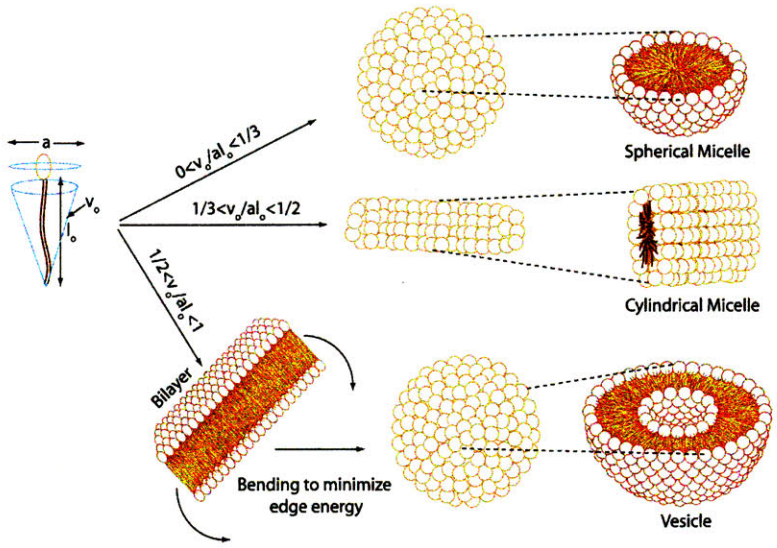

Figure 6-2: Schematic depicting how the ratio of the hydrophobic volume to the surface area and tail length determines the structure that is formed via self-assembly, parts of figure from http://med.tn.tudelft.nl

2R, width w and depth d. So $V = 2Rwd$ and $A = 2wd$, using the same reasoning as earlier we arrive at the following inequality $1/2 < v_o/al_o \leq 1$ for the formation of a bilayer, see figure 6-2. For polymeric amphiphilic molecules a more relevant metric is the ratio of the hydrophilic fraction to the hydrophobic fraction. As the fraction of the hydrophilic block is reduced at a constant hydrophobic block length the aggregate goes from a spherical to a worm-like micelle then finally toward a vesicular structure[91], see figure 6-3.

Now that the condition for the formation of a bilayer has been developed vesicle formation can be addressed by using the curvature model. One of the driving forces behind vesicle formation from bilayers is the minimization of edge energy. The edge energy is the energy due to the interaction of the exposed hydrophobic region at the edges of the bilayer with the solvent(water). The simplest energetically favorable solution to this problem is the formation of a closed surface that has no edges, for instance a sphere. However, the cost of forming a closed surface is the increase in bending energy of the membrane, so the shape of a vesicular assembly will be one that minimizes this bending energy.

A curved surface can be completely described by its principal radii of curvature

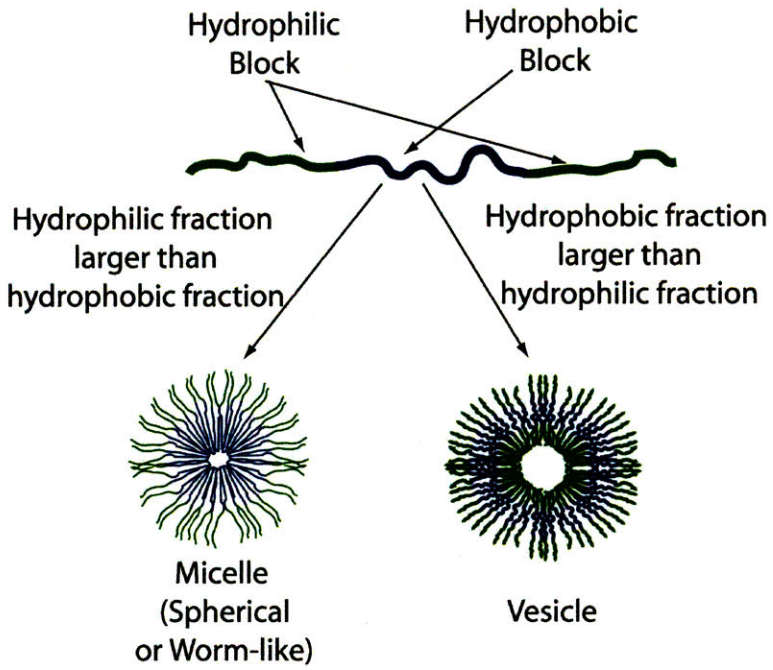

Figure 6-3: The structures formed by amphiphilic polymers is controlled by the fraction of hydrophilic block length to the hydrophobic block length as shown schematically in figure.

C_1 and C_2(see figure 6-4) and the gaussian curvature C_1C_2. The curvature model developed by Helfrich [52] gives the total bending energy in a membrane as a function of these terms

$$E_{bend} = \oint \kappa \left(C_1 + C_2 - C_0\right) dA + \oint \kappa_G \left(C_1 C_2\right) dA \tag{6.3}$$

The first term is the a Hookean elastic term, where C_0 is the spontaneous curvature of the membrane. The spontaneous curvature arising form asymmetries in the membrane due to different chain lengths or different amphiphiles. κ is the bending rigidity modulus or the first moment. The second term is necessary to take into account saddle deformations, since for certain saddle deformations $C_1 + C_2 = 0$ but the energy required is neither less than or equal to zero since this not a spontaneous or equilibrium condition, see figure 6-4.κ_G is the second moment and is function of the lateral stresses in the membrane. So the membrane will bend so as to minimize this energy under the constraint of area and volume and this minimum can be found by using

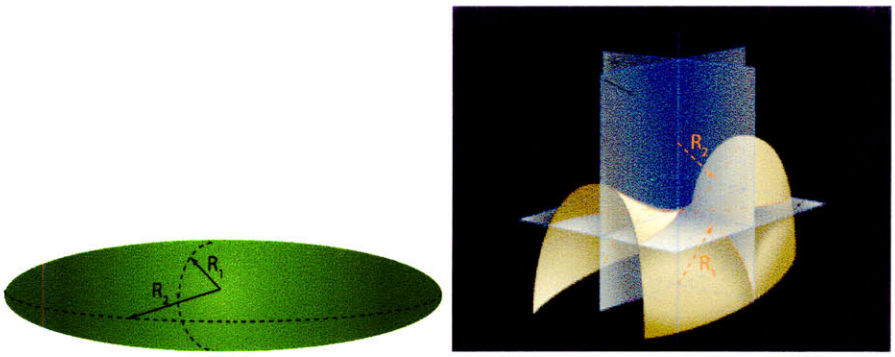

(a) (b)

Figure 6-4: (a) Shows a structure where both the principal radii of curvature is positive. Positive curvature is defined as being convex. (b) Shows a saddle deformation where one radius of curvature(R_1) is positive while the other, R_2, is negative (source:www.answers.com). If the curvatures are equal then the total curvature($C_1 + C_2$) is zero, while the gaussian curvature,C_1C_2, is negative.

the method of Lagrange multipliers [80]. Having developed a theoretical background to the formation of vesicles the self-assembling properties of the polymers that were developed in chapter 5 will now be examined.

6.2 Experimental

6.2.1 Materials

Polymeric structures and synthesis can be found in chapter 5. All reagents were used as received, Potassium Chloride (KCl), Sodium Chloride (NaCl) and Magnesium Chloride hexahydrate ($MgCl_2.6H_2O$) were purchased from Mallinckrodt Chemicals; CD_3OD, CD_3Cl and D_2O were purchased form Cambridge Isotope Laboratories. All salt solutions were prepared in deionized water or D_2O when appropriate. Ethanol (200 proof) was purchased from Pharmco products. Electroformation of vesicles was performed on Indium Tin Oxide (ITO) slides purchased from SPI, Inc. using an Agilent 33220A function generator, vesicles were imaged on a Zeiss inverted microscope, Zeiss Axiovert 200M fitted with a 63X phase objective.

6.2.2 Electroformation of Vesicles

Vesicles were electroformed by using a modified literature procedure [2]. Briefly, solutions of triblock copolymer in chloroform (c=20mg/mL) were applied to ITO slides and allowed to dry. To one of the slides a silicone gasket was affixed to create a solution reservoir. 100mM sucrose solution containing 200 g/mL fluorescein salt was gently placed into the reservoir and the gasket was then sandwiched between two ITO plates. The plates were then connected to an Agilent function generator and subjected to a 10Hz AC sinusoidal waveform, with peak-to-peak amplitude of 2V, for 2h and then 5Hz for another hour. The sucrose solutions were then gently dispersed into 2 mL of a 100mM glucose solution. The resultant solution was allowed to settle and imaged under phase contrast using a Zeiss microscope.

6.2.3 Vesicle Preparation by Solvent-injection-extrusion or Ethanol Method

This procedure was adapted and modified from existing procedure [6, 92]. Approximately 10mg of the polymer was dissolved in 1mL of Ethanol. The polymer solution was then added drop wise into 3mL of deionized water. The resultant solution turned slightly opaque indicating an emulsion. The solution was then filtered through a syringe fitted with a 0.5μm PTFE membrane filter with glass microfiber (Whatman). The resulting filtered solution was allowed to stand for a 2-3 hours during which time the vesicles coalesced enabling visualization via standard light microscopy, Zeiss Axiovert 200M. To ensure that vesicle coalescence was repeatable, the solutions were filtered through a 0.5 m syringe filter and then imaged again. Ion response was studied by adding a 1mL aliquot of the appropriate salt solution (1M) to a 1mL vesicle solution and then imaged subsequently.

6.2.4 ^{1}H NMR Sample Preparation

65mg of the appropriate polymer was mixed with 500μL of CD_3OD to enhance solubility. 5mL of D_2O was then added and was vigorously mixed. The resultant solution

was then filtered into a separate glass vial. Three 1M solutions of KCl, NaCl, and $MgCl_2$ were prepared in D_2O. Four samples of each polymeric composition were prepared in 5mm o.d. NMR tubes (Wilmad). The first was a 700μL reference solution containing just the polymer solution. The other three were prepared by adding 100μL of the appropriate salt solution to 600μL of the polymer solution. The ^{1}H NMR was then obtained in a 500MHz Varian Inova spectrometer.

6.3 Results and Discussion

6.3.1 Electroformed Vesicles

ABA triblock copolymers with the structures discussed in chapter 5 were electroformed as discussed in the section 6.2.2. The exact nature by which the vesicles are formed is still under debate. The most popular theory being direct electrostatic interactions between the bilayer and the electrodes. The other favored theory is the electroosmotically induced mechanical stress [2].

All polymers synthesized were electroformed to enable direct visualization of the self-assembling properties. The results of the experiments are shown in figure 6-5, the vesicle sizes seem to correlate with lipophilicity of the hydrophobic core. The smallest size arising from the amphiphilic co-polymer having the hydride as its side group in the siloxane backbone and largest size arising from the crown ether containing co-polymers.

6.3.2 Vesicle Fusion

All studies in this section were performed using the polymer with a 32% side chain density. An ethanolic solution containing the polymer (10mg/mL) was added dropwise via a syringe into a 3mL solution of deionized water. The solution was then filtered and imaged. It can be seen in figure 6-6 that the vesicles spontaneously tend to fuse. In images 6-6a and b the vesicle fusion is shown at the moment just before and just after. The time between the fusion events is in the order of a few minutes.

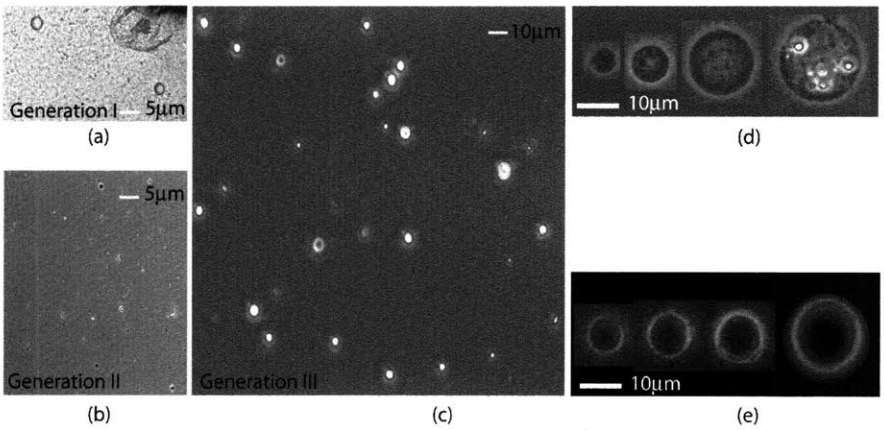

Figure 6-5: Vesicles formed by electroformation, the size of the vesicles formed corresponds to the side-chain lipophilicity. a) Vesicles from the PMOXA-PDMS-PMOXA polymer b) PMOXA-P(DMS-co-HMS)-PMOXA c) Triblock polymer containing a undecyl benzoate side-chain (30% density) d) Triblock polymer with 8% side-chain density of crown ethers e) 32% side-chain density of crown ethers

In 6-6c,d, and e the vesicle fusion event is shown as it progresses. First, the vesicles approach each other (6-6c), then they fuse (6-6d) and are in an elongated shape, and then in 6-6e the vesicles relax to the more energetically favorable spherical shape.

Amphiphilic molecules tend to form vesicles and micelles due the minimization of the total energy of the system according to the curvature model, see section 6.1.1. The cost of the bending energy that is encountered in the spherical structure is being compensated for by the reduction in edge energy (zero in the case of a spherical structure). In this model, there are primarily two factors that determine the shape of the vesicles - the bending rigidity κ and the Gaussian curvature modulus, κ_G. If spherical vesicles are considered then the both the principal radii of curvature are equal and $C_1 = C_2 = 1/R$ where R is the radius of the sphere. For simplicity the spontaneous curvature will be assumed to be 0 and the total energy is then equal to $4\pi(2\kappa + \kappa_G)$. If two vesicles were to fuse then the energy gained would also be given by the same term [80]. In order for the process to be spontaneous this energy must be positive i.e.

$4\pi(2\kappa + \kappa_G) \geq 0$ or $\kappa_G \geq -2\kappa$

The Gaussian curvature modulus κ_G is related to the lateral stress in the membrane or the second moment. $\kappa_G = \int_0^l \sigma(z)(z-\zeta)^2 dz$

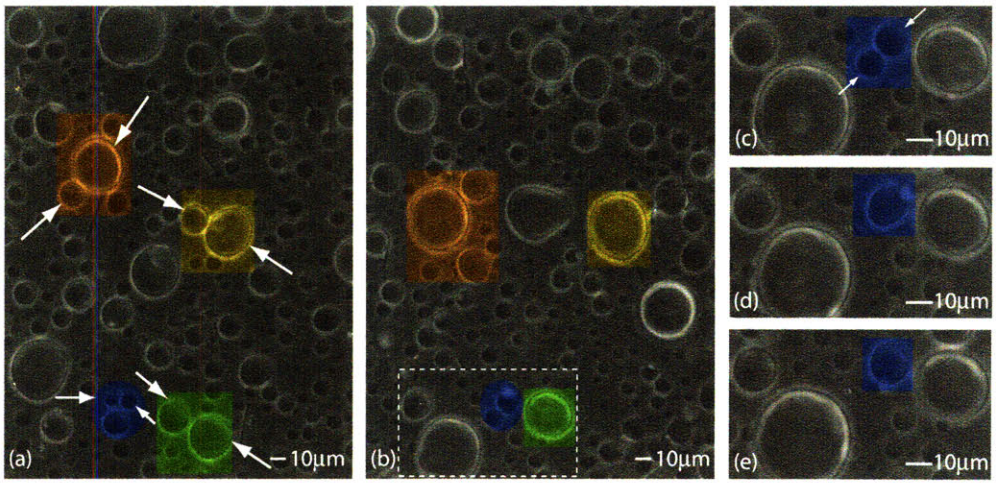

Figure 6-6: Vesicle fusion Images. (a) Vesicle before the fusion event, arrows and colors on image are to aid easy visualization of the vesicles involved (b) Vesicle after the fusion event, colors are correlated to 2a. (c) Vesicles meet and ready to fuse, the colors correlate to structures in 2b (d) The vesicles fuse but remain in a high energy ellipsoid shape. (e) Vesicle relaxes to the minimal energy spherical shape.

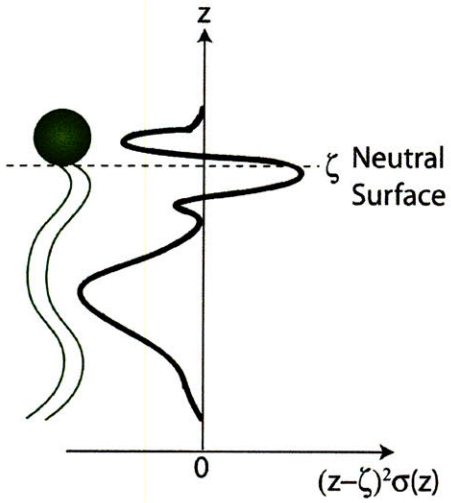

Figure 6-7: Schematic of the variation of integrand along the amphiphilic molecule in the bilayer. Also shown is the location of the neutral surface. The lateral pressure is positive at the interface of the apolar-polar interface and negative along the hydrophobic chains and the hydrophilic head group. Since the area under the curve is negative, the lateral pressure in a typical amphiphilic molecule in a bilayer is also negative. Adapted from references[52, 130].

ζ is the point where the neutral surface is located [130] realtive to the minimal surface and qualitatively defined as the point where the molecular density does not change during isothermal bending. The minimal surface is usually defined as the mid-point in the bilayer. It is common to place the neutral surface at the polar-apolar interface. $\sigma(z)$ is the lateral stress profile in the membrane as one traverses the membrane, see figure 6-7. Given the placement of the neutral surface at the polar-apolar interface, the lateral stress is negative in the region of the hydrocarbon chains (due to chain collisions), positive at the interface between the polar-apolar boundary due to the tension between the polar and apolar groups and slightly negative in the headgroup region due to headgroup-headgroup repulsion [130]. If we multiply this by the parabolic fuuction $(z-\zeta)^2$ we get the function that need to be integrated, see figure 6-7. From the figure 6-7 it can be seen that the area under the curve is negative giving a negative value of κ_G. As we noted earlier spontaneous fusion occurs when $\kappa_G \geq -2\kappa$, so we need to find out conditions under which this constraint can be satisfied. One obvious choice is to shorten the hydrophobic tails so that their contributions are less. The second method is to move the pivotal surface toward the minimal surface, though it is unclear how this could be physically achieved. The third method is to have a system with positive lateral stress in the chain region. Such molecules will exhibit dilation at the center of the membrane [130]. Normal amphiphilic molecules do not behave in this way. However, branched amphiphiles like the polymer under consideration certainly can. This can be proven qualitatively using a Gedanken experiment. It is known that inserting proteins or local mismatches in the lipids can cause packing stresses that lead to fusion [53]. Take a normal lipid like bilayer and periodically insert thin cylinders into them (for convenience the cylinders are all equal, though in reality they will be different), see figure 6-8. The cylinder need not be continuous so it can broken up into discs along the axis of the cylinder and connect each disc to a neighboring amphiphilic molecule. It is easy to see that the structure of each amphiphilic strand it very closely resembles a branched amphiphilic molecule crown ether functionalized triblock co-polymer under consideration. One thing that should also be noted is that no such fusion was observed when the receptor

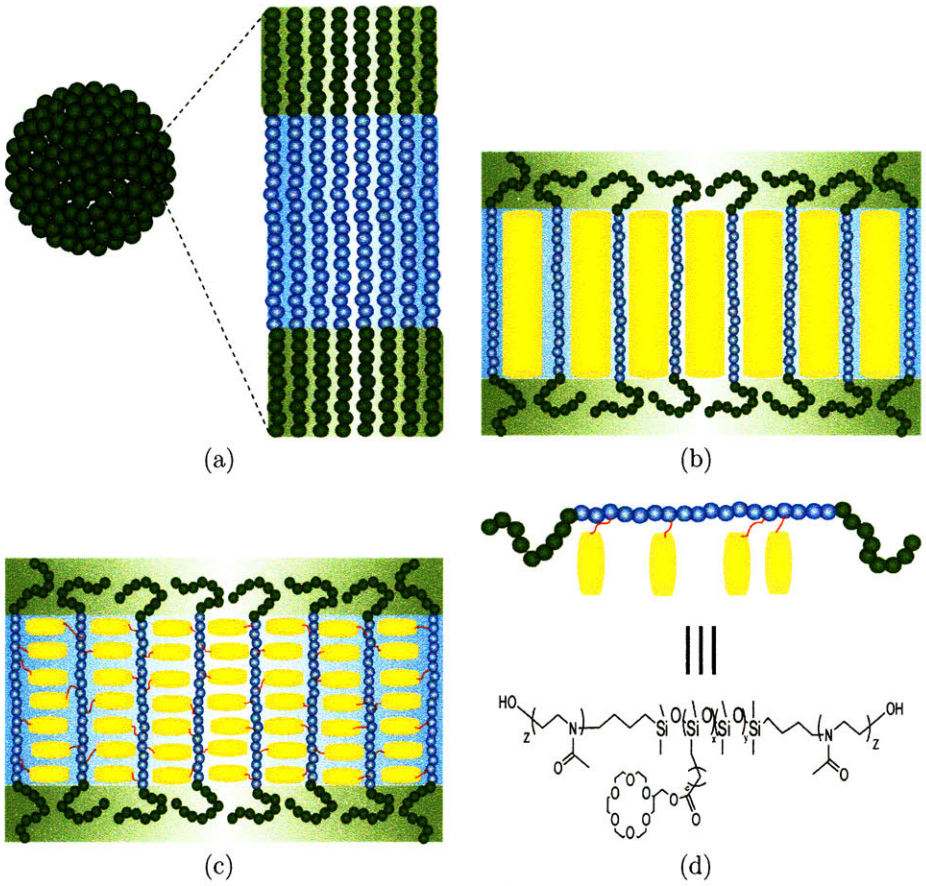

Figure 6-8: a) Polymeric membrane with negative lateral pressure in the membrane b) insertion of imaginary cylindrical objects that increases th elateral pressure in the membrane making it positive c) The cylinders can instead be replaced by imaginary discs that are connected to the hydophobic backbone d) Comparison of a polymeric strand from (c) compared to the chemical structure of the crown ether polymer.

was a methyl benzoate moiety. So the nature of the substituent matters. One of the important differences between the two receptors is their hydrophobicity, the benzoate being much more hydrophobic than the crown ether which has partial hydrophilic character. For the receptor to pack in the volume between the amphiphile the exposed portion of the receptor must have some amount of hydrophilicity. The discussion is, however, speculative and further characterization using advanced spectroscopy will be needed to understand the exact nature of the mechanism.

6.3.3 Vesicle to microtube transition

In the next set of experiments we subjected the vesicles that were drop formed and allowed to coalesce to various ionic stimuli. In the first experiment, we added 1mL of a 1M KCl solution to a 1mL vesicle solution. As soon as the salt solution was added, the vesicles ruptured due to osmotic stress. However, upon waiting a few minutes, small worm like objects were observed and these were imaged and are shown in figure 6-10. A similar response was obtained for a 1M NaCl solution, see figure 6-9, though the objects were predominantly rod like (see figure 6-11). Furthermore comparing figures 6-10 and 6-11 it can be seen that the density of rods is sparser for the sodium stimulus than the one for the potassium stimulus . To ensure that the effects observed were cation specific, a control experiment was performed using a 1M $MgCl_2$ stimulus. The vesicles ruptured as earlier but reformed into spherical vesicles as seen in the magnified view in figure 6-9 and the density is fairly high as seen in figure 6-11. Since the counter-ion is a chloride in all cases the effect of the counter-ion on the shape transformation can be ruled out.

These effects can be understood if one uses the curvature model as in the earlier case of vesicle fusion. To transition the shape from a sphere to a cylinder one of the radii of curvature needs to tend to toward infinity. This is possible if there is a high enough lateral pressure in the membrane. Before complexation when there is no ion present or when a divalent cation is present the crown ether ring remains flexible and exhibits a certain packing tendency, which as discussed earlier exerts a certain amount of lateral pressure. However, when a cation of the right size and charge is present in this case K^+ ions, the ring complexes the ion and becomes more rigid, see figure 6-12. This stiffening should increase the lateral pressure since there is a reduction in the number of packing possibilties with a stiff ring. It can also be seen from figure 6-12 that Na^+ ions also forms a complex with 18-crown-6 but this complex is not a planar complex and hence does not affect the lateral pressure as much. This difference should be reflected in the stiffness of the vesicular structures that are formed. Indeed the tubes that form when the sodium complex is formed is predominantly rod like while

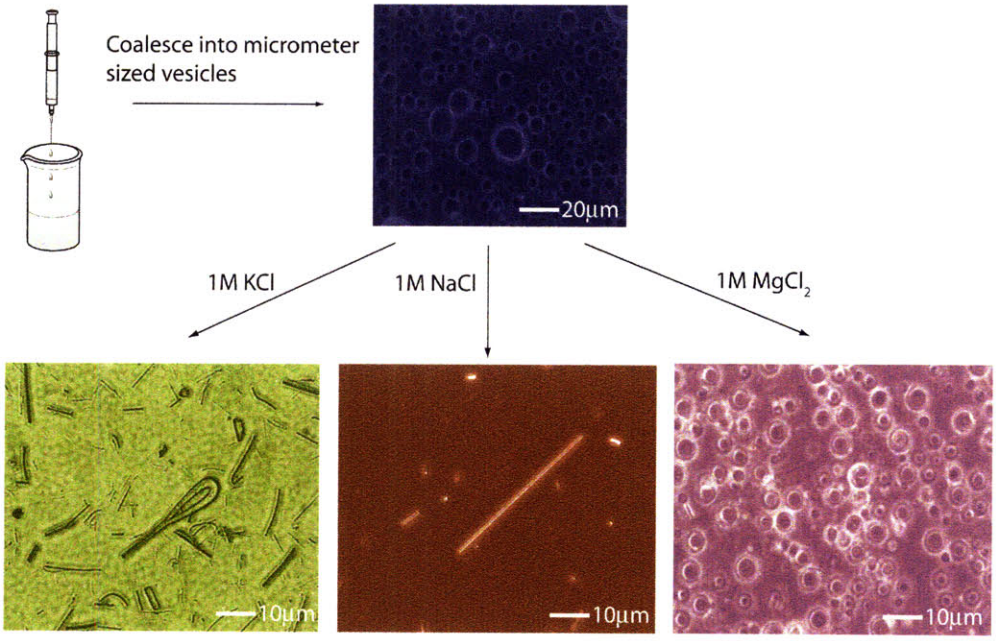

Figure 6-9: Shape transformations of the polymeric vesicles when subjected to various stimuli after initial rupturing due to osmotic stress. The vesicles adopt a curvy tube like configuration for KCl, a more rigid rod like configuration for NaCl and reform into spherical structure when subjected to $MgCl_2$.

the structures that are formed by the potassium complex is more worm like.

The increase in lateral pressure due to the increased packing stress explains the transition to a prolate object but does not explain the tube like dimension that indicates an increase in curvature of the system. One of the factors that we have not considered is the electrical effects that occur when a complex is formed. The complex formation at the surface gives rise to an electrostatic potential that contributes energy to the system. So the minimization of energy has to include this electrical energy term and when this is taken into account it can be shown [87] to contribute to the spontaneous curvature of the membrane. The expression, valid under the Debye-Huckel approximation, is given by

$$C_o^{el} = \frac{1}{4\kappa} \frac{\sigma^2 \chi^2}{\epsilon \epsilon_0} \tag{6.4}$$

κ is the bending rigidity,σ is the surface charge density, ϵ is the relative electrical permitivity of the medium and ϵ_0 is the electrical permitivity of free space and $\chi =$

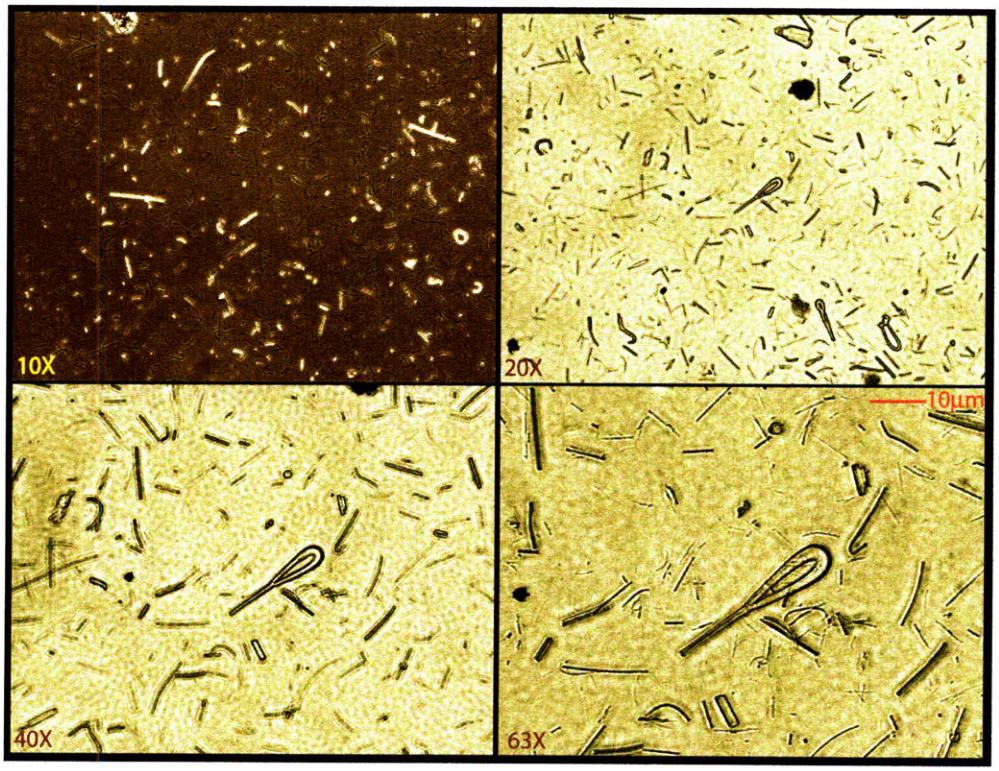

Figure 6-10: Microscope pictures of the vesicle system subjected to KCl at various magnifications. The figure illustrates the density of the tubes that are formed. When compared to figure 6-11 a and b it can be seen that there is much higher density of tubes in the KCl case than in the NaCl case. Additionally, the tubes are less rigid, see text for a detailed discussion.

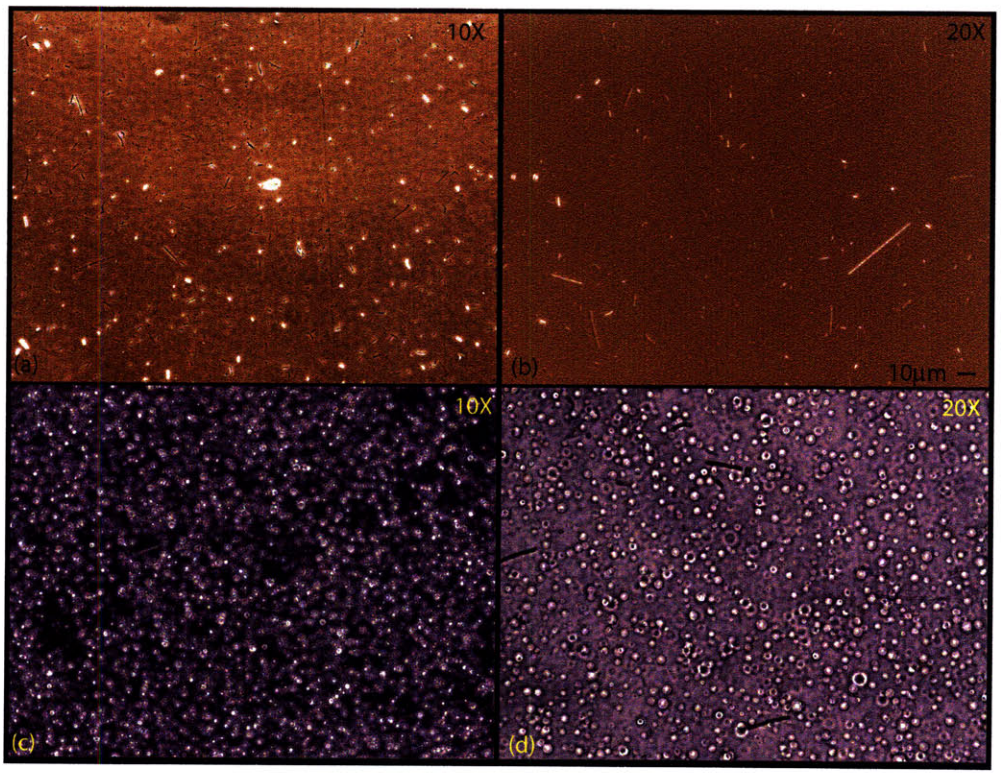

Figure 6-11: Figure illustrating the density of tubes and vesicles that are formed when the coalesced vesicles are subjected to NaCl (a nd b) and $MgCl_2$ (c and d).

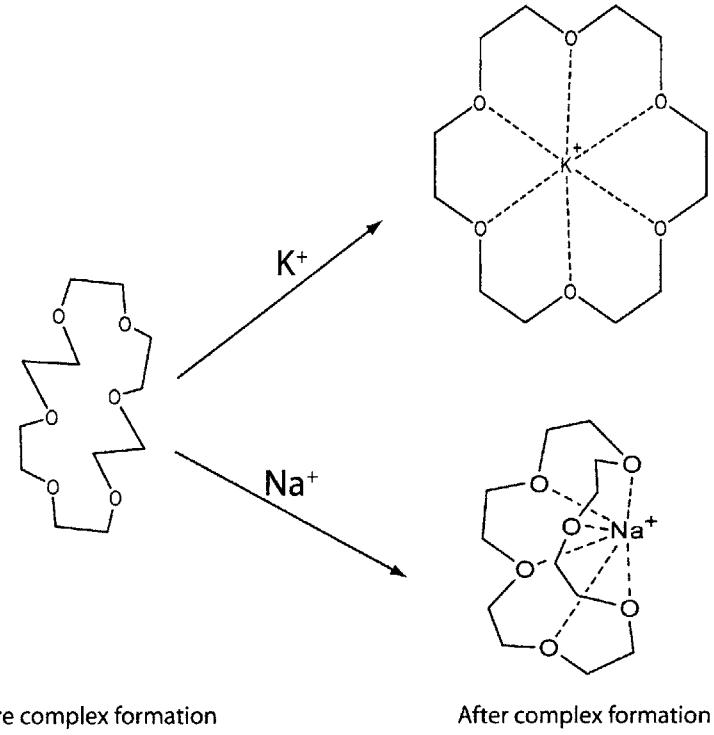

Figure 6-12: Schematic showing the ring stiffening upon metal complexation, the potassium complex is planar and rigid while the sodium complex is more of a puckered complex [24, 147]

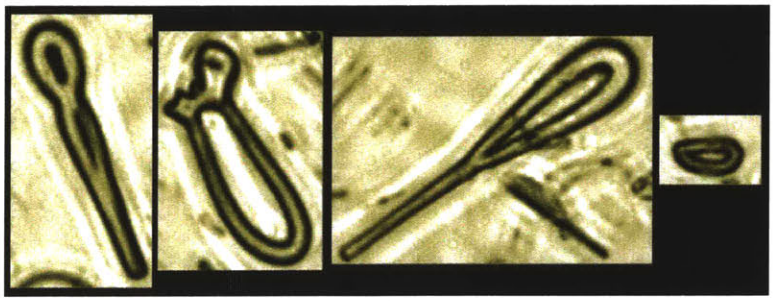

(a)

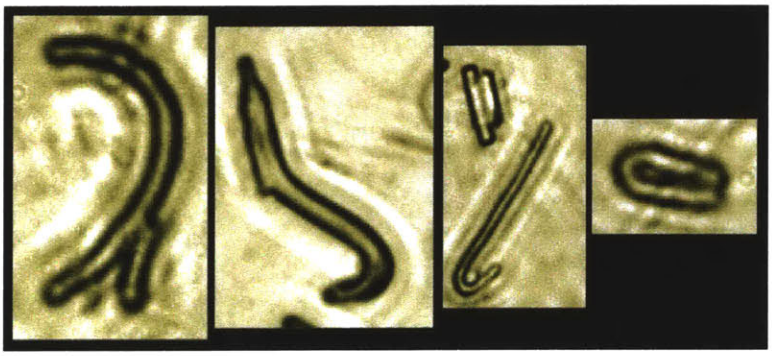

(b)

Figure 6-13: a) Pictures of various structures that exhibit an Euler number lesser than that of the starting structure b) Figure showing clearly that the tubes undergo fusion indicating that the change in genus of the shape happens after the shape transformation indicating that treating the integral of the gaussian curvature as a constant is valid.

$\sqrt{\frac{kT\epsilon\epsilon_0}{2z^2q^2C_{elec}}}$ is the Debye length and C_{elec} is the concentration of the electrolyte. The surface charge can be related to the crown ether-ion complex: $\sigma = q\delta C_{cmplx}$, where q is the unit charge, δ is the thickness of the complex layer at the surface and C_{cmplx} is the concentration of the complexed form of the crown ether. So the spontaneous curvature due to electrical effects can be rewritten as

$$C_o^{el} = \frac{1}{4\kappa}\frac{kT\delta^2 C_{cmplx}^2}{2z^2 C_{elec}} \tag{6.5}$$

From equation 6.5 it can be seen that the curvature increases with the concentration of the crown ether-ion complex. This is consistent with the effects that were observed i.e a thin tube instead of a prolate/oblate like object that would result based strictly on bending energy considerations.

There is a subtle assumption that was made in the above discussion that will be addressed now. The integral due to the gaussian curvature was assumed to be a constant in all the formulas utilized. As long as the surface has the same Euler numberξ, defined as the number of faces + number of vertices - number of edges, this is a valid assumption and the integral evaluates to $2\pi\xi$ by applying the Gauss-Bonnet theorem [80]. The Euler number can also be defined as 2-2g, where g is the genus of the surface or the number of holes. So as long as the system remains topologically equivalent under the shape transformation the analysis holds. However, when we examine the shapes shown in figure 6-9, the sodium and magnesium stimuli satisfy this requirement but it seems that the shape due to the potassium stimulus has a hole, as do the shapes shown in figure 6-13a that have been magnified for clarity. Upon careful investigation of other shapes a clearer picture emerges. As can be seen in figure 6-13b the shapes are the result of a fusion event between tubes. So the shapes observed are the result of a fusion event *after* the shape transfer to a tube, so the assumption of assuming the integral due to the gaussian curvature term remains a constant in still valid. This also validates the earlier observation that the tubes formed due to a potassium stimulus are more flexible.

6.3.4 ^{1}H NMR Studies

The hypothesis with respect to ring stiffening was further tested by ^{1}H NMR studies, if correct, the ^{1}H NMR peaks corresponding to the crown ether peaks should appear sharper and more like a singlet. Solutions of the polymer were prepared in D_2O and added to appropriate salt solutions also prepared in D_2O as outlined in the experimental section. The results of this experiment are shown in figures 6-14 and 6-15. There are several salient features of the presented spectra. 1) The reference solution along with NaCl and $MgCl_2$ spectra show no appreciable peaks for the undecenyl spacer and also for the siloxane backbone, specifically those that are covalently bonded(Si-CH2) to the backbone, indicating dense packing as discussed later. However, this is not the case for the KCl solutions where all peaks of the polymeric structure are visible. This spectrum is very similar to the one obtained in an apolar solvent such as $CDCl_3$. 2) The crown ether peaks for the reference, NaCl and $MgCl_2$ solutions are broad multiplets while the peak for the KCl solution is a broad singlet. 3) Though the NaCl crown ether rings appear as a multiplet (since 18-crown-6 only weakly complexes a Na^+ ion), the peaks of the other signals, such as polyoxazoline peaks and the stray solvent (toluene) peaks are shifted almost identical to that of the KCl solutions, indicating similar interaction under both NaCl and KCl stimuli. In contrast the peak shifts of the $MgCl_2$ solution are well correlated to those of the reference solution that contains no salts. This correlates with our experimental observation that $MgCl_2$ stimulus, apart from the initial osmotic stress response, is similar to that of the reference solution. The above results is for the polymer with a 32% side chain density. When the study was a repeated for a polymer containg a 8% side chain density this effect of detecting all polymeric peaks in the presence of KCl was not observed, see figure 6-15. However, the peak shifts in NaCl and KCl solutions were identical and so were the $MgCl_2$ and reference peaks shifts. This indicates that a critical side chain density is needed to observe these effects.

To draw useful conclusions from the ^{1}H NMR data some of the mechanism of the NMR spectroscopy need to be examined. The basics of nuclear magnetic res-

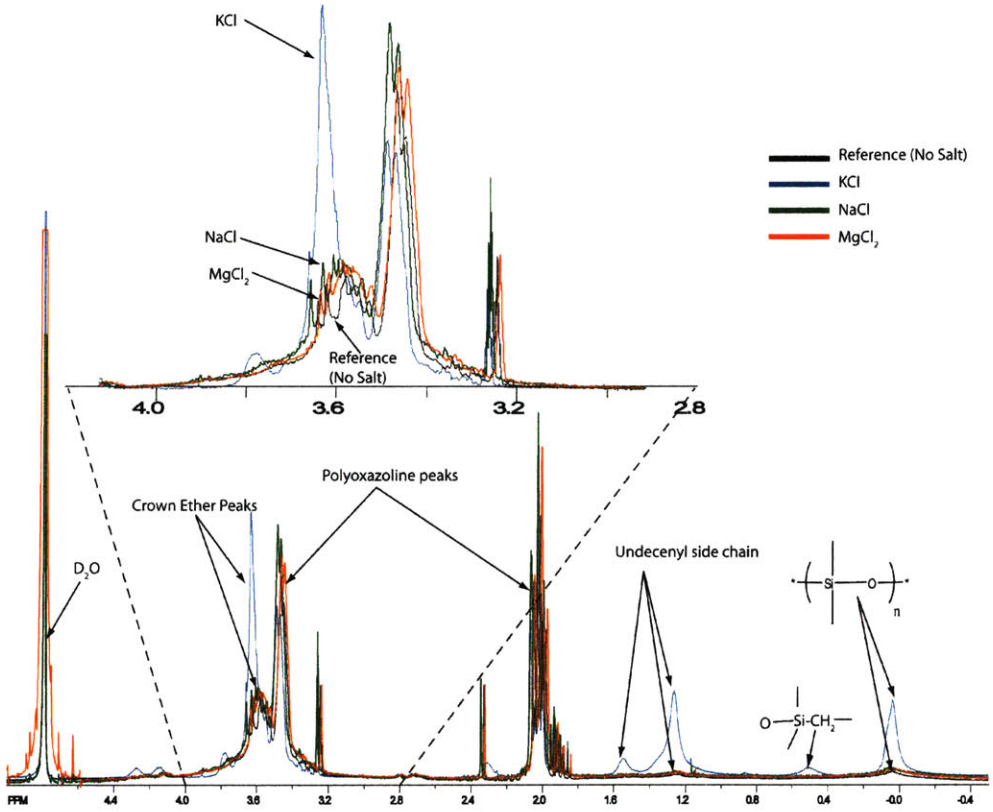

Figure 6-14: Superposed ^{1}H NMR spectra of four separate spectra. The reference peak was the D20 peak at 4.79 ppm. The broadening of the D2O peak for the $MgCl_2$ spectrum is due the presence of water since the $MgCl_2$ salt was purchased as its hexahydrate. Data was first processed in SpinWorks and then superposed using Adobe Illustrator, making sure that the ppm scales matched up. The inset in figure clearly shows the ring stiffening upon potassium ion complexation.

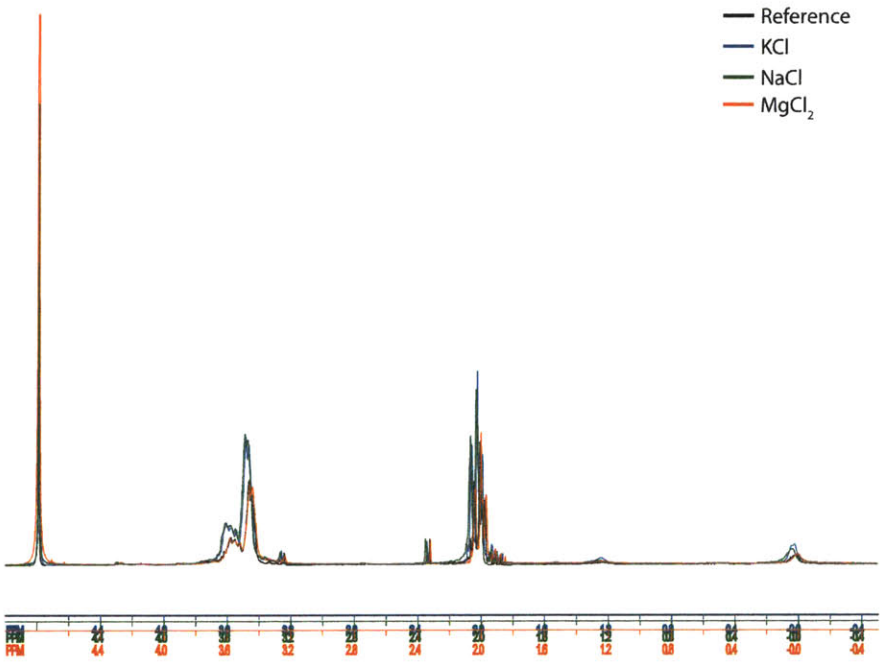

Figure 6-15: Superposed ^{1}H NMR spectra of four separate spectra for a triblock copolymer with 8% side-chain density. It can be seen that the reference solutions and the salt solutions all behave in a similar fashion, indicating that the complexing of the salt does not cause an appreciable change in the packing density in the polymer.

onance(NMR) spectroscopy is well explained in many textbooks [94, 82, 60] and is outside the scope of this thesis. However, the salient features will be briefly revisited to better understand the data. NMR spectroscopy relies on the population difference between different spin levels that arises when the nuclei are subjected to an external magnetic field. A small RF pulse then flips the spin, when tuned to the right resonance condition, by absorbing the energy from the RF pulse and by using this information the structure of the molecule can be elucidated. The reason there is a wealth of structural information is that local chemical environment either shields the nuclei from the external field or aids the field, giving rise to variations in energy needed to bring a nucleus into resonance.

However, there are two conditions that are implicit in the above discussion. Before the molecules are immersed in a magnetic field all the spin energy levels are degenerate and at the instant when the magnetic field is imposed, the spin levels are still equal. In order to come to an equilibrium Boltzmann distribution of spins which is necessary if NMR is to be a useful technique. In order to establish this equilibrium there needs to be a mechanism to relax the spins to the equilibrium distribution. The main method of spin relaxation comes from spin-lattice relaxation in liquid NMR which is what is used in this study. The origin of spin-lattice relaxation comes from the fluctuating magnetic fields that arise from neighboring molecules via dipolar coupling. The fluctuation arising from molecular random motion or molecular tumbling (to indicate that it is a complex motion) that arise from the constant buffeting of molecules by solvent molecules. If one imagines the path of a molecule projected on a sphere, then, after a small passage of time the molecule will be near its starting position and as time progresses the molecule will almost sample the entire surface of the sphere via a random walk [60]. The time that it takes for a molecule to move 1 radian from its starting position is called the correlation time τ_c. The correlation time and the time it takes a molecule to redistribute to its equilibrium Boltzmann distribution, T_1 are related. The reason can be intuitively understood by realizing that the spectral density of a signal depends on it correlation time. The spectral density gives the strength of a signal at a given frequency. Though the relaxation time to equilibrium,

T_1, is a characteristic of a given system, the necessary condition is that the modulated magnetic field by solution buffeting have a frequency component at the resonance frequency, ω_0 of the nucleus of interest. The strength of this frequency component is dependent on the correlation time, τ_c, which can be more conveniently expressed as $\omega_c = 1/\tau_c$. If $\omega_c \ll \omega_0$ then the strength of the signal at the resonance frequency, ω_0 is small,if $\omega_c \gg \omega_0$ then again this component is low and it reaches a maximum when $\omega_c = \omega_0$. Since the strength of the component varies the relaxation time will also accordingly vary with the correlation time. The variation of T_1 with τ_c is shown in figure 6-16.

The next important feature in relaxation processes is the one that arises due to spin-spin coupling. This relaxation time, T_2 is crucial in determining the line width of a NMR signal. This is a the amount of time it takes to dephase the coherence in the spins due to spin-spin interactions between molecules. The spin decoherence relaxation time, T_2, is inversely proportional to the correlation time and also inversely proportional to the line width. So fast tumbling leads to sharp line widths in the NMR spectrum while slow tumbling leads to broad peaks and in some cases the the peak broadening can be so large that the peak cannot be seen.

So it can be seen that the correlation time plays a key role in the features observed in the NMR spectrum. The factors that affect the correlation time are the temperature and the viscosity of the solvent and the molecular packing. A graph showing the various structures that correspond to the correlation time and the effect on line broadening is shown in figure 6-16. A lipid bilayer which is densely packed has a slow correlation time and fast spin-spin relation time and hence causes a very high line broadening (in the order of 10-100kHz, compared to the few kHz of the normal ^{1}H NMR spectrum) and cannot be distinguished from the base line.

From the above discussion on line broadening it becomes clear as to what is happening in the spectra shown in figure 6-14 and 6-15. The spectra of the reference, $MgCl_2$ and NaCl solutions exhibit characteristics of a lipid bilayer like packing. However, there are small signals due to the siloxane backbone showing its flexibility even under the dense packing of the bilayer. This in fact validates the hypothesis posed in

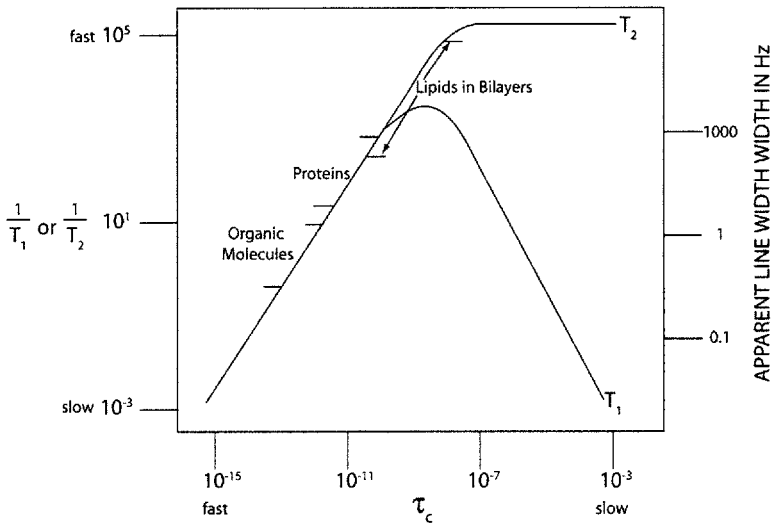

Figure 6-16: NMR Line broadening as a function of correlation time. The figure shows what line broadening can be expected for various types of molecules and/or aggregates. It also show the excessive line broadening that occurs for lipids in bilayers. Adapted from [82]

the fusion of vesicles i.e. there is considerable lateral pressure in the membrane, that relaxes the packing. Similarly, the packing of the crown ether is also not as dense. However, when subjected to the potassium stimulus the packing is considerably loose and almost identical to the molecule in a free solution. However, modeling this effect as though the entire molecule has enhanced solubility due to charge incorporation is not consistent with the other experimental data. One result that strongly supports the aggregate hypothesis is the spectrum of the amphiphilic polymers with low side-chain density. In this case all the solutions exhibit the same spectrum, indicating that even under complexation conditions the packing is still dense. This indicates that just complexing the ion and incorporating charge is not a sufficient condition. Though this does not rule out the possibility the spectrum is due to the solubilization of the polymer molecules it is not consistent with the physically observed behavior. This loose packing of the crown ether ring upon forming an ion complex will exert a lateral pressure in the membrane forcing a prolate/oblate transition. This coupled with the electrostatic energy in the membrane due to ion incorporation will increase

the radius of curvature will result in the transformation to a tube, as discussed earlier.

6.4 Conclusions

This chapter examined the self-assembling properties of functionalized and non-functionalized amphiphilic triblock co-polymers. All the polymers synthesized were successfully electroformed into vesicles, the size correlating with the side-chain lipophilicity. The polymers that contain crown-ethers in the side-chain at high densities spontaneously fuse to form micrometer sized vesicles. The hypothesis proposed is that this is partially due the lowering of the energy of the structure due to the packing constraints posed by the crown ether ring. It was also demonstrated that these vesicles undergo shape transformations when subjected to appropriate stimuli, such as K^+ and Na^+ ions. The hypothesis is consistent with the experimental data is that the ring stiffening of the crown ether moiety along with the curvature reduction due to the adsorbed ionic charge is primarily responsible for this behavior. This hypothesis was validated by ^1H NMR studies. Advanced spectrometric studies will reveal the true nature of these interactions and warrants further investigation in the future.

Chapter 7

Conclusions and Outlook

7.1 Summary

The penultimate challenge ahead in the area of biomedical engineering is the interface of man-made technology with that of biology with the hope of restoring lost function. The key component to that challenge is to develop an efficient and self-sufficient neural interface. This thesis examined the state of the art in terms of conventional technology. Though it is completely feasible to develop the necessary processing capability with the current technology, the fundamental bottle-neck is the interface which limits the applicability of the approach.

An alternative to electrical stimulation is chemical stimulation, the ideal chemical species would be neurotransmitters, though renewing their supply is a key issue that limits the applicability of the approach. The simpler approach would be to use a chemical species that is easy to replenish. One such neuroactive species are potassium ions. To develop a neural prosthesis with this approach, the neurophysiological parameters were determined by performing *in-vitro* experiments on rabbit retina. The concentrations needed to stimulate neural tissue are fairly low ($\approx$10mM). This low threshold makes it feasible to develop the idea of building a chemical prosthesis possible.

In the second part of this thesis a self-assembling potassium selective membrane was synthesized. Since currently available synthetic techniques do not lend them-

selves to developing such membranes a new technique was developed. The fusion of form and function led to some unexpected behavior of these self-assembling membranes. The self-assembling membranes had a tendency to spontaneously fuse and also change their shape to particular stimuli. Though this thesis primarily concentrated on developing a visual prosthesis, the method is applicable to developing any neural prosthesis.

7.2 Future Direction

The next key step that needs to be addressed is the method of delivery. One method is to use a cation selective nanopore as described in chapter 3. This needs to be pursued in parallel with a passive method, like hydrogel pumping, to achieve the optimal solution in terms the amount of power dissipated. The second aspect that warrants detailed investigation is the development of glucose sensitive self-assembling polymer that does not undergo adverse physical cross-linking. One way of achieving this is to use a glucose carrier that has a tertiary amino group as a side arm. Furthermore, one of the aspects that was not addressed in the synthesis of the self-assembling triblock polymer membranes was a strategy to deprotect functional groups. This is important in synthesizing triblock copolymers which contain carboxylic crown ether side-chains. In some attempted deprotection schemes it was realized that the only effective protecting groups are acid labile groups, since bases tend to cleave the polymers. Additionally, terminating the polyoxazoline polymerization with deprotonated methacrylic acid needs to be pursued to allow cross-linking of the self-assembled superstructure. Biocompatibilty studies of all the polymers synthesized need to be conducted either by implanting strips or by injecting vesicular suspensions in animal eyes.

Appendix A

^{1}H NMR

This appendix contains all the relevant ^{1}H NMR data for the syntheses discussed in chapter 5. The ^{1}H NMR data also contains integration information to verify the structural information. In the case of the polymers this was used to evaluate the molecular weight and a rough calculation is shown in each figure when relevant. The values reported closely match the data given in tables 5.4, 5.5 and 5.6. Minor discrepancies are due to software differences. The values in the tables are processed from the Varian software and the integration was more carefully performed. Additionally, the calculation used was more sophisticated than the one shown in the inset of the figures. The data shown below was processed using SpinWorks which is freely available from : http://www.umanitoba.ca/chemistry/nmr/spinworks/. The order of the NMR's follows the same order as the syntheses presented in section 5.3.1.

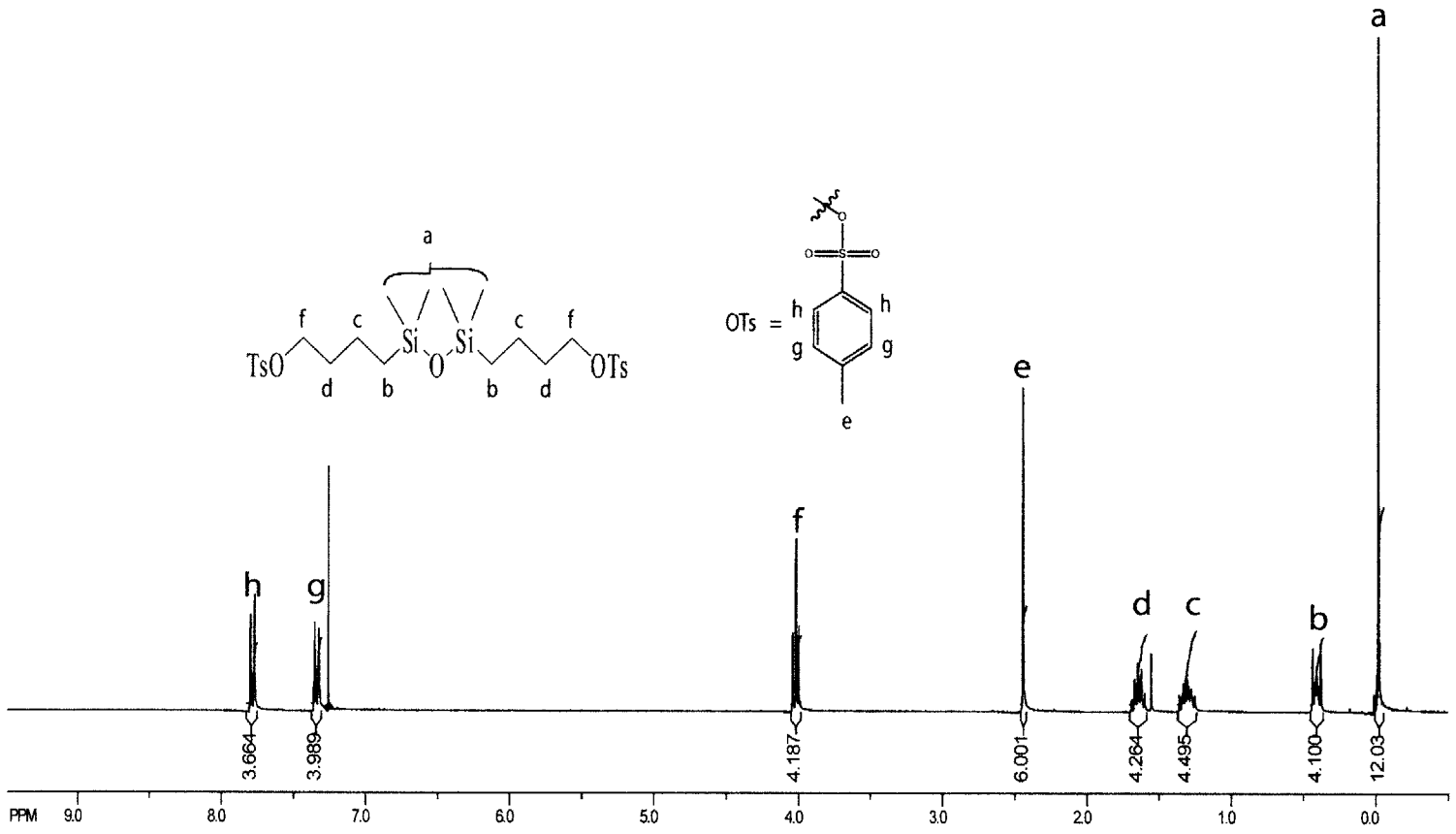

Figure A-1: ^{1}H NMR of 1,3-bis(tosyloxybutyl)tetramethyldisiloxane

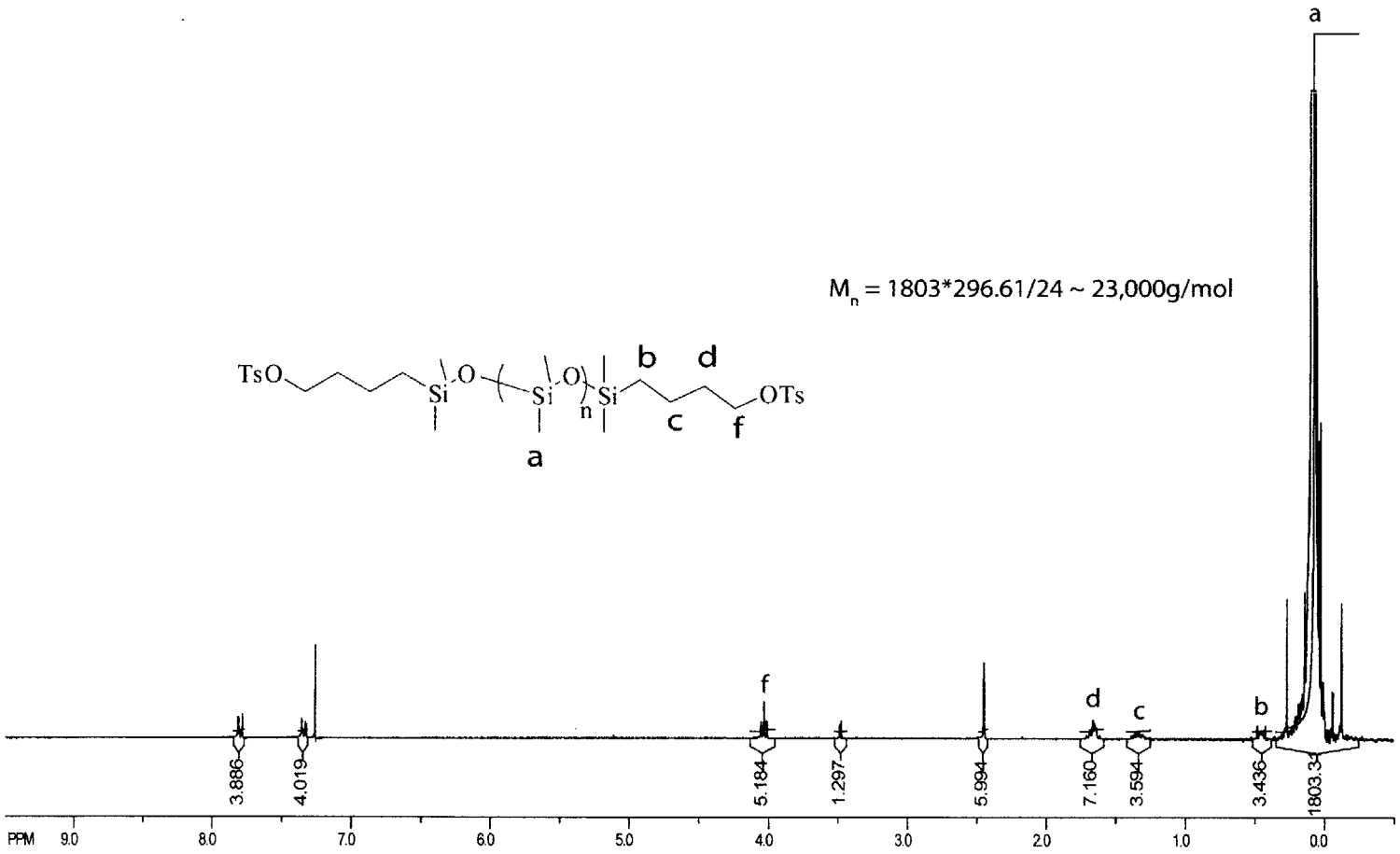

Figure A-2: ^{1}H NMR of bistosylated PDMS macrointiator. The methyl protons of the toluensulfonate protons(e) were used as the integration reference (set to 6). This result corresponds to entry 2 in Table 5.4

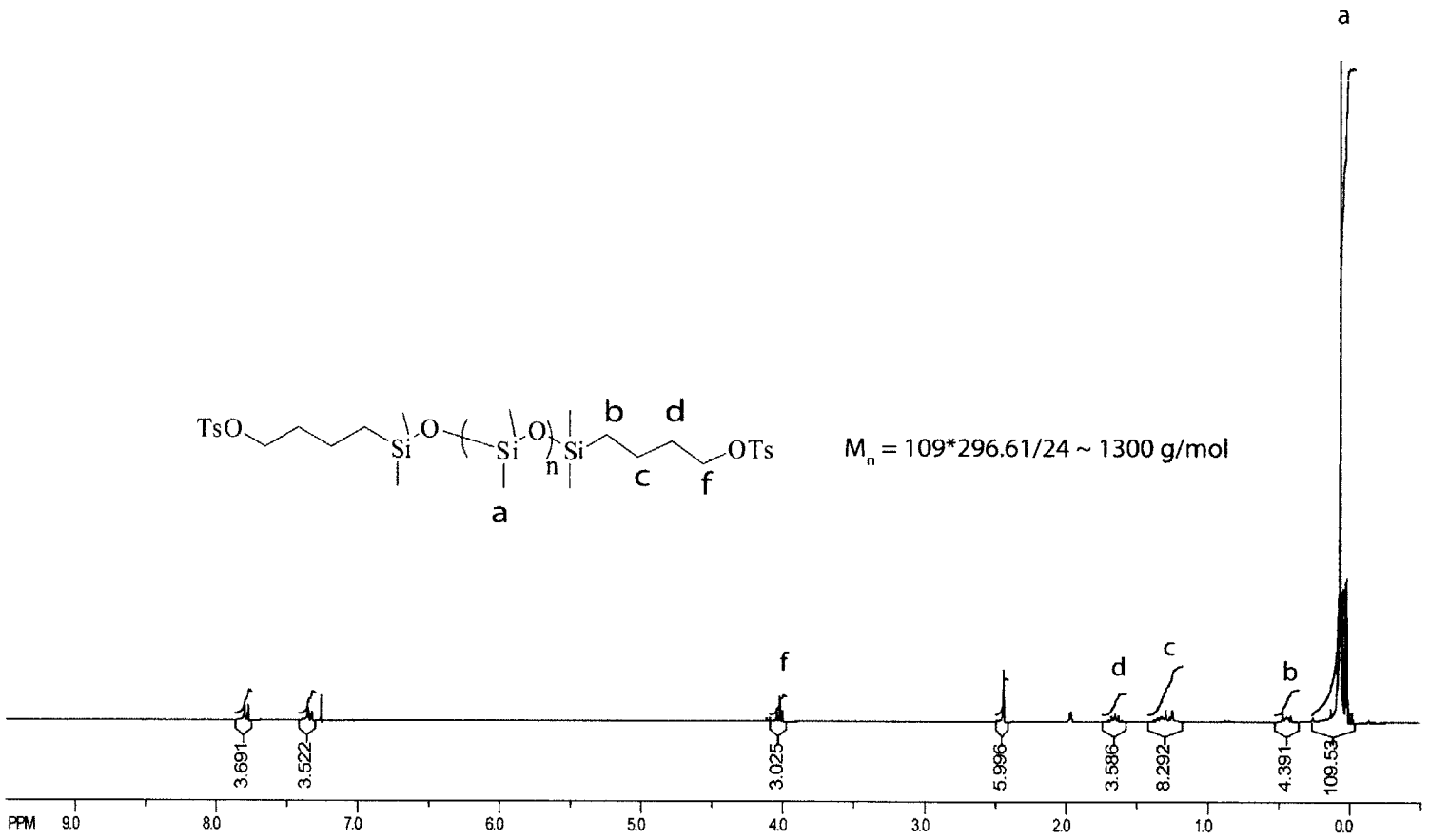

Figure A-3: ^{1}H NMR of bistosylated PDMS macrointiator. The methyl protons of the toluensulfonate protons(e) were used as the integration reference (set to 6). This result corresponds to entry 3 in Table 5.4

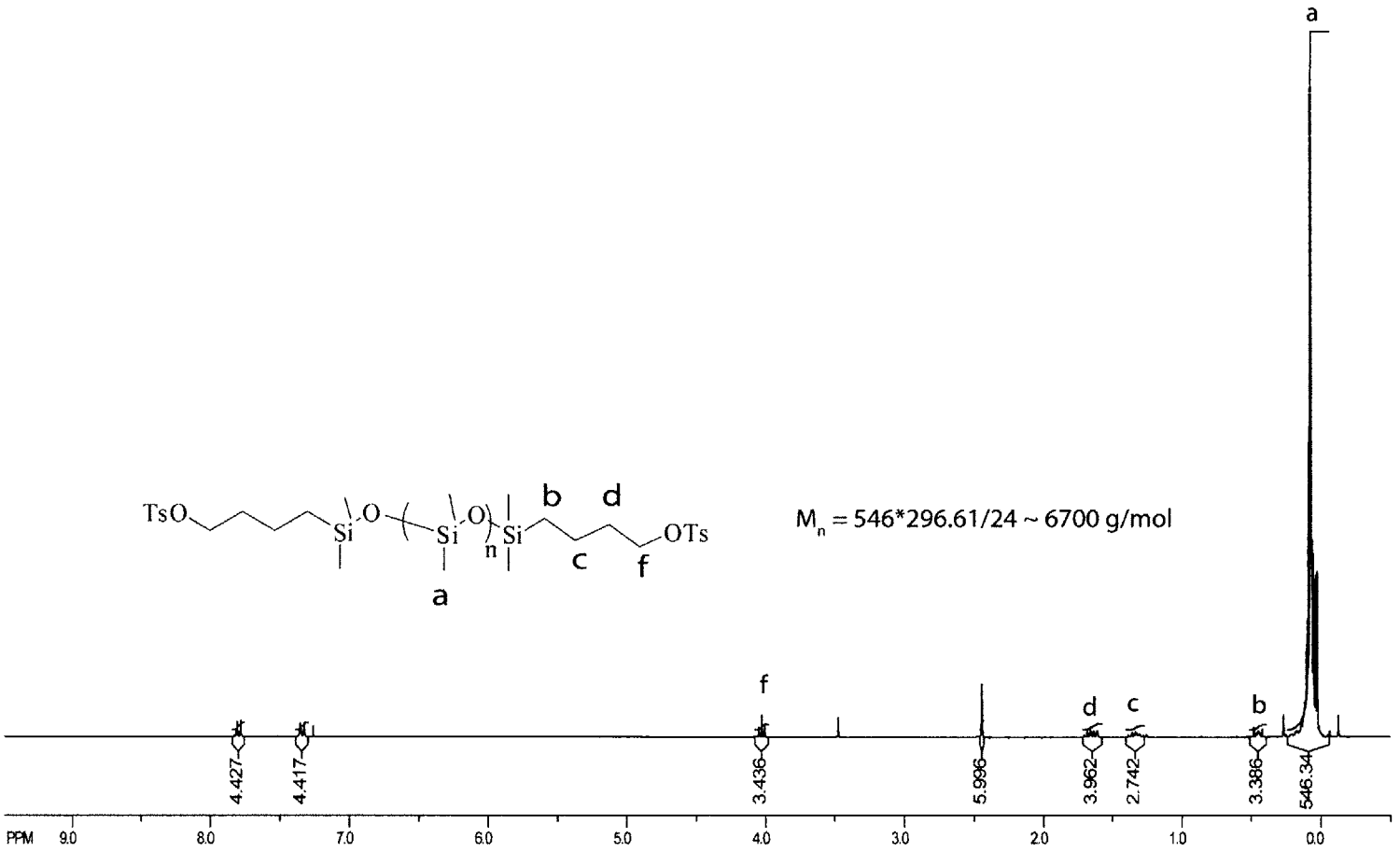

Figure A-4: ^{1}H NMR of bistosylated PDMS macrointiator. The methyl protons of the toluensulfonate protons(e) were used as the integration reference (set to 6). This result corresponds to entry 4 in Table 5.4

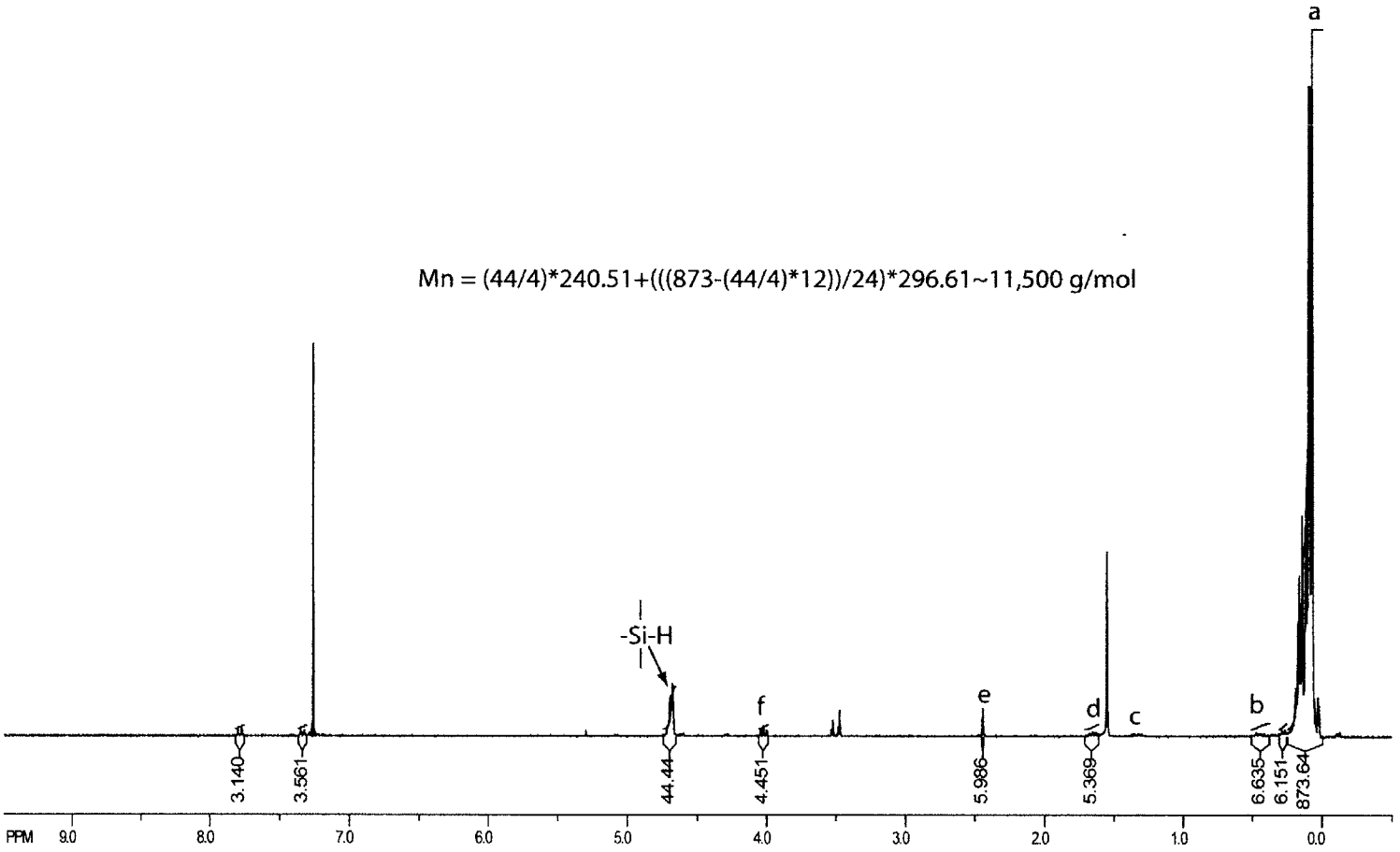

Figure A-5: ^{1}H NMR of bistosylated P(DMS-co-HMS) macrointiator allowing for receptor moiety attachment. The methyl protons of the toluensulfonate protons(e) were used as the integration reference (set to 6). The letter assignments of the peaks are the same as the ones used in figures A-1 and A-2. This result corresponds to entry 1 in Table 5.5. Also shown is the number of Si-H protons reported in Table 5.5.

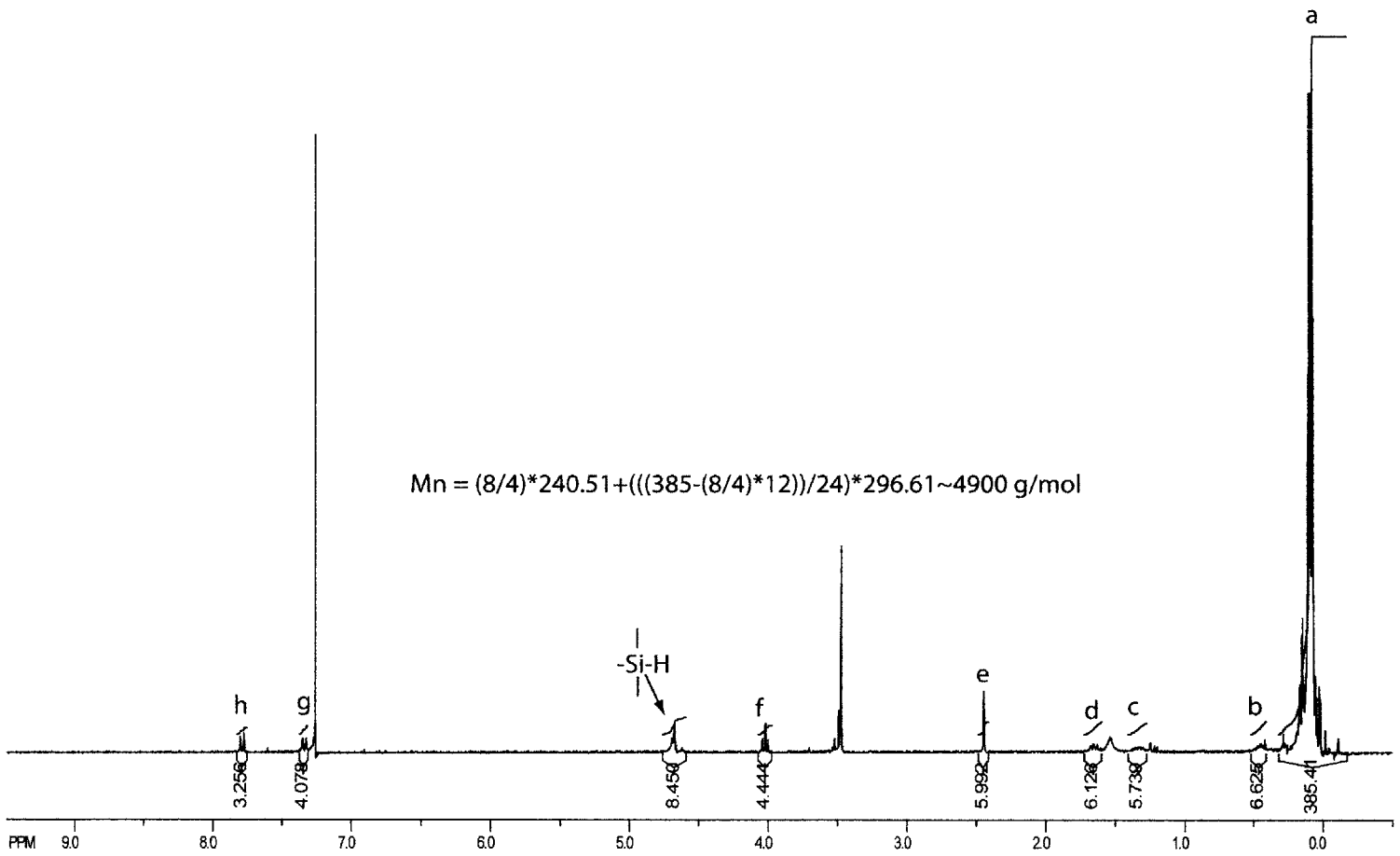

Figure A-6: ^{1}H NMR of bistosylated P(DMS-co-HMS) macrointiator allowing for receptor moiety attachment with 8% Si-H content. The methyl protons of the toluensulfonate protons(e) were used as the integration reference (set to 6). The letter assignments of the peaks are the same as the ones used in figures A-1 and A-2. This result corresponds to entry 2 in Table 5.5. Also shown is the number of Si-H protons reported in Table 5.5.

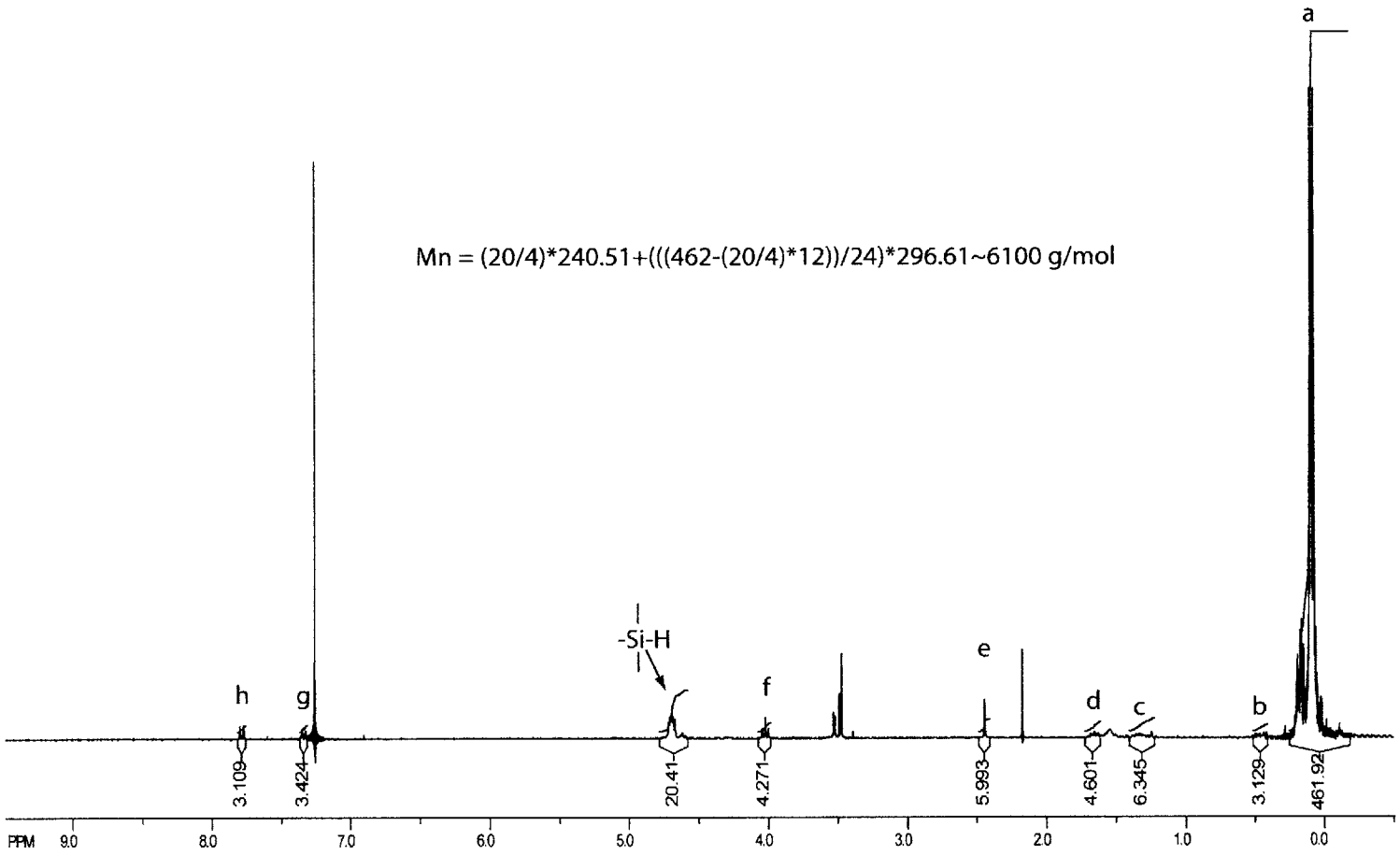

Figure A-7: ^{1}H NMR of bistosylated P(DMS-co-HMS) macrointiator allowing for receptor moiety attachment with 32% Si-H content. The methyl protons of the toluensulfonate protons(e) were used as the integration reference (set to 6). The letter assignments of the peaks are the same as the ones used in figures A-1 and A-2. This result corresponds to entry 3 in Table 5.5. Also shown is the number of Si-H protons reported in Table 5.5.

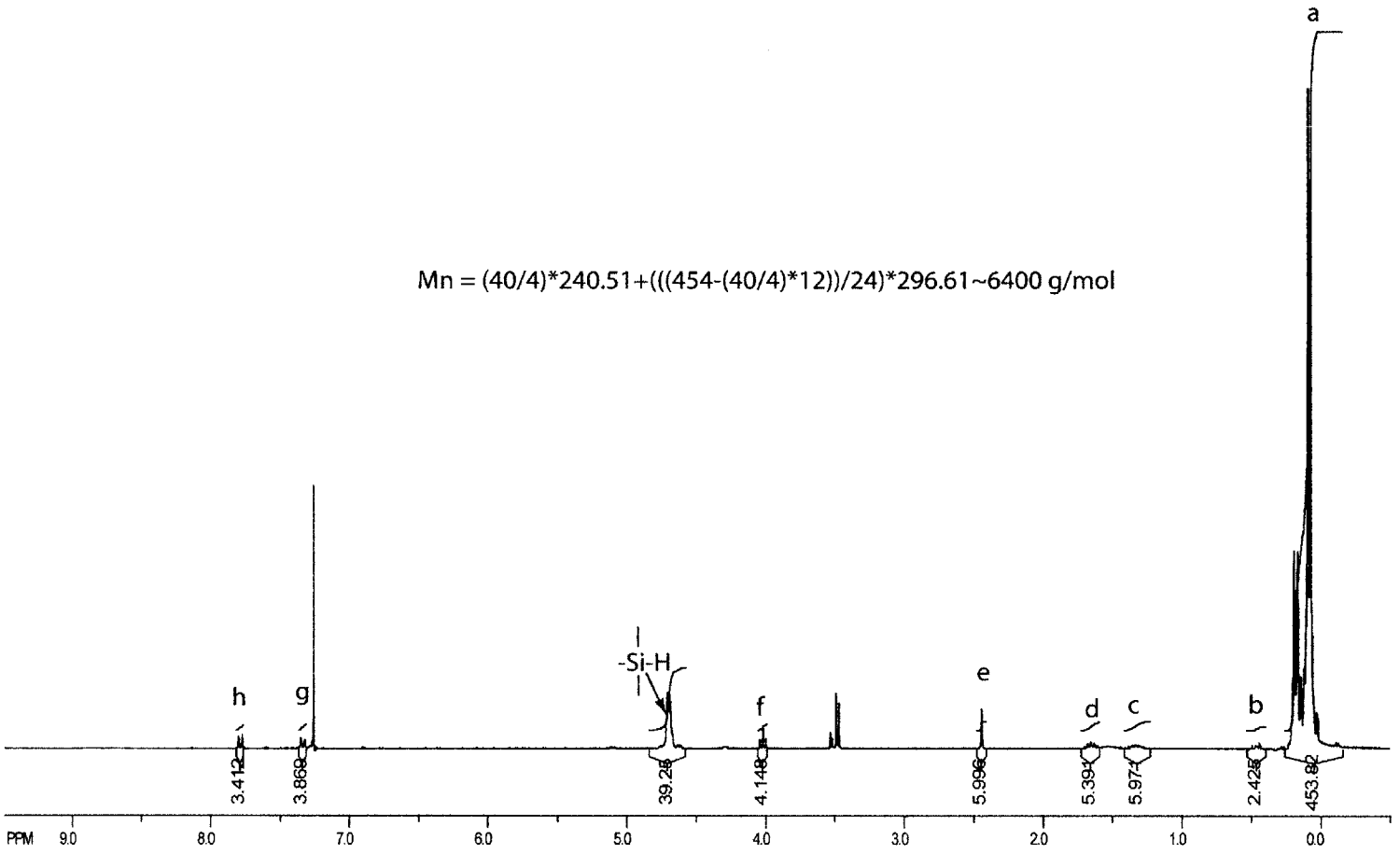

Figure A-8: ^{1}H NMR of bistosylated P(DMS-co-HMS) macrointiator allowing for receptor moiety attachment with 16% Si-H content. The methyl protons of the toluensulfonate protons(e) were used as the integration reference (set to 6). The letter assignments of the peaks are the same as the ones used in figures A-1 and A-2. This result corresponds to entry 4 in Table 5.5. Also shown is the number of Si-H protons reported in Table 5.5.

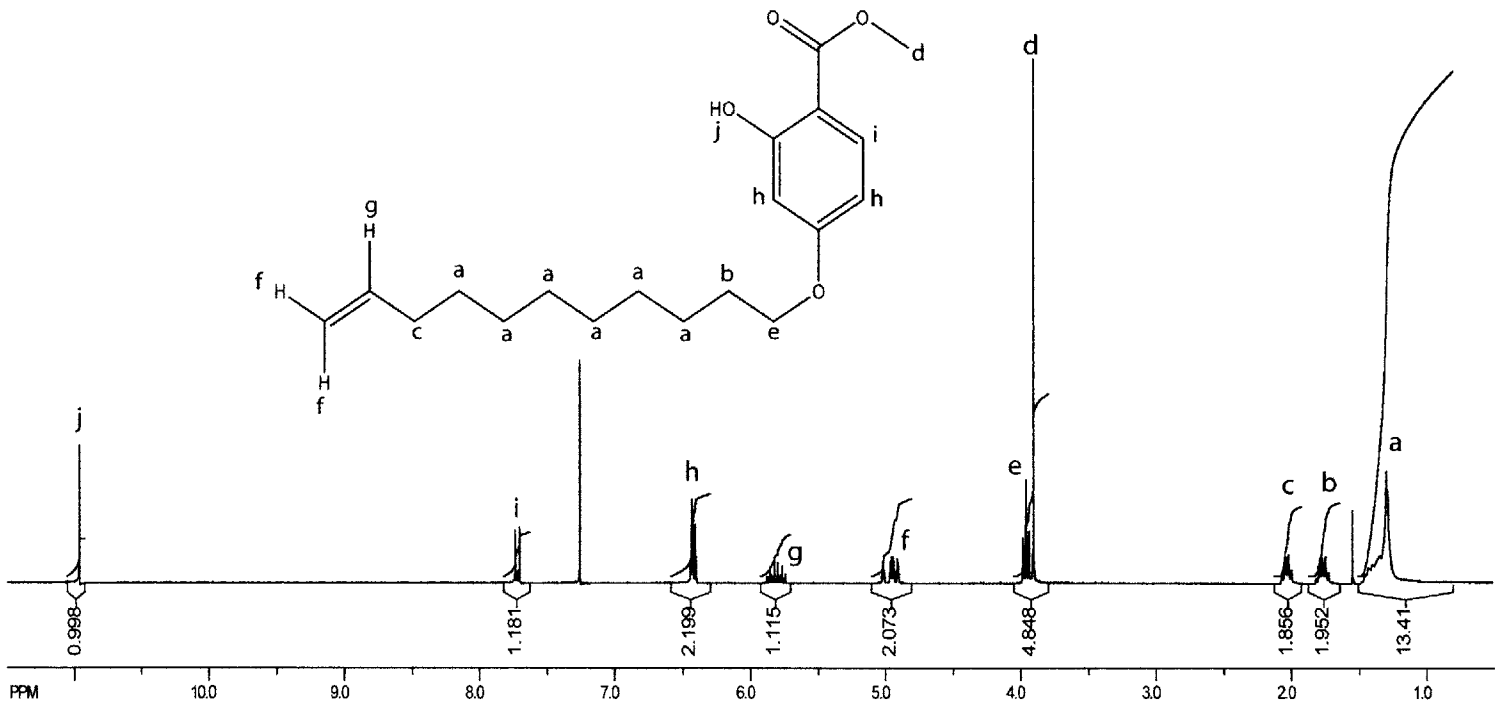

Figure A-9: ^{1}H NMR of methyl-(2-hydroxy-4-undecenyloxy) benzoate

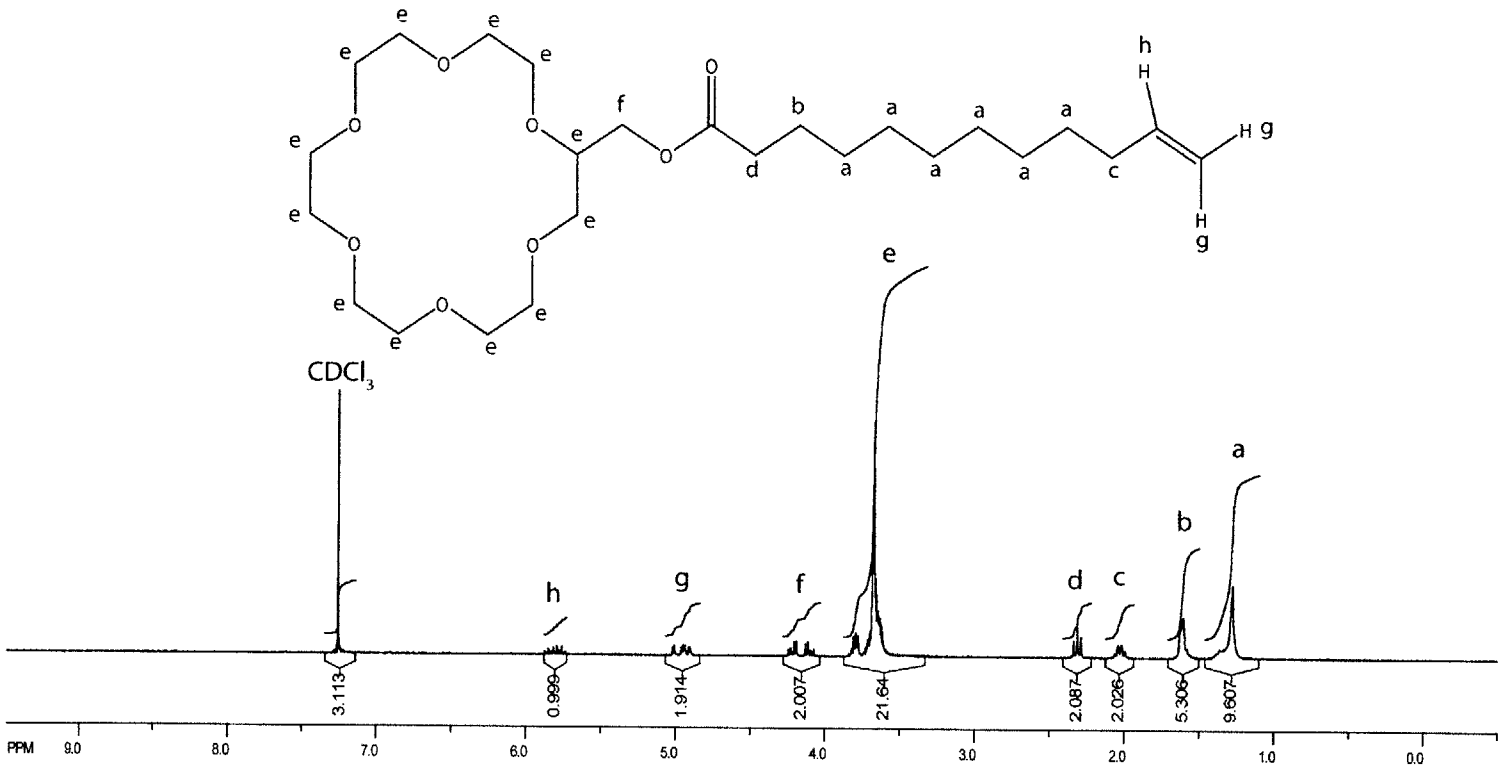

Figure A-10: ^{1}H NMR of (undec-10-enoyloxy)methyl 18-crown-6

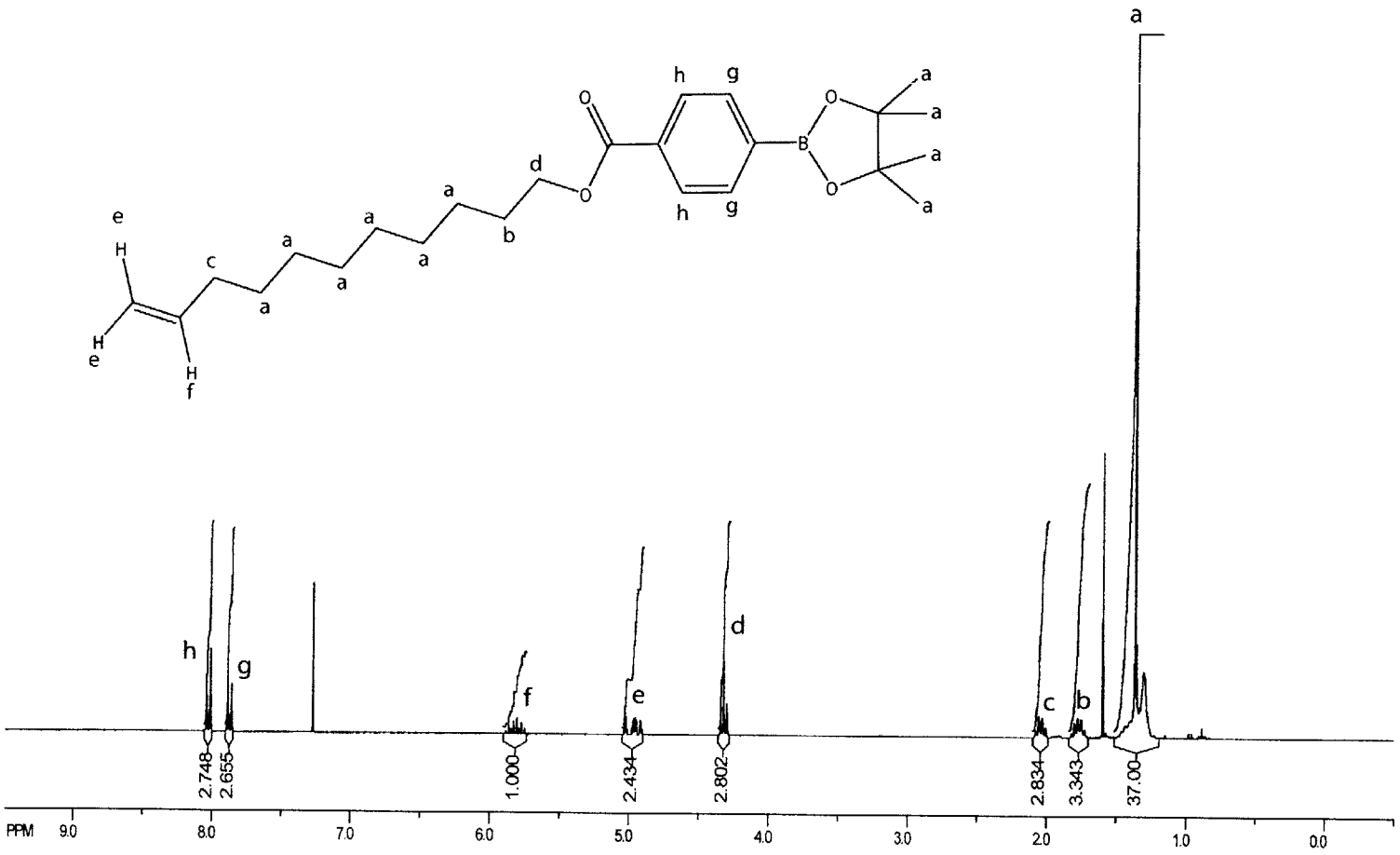

Figure A-11: ^{1}H NMR of undec-10-enyl 4-(4,4,5,5-tetramethyl-1,3,2-dioxaborolan-2-yl)benzoate

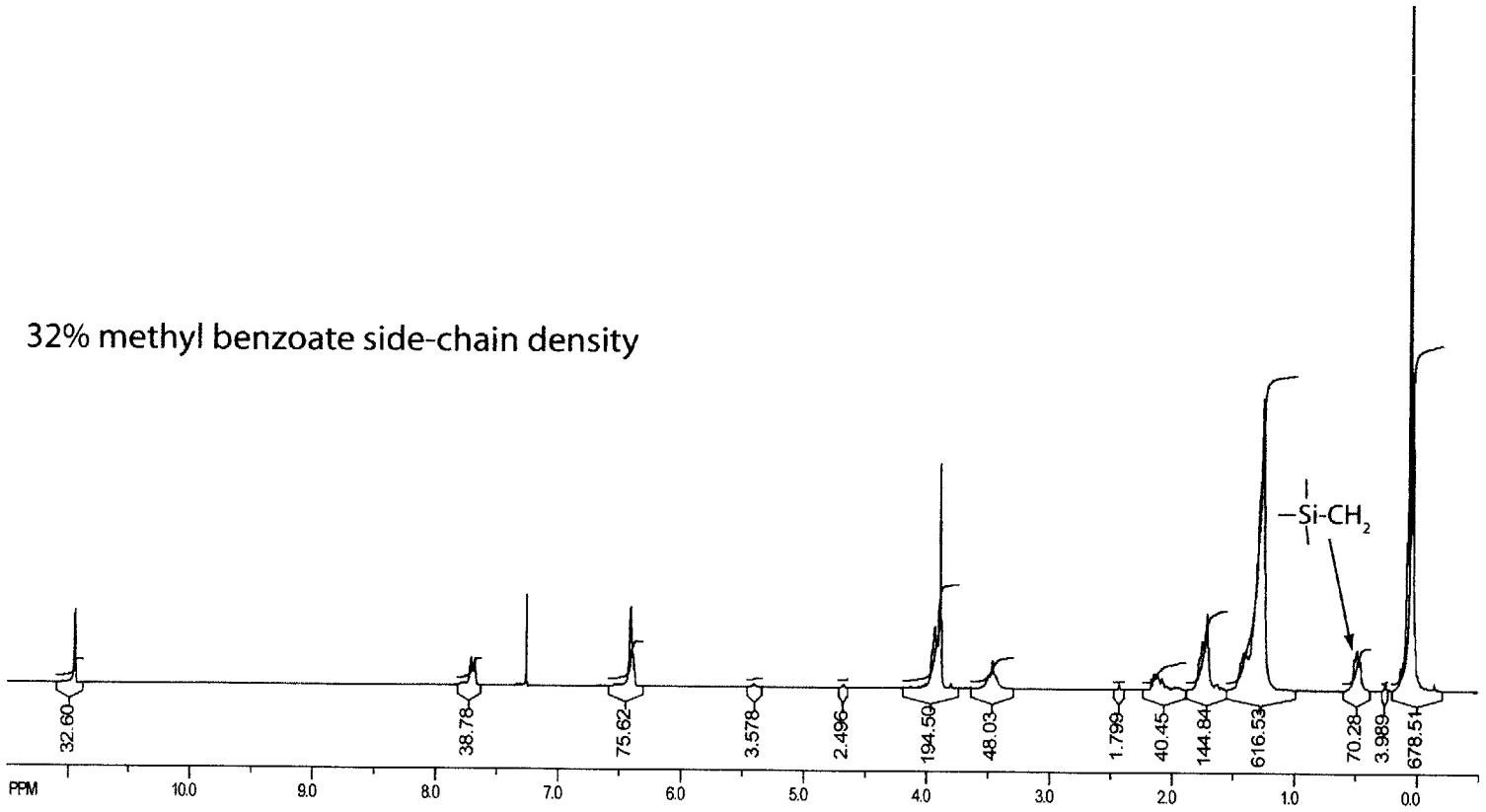

Figure A-12: ^{1}H NMR indicating the successful hydrosilylation of methyl-(2-hydroxy-4-undecenyloxy) benzoate with P(DMS-co-HMS) evidenced by the disappearance of the vinyl protons and appearance of the Si-CH_2 protons as indicated in the figure. The copolymer used in this case corresponds to entry 1 in table 5.5 and whose ^{1}H NMR is shown in figure A-5.

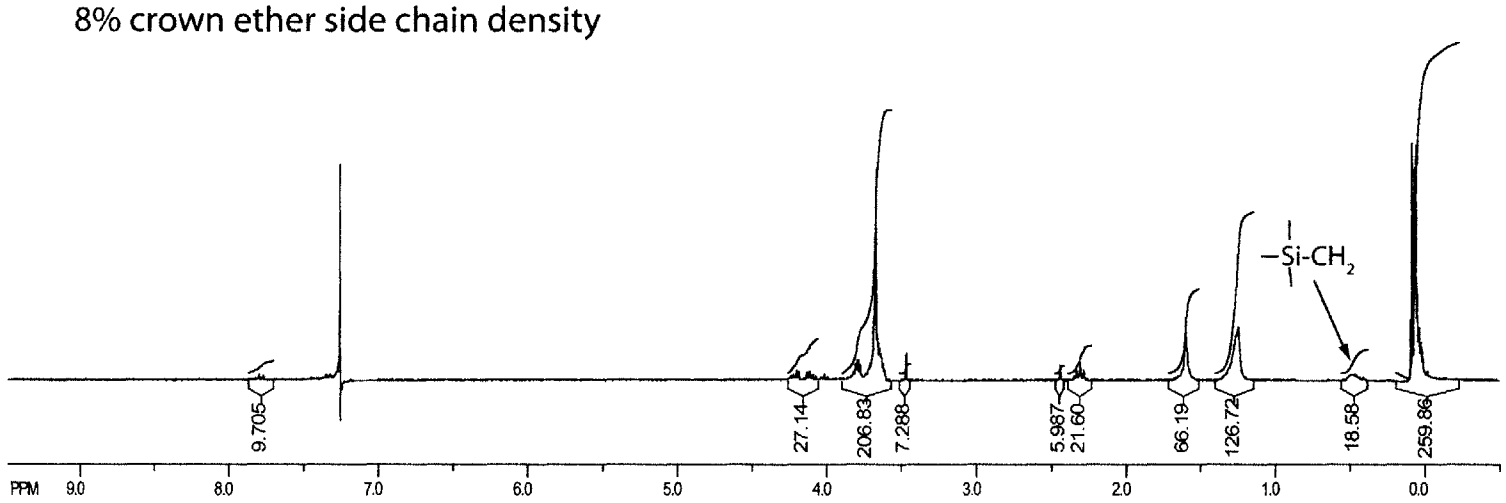

Figure A-13: ^{1}H NMR indicating the successful hydrosilylation of (undec-10-enoyloxy)methyl 18-crown-6 with P(DMS-co-HMS) having 8% Si-H content. The sucess of the hydrosilylation can be evidenced by the disappearance of the vinyl protons and appearance of the Si-CH_2 protons as indicated in the figure. The copolymer used in this case corresponds to entry 2 in table 5.5 and whose ^{1}H NMR is shown in figure A-6

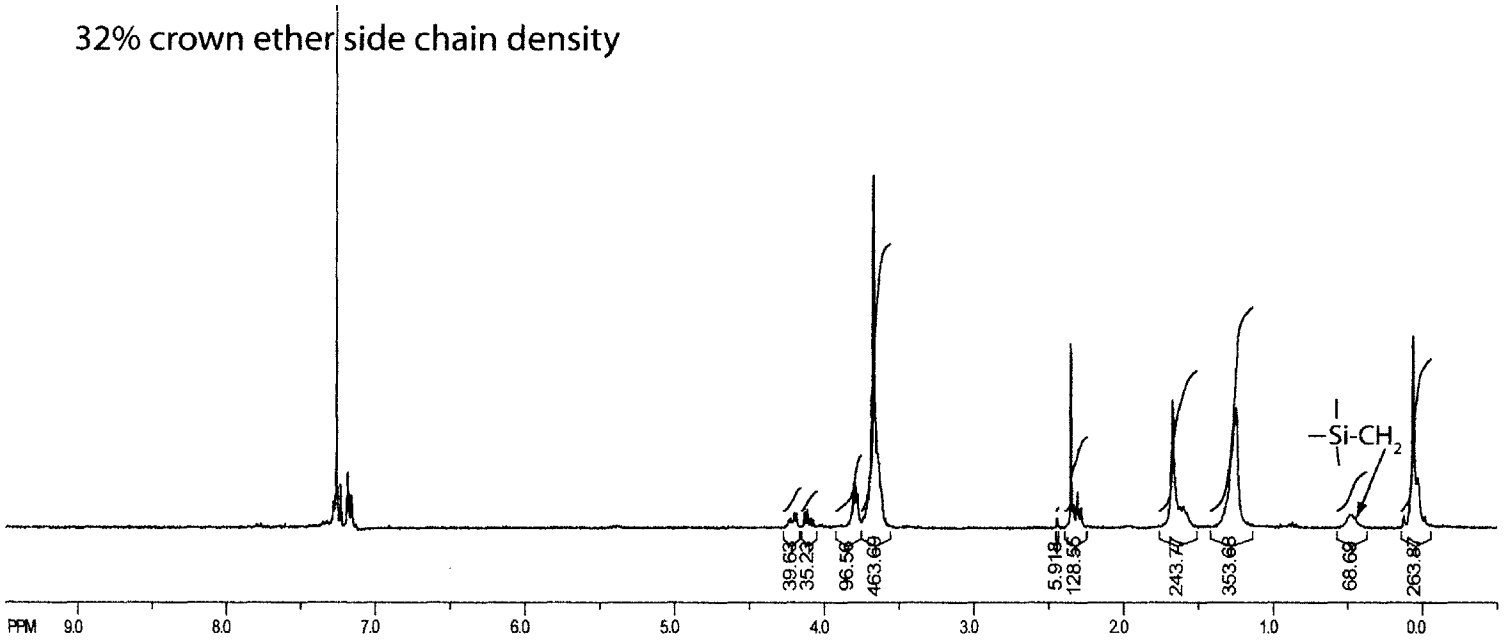

Figure A-14: ^{1}H NMR indicating the successful hydrosilylation of (undec-10-enoyloxy)methyl 18-crown-6 with P(DMS-co-HMS) having 32% Si-H content. The sucess of the hydrosilylation can be evidenced by the disappearance of the vinyl protons and appearance of the Si-CH_2 protons as indicated in the figure. The copolymer used in this case corresponds to entry 4 in table 5.5 and whose ^{1}H NMR is shown in figure A-8

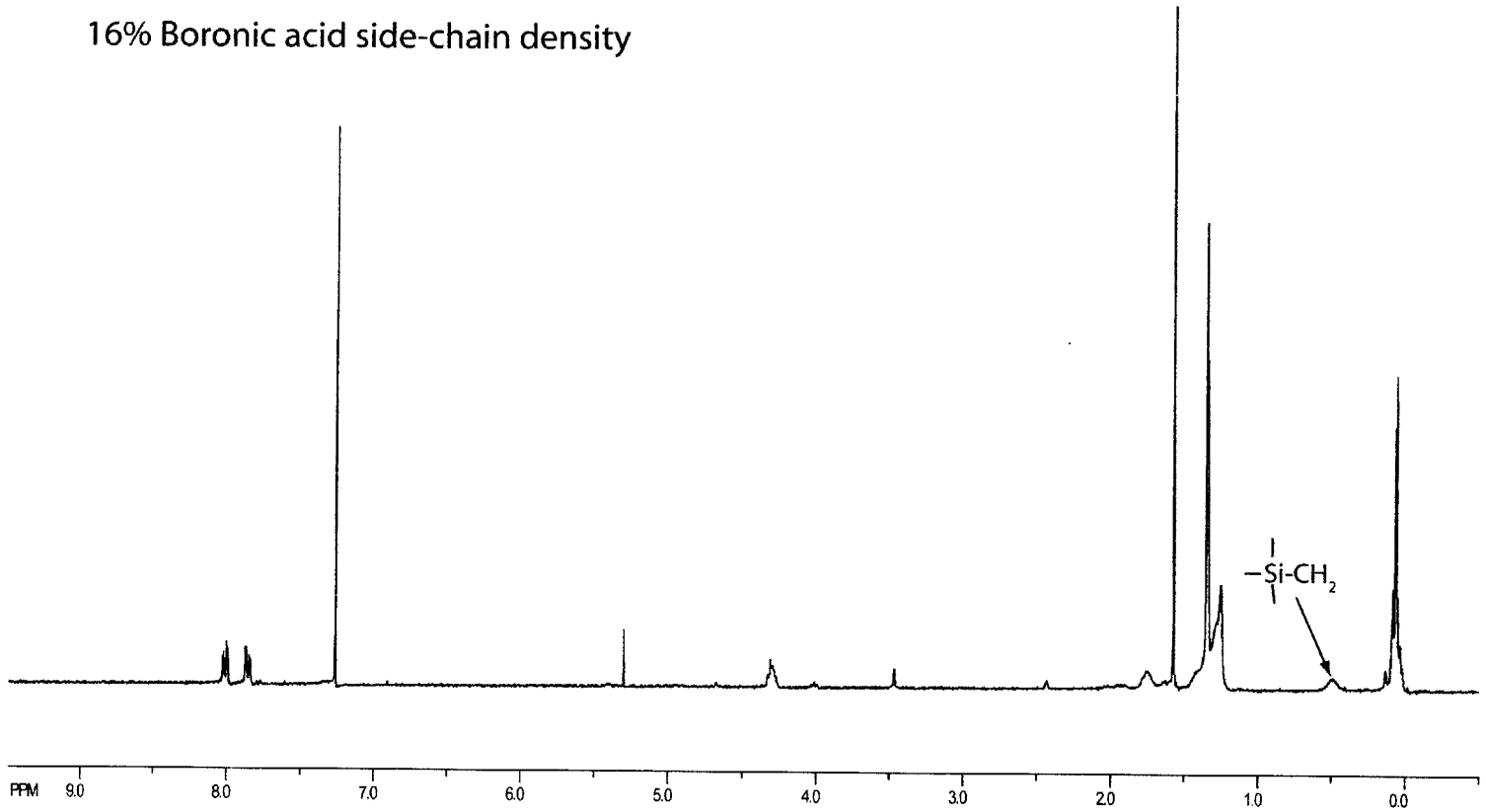

Figure A-15: ^{1}H NMR indicating the successful hydrosilylation of undec-10-enyl 4-(4,4,5,5-tetramethyl-1,3,2-dioxaborolan-2-yl)benzoate with P(DMS-co-HMS) having 16% Si-H content. The sucess of the hydrosilylation can be evidenced by the disappearance of the vinyl protons and appearance of the Si-CH_2 protons as indicated in the figure. The copolymer used in this case corresponds to entry 3 in table 5.5 and whose ^{1}H NMR is shown in figure A-7

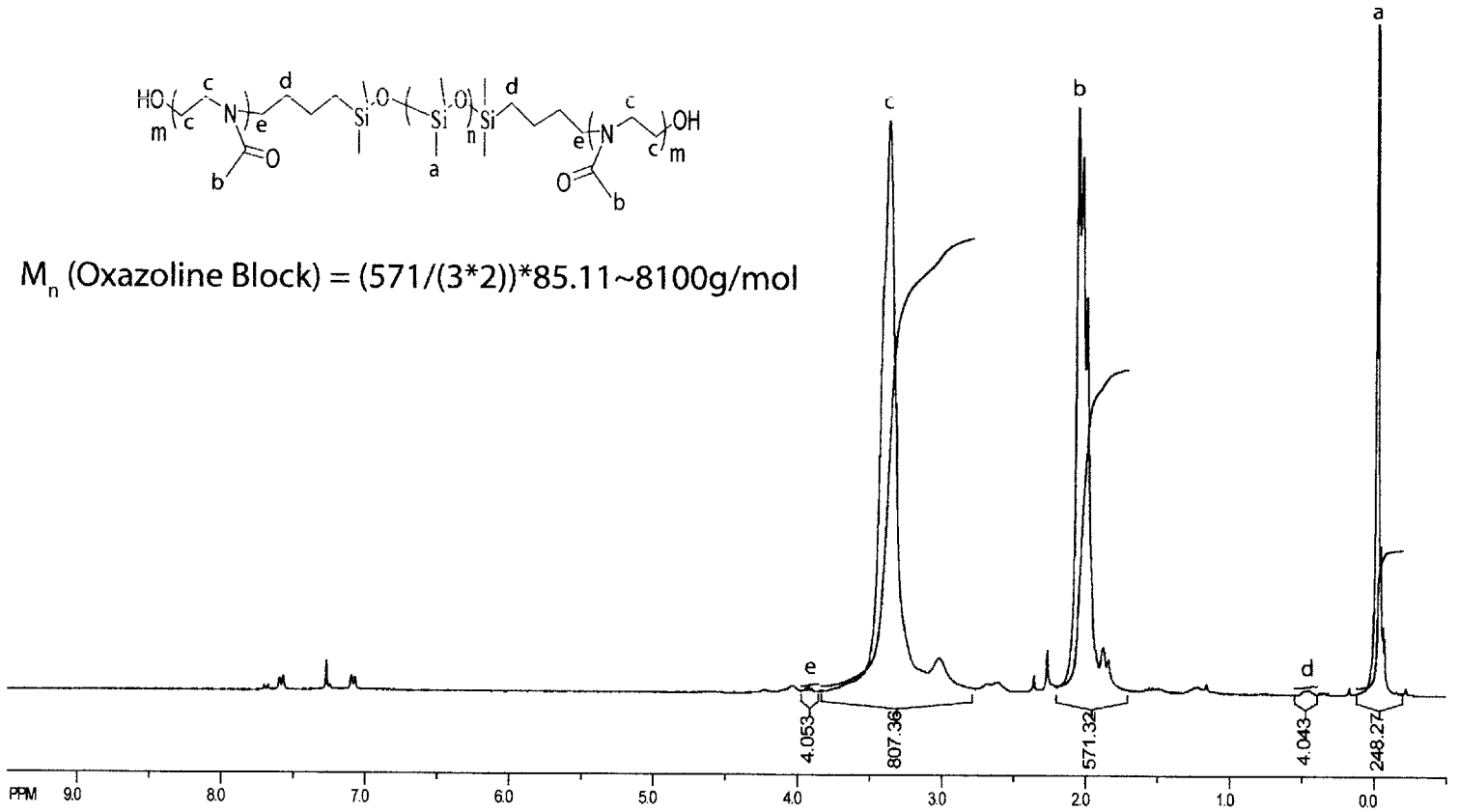

Figure A-16: ^{1}H NMR of the Triblock copolymer PMOXA-PDMS-PMOXA. The molecular weight determination was based the refernce peak d indicated in the figure and corresponds to entry 1 in table 5.6. Using the Si-CH_3 protons as a reference lead to large errors since it did not correspond to experimentally used weights,volumes of monomer,intiator e.t.c. and hence was not used. The PDMS telechelic corresponds to entry 4 in table 5.4 and whose ^{1}H NMR is shown in figure A-4

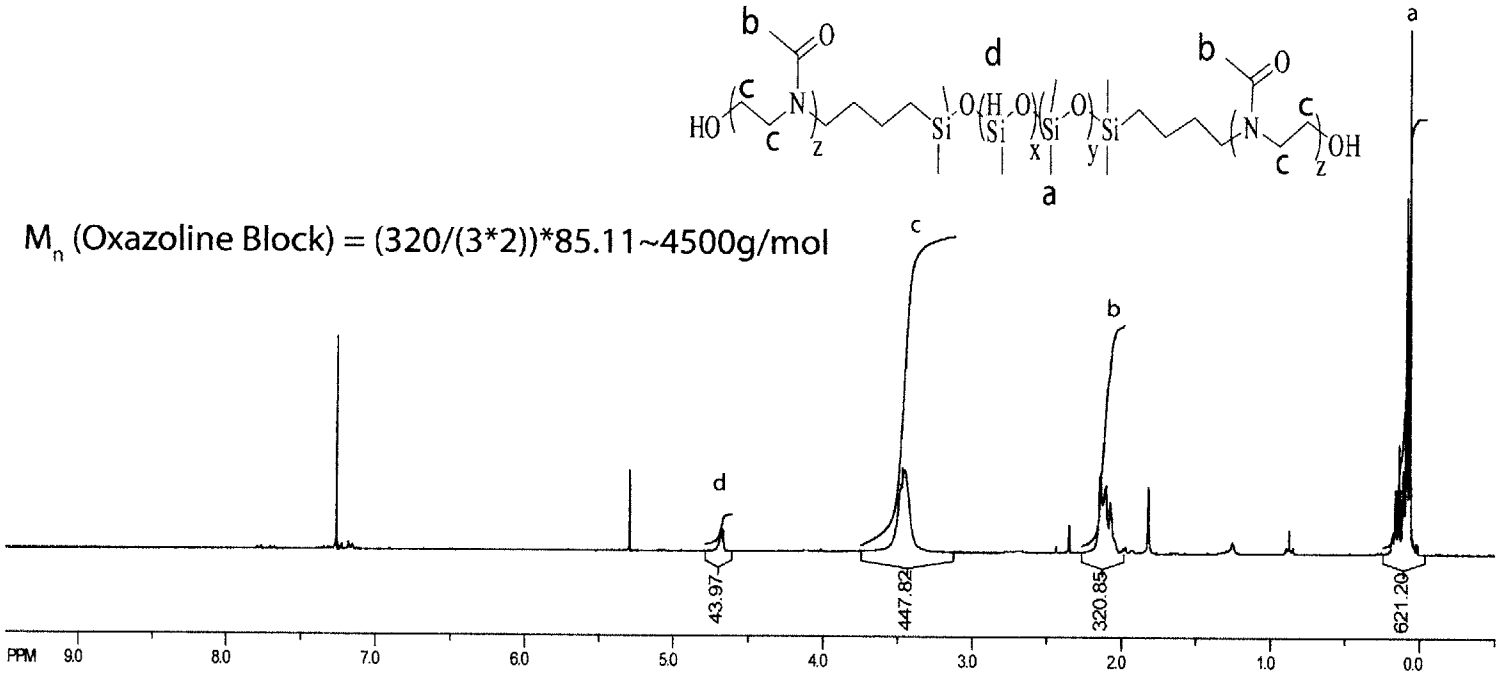

Figure A-17: ^{1}H NMR of the Triblock copolymer that has Si-H moieties in the backbone and corresponds to entry 2 in table 5.6. This triblock was synthesized using the copolymer telechelic entry 1 in table 5.5. The reference used was the value of the Si-H protons from figure A-5

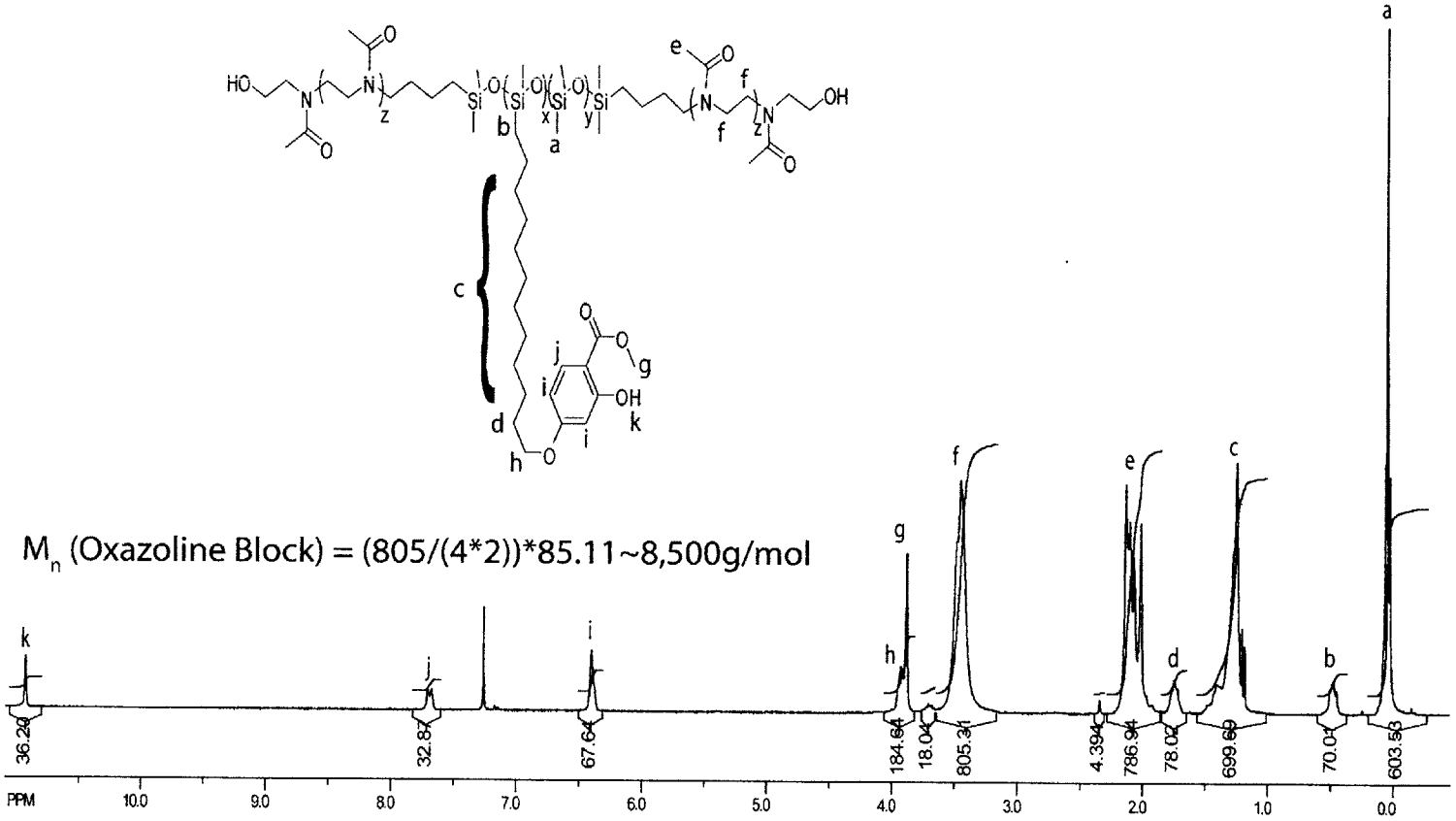

Figure A-18: ^{1}H NMR of the Triblock copolymer that has methyl-(2-hydroxy-4-undecenyloxy) benzoate moieties in the backbone and corresponds to entry 3 in table 5.6. This triblock was synthesized using the derivatized copolymer telechelic shown in figure A-12. The reference used was the value of the Si-CH_2 protons from figure A-12

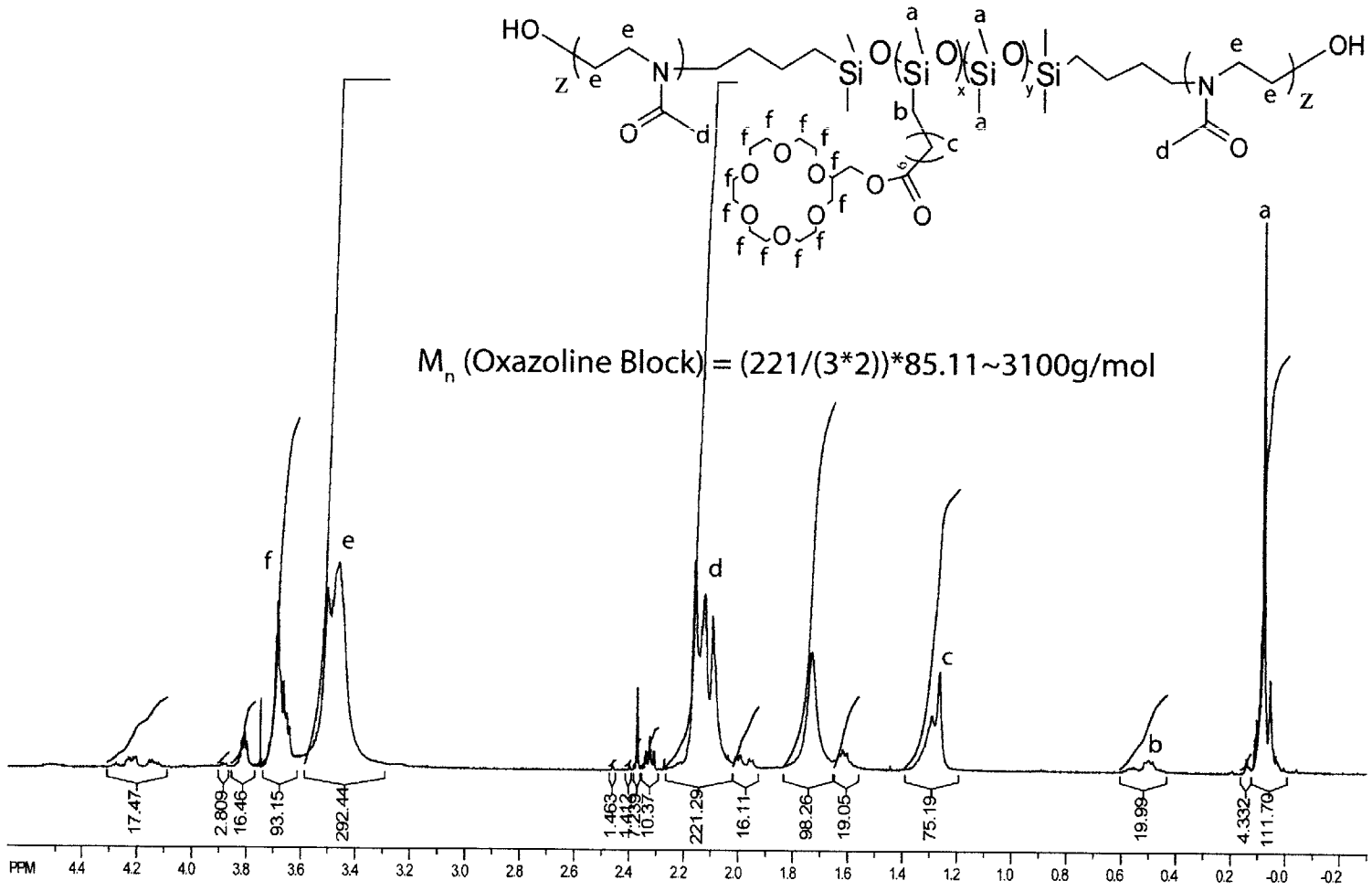

Figure A-19: ^{1}H NMR of the Triblock copolymer that has 8% (undec-10-enoyloxy)methyl 18-crown-6 moieties in the backbone and corresponds to entry 4 in table 5.6. This triblock was synthesized using the derivatized copolymer telechelic shown in figure A-13. The reference used was the value of the Si-CH_2 protons from figure A-13

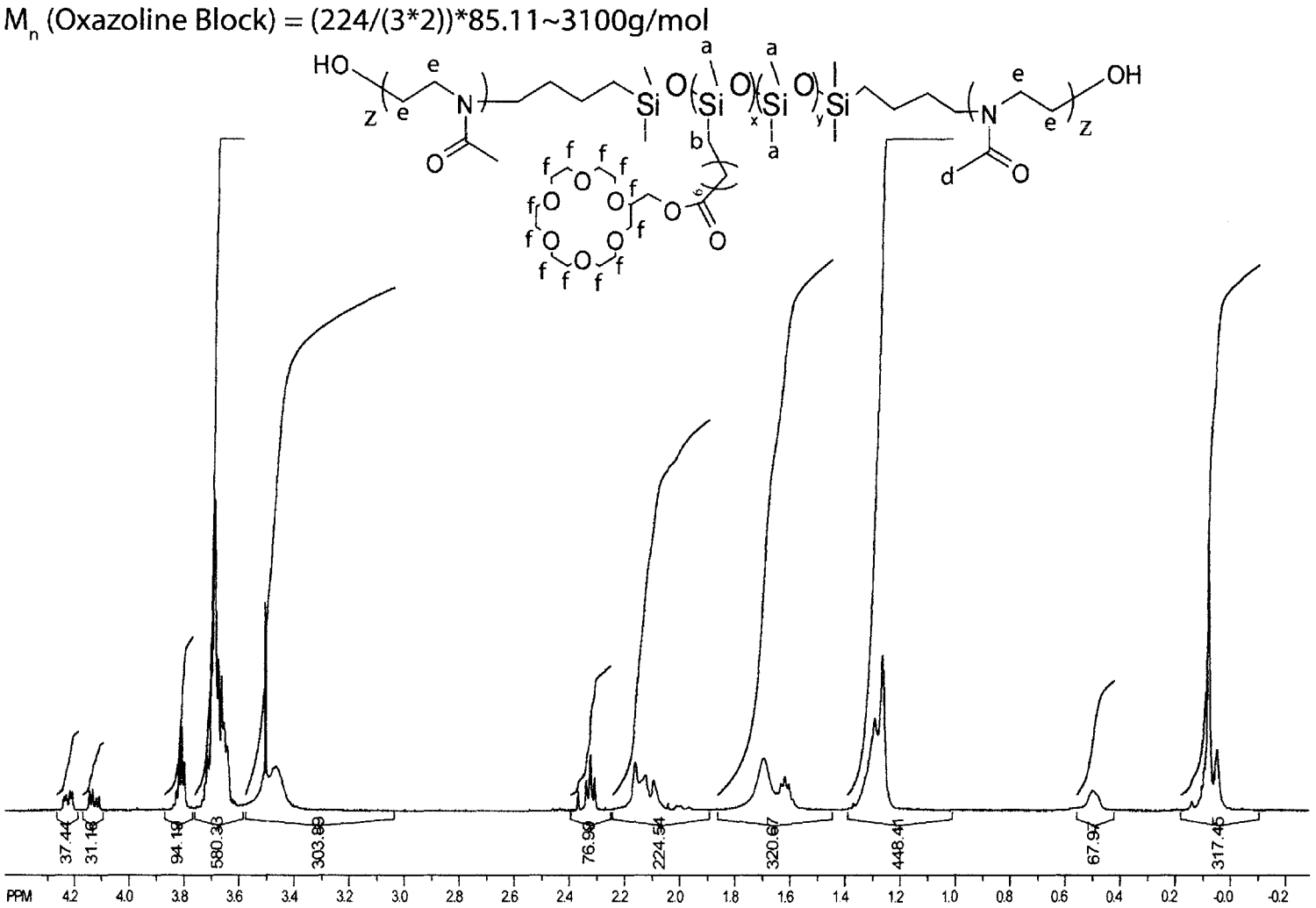

Figure A-20: ^{1}H NMR of the Triblock copolymer that has 32% (undec-10-enoyloxy)methyl 18-crown-6 moieties in the backbone and corresponds to entry 5 in table 5.6. This triblock was synthesized using the derivatized copolymer telechelic shown in figure A-14. The reference used was the value of the Si-CH_2 protons from figure A-14

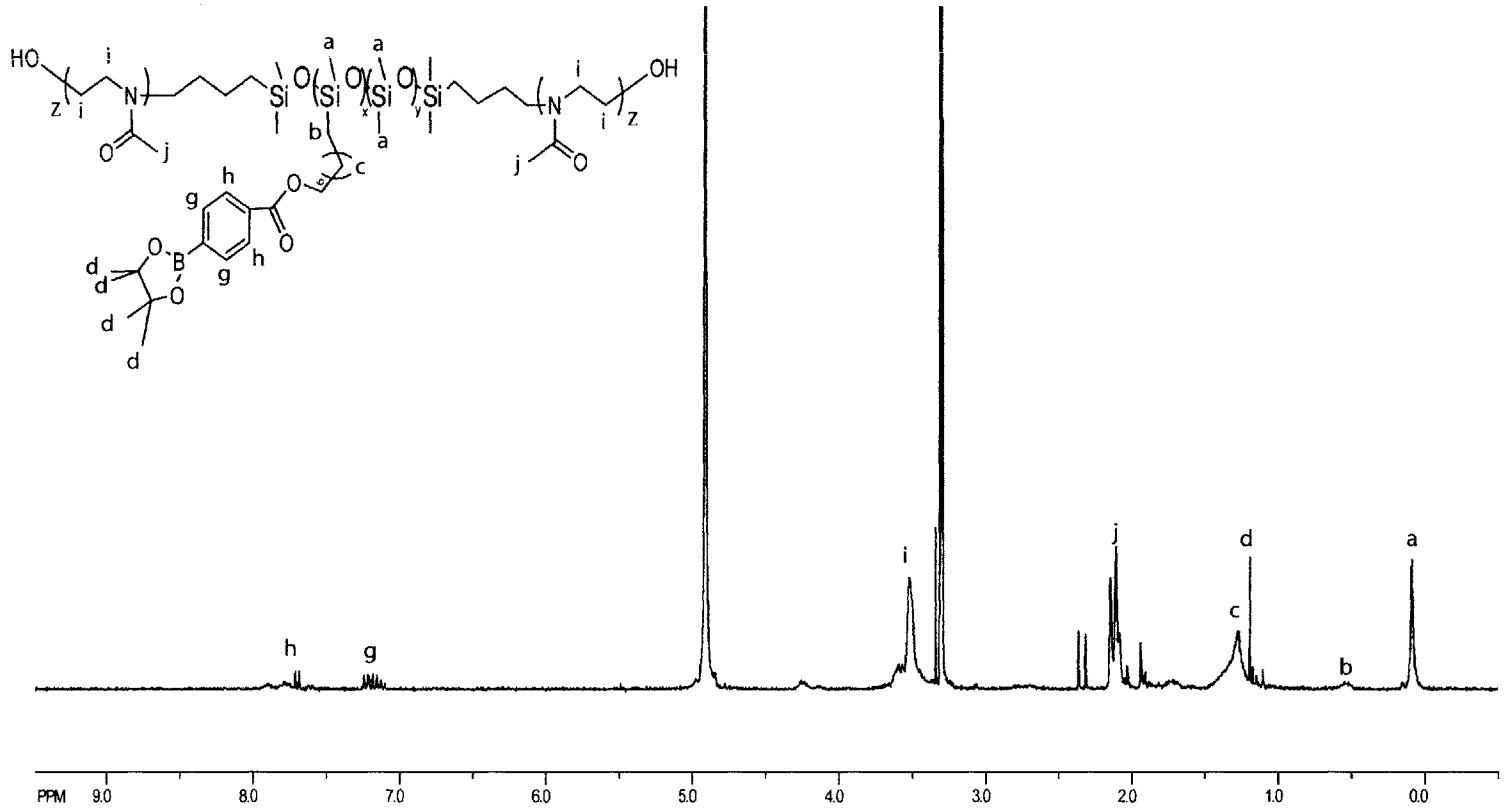

Figure A-21: ^{1}H NMR of the Triblock copolymer that has 16% undec-10-enyl 4-(4,4,5,5-tetramethyl-1,3,2-dioxaborolan-2-yl)-benzoate in the backbone. This polymer does not show the desired physical behavior as discussed in section 5.4.2

Bibliography

[1] C. Alvarez-Lorenzo, Hiratani, K. H., Tanaka, K. Stancil, A. Y. Grosberg, and T Tanaka. Simultaneous multiple-point adsorption of aluminum ions and charged molecules by a polyampholyte thermosensitive gel: Controlling frustrations in a heteropolymer gel. *Langmuir*, 17:3616–3622, 2001.

[2] M. Angelova. *Liposome Electroformation*, pages 27–36. Giant Vesicles,Pier Luigi Luisi (Editor), Peter Walde (Editor). John Wiley and Sons, 1999.

[3] R. D Astumian. Thermodynamics and kinetics of a brownian motor. *Science*, 276:917–922, 1997.

[4] D. Atwell, B. Barbour, and M. Szatkowski. Nonvesicular release of neurotransmitter. *Neuron*, 11:401–407, September 1993.

[5] G. Belorey and G. Sauvet. *Organosiloxane block and graft copolymers*, pages 43–78. Silicon Containing Polymers:The Science and Technology of Their Synthesis and Applications. Kluwer Academic Publishers, 2000.

[6] S. M. Benito. *Functionalized Polymer Nanocontainers for Targeted Drug Delivery*. PhD thesis, University of Basel, 2006.

[7] R. Bischoff and P. Sigwalt. Polycondensation of tetramethyldisiloxane 1,3- diol catalyzed by trifluoromethanesulfonic acid. *Polymer International*, 36:57–71, 1995.

[8] R. Bischoff and P. Sigwalt. Mechanism of octamethylcyclotetrasiloxane polymerization in the presence of siloxanediols. *Polymer International*, 40:99– 109, 1996.

[9] R. Bischoff and P. Sigwalt. Mechanism of hexamethylcyclotrisiloxane polymerization in the presence of siloxanediols. *Polymer International*, 48:217–227, 1999.

[10] M.P. Blaustein and J.M. Goldring. Membrane potential in pinched-off presynaptic nerve terminals monitored with fluorescent probe: evidence that synaptosomes have potassium diffusion potentials. *Journal of Physiology*, 247:589–615, 1975.

[11] S. Brahim, D. Narinesingh, and A. Guiseppi-Elie. Bio-smart hydrogels: co-joined molecular recognition and signal transduction in biosensor fabrication and drug delivery. *Biosensors and Bioelectronics*, 17:973–981, 2002.

[12] S. Brahim, D. Narinesingh, and A. Guiseppi-Elie. Synthesis and hydration properties of pH-sensitive p-(hema)-based hydrogels containing 3-(trimethylsilyl)propyl methacrylate. *Biomacromolecules*, 4:497–503, 2003.

[13] A. Bringmann, S. N.Skatchkov, T. Pannicke, B. Biedermann, H. Wolburg, Ri. K. Orkand, and A. Reichenbach. Müller glial cells in anuran retina. *Microscopy Research and Technique*, 50:384393, 2000.

[14] M.A. Buese. Equilibrium cyclic compositions in the preparation of α,ω-functionalized poly (dimethylsiloxanes). *Macromolecules*, 20:696–698, 1987.

[15] P. Cancouet, E. Daudet, G. Helary, M. Moreau, and G. Sauvet. Functional polysiloxanes. I. Microstructure of poly(hydrogenmethylsiloxane-co-dimethylsiloxane)s obtained by cationic copolymerization. *Journal of Polymer Science: Part A: Polymer Chemistry*, 38:826836, 2000.

[16] S. D. Caras, D. Petelenz, and J. Janata. pH- based enzyme potentiometric sensor. part 2. glucose-sensitive field effect transistor. *Analytical Chemistry*, 57:1920–1923, 1985.

[17] R.G. Carvajal, J. Ramiriez-Angulo, and J. Martinez-Heredia. High-speed high-precision min/max circuits in cmos technology. *IEEE Trans. on Circuits and Systems II: Analog and Digital Signal Processing*, 36(8):697–699, April 2000.

[18] B.A. Chappell, T.I. Chappell, S.E. Schuster, H.M. Segmuller, J.W. Allan, R.L. Franch, and P.J. Restle. Fast cmos ecl receivers with 100mV worst-case sensitivity. *IEEE Journal of Solid State Circuits*, 23(1):59–67, February 1988.

[19] Y. Choi, L.A. Baker, H. Hillebrenner, and C. R Martin. Biosensing with conically shaped nanopores and nanotubes. *Phys. Chem. Chem. Phys*, 8:4976–4988, 2006.

[20] J. Chojnowski and M. Crpryk. *Synthesis of Linear Polysiloxanes*, pages 1–41. Silicon Containing Polymers:The Science and Technology of Their Synthesis and Applications. Kluwer Academic Publishers, 2000.

[21] J. Chojnowski, M. Cypryk, and K. Kazmierski. Cationic polymerization of a model cyclotrisiloxane with mixed siloxane units initiated by a protic acid. mechanism of polymer chain formation. *Macromolecules*, 35:9904–9912, 2002.

[22] J. Chojnowski and M. Scibiorek. Cationic polymerization of siloxanes kinetically controlled oligomerization in hexamethylcyclotrisiloxane - linear dimethylsiloxane systems. *Makromol. Chem*, 177:1413–1431, 1976.

[23] E. K. Chow, E. Pierstorff, G. Cheng, Y-C. Tai, and D. Ho. Attenuation of cellular inflammation using glucocorticoid-functionalized copolymers. *IEEE International Conference on Nano/Micro Engineered and Molecular Systems*, pages 1039–1043, 2007.

[24] D. J. Cram. The design of molecular hosts, guests, and their complexes. *Nobel Lectures: Chemistry*, pages 419–437, 1987.

[25] E.L. Cussler, R. Aris, and A. Bhown. On the limits of facilitated diffusion. *Journal of Membrane Science*, 43:149–164, 1989.

[26] E.L. Cussler, D. Fennell Evans, and Sister M.A. Matesich. Theoretical and experimental basis for a specific counter-transport system in membranes. *Science*, 172(3981):177–179, 1971.

[27] W. J. Dally and J. W. Poulton. *Digital Systems Engineering.* Cambridge University Press, New York, U.S.A, 1998.

[28] J. Deisenhofer and H. Michel. The photosynthetic reaction center from the purple bacteria *Rhodopseudomonas viridis. Science*, 245(4925):1463–1473, November 1989.

[29] T. Delbrck and C.A.Mead. Analog vlsi phototransduction by continuous-time, adaptive, logarithmic photoreceptor circuits. *Vision Chips: Implementing vision algorithms with analog VLSI circuits, C. Koch and H. Li editors, IEEE Computer Society Press*, pages 139–161, 1995.

[30] T. Delbruck and A. van Schaik. Bias current generators with wide dynamic range. *Proceedings of the 2004 International Symposium on Circuits and Systems, 2004.*, 1(I):337–340, May 2004.

[31] S.C. DeMarco, Wentai Liu, P.R. Singh, G. Lazzi, M.S. Humayun, and J.D Weiland. An arbitrary waveform stimulus circuit for visual prostheses using a low-area multibias dac. *IEEE Journal of Solid State Circuits*, 38(10):1679–1690, October 2003.

[32] K. Dill and S. Bromberg. *Molecular Driving Forces: Statistical Thermodynamics in Chemistry and Biology.* Garland Science, New York, 2002.

[33] J. E. Dowling. *The Retina: An Approachable Part of the Brain.* Belknap Press, Cambridge, MA, 1987.

[34] W.A. Drohan, L. Theogarajan, S.K. Kelly, J.L. Wyatt, B.M. Yomtov, and J.F. Rizzo. Development of retinal implant driver software for the retinal implant project. *The Association for Research in Vision and Ophthalmology (ARVO)*, page Poster 3168, May 2006.

[35] P. R. Dvornic. *Thermal Properties of Polysiloxanes*, pages 185–212. Silicon Containing Polymers:The Science and Technology of Their Synthesis and Applications. Kluwer Academic Publishers, 2000.

[36] N. W. Eduardo, W. M. Grill, and D. Durand. Modeling the effects of electric fields on nerve fibers: determination of excitation thresholds. *IEEE Trans. On Biomedical Engineering*, 39(12):1244–1254, December 1992.

[37] M. Einzmann and W. H. Binder. Novel functional initiators for oxazoline polymerization. *Journal of Polymer Science: Part A: Polymer Chemistry*, 39:28212831, 2001.

[38] G. Eisenmann, G. Szabb, S.G.A McLaughlin, and S.M. Ciani. Molecular basis for the action of macrocyclic carriers on passive ionic translocation across lipid bilayer membranes. *Bioenergetics*, 4:93–148, 1973.

[39] D. B. Fenske, K. F. Wong, E. Maurer, N. Maurer, J. M. Leenhouts, N. Boman, L. Amankwa, and P. R. Cullis. Ionophore-mediated uptake of ciprooxacin and vincristine into large unilamellar vesicles exhibiting transmembrane ion gradients. *Biochimica et Biophysica Acta*, 1414:188–204, 1998.

[40] H. Fishman, M. Peterman, T. Leng, and textitet al. The artificial synapse chip: a novel interface for a retinal prosthesis based on neurotransmitter stimulation and nerve regeneration. *Invest. Ophthalmol.*, 43:114, 2002.

[41] P. J. Flory. Fundamental principles of condensation polymerization. *Chemical Reviews*, 39:137–197, 1943.

[42] P. J. Flory and J. A. Semlyen. Macrocyclization equilibrium constants and the statistical configuration of poly(dimethylsiloxane) chains. *Journal of the American Chemical Society*, 88(14):3209–3212, 1966.

[43] L. A. Fredrick, T. F. Fyles, N. P. Guruprasad, and D. M. Whitefield. Membrane transport system. i. synthesis and characterization of carriers for a proton driven alkali metal cation pump. *Canadian Journal of Chemistry*, 59:1724–1733, 1981.

[44] T. M. Fyles, V. A. Malik-Diemer, C. A. McGavin, and D. M. Whitfield. Membrane transport systems. iii. a mechanistic study of cation-proton coupled countertransport. *Canadian Journal of Chemistry*, 60:2259–2267, 1981.

[45] T.M. Fyles, V.A. Malik-Diemer, and D. M. Whitfield. Membrane transport systems. ii. transport of alkali metal ions against their concentration gradients. *Canadian Journal of Chemistry*, 59:1734–1744, 1981.

[46] G.W. Gokel, W.M. Leevy, and M.E. Weber. *Model Systems for Biological Processes*, pages 253–265. Macrocyclic Chemistry Current Trends and Future Perspectives Gloe, Karsten (Ed.). Springer Netherlands, 2005.

[47] A. Graff, M. Sauer, P. van Gelder, and W. Meier. Virus-assisted loading of polymer nanocontainer. *PNAS*, 99(8):5064–5068, 2002.

[48] P.R. Gray, P.J. Hurst, S.H. Lewis, and R.G. Meyer. *Analysis and Design of Analog Integrated Circuits, 4th ed.* John Wiley & Sons, Inc., New York, U.S.A, 2001.

[49] P.D. Hale, L.I. Boguslavsky, T. Inagaki, H. I. Karan, H.S. Lee, T. A. Skotheim, and Y. Okamoto. Amperometric glucose biosensor based on redox polymer-mediated electron transfer. *Analytical Chemistry*, 63:677–682, 1991.

[50] C. H. Harrell, Z. S. Siwy, and C. R Martin. Conical nanopore membranes: Controlling the nanopore shape. *Small*, 2(2):194–198, 2006.

[51] T. Hayashita, J. H. Lee, S. Chen, and R. A. Bartsch. Selective column concentration of alkali-metal cations with a crown ether carboxylic acid resin. *Analytical Chemistry*, 63:1844–1847, 1991.

[52] W. Helfrich. *Bending Elasticity of Fluid Membranes*, pages 51–70. Giant Vesicles,Pier Luigi Luisi (Editor), Peter Walde (Editor). John Wiley and Sons, 1999.

[53] C. A. Helm, J. N. Israelachvili, and P. M. McGuiggan. Role of hydrophobic forces in bilayer adhesion and fusion. *Biochemistry*, 31:1794–1805, 1992.

[54] M. A. Hempenius, R. G. H. Lammertink, and G. J. Vancso. Side-chain liquid-crystalline polysiloxanes via anionic polymerization: (n-undecyloxy)arenecarboxylic acid mesogens linked to poly(dimethylsiloxane-co-methylvinylsiloxane). *Macromolecules*, 30:266–272, 1997.

[55] D. Ho, B. Chu, H. Lee, and C.D. Montemagno. Protein-driven energy transduction across polymeric biomembranes. *Nanotechnology*, 15:1084–1094, 2004.

[56] A. F. Hodgkin and A. L. Huxley. The components of membrane conductance in the giant axon of *Loligo*. *Journal of Physiology*, 116:473–496, 1952.

[57] A. F. Hodgkin and A. L. Huxley. Currents carried by sodium and potassium ions through the membrane of the giant axon of *Loligo*. *Journal of Physiology*, 116:449–472, 1952.

[58] A. F. Hodgkin and A. L. Huxley. The dual effect of membrane potential on the sodium conductance in the giant axon of *Loligo*. *Journal of Physiology*, 116:497–506, 1952.

[59] A. F. Hodgkin and A. L. Huxley. A quantitative description of membrane current and its application to conduction and excitation in nerve. *Journal of Physiology*, 117:500–544, 1952.

[60] P. J. Hore. *Nuclear Magnetic Resonance*. Oxford University Press, Bath, UK, 1995.

[61] D. H. Hubel and T. N. Wiesel. Ferrier lecture: Functional architecture of macaque monkey visual cortex. *Proceedings of the Royal Society of London. Series B, Biological Sciences*, 198(1130):1–59, May 1977.

[62] R. Iezzi, M. Safadi, J. Miller, J. II McAllister, G. Auner, and G.W. Abrams. Feasibility of retinal and cortical prosthesis based upon spatiotemporally controlled release of l-glutamate. *Invest. Ophthalmol.*, 42:S491, 2001.

[63] R. M. Izatt, G.C. Lindh, G. A. Clark, Y. Nakatsuji, J.S. Bradshaw, J. D. Lamb, and J. J. Christensen. Proton ionizable crown compounds: 5. macrocycle-mediated proton coupled transport of alkali metal cations in h_2o-ch_2cl_2-h_2o liquid membrane systems. *Journal of Membrane Science*, 31:1–13, 1987.

[64] H. Jacobson and W. H. Stockmayer. Intramolecular reaction in polycondensations. i. the theory of linear systems. *The Journal of Chemical Physics*, 18(12):1600–1606, December 1950.

[65] R. J. Jensen. Potassium-evoked directionally selective resposes from rabbit retinal ganglion cells. *Visual Neuroscience*, 13:705–719, 1996.

[66] D. A. Johns and K. Martin. *Analog Circuit Design.* John Wiley & Sons, Inc., New York, 1997.

[67] D-Y. Jung, J. J. Magda, and I. S. Han. Catalase effects on glucose-sensitive hydrogels. *Macromolecules*, 33:3332–3336, 200.

[68] Y. Kaneko, S. Nakamura, K. Sakai, T. Aoyagi, A. Kikuchi, Y. Sakurai, and Y Okano. Rapid deswelling response of poly(n-isopropylacrylamide) hydrogels by the formation of water release channels using poly(ethylene oxide) graft chains. *Macromolecules*, 31:6099–6105, 1998.

[69] S. W. Kantor, W. T. Grubb, and R. C. Osthoff. The mechanism of the acid and base catalyzed equilibration of siloxanes. *Journal of the American Chemical Society*, 76:5190–5197, 1954.

[70] C. J. Karwoski, H-K. Lu, and E. A. Newman. Spatial buffering of light-evoked potassium increases by retinal Müller(glial) cells. *Science*, 244(4904):578–580, May 1989.

[71] H. Kazama, Y. Tezuka, and K. Imai. Syntheses and reactions of uniform size poly(dimethylsiloxane) with various reactive end groups. *Polymer*, 19(9):1091–1100, 1987.

[72] S.K. Kelly, M. Markova, L. Theogarajan, W.A. Drohan, G.W. Swider, B. Yomtov, J.L. Wyatt, and J.F. Rizzo. Development of a telemetry system for the boston retinal implant. *The Association for Research in Vision and Ophthalmology (ARVO)*, page Poster 3167, May 2006.

[73] S. J. Kim, C. K. Lee, and S. I Kim. Electrical/pH responsive properties of poly(2-acrylamido-2-methylpropane sulfonic acid)/hyaluronic acid hydrogels. *Int. Journal of Applied Polymer Science*, 92:1731–1736, 2004.

[74] A. J. Kirby. *Stereoelectronic Effects.* Oxford University Press, Great Britain, UK, 1996.

[75] K. Kita-Tokarczyk, J. Grumelard, T. Haefele, and W. Meier. Block copolymer vesicles-using concepts from polymer chemistry to mimic biomembranes. *Polymer*, 46:3540–3563, 2005.

[76] H-A. Klok, P. Eibeck, M. Moller, and D. N. Reinhoudt. Synthesis and characterization of polysiloxane-bound receptor molecules for ion-selective supported membranes. *Macromolecules*, 30:795–802, 1997.

[77] S. Kobayashi and H. Uyama. Polymerization of cyclic imino ethers: From its discovery to the present state of the art. *Journal of Polymer Science: Part A: Polymer Chemistry*, 40:192209, 2002.

[78] J. Lebrun, G. Sauvet, and P. Sigwalt. Polymerization of octamethylcyclotetrasiloxane initiated by a superacid. *Makromol. Chem. Rapid Commun.*, 3:757–763, 1982.

[79] M. Lee, W. Dally, and P. Chiang. Low power area-efficient high speed i/o circuit techniques. *IEEE Journal of Solid-State Circuits*, 35(11):1591–1599, November 2000.

[80] R. Lipowsky. The conformation of membranes. *Nature*, 349:475–481, February 1991.

[81] W. Liu, K. Vichienchom, M. Clements, S.C. DeMarco, C. Hughes, E. McGucken, M.S. Humayun, E. De Juan, J.D. Weiland, and R. Greenberg. Neuro-stimulus chip with telemetry unit for retinal prosthetic device. *IEEE Journal of Solid-State Circuits*, 35(10):1487–1497, October 2000.

[82] R. S. Macomber. *A Complete Introduction to Modern NMR Spectroscopy.* John Wiley and Sons, New York, 1998.

[83] J. G. Maneatis. Low-jitter process-independent DLL and PLL based on self-biased techniques. *IEEE Journal of Solid-State Circuits*, 31(11):1723–1732, November 1996.

[84] D.R. McNeal. Analysis of a model of a model for excitation of mylineated nerve. *IEEE Trans. On Biomedical Engineering*, 23:329–337, April 1976.

[85] C. Mead. *Analog VLSI and Neural Systems.* Addison Wesley, Reading, MA, 1989.

[86] W. Meier, C. Nardin, and M. Winterhalter. Reconstitution of channel proteins in (polymerized channel proteins in (polymerized) aba triblock copolymer membranes. *Angew. Chem. Int. Ed.*, 39(24):4599–4602, 2000.

[87] D. Meyuhas, A. Bor, I. Pinchuk, A. Kaplun, Y. Talmon, M. M. Kozlov, and D. Lichtenberg. Effect of ionic strength on the self-assembly in mixtures of phosphatidylcholine and sodium cholate. *Journal of Colloid and Interface Science*, 188:351–362, 1997.

[88] D. Mijuskovic, M. Bayer, T. Chomicz, N. Garg, F. James, P. McEntarfer, and J.D. Porter. Cell-based fully integrated cmos frequency synthesizers. *IEEE Journal of Solid-State Circuits*, 29(3):271–279, March 1994.

[89] P. Mitchell. Chemiosmotic coupling in oxidative and photosynthetic phosphorylation. *Biol. Rev.Camb. Phil. Soc*, 41(1):445–502, 1966.

[90] R. Nagarajan. Molecular packing parameter and surfactant self-assembly: The neglected role of the surfactant tail. *Langmuir*, 18:31–38, 2002.

[91] A. Napoli, D. Sebok, A. Senti, and W. Meier. *Block Copolymer Vesicles*, pages 39–71. Block Copolymers in Nanoscience, Massimo Lazzari, Guojun Liu and Sebastien Lecommandoux (Editors). Wiley-VCH, 2006.

[92] C. Nardin, T. Hirt, J. Leukel, and W. Meier. Polymerized aba triblock copolymer vesicles. *Langmuir*, 16:1035–1041, 2000.

[93] C. Nardin, S. Thoeni, J. Widmer, M. Winterhalter, and W. Meier. Nanoreactors based on polymerized aba triblockcopolymer vesicles. *Chemical Communiations*, pages 1433–1434, 2000.

[94] J. H. Nelson. *Nuclear Magnetic Resonance Spectroscopy.* Prentice Hall, New Jersey, 2003.

[95] E. Newman and A. Reichenbach. The Müller cell: A functional element of the retina. *Trends in Neuroscience*, 19(8):307–312, 1996.

[96] E. A. Newman. Potassium conductance block by barium in amphibian Müller cells. *Brain Research*, 498:308–314, 1989.

[97] P. Nicol, M. Masure, and P. Sigwalt. Cationic polymerization of hexamethylcyclotrisiloxane by trifluoromethanesulfonic acid and its derivatives, 1: Initiation by trifluoromethanesulfonic acid. *Macromol. Chem. Phys.*, 195:2327–2352, 1994.

[98] M. Niwa, T. Sawada, and N. Higashi. Surface monolayers of polymeric amphiphiles carrying a copolymer segment composed of phenylboronic acid and amine. interaction with saccharides at the air-water interface. *Langmuir*, 14:3916–3920, 1998.

[99] J.C. Norrild and H. Egged. Evidence for mono- and bisdentate boronate complexes of glucose in the furanose form. application of jc-cc oupling constants as a structural probe. *Journal of the American Chemical Society*, 117:1479–1484, 1995.

[100] J.C. Norrild and H. Egged. Evidence for mono- and bisdentate boronate complexes of glucose in the furanose form. application of j_{c-c} coupling constants as a structural probe. *Journal of the American Chemical Society*, 117:1479–1484, 1995.

[101] I.E. Opris. Rail-to-rail multiple-input min/max circuit. *Electronics Letters*, 45(1):137–140, January 1998.

[102] M. J. Owen. *Surface Properties and Applications*, pages 213–232. Silicon Containing Polymers:The Science and Technology of Their Synthesis and Applications. Kluwer Academic Publishers, 2000.

[103] J. Y. Park, M. H. Acar, A. Akthakul, W. Kuhlman, and A. M. Mayes. Polysulfone-graft-poly(ethylene glycol) graft copolymers for surface modification of polysulfone membranes. *Biomaterials*, 27:856–865, 2006.

[104] A. Pollack, H. Blumenfeld, M. Wax, R. L. Baughn, and G. M. Whitesides. Enzyme immobilzation by condensation co-polymerization into cross-linked polyacrylamide gels. *Journal of the American Chemical Society*, 102:6324–6336, 1980.

[105] B.C. Pressman, E.J. Harris, W.S. Jagger, and J.H. Johnson. Antibiotic mediated transport of alkali ions across lipid barriers. *Proceedings of the National*

Academy of Sciences of the United States of America, 58(5):1949–1956, November 1967.

[106] J. B. Ranck. Which elements are excited in electrical stimulation of mammalian central nervous system: A review. *Brain Research*, 98:417–440, 1975.

[107] F. Rattay. The basic mechanism for the electrical stimulation of the nervous system. *Neuroscience*, 89(2):335–346, 1999.

[108] F. Rattay, S. Resatz, P. Lutter, K. Minassian, B. Jilge, and M. R. Dimitrijevic. Mechanisms of electrical stimulation with neural prostheses. *Neuromodulation*, 6(1):42–56, 2003.

[109] F. G. Riddell. Structure, conformation, and mechanism in membrane transport of alkali metal ions by ionophoric antibiotics. *Chirality*, 14:121–125, 2002.

[110] F. G. Riddell, S. Ammugam, P. J. Brophy, B. G. Cox, M. C. H. Payne, and T. E. Southonts. The nigericin-mediated transport of sodium and potassium ions through phospholipid bilayers studied by ^{23}Na and ^{39}K nmr spectroscopy. *Journal of The American Chemical Society*, 110:734–738, 1988.

[111] J.A. Riggs and B.D. Smith. Facilitated transport of small carbohydrates through plasticized cellulose triacetate membranes. evidence for fixed-site jumping transport mechanism. *Journal of the American Chemical Society*, 119:2765–2766, 1997.

[112] J.F. Rizzo and J. L. Wyatt. Prospects for a visual prosthesis. *Neuroscientist*, 3(4):251–262, July 1997.

[113] R.W. Rodieck. *The First Steps in Seeing*. Sinauer associates Inc., Sunderland, MA, 1998.

[114] A. K. Roy and R. B. Taylor. The first alkene-platinum-silyl complexes: Lifting the hydrosilylation mechanism shroud with long-lived precatalytic intermediates and true pt catalysts. *Journal of the American Chemical Society*, 124:9510–9524, 2002.

[115] M. Rutnakornpituk. *Synthesis Of Silicone Magnetic Fluids For Use In Eye Surgery.* PhD thesis, Virginia Polytechnic Institute and State University, 2002.

[116] E. Sackinger and W. Guggenbuhl. A versatile building block: the cmos differential difference amplifier. *IEEE Journal of Solid-State Circuits*, 22(2):287–294, April 1987.

[117] M. A. Schiefer and W. M. Grill. Sites of neuronal excitation by epiretinal electrical stimulation. *IEEE Trans. On Neural Systems and Rehabilitation engnieering*, 14(1):5–13, March 2006.

[118] E. M. Sentovich, K. J. Singh, L. Lavagno, C. Moon, R. Murgai, A. Saldanha, H. Savoj, P. R. Stephan, R. K. Brayton, and A. Sangiovanni-Vincentelli. SIS: A system for sequential circuit synthesis. Technical report, University of California, Berkeley,CA, 1992.

[119] B. D. Sheperd. Siloxane basicity toward strong acid in nonpolar solution. *Journal of the American Chemical Society*, 113:5581–5583, 1991.

[120] Z. Siwy, E. Heins, C. C. Harrell, P Kohli, and C. R Martin. Conical-nanotube ion-current rectifiers: The role of surface charge. *Journal of the American Chemical Society*, 126(35):10850–10851, 2004.

[121] P. Steffanut, J. A. Osborn, A. DeCian, and J. Fisher. Efficient homogeneous hydrosilylation of olefins by use of complexes of Pt^0 with selected electron deficient olefins as ligands. *Chem. Eur. J.*, 4(10):2008–2017, 1998.

[122] W. Stoeckenius. The purple membrane of salt-loving bacteria. *Scientific American*, 234(6):38–46, 1976.

[123] J. Strzelblcki and R. A. Bartsch. Solvent extraction of alkali metal cations from aqueous solutions by highly lipophilic crown ether carboxylic acids. *Analytical Chemistry*, 53:2251–2253, 1981.

[124] K. De Sudipto, N. R. Aluru, B. Johnson, W. C. Crone, D. J. Beebe, and J Moore. Equilibrium swelling and kinetics of pH-responsive hydrogels: Models, experiments, and simulations. *Journal of Microelectromechanical Systems*, 11(5):544–555, October 2002.

[125] M. Sugawara, M. Omoto, H. Yoshida, and Y. Umezawa. Enhancement of uphill transport by a double carrier membrane system. *Analytical Chemistry*, 60:2301–2303, 1988.

[126] G. Swider, L. Theogarajan, W.A. Drohan, S.K. Kelly, B.M. Yomtov, J.L. Wyatt, and J.F. Rizzo. Testing and qualification of the boston retinal implant chip. *The Association for Research in Vision and Ophthalmology (ARVO)*, page Poster 3187, May 2006.

[127] M. Szatkowski, B. Barbour, and D. Atwell. Non-vesicular release of glutamate from glial cells by reversed electrogenic glutamate uptake. *Nature*, 348(29):443–446, November 1990.

[128] M. Takahashi, B. Billups, D. Rossi, M. Sarantis, M. Hamann, and D. Attwell. The role of glutamate transporters in glutamate homeostasis in the brain. *The Journal of Experimental Biology*, 200:401409, 1997.

[129] T. Tanaka, I. Nishio, S-T. Sun, and S. Ueno-Nishio. Collapse of gels in an electric field. *Science*, 218:467–469, October 1982.

[130] R. H. Templer, B. J. Khoo, and J. M. Seddon. Gaussian curvature modulus of an amphiphilic monolayer. *Langmuir*, 14:7427–7434, 1998.

[131] L. Theogarajan, C. Scholz, S. Desai, R. Jensen, Baldo M., and J.F. Rizzo. Self-assembling amphillic triblock polymer with side-chain mesogens in the hydrophobic core for neural prosthetic devicecs. *Polymer Preprints*, 47(2):145–146, 2006.

[132] G. Toskas, G. Besztercey, M. Moreau, M. Masure, and P. Sigwalt. Cationic polymerization of hexamethylcyclotrisiloxane by trifluoromethanesulfonic acid

and its derivatives, 2: Reaction involving activated trifluoromethylsulfonates. *Macromol. Chem. Phys*, 196:2715–2735, 1995.

[133] D. S. Touretzky, M. V. Albert, N. D. Daw, and A. Ladsariya. Hhsim: Graphical hodgkin-huxley simulator. Technical report, Carnegie Mellon University, Pittsburgh, PA, 2004.

[134] M. Uto, M. Sugawara, H. Yoshida, and Y. Umezawa. Uphill transport membrane systems. *Analytical Chemistry*, 58:1798–1803, 1986.

[135] A. van den Berg, A. Grisel, M. Koudelka, and B. H. Van Der Schoot. A universal on-wafer fabrication technique for diffusion limiting membranes for use in microelectrochemical amperometric sensors. *Sensors and Actuators B*, 5:71–74, 1991.

[136] J. H. van den Hende. Macrocyclic polydimethylsiloxanes. *Journal of the American Chemical Society*, 87(4):931–932, February 1965.

[137] Vera-Adam-Vizi. External ca2+-independent release of neurotransmitters. *Journal of Neurochemistry*, pages 395–405, 1992.

[138] C. Veraart, C. Raftopoulos, J. T. Mortimer, J. Delbeke, D. Pins, G. Michaux, A. Vanlierde, S. Parrini, and M-C. Wanet-Defalque. Visual sensations produced by optic nerve stimulation using an implanted self-sizing spiral cuff electrode. *Brain Research*, 813:181–186, 1998.

[139] Q. Wang, H. Zhang, G. K. Suryaprakash, T. E. Hogen-Esch, and G. A. Olah. Cationic ring-opening polymerization of cyclosiloxanes initiated by electron-deficient organosilicon reagents. *Macromolecules*, 29:6691–6694, 1996.

[140] Thomas Fischer Weiss. *Cellular Biophysics, Volume 1: Transport.* The MIT Press, Cambridge, MA, 1997.

[141] Thomas Fischer Weiss. *Cellular Biophysics, Volume 2: Electrical Properties.* The MIT Press, Cambridge, MA, 1997.

[142] P. R. Westmark, S. J. Gardiner, and B. D. Smith. Selective monosaccharide transport through lipid bilayers using boronic acid carriers. *Journal of the American Chemical Society*, 118:11093–11100, 1996.

[143] P. R. Westmark, S. J. Gardiner, and B. D. Smith. Selective monosaccharide transport through lipid bilayers using boronic acid carriers. *Journal of the American Chemical Society*, 118(45):11093–11100, 1996.

[144] P. R. Westmark and B. D. Smith. Boronic acids selectively facilitate glucose transport through a lipid bilayer. *Journal of the American Chemical Society*, 116(20):9343–9344, 1994.

[145] L. Wilczek and J. Chojnowski. Acidolytic ring opening of cyclic siloxane and acetal monomers. role of hydrogen bonding in cationic polymerization initiated with protonic acids. *Macromolecules*, 14:9–17, 1981.

[146] L. Wilczek, S. Rubinsztajn, and J. Chojnowski. Comparison of the cationic polymerization of octamethylcyclotetrasiloxane and hexamethylcyclotrisiloxane. *Makromol. Chem.*, 181:39–51, 1986.

[147] A. Wong and G. Wu. Solid-state ^{23}Na nuclear magnetic resonance of sodium complexes with crown ethers, cryptands, and naturally occurring antibiotic ionophores: A direct probe to the sodium-binding sites. *J. Phys. Chem. A*, 104:11844–11852, 2000.

[148] I. Yabe, S. Morishita, and K. Toda. Temperature and applied voltage dependency of valinomycin mediated ion trasnport across planar lipid bilayer membrane by voltage jump method. *Journal of Chemical Engineering of Japan*, 23(6):715–67, 1990.

[149] I Yilgor, J Riffle, and J. McGrath. *Reactive Difunctional Siloxane Oligomers: Synthesis and Characterization*, pages 162–174. Reactive Oligomers, Eds. F. W. Harris and H. J. Spinelli, ACS Symposium Series, No. 282, Washington, D. C. Oxford University Press, 1985.

[150] I. Yilgor, W. P. Steckle, E. Yilgor, G. Freelin, and J. Riffle. Novel triblock siloxane copolymers: Synthesis, characterization, and their use as surface modifying additives. *Journal of Polymer Science: Part A: Polymer Chemistry*, 27:3673–3690, 1989.

[151] I. Yilgor and E. Yilgor. Thermal stabilities of end groups in hydroxyalkyl terminated polydimethylsiloxane oligomers. *Polymer Bulletin*, 40:525–532, 1998.

[152] B. B. Zhao and J. S. Moore. Fast pH- and ionic strength-responsive hydrogels in microchannels. *Langmuir*, 17:4758–4763, 2001.

[153] E. Zrenner. Will retinal implants restore vision? *Science*, 295(8):1022–1025, February 2002.